# Optical Properties of Colloidal II-VI and III-V Semiconductor Nanocrystals: Single Nanocrystal Photon Correlation Spectroscopy

by

David Berkinsky

B.A. Chemistry, Pomona College (2019)

Submitted to the Department of Chemistry
in partial fulfillment of the requirements for the degree of

Doctor of Philosophy in Chemistry

at the

MASSACHUSETTS INSTITUTE OF TECHNOLOGY

May 2024



Signature of Author……

Department of Chemistry

April 22, 2024

Certified by……

Moungi G. Bawendi

Lester Wolfe Professor of Chemistry

Thesis Supervisor

Accepted by…….....

Adam Willard

Professor of Chemistry

Graduate Officer

This doctoral thesis has been examined by a Committee of the Department of Chemistry as follows:

Professor Keith A. Nelson……..

Chairman, Thesis Committee

Haslam and Dewey Professor of Chemistry

Professor Moungi G. Bawendi……

Thesis Supervisor

Lester Wolfe Professor of Chemistry

Professor William A. Tisdale……..

Member, Thesis Committee

Warren K. Lewis Professor of Chemical Engineering

# Optical Properties of Colloidal II-VI and III-V Semiconductor Nanocrystals: Single Nanocrystal Photon Correlation Spectroscopy

by

David Berkinsky

Submitted to the Department of Chemistry
on April 22, 2024, in partial fulfillment of the
requirements for the degree of
Doctor of Philosophy

## Abstract

Colloidal nanocrystals (NCs), also known as quantum dots, are nanometer-sized semiconductor crystalline structures comprised of thousands to tens of thousands of atoms placing them in a world between the molecular-sized and the bulk-sized world, allowing them to harness unique qualities from both. Colloidal NCs are used in many applications including light-emitting diodes (LEDs), photovoltaics (solar cells), lasers, transistors, photocatalysis, and many more.

In this thesis, I investigate the optical properties of colloidal NCs, specifically InP/ZnSe/ZnS, CdSe/CdS/ZnS, and ZnSe/ZnS NCs using a combination of ensemble and single NC photon correlation spectroscopic techniques. In the first chapter, I introduce the photophysical properties of colloidal NCs and spectroscopic techniques relevant to my studies. In the second chapter, I determine the dominant photoluminescent line shape broadening mechanisms in single InP/ZnSe/ZnS and CdSe/CdS/ZnS NCs using temperature dependent photoluminescent spectroscopic techniques. In the third chapter, I investigate the coherent emissive properties of single InP/ZnSe/ZnS and CdSe/CdS/ZnS at cryogenic temperatures, demonstrating the longest coherence time measured in a colloidal NC system to date. In the fourth chapter, I develop an ensemble third-order correlation technique to elucidate the average single ZnSe/ZnS NC triexciton efficiency and dynamics. Finally, I propose future directions in the fifth chapter, including a fourth order correlation technique to resolve absolute energy information on timescales faster than CCD-base spectroscopic techniques, and an open-access photon correlation Monte Carlo toolkit with the aim of filling education gaps and provide the colloidal NC community with a database of analytical tools that will encourage a wider audience to engage with photon correlation spectroscopy

Thesis Supervisor: Moungi G. Bawendi

Title: Lester Wolfe Professor of Chemistry

# Acknowledgements

There are so many people I need to recognize in my life. Not only for the support I have received over the last five years, but over the course of my life. I've been supported by so many people throughout the years in so many different ways.

I want to start by thanking Moungi Bawendi for being an amazing advisor. I am inspired by the way you have remained curious, even after all these years. I admire the way you treat all your graduate students on an equal level as soon as they enter the door in their first year. The respect and trust that you have in your students fosters an incredible environment for us to figure out how we want to navigate the scientific world. It has been a gift to learn from you.

Thank you to my thesis committee, Professor Keith Nelson and Professor William Tisdale. Thank you for providing me with another lens to think about the problems related to my work. My research is richer for it.

There are so many people who I have considered mentors while here at MIT. I want to start by thanking Dr. Jian Cui and Dr. Andrew Beyler. Although you have been out of the lab for over a decade, you both have been so willing to talk through difficult problems with me. Similarly, I want to thank Dr. Katherine Shulenberger for your guidance over the years. I cannot wait to learn more from you over the next few years when I get to work in your lab at Brandeis University. Thank you to Dr. Michel Nasilowski, Dr. Megan Klein, Dr. Matthias Ginterseder for being so kind and welcoming. You made the Bawendi Lab feel like a place I could call home. Thank you to Dr. Weiwei Sun for being my first in lab mentor, teaching me how to do basically anything that we do in the lab. And of course, thank you Dr. Andrew Proppe. You set an example for me on what a well-rounded scientist can be. I watched how hard you worked, how much you cared about your research. But I also watched how much fun you had while doing it, and how you always tried to include as many people as you could into your adventures. I always appreciated the balance we struck between having fun and working hard in the lab. I'll cherish our memories together in the Bawendi Lab for many years to come.

My time learning at MIT did not only come from advisors and mentors. I started my time at MIT with the Physical Chemistry cohort of 2019. Specifically, I want to thank Angela Lee, Audrey Norris, Maddie Hoffmann, Paul Cesana, Sarah Quinn, Shirley Chen, and Tara Šverko. We got through crazy times together, figuring out how to get through our classes, and also trying to navigate the Covid world when everything shut down in the middle of our second semester. I want to give a special thank you to Tara Šverko who joined the Bawendi Lab with me our first year. It has been a wild journey since our first days in the Bawendi Lab. The seemingly impossible challenges that we overcame together is insane. I know that I couldn't, and

wouldn't want to have done any of it without you. Thank you to Spectroscopy Subgroup, Dr. Alex Kaplan, Dr. Weiwei Sun, Dr. Megan Klein, Professor Lili Wang, Tara Šverko, Niamh Brown, Oliver Tye, Jonah Horowitz, Shelby Elder, Kaelyn McFarlane-Connelly, Shreyas Srinivasan, Annette Jones, and Dr. Linjie Dai. Our inquisitive conversations in subgroup, in the kitchen, or to and from the food truck were so helpful. To Jonah, Niamh, and Kaelyn, I have loved thinking through problems with you. I loved seeing you guys grow into amazing scientists. I can't wait to see the amazing things you do in the rest of your time during your PhD. To the rest of the Bawendi lab, to Dimuthu Hasanthi Thanippuli Arachchi, Meng-Chen Shih, Chantalle Krajewska, Oliver Nix, Aaron Li, Finn Beigelbock, Linda Koth, Dr. Cole Perkinson, Dr. Juanye Zhang, Yongli Lu, Yu-Kuan Lin, Dr. Ulugbek Barotov, Dr. Hua Zhu, Dr. Matthias Grotevent, Dr. Shaun Tan, and Dr. Mari Saif, thank you for the community we all helped create together. The Bawendi Lab is a special place that I'm not quite ready to let go of quite yet. I am thankful I will be in Boston for the next few years at the very least.

My education did not start at MIT. There were so many teachers and mentors through my life. I want to start by thanking my middle school band teacher, Mrs. Carpenter. I was a bit of a troublemaker in this time of my life. My relationship with most teachers were neutral to antagonistic, but Mrs. Carpenter created a safe space for me. Although I wasn't quite ready to become a serious student, she gave me the space and trust that made me feel comfortable. To my high school Physics teacher, Mr. Khalil, you were an unconventional role model for me. You were unapologetically you in an environment that did not encourage that. At the same time, you maintained a learning environment that was exciting and fostered genuine curiosity. To my undergraduate advisor at Pomona College, Professor Grieman, thank you for creating a home away from home for so many students. I saw how much you cared for the development of your student's scientific progression, but always took the time to ask about the other parts of our life. I always felt I could come to you with any problem that I had. Finally, to my high school football coach, Bill Carpluk, I watched and learned from you on what it really means to be a leader. You put your heart and soul into making all of us better men. The way every single person on our team felt that you truly loved and cared for us meant so much for me. I strive to carry myself in the same way you do.

It took a village to raise me and to support me while I tried to find, and am still trying to find who I want to become. To Mimi and Poppi, you have been so grounding for me over the years. Mimi, you have shown me what it means to be composed, graceful, wise, yet a strong force in any room. Poppi, you've taught me how to fight for what I believe in, while having a damn good time doing it. To Grandma Rhea, I have always felt your unconditional love and always feel safe in your presence. To Grandpa Norman, I love you and wish I had more time to get to know you. People always tell me the ways we are similar, and that makes me so happy to hear. I hope I make you proud. To Grandpa Ootah, you have shown me that there is no age

limit to having a child-like sense of curiosity. I strive to approach learning for the sake of learning like you. To Aunt Jessi and Uncle Santino, thank you for being such an incredible example. I don't know if I ever would have considered a PhD if it wasn't for you guys. There was so much family that have given me the confidence to be my own person, to be kind, loving, and so much more. Thank you to Aunt Kristine, Aunt Joanna, Uncle Sam, Aunt Pamela. Thank you to the Slaughters, the Franks, the Blumers, the Cohns. Thank you to my friends' families who were always loving to me, to the Hogobooms, the Caravettas, the Ragos, the Masiellos, and the Smiths.

I want to highlight my friends who have been absolutely amazing to me. To Ben, we have been friends since the second grade. I've had the pleasure of growing up together in many chapters of our lives. I can't believe I just went to your wedding this last year! Thank you for always being there for me. To Harry, we have been on this crazy academic journey together at the same time. I am so thankful that we can celebrate each other's achievements, and I'm so thankful we have always been able to keep each other up when it gets hard. Also of course, thank you for entertaining this wild project that may or may not ever get done. To my Boston friends Erin, Clark, Nicolai, Reef, and Yasmine, you all have kept me so grounded through the years we have all been in the Boston area. Love you guys. To Stuart, thank you for making the Beacon Capitol Market feel like family. Thank you to Andre and Rose for helping foster such a lovely community. And to my friends in the Coalition for Palestine and the Jews for Ceasefire, thank you for being in such a loving and supporting community over the last seven months. I would not have been able to do it without you. The Coalition for Palestine is a necessary reminder to me and to scientists everywhere that our labor can never be disconnected from its impact, good or bad. We all have a responsibility to make ethical choices about how we want our labor to contribute to society.

Finally, I wanted to save the last part of my acknowledgements for a few special people that are dear to me.

To Lea, you are my guiding light. We met on our first day of school at Pomona College in 2015, and I am so thankful we have found a way to still be in each other's lives. We have held each other up through so much over these last few years. I wouldn't want to do it with anyone else. I love you.

To Nora, I couldn't ask for a better sister. You are growing into such an amazing, confident person with a huge heart. I cannot wait to see you grow into who you want to be. I love you.

To my Mom and Dad, thank you for everything. I can't imagine it was always easy to raise me. I have always loved to cause a little trouble here and there. Thank you for creating a home that allowed me to figure things out on my own terms, in a way that has made me more confident in who I am. Thank you for your patience, your unwavering support, and your love. I have always felt it. I love you.

# Contents

# List of Figures

## Chapter 1



## Chapter 2

**Chapter 3**

**Chapter 4**

**Chapter 5**

# List of Tables

**Chapter 2**



**Chapter 3**

# Chapter 1

# Introduction

## 1.1. A Little Background

Colloidal nanocrystals (NCs), also known as quantum dots, are nanometer-sized semiconductor crystalline structures comprised of thousands to tens of thousands of atoms. Colloidal NCs exist between the molecular-sized and the bulk-sized world, allowing them to harness unique qualities from both. Bulk semiconductors have an intrinsic bandgap energy, the energy difference between the valence band (VB) and conduction band (CB), spanning across the ultraviolet (UV), visible, and infrared (IR) sections of the electromagnetic spectrum. The bandgap in semiconductors are utilized in many optical and electronic applications including light-emitting diodes (LEDs), photovoltaics (solar cells), lasers, transistors, photocatalysis, and many more.[1] The bandgap energy differs depending on the semiconducting material, and can also be tuned by doping other semiconductor materials into the system.

In 1982, Louis Brus sought to increase catalytic efficiencies using semiconductor particles by increasing the surface area – decreasing semiconductor particle size.[2] Depending on the particular synthesis, Brus observed a change in color of the aqueous solution of semiconductor particles, and made the Nobel Prize-worthy speculation that the change in color was due to the quantum size effect. The quantum size effect is introduced in one of the first lessons taught in any undergraduate class on quantum mechanics or physical chemistry, through the example of the particle in a box.[3]

The particle in a box is a thought experiment where a single particle is confined in an infinitely deep well. Given the mass of the particle $m$ and the length of the box $L$, the energy of the particle (**Equation 1.1**) can be derived using the Schrödinger equation:

$$E_n = \frac{n^2 h^2}{8mL^2} \tag{1.1}$$

where $n$ is the energy level and $h$ is Planck's constant. This equation provides us with several interesting implications of the wave-particle duality of matter. For one, the energy of this system can never be zero because $n > 0$. Also, $n$ being an integer indicates that the energy of the system is quantized. And lastly, the energy of the particle can change by tuning the length of the box. The smaller the box the particle is contained within, the higher the energy of the particle. The particle in a box is a fantastic introduction into the peculiarities of quantum mechanics that do not manifest in our macroscopic world experience.

An exciton, an electron-hole pair, within a semiconductor behaves like particle in a box — or rather a particle in a sphere — if the semiconductor is small enough. In any given semiconductor, the exciton has a material-dependent radius referred to as the Bohr radius. If the semiconductor NC is smaller than twice the Bohr radius, the exciton will be quantum mechanically confined in a similar manner as the particle in a box. Taking into account the additional two dimensions and coulombic interactions of the electron and hole, Louis Brus developed the Brus Equation[4]

$$E_{NC}(R) = E_{bulk} + \frac{h^2}{8R^2}\left(\frac{1}{m_e^*} + \frac{1}{m_h^*}\right) - \frac{1.8e^2}{4\pi\varepsilon_0\varepsilon_r R^2} \tag{1.2}$$

where $E_{bulk}$ is the band gap energy of the bulk semiconductor, $h$ is Planck's constant, $R$ is the radius of the NC (in place of $L$ in the 1D case), $m_e^*$ is the effective mass of the excited electron, $m_h^*$ is the effective mass of the excited hole, $\varepsilon_0$ is the permittivity of vacuum, and $\varepsilon_r$ is the relative permittivity. The first term takes into account the bulk bandgap energy, the second term takes into account the quantum confinement effect, and the third term takes into account the coulombic interactions within the NC.[5] Since the publication of the Brus Equation in 1984, there have been attempts at providing further detail to accurately describe the energy in a quantum confined NC system.[6,7] Regardless of the Brus Equation's ability to describe real NC systems accurately, the theoretical principle birthed a field that has just received the Nobel Prize in 2023.

Moungi Bawendi, who worked for Louis Brus as a postdoc, started his career as a professor at MIT with the goal of synthesizing semiconductor NCs with precise control. Moungi Bawendi, Chris Murray, and David Norris made an experimental breakthrough in 1993 demonstrating the synthesis of relatively monodisperse CdE (E = S, Se, Te) NCs – credited in the 2023 Nobel Prize in Chemistry.[8] These colloidal NCs were synthesized using the hot-injection method which works in two phases. The first phase is the nucleation phase where one of the semiconductor precursors – in this case, the E = S, Se, Te precursor – is rapidly injected into a heated-up mixture containing the other semiconductor precursor – in this case, the Cd precursor. The small NC nuclei saturate the solution such that no new nuclei are made. The second phase is the growth phase where the injected precursors react with the NC nuclei to increase the size of the nuclei.[9] The experimental realization of a quantum confined semiconductor system has led to decades of NC research contributing to several industries from the television display industry[10] to the biomedical imaging industry[11] to the solar cell industry, and continues to push into new fields like the quantum information sciences (QIS)[12].

To go from the initial inception of quantum confined NCs to their application in industry, a great deal of research was required. There were early challenges in NC synthesis and spectroscopy that limited their ability to perform in any industry. Semiconductor NCs were not photostable, they had low quantum yield (emission efficiency), and low color purity. There were issues beyond the ideal theoretical system that

had to be understood and controlled. Creative and intelligent people from all over the world took on the challenge and gathered a tremendous amount of knowledge on semiconductor NC photophysics. Researchers in the semiconductor NC field have become skillful nanoengineers pushing the bounds on what we can manipulate at the nanoscale.

In my attempt to contribute to this field, my research focused on studying the electronic and photophysical properties of InP and ZnSe NCs investigated using a combination of ensemble and single-NC spectroscopy techniques, and I aimed to contribute to advancements of the correlation spectroscopy techniques used in the Bawendi Lab. The rest of the Introduction serves to provide more background on colloidal NCs and the spectroscopic methods used to study them. Chapter 2 of my thesis seeks to investigate the line shape broadening mechanisms that reduce the color purity of InP NCs. Chapter 3 of my thesis explores the potential for single InP NCs as single photon emitters for QIS applications. Chapter 4 of my thesis extends a third-order correlation technique to characterize the ensemble-averaged ZnSe NC triexciton QY and dynamics in solution. Chapter 5 of my thesis explores two future directions: the first is the advancement of a Bawendi Lab technique, photon-correlation Fourier spectroscopy (PCFS), to resolve asymmetric line shapes using fourth-order correlations, and the second explores the development of the Photon Correlation Monte Carlo toolkit for the purpose of providing the semiconductor NC community with easy access simulated photon streams to aid in developing fundamental understanding of photon-correlation experiments and to test analysis methods. I hope this chapter serves to spark the interest and direction of future graduate students. For whoever reads this thesis, thank you for taking the time to see a glimpse of the semiconductor NC field through my perspective.

## 1.2. Colloidal Nanocrystals

In this section, I will cover the basics of colloidal NCs including their structure and relevant photophysical properties that were relevant to my research. This introduction into colloidal NCs will consist of general information relevant to most semiconductor NC systems; however, I will include interesting and relevant information about InP and ZnSe NCs specifically as they were the focus of my experimental research.

### 1.2.1. Nanocrystal Structure

Early demonstrations of colloidal NCs showed low emission efficiencies, were broad in their emission spectra, and were prone to permanent photobleaching.[8] The surface was identified as playing a significant role in NC emission. As a semiconductor particle size decreases, the surface-to-volume ratio grows, meaning a high number of the atoms in colloidal NCs are on the surface. Colloidal NCs are never perfectly crystalline and as a result there will always be atoms that are not coordinated, particularly on the surface.[13] These uncoordinated atoms have what are called dangling bonds. Organic ligands are

incorporated into the synthetic procedure because they play a crucial role in colloidal NC stability and solubility. Without organic ligands, inorganic NCs would not be able to be suspended in typical organic solvents. Common ligand groups are carboxyl, amino, thiol, and phosphate groups.[13] These ligand types can be split into three categories: (1) L-type ligands are neutral donors that datively bond to the NC surface. These bonds are weak and will often lose their bonds to the NC surface when in the presence of other ligands. (2) X-type ligands have strong electron affinity allowing them to bond strongly to the NC surface. These ligands form covalent bonds with metal surface orbitals. (3) Z-type ligands bind to surface anion sites acting as a Lewis acid.[14] There is much work on developing new ligand structures to improve colloidal NCs for a variety of applications such as increasing charge carrier mobility in NC solar cells,[15] functionalization for biological applications,[16] passivating defect sites,[17,18] and increasing the coherent fraction of emission from single NCs.[19] The versatility of organic ligands enables colloidal NCs to be functionalized for a wide range of applications.

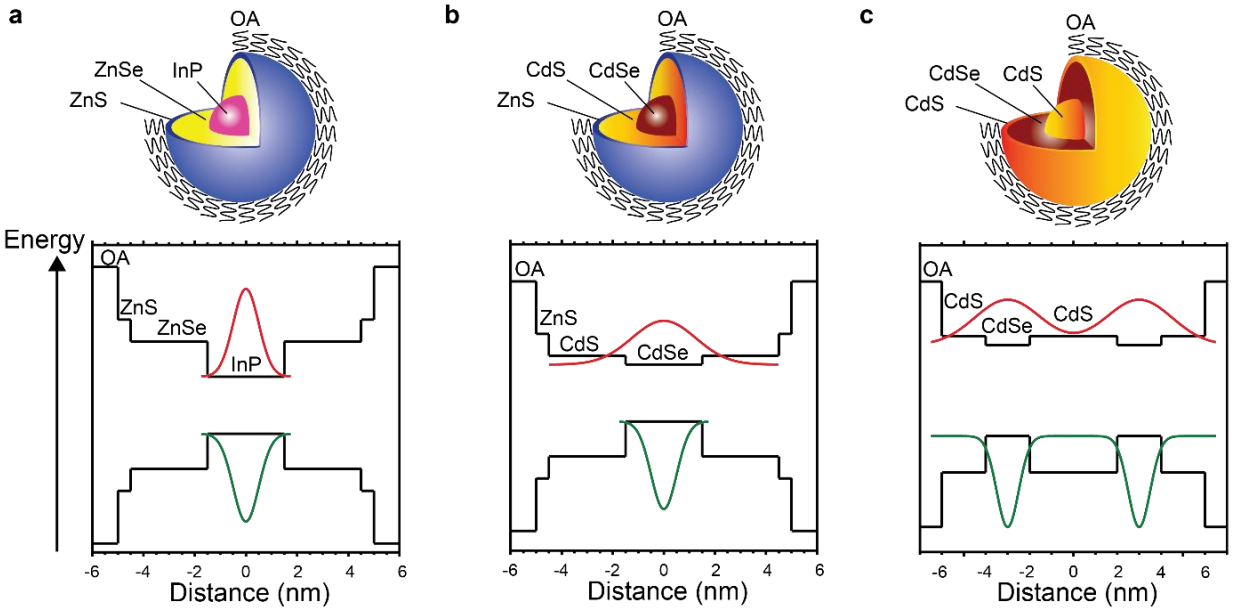


**Figure 1.1.** Core/shell/shell NC heterostructure diagram for **a.** InP/ZnSe/ZnS, **b.** CdSe/CdS/ZnS, and **c.** CdS/CdSe/CdS NCs, all with oleic acid (OA) ligands covering the outer surface of the NC. Below each NC structure is its respective band energy diagram displaying the electron and hole wavefunction spread across the NC.

The use of organic ligands to cap the inorganic NC surface is crucial for NC stability and solubility, however it has proven to be an incomplete solution to optimize photophysical properties of colloidal NCs. The dynamic environment of NCs in solution makes it challenging to avoid ligand loss, leaving dangling bonds on the NC surface. Additionally, steric hindrance between these long carbon chain ligands leads to unideal surface coverage.[18] In 1996, Margaret A. Hines and Philippe Guyot-Sionnest demonstrated the synthesis of CdSe NCs with an inorganic ZnS shell improving the QY of the NCs to 50%, attributing the

increased emission efficiency to a better passivation of the CdSe surface.[20] Increasing the shell thickness acts to protect the exciton from the surface, further improving the emission efficiencies.[21] The ability to synthesize core/shell heterostructures has opened up opportunities for colloidal NCs in many optical applications. The most commonly used NC heterostructures are designed to have a Type I or quasi-Type II band structure. These heterostructures are designed such that the electron and hole are confined within the center of the NC, away from the surface. Type I heterostructures such as InP/ZnSe/ZnS (core/shell/shell) confine both the electron and hole within the core material (**Figure 1.1a**). The large energy difference between the core and inner shell CB and VB prevents the electron and hole wavefunctions from tunneling into the inner shell material. On the other hand, quasi-Type II heterostructures like CdSe/CdS/ZnS have a much smaller energetic difference between the core and inner shell CB levels such that a significant degree of the electron wavefunction can tunnel into the inner shell. In quasi-Type II heterostructures, the electron delocalizes across the core and shell, but the hole remains confined within the core (**Figure 1.1b**). The hole is often heavier and as a result cannot tunnel as far, even with similar CB and VB energy differences between the core and shell.[22,23] Many NC heterostructures include an additional outer shell to further passivate the surface and ensure the electron and hole wavefunctions are prevented from reaching the surface.

Over the years, chemists have harnessed the synthetic handles governing colloidal NC synthesis leading to creative systems such as the colloidal quantum shell where the active emitting layer is actually the inner shell rather than the core (**Figure. 1.1c**). The quantum shell has a unique electron and hole wavefunction that spreads across a much larger distance allowing the quantum shell NC to be pumped with higher fluxes useful for lasing applications.[24,25] Additionally, NC structures are not restricted to the classic three-dimensional 'quantum dot' shape. There are NC two-dimensional platelets,[26–28] one-dimensional rods,[29,30] and all sorts of shapes with interesting and unique photophysical properties.[23,31–34]

Synthetic chemists in the colloidal NC field have opened up a world of opportunities to explore the underlying photophysics guiding NC emission. The next section will cover the colloidal NC properties relevant to my studies including exciton recombination, exciton fine structure, phonon coupling, photoluminescence (PL) intermittency, spectral diffusion, Auger recombination, and line shape broadening mechanisms.

### 1.2.2. Photophysical Properties of Colloidal Nanocrystals

As I am writing my thesis, I am reflecting on the fact that I wish I started writing years ago. There are so many important and interesting qualities of colloidal NC photophysics. It feels like I could talk endlessly on just the topics related to my work over the last five years. As a result, I will only scratch the

surface in this introduction and encourage anyone who reads this to explore the cited work and see for themselves the infinite depth that colloidal NC photophysics has to offer.

#### *1.2.2.1. Exciton Recombination*

Exciton (electron-hole) recombination in its simplest form depends on the interactions of the NC energetic states with the surrounding electromagnetic field. Building up from quantum mechanical principles – which we learned in 5.74, Introductory Quantum Mechanics II – we can describe the rate of exciton radiative recombination using the Weisskopf-Wigner Theorem (**Equation 1.3**).[35]

$$\mathrm{k_r} = \frac{\omega^3 n|\mu_{12}|^3}{3\pi\varepsilon_0\hbar c^3} \tag{1.3}$$

$k_r$ is the radiative rate, $\omega$ is the emission frequency, $n$ is the refractive index, $|\mu_{12}|$ is the exciton transition dipole moment, $\varepsilon_0$ is the vacuum permittivity, $\hbar$ is the reduced Planck's constant, and $c$ is the speed of light. When considering the radiative emission of a semiconductor material, we consider properties such as the absorption cross-section,[36] the oscillator strength,[37] and the electron hole overlap integral.[38]

In real systems, there is much more interacting with the excitons within the NC than just the surrounding electromagnetic field. Excitons interact with external charges and other excitons, they interact with the imperfections of the NC lattice, with vibrations through the NCs typically referred to as phonons, with other NCs, and many more.[39] All of these additional interactions contribute to unideal radiative recombination, or even nonradiative recombination of the exciton. We can draw the relationship of the radiative rate $\mathrm{k_r}$ and the nonradiative rate $\mathrm{k_{nr}}$ of emission and its impact on the overall quantum yield QY of NC emission through **Equation 1.4**.

$$QY = \frac{k_r}{k_r + k_{nr}} \tag{1.4}$$

Descriptions of relevant unideal radiative and nonradiative recombination mechanisms will be described in following sections.

#### *1.2.2.2. Photoluminescence Intermittency*

There are several optical properties of colloidal NCs that are averaged out, or clouded by ensemble emission effects, requiring single NC PL studies to elucidate the more subtle properties of NC photophysics. In 1996, Nirmal et al. showed the PL from single CdSe NCs appeared to turn "on" and "off" in a binary like process.[40] For NC applications requiring efficient photon emission, this PL intermittency is obviously unideal. On the other hand, if an optical application requires photon absorption with negligible photon emission, it would be ideal to encourage NCs to permanently remain in the "off" state. This observation triggered a number of studies aimed at understanding and controlling PL intermittency in colloidal NCs.[41–44] It is conventionally understood that there are two types of PL intermittency: Type A and Type B.

Intermittency is identified as Type A blinking when the PL intensity is correlated with the PL lifetime. This kind of blinking is often times associated with charged emission referred to as trion emission, which is dimmer and has a faster lifetime.[45] Type B intermittency has no correlation between the PL intensity and PL lifetime and arises from the reversible trapping of higher energy holes by surface states.[46] PL intermittency arises in many other systems studied to this day such as InP (**Figure 1.2**),[47] $CsPbBr_3$,[48] and PbS.[49]

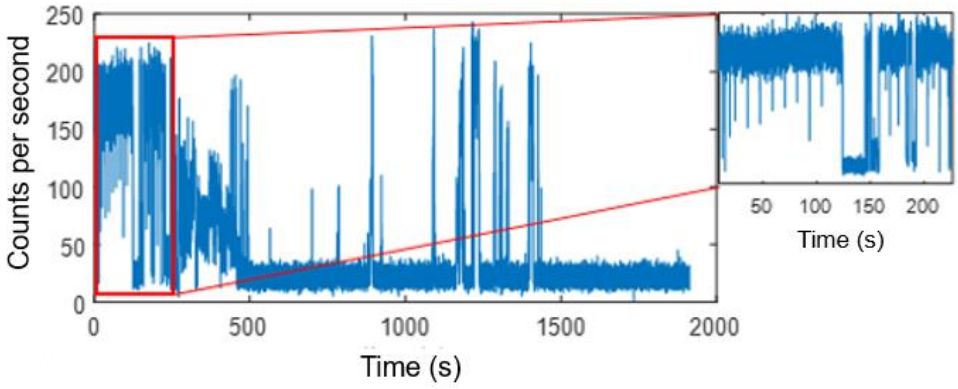


**Figure 1.2.** Intensity time trace of a single InP/ZnSe/ZnS NC at room temperature. Inset shows the intensity time trace from 0-240 seconds to see the PL intermittency more clearly.

#### *1.2.2.3. Exciton and Multiexciton Generation and Recombination*

Photon absorption in NCs follows a Poisson distribution, a discrete probability distribution that describes the likelihood of generating a number of events $m$ in a given interval, given a rate $p$ of occurring events. For NCs, given an average excitation rate (or excitation density) $p$, the probably of absorbing $m$ photons is

$$Poi(m,p) = \frac{p^m e^{-p}}{m!}. \tag{1.5}$$

One of the major implications of the Poisson nature of photon absorption in semiconductor NCs is the fact that NCs can hold multiple excitons at once. When an NC absorbs two photons at once, the two excitons that are created are referred to as the biexciton. When three excitons are created, it is referred to as the triexciton, and so on. Multiexcitons are characterized in this way because the excitons see and feel each other in the small space within the NC and as a result, behave differently than single excitons.

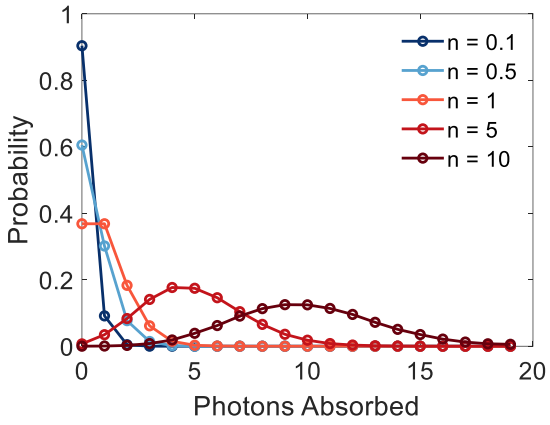


**Figure 1.3.** Poisson distribution describing the probability of absorbing $m$ photons given a particular excitation density $n$.

For instance, in the example where the NC holds a single exciton (**Figure 1.4a**), the exciton can only radiatively recombine when the electron and hole have inverse spins. At room temperature these spins can flip up and down at a rate significantly faster than $k_r$. Therefore, the electron-hole pair is in the correct spin orientation half of the time which leads to the exciton radiative rate $k_X = \frac{1}{2}k_r$. Now let's consider the example where the NC holds two excitons, the biexciton (**Figure 1.4b**). In this case, there are two electron-hole pairs, preventing individual charges from flipping their spins. For the biexciton, the overall radiative rate $k_{BX} = 2k_r$. This thought experiment describes the basic principle of statistical scaling of multiexciton emission. It is important to keep in mind that imperfect exciton-exciton interactions can lead to deviations from statistical scaling.

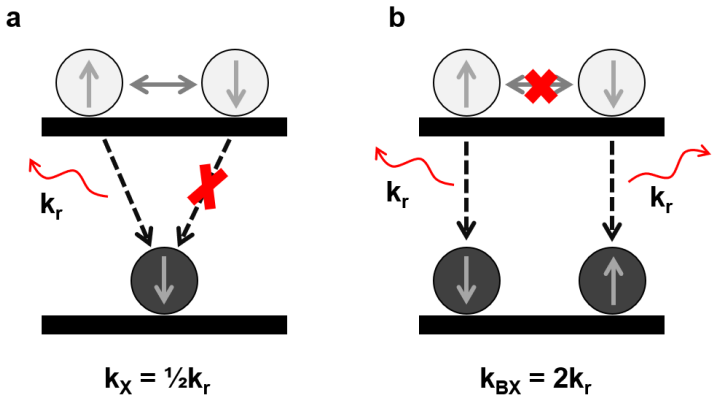


**Figure 1.4. a.** Example of a single exciton where the electron flips spins from spin-up to spin-down. While spin-up, the electron-hole pair radiatively recombines with rate $k_r$. While spin-down, the electron-hole pair cannot radiatively recombine. **b.** Example of a biexciton where the electrons and holes cannot flip spins. In this case, both electron-hole pairs radiatively recombine with rate $k_r$.

The ability for semiconductor NCs to hold multiple excitons at once allows NCs to have a higher photon output, making them great for light emitting applications, and also introduces interesting

photophysical interactions of excitons that can be explored for applications such as quantum entanglement of excitonic states.[50] However excitons can interact in ways that lead to nonradiative recombination of multiexcitons. The dominant mechanism of nonradiative multiexciton recombination is Auger recombination, which occurs when the energy from an electron-hole recombination promotes another charge into a higher-lying energetic state instead of outputting as a photon (**Figure 1.5a**). The excess energy of the charge is then lost to thermal energy as the charge relaxes back to the band edge (**Figure 1.5b**), leaving a single exciton in the NC (**Figure 1.5c**). **Figure 1.5** shows an example of negative Auger recombination, which promotes a second electron to a higher lying energetic state, however Auger recombination can occur by promoting the electron or hole to a higher lying state. An extensive amount of research has been produced to understand Auger recombination and learn how to prevent it.[51–53]

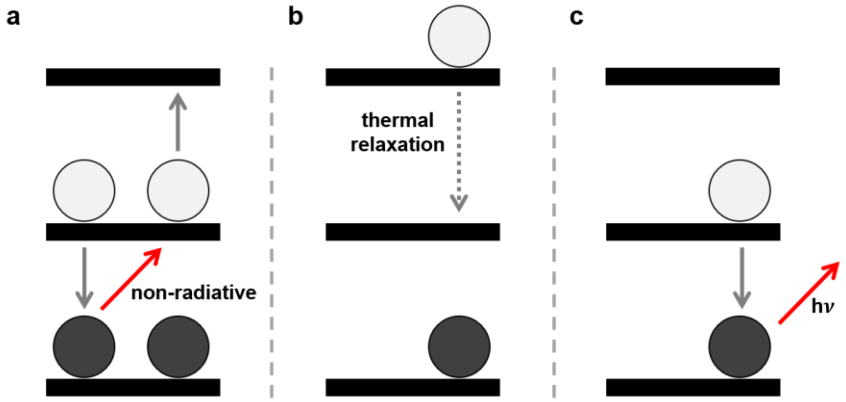


**Figure 1.5. a.** Energy from the recombination of an electron-hole pair promotes another electron into a higher lying energetic state. **b.** Higher energy electron thermally relaxes back to the band edge. **c.** Single electron-hole pair radiatively recombines, emitting a photon.

#### *1.2.2.4. Fine-Structure Splitting in II-VI and III-V Semiconductor Nanocrystals*

Fine-structure splitting (FSS) plays a significant role in exciton photophysics of colloidal NCs. In II-VI and III-V semiconductor NCs, the lowest lying excitonic state originates from the two-fold degenerate $1S_e$ ground electron level and the four-fold degenerate $1S_{3/2}$ ground hole level, resulting in an overall $1S_{3/2}1S_e$ excitonic state that is eight-fold degenerate. Due to the electron-hole exchange interaction, which is significant in small colloidal NCs,[54] the eight-fold degenerate state splits into a five-fold degenerate state with total momentum $F = 2$ and a three-fold degenerate state with total momentum $F = 1$.[55] The $F = 2$ state is optically forbidden and has been directly observed in systems like CdSe and InP at low temperature,[47,56] and the $F = 1$ state is optically allowed. The degeneracy of these states can be split even further by a combination of the crystal field and shape anisotropy interactions with the exciton. In both of these cases, deviation from perfect symmetry of the NC leads to the exciton "feeling" a unique axis within the NC. Depending on whether the asymmetry contributes negatively or positively, the $F_z = \pm 2$ fine-

structure state will increase in energy or decrease, respectively. The $F_z = 0$ fine-structure state will have the opposite reaction to the anisotropy of the NC.[57]

Fine-structure splitting impacts exciton dynamics and line shape broadening, affecting colloidal NC systems ability to be used in several applications including light-emitting and quantum optical applications, among many others. Many studies have attempted to understand and control fine-structure splitting in colloidal NCs, and will continue to be a topic of research for many years to come.[47,54,57–61]

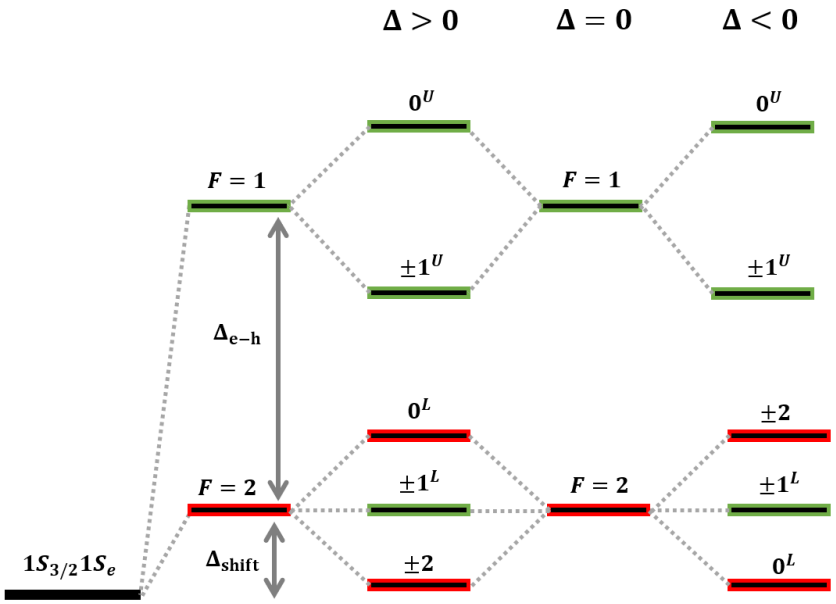


**Figure 1.6.** Adapted from Efros et al.[62] Fine-structure splitting of the 8-fold $1S_{3/2}1S_e$ exciton energetic state. $\Delta_{shift}$ corresponds to an overall shift of the fine-structure manifold, $\Delta_{e-h}$ corresponds to the splitting between the total momentum $F = 2$ and $F = 1$ energetic states resulting from the electron-hole exchange interaction, $\Delta = \Delta_{int} + \Delta_{sh}$ is the splitting energy of the $F = 2$ or $F = 1$, where $\Delta_{int}$ is the splitting energy from crystal field's deviation from a symmetric cubic structure and $\Delta_{sh}$ is the splitting energy from the overall NC shape asymmetry. The numbers associated with the fine-structure states correspond to the angular momentum projections total. Red colored states correspond to optically forbidden fine-structure states and green colored states correspond to optically allowed fine-structure states.

#### *1.2.2.5. Coherence Time and Photon Indistinguishability*

The fundamental limit to the line width Γ of an emitter is referred to as the transform limit

$$\Gamma = \frac{\hbar}{T_1}, \tag{1.6}$$

where $T_1$ is the radiative lifetime and $\hbar$ is the reduced Planck's constant. We can also rephrase the line width in units of time which we refer to as the coherence time $T_2$. The fundamental relationship between the coherence time and radiative lifetime in the ideal transform limit is

$$\frac{1}{T_2} = \frac{1}{2T_1}. \quad (1.7)$$

The inverse relationship between Γ and $T_1$ is related to the time-energy uncertainty principle. The faster the radiative process, the less certain – or broader – the energetic spectrum. In this ideal picture, one would think that emitters with long lifetimes would be ideal candidates to achieve the narrowest emitter line width possible. In reality there are many ways the exciton wavefunction loses its phase by interacting with the system surrounding it that leads to significant broadening of the line width.

These dephasing mechanisms fit under the category of pure dephasing mechanisms. If a mechanism of dephasing interacts with the exciton prior to its radiative recombination and interferes with the phase of the exciton, but does not change the specific transition from one energetic state to another, then it is considered pure dephasing. Here is another situation where the time-energy uncertainty principle comes into play. The faster the interaction of the exciton with its surroundings, the more the exciton loses its phase and the more uncertain the energy becomes. We characterize the loss of coherence by the dephasing time $T_2^*$ which affects the coherence time (line width) of the emitter according to **Equation 1.8**.

$$\frac{1}{T_2} = \frac{1}{2T_1} + \frac{1}{T_2^*} \quad (1.8)$$

To achieve transform-limited emission, or indistinguishable photon emission, of colloidal NC systems, in depth studies of material optimization,[63] fine-structure,[58,64] exciton-phonon coupling,[47] electric- and magnetic-field interactions,[65,66] and integration into photonic devices[67] must be performed to optimize these systems for quantum information science applications.

#### *1.2.2.6. Photoluminescence Line Shape Contributions*

The PL line shape of an ensemble of colloidal NCs at room temperature can typically be fit with one or two Gaussians. The line shape is rather featureless, clouded by ensemble averaging and thermal broadening. If we take a closer look by isolating single NCs and cooling down the temperature, we can start to see the complex nature of the PL line shape. There is fine-structure, exciton-phonon coupling, spectral diffusion, and pure dephasing that push the NC line shape far from the transform-limited ideal. In this section, I aim to provide a brief conceptual picture of these various mechanisms of line shape broadening.

***Ensemble Broadening***

Ensemble broadening is a result of NC size and morphology polydispersity as well as a distribution in local chemical environments.[68,69] The variations in NC structure and environment lead to variations in the energetic spectra of the NCs. By measuring the ensemble PL spectrum, we end up taking a look at the sum of all NC spectra together (**Figure 1.7**). Ensemble broadening can be one of the most significant

sources of broadening in NC systems, contributing hundreds of meV in some systems.[68] It is a significant synthetic challenge to create monodisperse, uniform NCs colloidally.

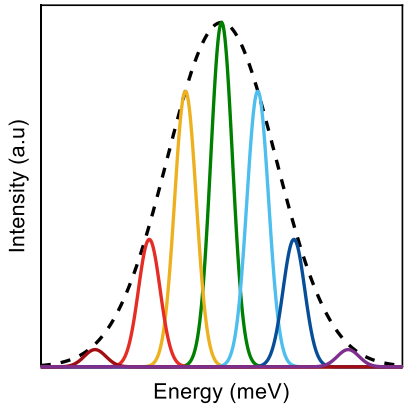


**Figure 1.7.** Variations in NC structure and environment lead to a distribution of PL spectra (colored spectra). Ensemble PL spectra (dotted black spectra) is the sum of all individual NC PL spectra.

### *Fine-Structure Splitting*

The origin of fine-structure splitting has been discussed in **Section 1.2.2.4.** Depending on the system, fine-structure splitting can contribute anywhere from 1 meV to 30 meV to colloidal NC PL line shapes.[27,47,70] In **Figure 1.8**, a second fine-structure state grows in at 30K, broadening the line shape by approximately 4 meV.

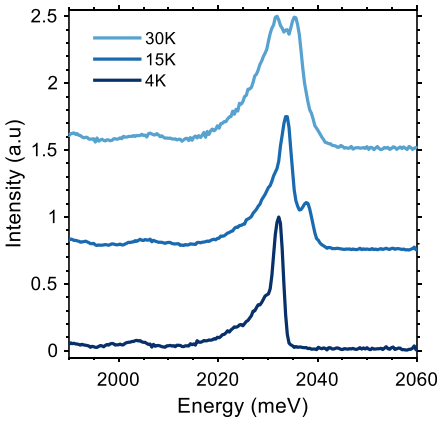


**Figure 1.8.** Three single InP NC spectra at 4K, 15K, and 30K.

### *Spectral Diffusion*

Local fluctuations in the electric field surrounding NCs results in a Stark effect that shifts the energy of the NC PL tens of $\mu$eV to tens of meV across timescales ranging from picoseconds to seconds.[58,71,72] **Figure 1.9a** shows a narrow Lorentzian PL spectra jumping to different center emission energies as a result of the local fluctuations of the electric field in the environment. If someone were to take a PL spectrum

with a long integration time, they would see a broad Gaussian-like spectrum (**Figure 1.9a**, dotted-black) instead of the narrow Lorentzian PL spectrum. **Figure 1.9b** shows a series of PL spectra taken of a single ZnSe NC at 4K. The spectrum appears to jump to different energies over time. If a single PL spectrum was taken over a long period of time, the sum spectra would appear as a number of different peaks, possibly suggesting the emission is coming from multiple NCs. However, taking a series of PL spectra helps elucidate that this spectrum is indeed coming from a single NC that is affected by spectral diffusion. We can isolate specific frames of this series of spectra where the NC was spectrally stable and take a closer look at the PL spectrum (**Figure 1.9c**). We can see that the PL spectrum of this single ZnSe NC is actually quite narrow, and that if these ZnSe NCs could become more spectrally stable, they could make good candidates for quantum emitter applications in the future.

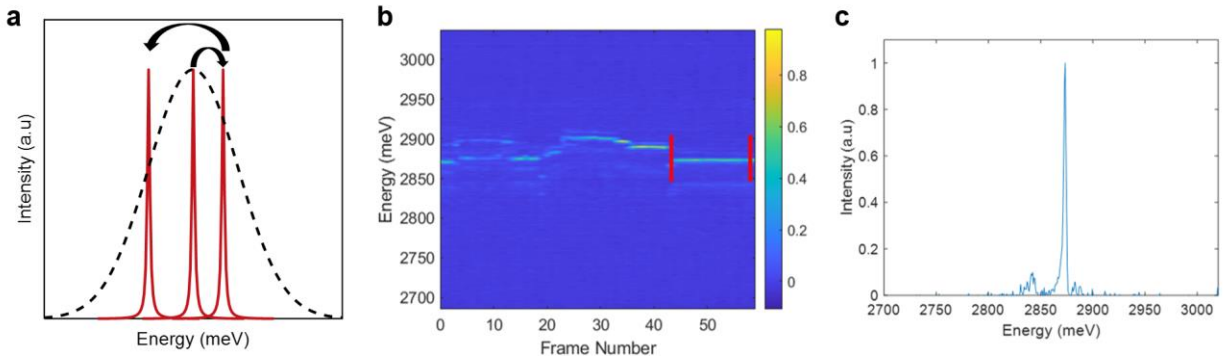


**Figure 1.9. a.** Narrow Lorentzian PL (red) spectrum hopping to different emission energies. Over time, the sum PL spectrum sums to a broader Gaussian (dotted black). **b.** A series of individual spectra of a single ZnSe/ZnS NC at 4K. The series of spectra show that the single NC energy jumps around due to spectral diffusion. The series of spectra from frames 43-60 (within the red lines) are summed together to show **c.** a narrow, stable PL spectrum of a single ZnSe/ZnS NC.

### *Exciton-Phonon Coupling*

Exciton-phonon coupling is a broad term to describe the effect of vibrations in the NC lattice on the exciton. Exciton-phonon coupling can arise through inelastic or elastic phonon scattering.

Inelastic phonon scattering involves the real emission or absorption of phonons as a result of the exciton coupling to the lattice vibrations (**Figure 1.9a,b**), characterized by the Huang-Rhys parameter[73] and gives rise to phonon sidebands (replicas of the zero-phonon line, ZPL) seen in many QD systems (**Figure 1.9c,d**).[61,74–77] In the single InP NC system at 4K shown in **Figure 1.9a,c**, the excited exciton recombines through the ZPL transition, or through processes involving the emission of a number of phonons. At low temperature, there is not enough energy in the system for the NC lattice to move, meaning there are no phonons accessible to absorb. All transitions at low temperature result from the ZPL or from transitions

lower than the ZPL. Once the temperature is raised to 30K in **Figure 1.9b,d**, the exciton is able to absorb phonons, resulting in radiative recombination transitions that are higher than the ZPL.

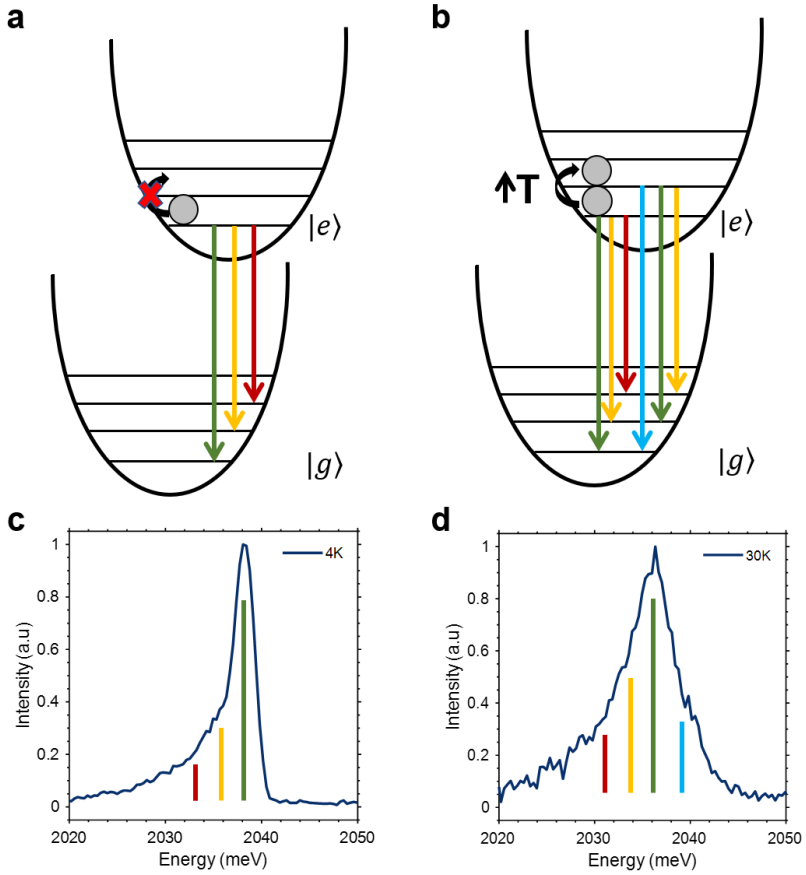


**Figure 1.10.** Ground and excited electronic states are approximated to be harmonic oscillators. **a.** At 4K, the energy of the system is low such that the exciton does not have enough energy to transition into higher vibrational states within the excited electronic state. All radiative transitions occur at the ZPL (green), or lower in energy than the ZPL (yellow, red). **b**. At 30K, the energy of the system is sufficient such that the exciton can absorb a phonon to transition to a higher vibrational state within the excited electronic state. Radiative transitions can now occur at the ZPL (green), lower in energy than the ZPL (yellow, red), and higher in energy than the ZPL (blue). **c**. PL spectrum of a single InP NC at 4K, superimposed with the ZPL transition (green), one-phonon emission line transition (yellow), and two-phonon emission line transition (red). **d.** PL spectrum of a single InP NC at 30K, superimposed with the ZPL transition (green), one-phonon emission line (yellow), two-phonon emission line (red), and one-phonon absorption line (blue).

Elastic phonon scattering, a mechanism of pure dephasing, involves the virtual emission and absorption of phonons. This process randomizes the phase of the electronic wavefunction, causing a loss of coherence and a broadening of the ZPL, but does not change the central emission energy.[78] In the absence of elastic phonon scattering, the exciton remains in the ground vibrational state of the excited electronic state, undisturbed prior to radiatively recombining (**Figure 1.11a**). The exciton wavefunction remains in phase, leading to a coherent radiative recombination process (**Figure 1.11c**) that is narrow in its PL

spectrum (**Figure 1.11e**, solid green spectrum). As the temperature increases, the exciton becomes more susceptible to interactions with phonons. After the generation of the exciton but prior to its radiative recombination, the exciton may interact with many phonons. It may absorb some, emit some, absorb some more, and so on until the exciton ends up back at the ground vibrational state of the excited electronic state (**Figure 1.11b**). These transitions are considered virtual transitions since they do not contribute to the change in energy of the exciton when it radiatively recombines. However, each time one of these virtual transitions occurs, the phase of the exciton wavefunction is randomized. The more virtual transitions occur, the further the coherence is lost in the electronic wavefunction of the exciton (**Figure 1.11d**), and the broader the line width of the transition (**Figure 1.11e**, rainbow spectrum).

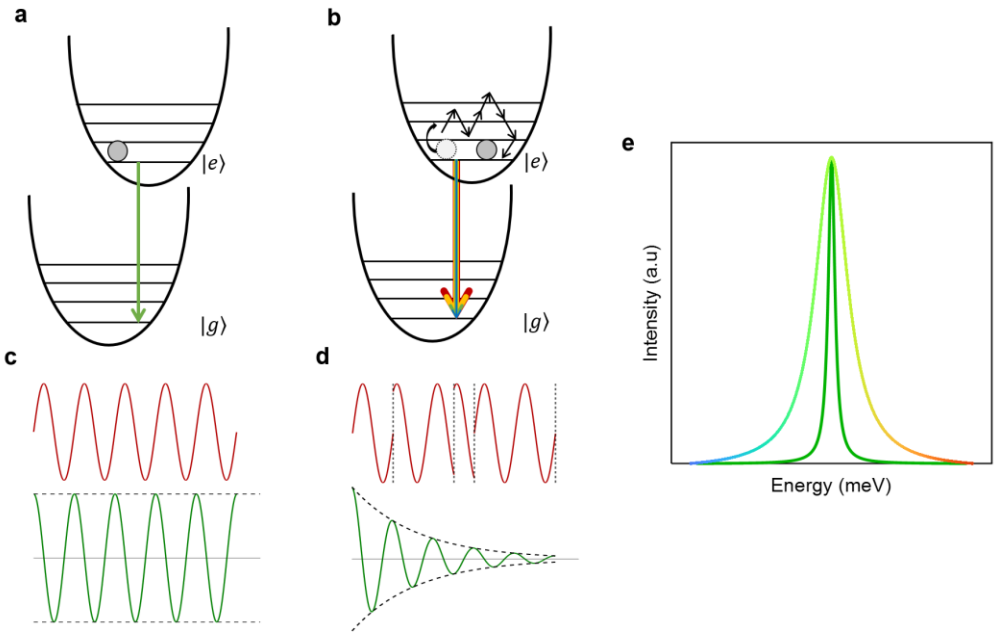


**Figure 1.11.** Ground and excited electronic states are approximated to be harmonic oscillators. **a.** In the absence of elastic phonon scattering, the exciton remains in the ground vibrational state of the excited electronic state. Radiative recombination occurs through one transition. **b.** In the presence of elastic phonon scattering, the exciton can absorb and emit phonons virtually prior to the recombination of the exciton. **c.** Electronic wavefunction (red) maintains a constant phase throughout the lifetime of the exciton, resulting in fully coherent emission (green). **d.** As a result of the interactions of the exciton with phonons prior to its radiative recombination, the electronic wavefunction (red) gets randomized each time it interacts with one of the phonons (signified by dotted black lines). Coherence is lost as a result (green). **e.** Lorentzian PL spectra of the example system without elastic phonon scattering (narrow green PL spectrum) and with elastic phonon scattering (broad rainbow PL spectrum).

Elastic and inelastic phonon scattering contribute significantly to the PL spectrum of colloidal NCs, particularly at elevated temperatures. Inelastic phonon scattering contributes anywhere from 5-30 meV in colloidal NC systems, depending on the degree of the phonon coupling and the energy of the dominant phonon modes. Elastic phonon scattering can contribute anywhere from 20 meV to hundreds of meV, depending on the system.

**Chapter 2** of my thesis investigates the various line shape broadening mechanisms of InP NCs, determining the dominant mechanisms.

## 1.3. Spectroscopic Techniques

The spectroscopy of colloidal NC systems began with ensemble measurements. As synthetic methods improved, NC stability improved such that single NC spectroscopy became feasible. The next section of my introduction will cover the ensemble and single NC spectroscopic techniques that were crucial to completing the studies in my thesis. The Bawendi lab uses a collection of photon correlation techniques, taking advantage of the many ways in which the 'photon stream' can be analyzed. The following section will be a survey of spectroscopic techniques, excluding many of the nitty gritty details, but will hopefully sufficiently cover the broader concepts underlying each technique.

### *1.3.1. Intensity Binning*

The photon stream can be manipulated in a number of ways. It can be binned on a linear timescale to observe how the PL intensity changes over the course of an experiment (**Figure 1.12a**). **Figure 1.12b** shows an example of a single InP NC intensity trace, tacking the PL intensity for a little over four hours. The intensity appears to jump between several positions over the course of the experiment. The inset of **Figure 1.12b** shows a zoomed in look at the intensity trace over a ~5 minute period. The intensity trace shows that the NC emits in a binary-like fashion. To be a little more quantitative, we can take a histogram of the histogram in **Figure 1.12b** to get the graph in **Figure 1.12c**. This figure shows that intensity is centered around three different intensities: a bright state (centered around 150), a dark state (centered around 20), and a third state (centered around 75). The presence of a third state suggests that there may be more that is happening inside the NC other than binary blinking "on" and "off". These middle states are often referred to as a "grey" state – not quite bright but not quite dark, and often is attributed to trion emission.[79]

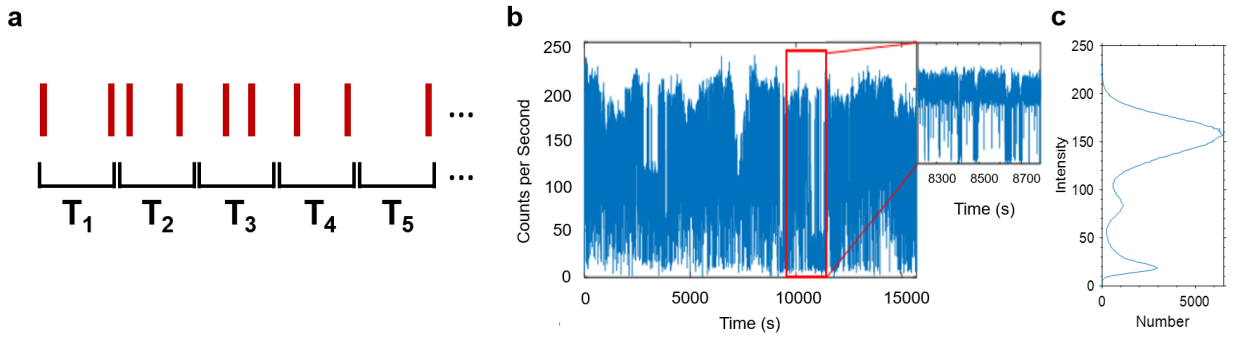


**Figure 1.12. a.** Illustration of a photon stream that is placed into linearly spaced bins. $T_1$, $T_2$, etc. make up the x-axis of an intensity trace**. b.** Intensity trace of a single InP NC at room temperature. The single NC exhibits PL intermittency into a "grey" and "off" state. Inset show a zoomed in picture of the intensity trace within the red box. **c.** Histogram plot representing the number of bins in **b** that have a specific intensity. According to this plot, the intensity from the single InP NC jumps between three intensities.

### *1.3.2. Photoluminescence Lifetimes*

Photoluminescence (PL) lifetimes record the histogram of time differences between the generation of the exciton and the recombination of the exciton. In an experiment, the creation and recombination of the exciton are quantified by recording the laser excitation pulse time and the photon arrival time at a single photon detector, respectively. The lifetime is sometimes denoted as $g^{(1)}(\tau)$. Complexity can be added to the post-processing analysis of the lifetime by parsing the photon stream based on how many photons are detected by a single excitation pulse. We can parse the photon stream into one-photon events (**Figure 1.13a**), two-photon events (**Figure 1.13b**), and three-photon events (**Figure 1.13c**). We can take another step further and pick out the first photon in an event to measure the biexciton or triexciton lifetime in the case of a two-photon event or a three-photon event, respectively (**Figure. 1.13b,c**). This method is generally referred to as the photon number resolved lifetime method $PNRL^{(n,m,l)}(\tau)$, where $n$ tells us that we are looking at the photon stream of $n$-photon events, and $m$ and $l$ correspond to the indices of the photons involved in the photon time difference $\tau$. **Figure 1.13d** shows a Monte Carlo simulation demonstrating the power of the $PNRL$ method to isolate the contributions of the exciton (X), biexciton (BX), and triexciton (TX) in the recombination dynamics in NC systems. In this case we can see that the X lifetime is significantly longer than the BX and TX lifetime, as a result of statistical scaling of the BX and TX lifetimes.

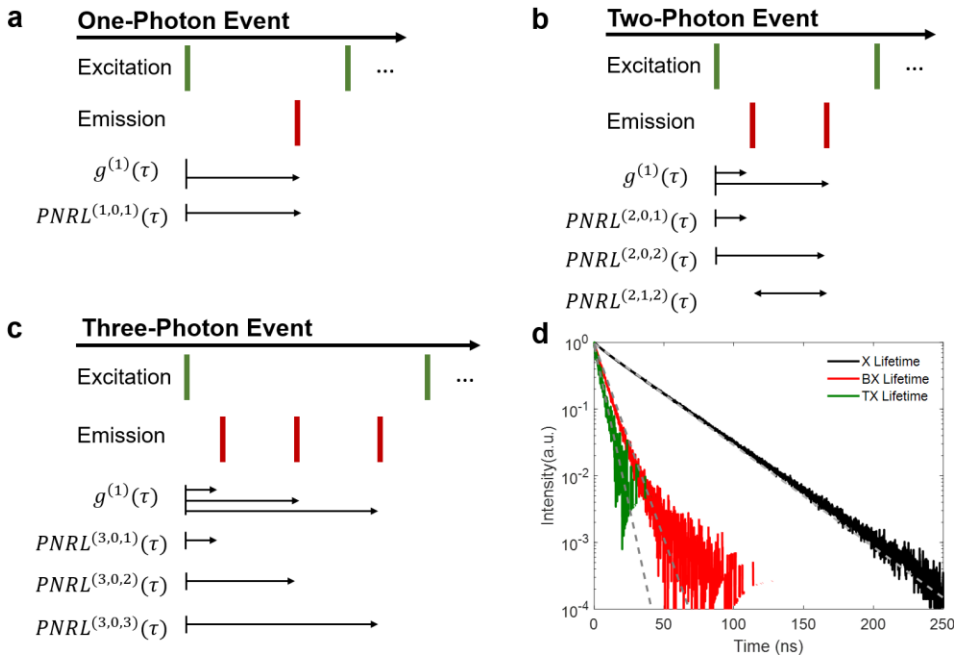


**Figure 1.13.** Pulsed photon streams can be parsed into **a.** one-photon events, **b.** two-photon events, **c**. three-photon events, and so on. Within an n-photon event, every photon time difference with the excitation contributes to $g^{(1)}(\tau)$, the lifetime without any post-processing. The photon streams can be selectively organized in a method called photon number resolved lifetimes (PNRL). The $PNRL^{(n,m,l)}(\tau)$ allows us to selectively look at the exciton, biexciton, or triexciton lifetime in a photon stream where $n$ corresponds to the number of photons involved in the excitation event, and $m$ and $l$ correspond to the indices of the photons involved in the photon time difference $\tau$. For instance,

$PNRL^{(3,0,1)}(\tau)$ looks at the photon time difference between the excitation pulse and the first photon in the three-photon event. In another example $PNRL^{(2,1,2)}(\tau)$ looks at the photon time difference between the first photon in a two-photon event and the second photon in a two-photon event. **d.** Monte Carlo simulation showing the $PNRL^{(2,1,2)}(\tau)$ (exciton (X) lifetime, black), $PNRL^{(2,0,1)}(\tau)$ (biexciton (BX) lifetime, red), and $PNRL^{(3,0,1)}(\tau)$ (triexciton (TX) lifetime, green).

The measured lifetime $g^{(1)}(\tau)$ can be a complex quantity that includes the radiative recombination of the exciton, the radiative recombination of multiexcitons, the radiative recombination of charged states, and nonradiative recombination. We can combine multiple methods of photon stream post-processing analysis to isolate these contributions. **Figure 1.14a,b** shows the intensity trace of a single InP NC being parsed into three distinct photon streams: "on" (shaded green), "grey" (shaded yellow), and "off" (shaded red). Monte Carlo simulations in **Figure 1.14c** demonstrate that there can be a difference between the bright and grey state emission in terms of its PL decay dynamics. Trion emission has been observed in several NC systems and will show up with a faster PL lifetime and a lower intensity of photon emission than the bright state. The off state is purely nonradiative which is often times much faster than the instrument response function of the single photon detector.

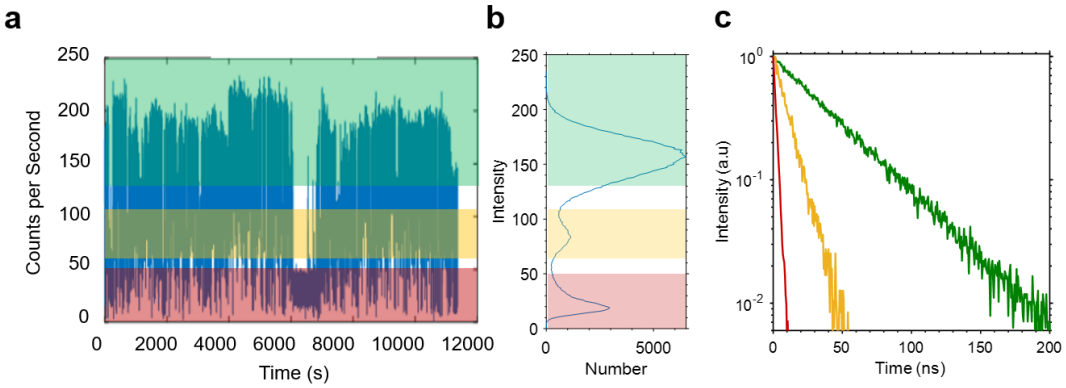


**Figure 1.14. a.** Photon stream parsed between on (green), grey (yellow) and off (red) to do further analysis on parsed photon streams. **b.** Another histogram plot to identify cut off values to isolate photon streams. Monte Carlo simulation showing the lifetime of the on, grey, and off state photon streams. In this case, the on state (green) has a long lifetime, the grey state – simulated to be trion emission – has a faster lifetime, and the off state – simulated to be nonradiative emission – has a lifetime so fast that it is limited by the instrument response function (IRF) of the detector.

### *1.3.3. CCD-based Photoluminescence Spectra*

Standard CCD-based PL spectroscopy is a core tool of the Bawendi lab. The basics of the spectrometer is shown in **Figure 1.15a** where the photon stream reflects off a grating into the CCD detector. Photon emission will reflect at a specific angle off of the grating, depending on the wavelength of the light. The positions on the CCD camera are calibrated such that it recognizes the wavelength of light depending on where it hits on the camera. PL spectroscopy provides us with insight on the energetic distribution of photon emission from our NC samples. For instance, **Figure 1.15b** shows the ensemble InP PL spectrum (black) and the PL spectrum of three single InP NCs (red) at room temperature. The single InP NC PL

spectra are considerably narrower than the ensemble PL spectrum suggesting NC polydispersity contributes significantly to the ensemble PL spectrum.

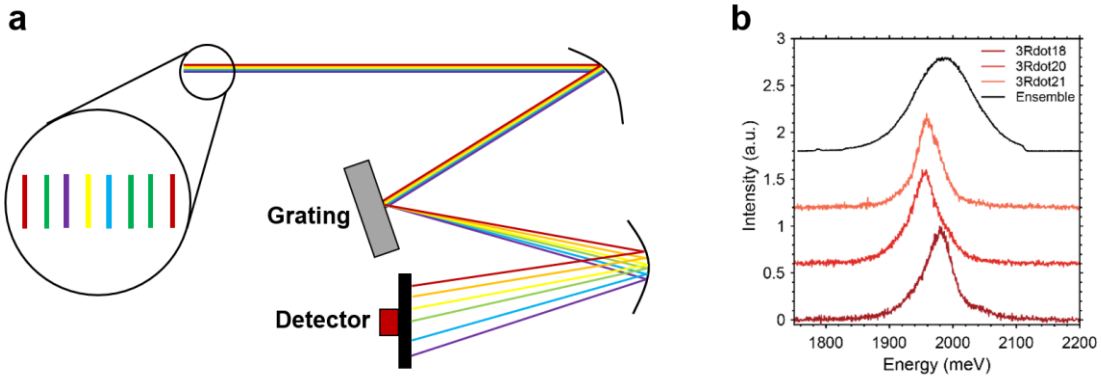


**Figure 1.15. a.** Basic concept of a CCD-based spectrometer. A photon stream, comprised of photons with a distribution of wavelengths, enter a spectrometer where they reflect off of a grating at different angles depending on the wavelength of light. A histogram of the reflected photon stream is recorded at a CCD camera (often times 1024 x 1024 or 512 x 512 pixels), providing information on the energy distribution of the photon emission. **b.** PL spectra of three single InP NCs (red) and the ensemble InP PL spectrum (black).

### *1.3.4. Single NC Multiexciton Correlations*

We touched on the dynamic information that can be gained by correlating photons through the $PNRL$ method in **Section 1.3.2**. In this section, we will look at how photon correlations can be utilized to explore the quantum yield of multiexcitons, specifically the biexciton and triexciton. If we set up an experiment where a pulsed laser excites a single NC, and we send the NC emission through a Hanbury Brown and Twiss (HBT) configuration (**Figure 1.16a**), we can measure all the photon time differences between photons arriving at Detector 1 and Detector 2 (**Figure 1.16b**). In terms of the $PNRL$ method, we are recording the $PNRL^{2,1,2}(\tau)$. **Figure 1.16c** shows a single InP NC second-order cross-correlation $g_x^{(2)}(\tau)$ for photon time differences ranging from -1500 ns to 1500 ns. In this experiment, the repetition rate of the laser was set to 1 MHz – in another words an excitation pulse is sent every 1000 ns. Correlation counts in the center peak originate from photon pairs that emit within the same excitation pulse. These photon pairs are interpreted to be the biexciton-exciton photon pairs. Correlation counts in the side peak are from two single exciton photons one excitation pulse separated from one another. By taking the ratio of the integrated area of the center peak (shaded in green) and the integrated area of the side peak, we can determine the biexciton quantum yield (BXQY) (**Equation 1.9**). Detailed explanations are given elsewhere.[80,81]

$$\frac{g_x^{(2)}(0)}{g_x^{(2)}(T_{rep})} = \frac{BXQY}{XQY} \tag{1.9}$$

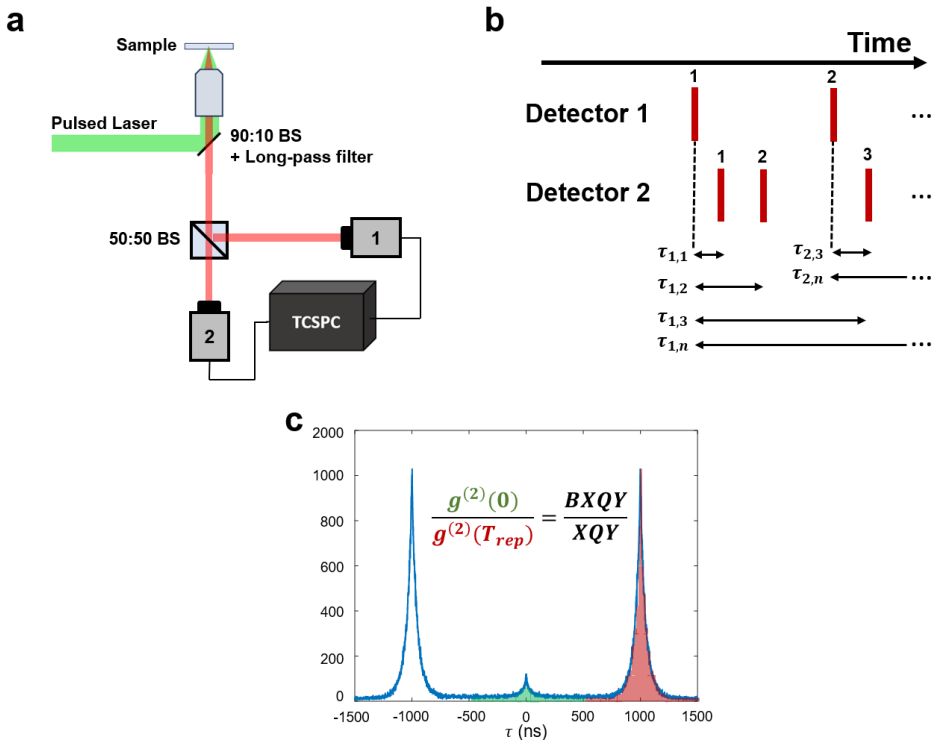


**Figure 1.16. a.** Hanbury Brown-Twiss optical setup for second-order correlation measurements. Following the excitation of a NC sample using a pulsed laser, NC photons travel through a 50:50 beamsplitter, arriving at one of the two avalanche photodiode detectors (APDs). Photon streams are recorded and analyzed in post-processing software. **b.** Illustration of a set of photon streams. Second-order cross-correlations, $g_x^{(2)}(\tau)$, are a histogram of photon time differences $\tau$ of photons arriving at Detector 1 and Detector 2. **c.** Pulsed-$g_x^{(2)}(\tau)$ of a single InP NC at room temperature. The biexciton quantum yield can be determined by taking the ratio of the integrated area of the center peak (green) and the integrated area of the side peak (red).

A similar correlation technique can be applied to quantify the triexciton quantum yield of single NCs. Instead of second-order cross-correlations, we now have to measure third-order cross-correlations $g_x^{(3)}(\tau)$. This is not feasible with the optical setup in **Figure 1.16a** because each single photon detector is only able to measure the arrival time of a single photon per excitation pulse. A modified HBT with four detectors is required to perform this measurement (**Figure 1.17a**). The $g_x^{(3)}(\tau_1, \tau_2)$ looks at photon time differences $\tau_1$ between photons at Detector 1 and Detector 2 while simultaneously looking at photon time differences $\tau_2$ between photons at Detector 2 and Detector 3. Since there are now two separate time difference variables, the resulting $g_x^{(3)}(\tau_1, \tau_2)$ is two-dimensional (2D). To determine the triexciton quantum yield, we look at the ratio of the integrated area of the center peak $g_x^{(3)}(0,0)$ and the integrated area of the side peak $g_x^{(3)}(0, T_{rep})$ where $T_{rep}$ is repetition time of the laser excitation **(Equation 1.10)**. Center peak contributions to the $g_x^{(3)}(\tau_1, \tau_2)$ originate from the correlations between photons from the exciton, biexciton, and triexciton recombination, and side peak contributions originate from the correlations

between photons from the biexciton and exciton recombination from the same pulse, and a photon from another exciton recombination from the next subsequent pulse. Detailed explanations are given elsewhere.[82]

$$\frac{g_x^{(3)}(0,0)}{g_x^{(3)}(0,T_{rep})} = \frac{TXQY}{XQY} \tag{1.10}$$

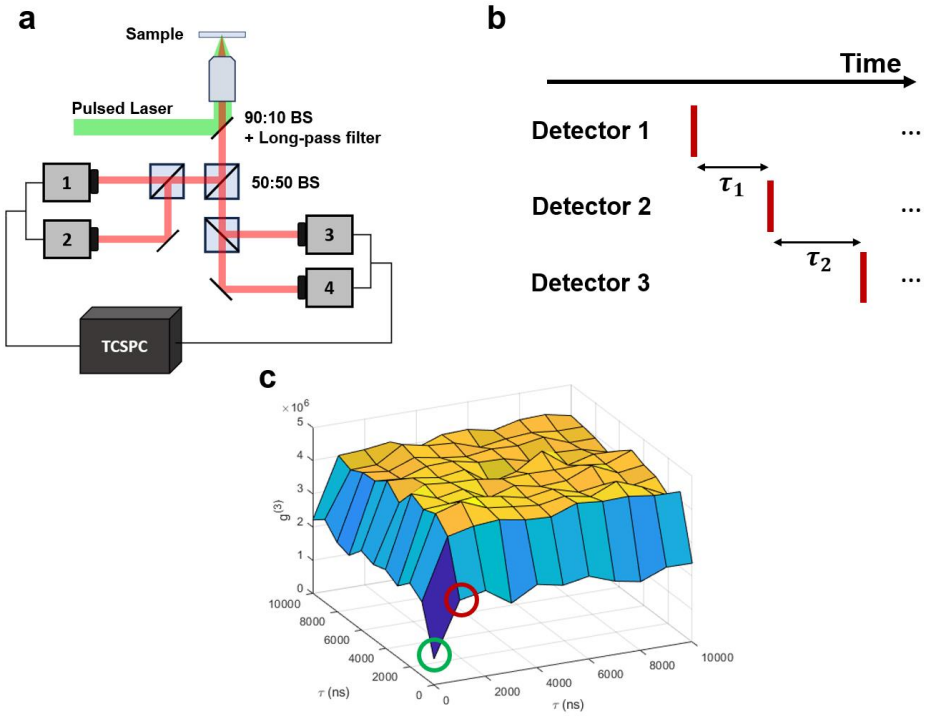


**Figure 1.17. a.** Hanbury Brown-Twiss optical setup for third-order correlation measurements. Following the excitation of a NC sample using a pulsed laser, NC photons travel through two 50:50 beamsplitters, arriving at one of the four avalanche photodiode detectors (APDs). Photon streams are recorded and analyzed in post-processing software. **b.** Illustration of a set of photon streams. Third-order cross-correlations $g_x^{(3)}(\tau_1, \tau_2)$ are a histogram of photon time differences of photons arriving at Detector 1 and Detector 2 ($\tau_1$) and photon time difference of photons arriving at Detector 2 and Detector 3 ($\tau_2$). **c.** Monte Carlo simulation of a pulsed-$g_x^{(3)}(\tau_1, \tau_2)$experiment. The triexciton quantum yield can be determined by taking the ratio of the integrated area of the center peak (green circle) and the integrated area of the side peak (red peak).

### *1.3.5. Photon Correlation Fourier Spectroscopy*

Photon-correlation Fourier Spectroscopy (PCFS) is an interferometric second-order correlation technique that draws a relationship between time-correlations, measured by a HBT configuration, with the energy-dependent interference from a Michelson interferometer (**Figure 1.18a**). PCFS enables access to energy information well beyond the time resolution of a standard CCD-based spectrometer (sub-microsecond vs. tens of milliseconds. I will cover the basics of the PCFS derivation to make the connection between the time correlations and energetic interferometry clear. We start with the definition of the second-order cross-correlation:

$$g_x^{(2)}(\delta_0,\tau) = \frac{\langle I_a(t) I_b(t+\tau)\rangle}{\langle I_a(t)\,\rangle\langle I_b(t+\tau)\rangle} \tag{1.11}$$

$I_a(t)$ is the intensity at detector $a$ at time $t$, $I_b(t+\tau)$ is the intensity at detector $b$ at time $t+\tau$, and $\langle \dots \rangle$ denotes a time average. Since we know the NC emission travels through a Michelson interferometer, we can rephrase the intensities to take into account the constructive and destructive interference through the interferometer.

$$I_{a/b}(t) = \frac{1}{2} I(t)\big(1 \pm F_{cos}[s(\omega,t)]_{\delta(t)}\big) \tag{1.12}$$

$I(t)$ is the total intensity of the NC emission, $s(\omega,t)$ is the spectrum of the emitter, and $\delta(t)$ is the time-dependent stage position of the Michelson interferometer. Inserting **Equation 1.12** into **Equation 1.11**, we get **Equation 1.13**.

$$g_x^{(2)}(\delta_0,\tau) = \frac{\langle I(t)I(t+\tau)(1+F_{cos}[s(\omega,t)]_{\delta(t)})(1-F_{cos}[s(\omega,t+\tau)]_{\delta(t+\tau)})\rangle}{\langle I(t)(1+F_{cos}[s(\omega,t)]_{\delta(t)})\rangle\langle I(t+\tau)(1-F_{cos}[s(\omega,t+\tau)]_{\delta(t+\tau)})\rangle} \tag{1.13}$$

We now have a second-order cross-correlation that is dependent on intensity terms and spectral terms. We now need to find a way to isolate terms related to the NC spectrum and find a method to reasonably interpret the spectral terms. First, we note that time averages of first-order terms can be cancelled out, simplifying our function.

$$g_x^{(2)}(\delta_0,\tau) = \frac{\langle I(t)I(t+\tau)\rangle - \langle I(t)I(t+\tau)F_{cos}[s(\omega,t)]_{\delta(t)}F_{cos}[s(\omega,t+\tau)]_{\delta(t+\tau)}\rangle}{\langle I(t)\rangle\langle I(t+\tau)\rangle} \tag{1.14}$$

Next, we factor out the intensity terms by assuming that intensity fluctuations are independent of the spectral fluctuations.

$$g_x^{(2)}(\delta_0,\tau) = \frac{\langle I(t)I(t+\tau)\rangle}{\langle I(t)\rangle\langle I(t+\tau)\rangle}\big(1 - \langle F_{cos}[s(\omega,t)]_{\delta(t)}F_{cos}[s(\omega,t+\tau)]_{\delta(t+\tau)}\rangle\big) \tag{1.15}$$

Now that the intensity terms are separated from the spectral terms, we recognize that the intensity terms are simply the definition of the second-order cross-correlation $g(\tau)$.

$$g_x^{(2)}(\delta_0,\tau) = g(\tau)(1 - \langle F_{cos}[s(\omega,t)]_{\delta(t)}F_{cos}[s(\omega,t+\tau)]_{\delta(t+\tau)}\rangle \tag{1.16}$$

Isolating for the spectral term we get

$$1 - \frac{g_x^{(2)}(\delta_0,\tau)}{g^{(2)}(\tau)} = \langle F_{cos}[s(\omega,t)]_{\delta(t)}F_{cos}[s(\omega,t+\tau)]_{\delta(t+\tau)}\rangle \tag{1.17}$$

where $F_{cos}[s(\omega,t)]_{\delta(t)}F_{cos}[s(\omega,t+\tau)]_{\delta(t+\tau)}$ can be interpreted as the spectral correlation term $p(\zeta,\tau)$, where $\zeta$ is a new energy variable that represents the energy difference, analogous to the time difference variable $\tau$. The spectral correlation can also be thought of as the auto-correlation of the spectrum.

$$p(\zeta,\tau) = \langle \int s(\omega,t)s(\omega+\zeta,t+\tau)\,d\omega \rangle \tag{1.18}$$

The last thing we must do is remove the time-dependence out of the evaluation of the Fourier transform. In reality, this last step is most of the derivation, but I will skip that and encourage the reader to look into more detailed explanations elsewhere.[81]

$$1 - \frac{g_x^{(2)}(\delta_0,\tau)}{g^{(2)}(\tau)} = \frac{1}{2}F_{cos}[p(\zeta,\tau)]_{\delta_0} \tag{1.19}$$

**Equation 1.19** is the final result we were looking for! The spectral correlation term can be constructed by measuring the second-order auto- and cross-correlation at a series of stage positions $\delta_0$.

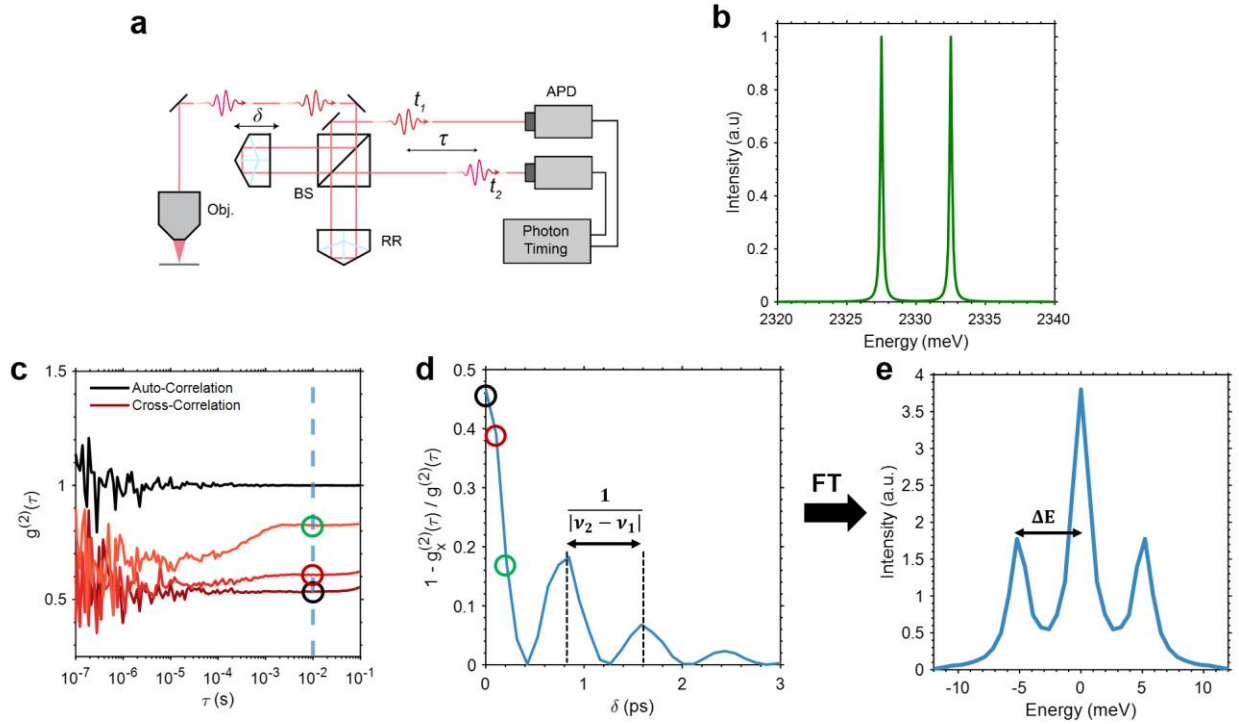


**Figure 1.18. a.** Interferometer schematic. BS = beamsplitter, RR = retroreflector, Obj. = microscope objective. **b.** Dynamic doublet model PL system. **c**. Second-order auto-correlation $g^{(2)}(\tau)$ (black) and the second-order cross-correlation $g_x^{(2)}(\delta_0,\tau)$ measured at the first three stage positions $\delta_0$ of the simulated PCFS experiment. First stage position $g_x^{(2)}(\delta_0,\tau)$ is dark red (bottom) and third stage position $g_x^{(2)}(\delta_0,\tau)$ is light red (top). Dotted blue line signifies where the PCFS interferogram is measured. **d.** PCFS interferogram of the simulated PL system. First three data points are constructed from the equation $\frac{1-g_x^{(2)}(\delta_0,\tau)}{g^{(2)}(\tau)}$, where the value for $g_x^{(2)}(\delta_0,\tau)$ is extracted for the first, second, and third data point at the black, red, and green circles, respectively. **e.** PCFS spectral correlation $p(\zeta,\tau)$ with a fine-structure splitting energy $\Delta E$.

Let's model a doublet PL spectrum as an example system to demonstrate how to perform a PCFS experiment (**Figure 1.18b**). To run a PCFS experiment, $g_x^{(2)}(\delta_0\tau)$ and $g^{(2)}(\tau)$ are measured at a series of stage positions $\delta_0$ on the Michelson interferometer (**Figure 1.18c**). To build up the PCFS interferogram in **Figure 1.18d**, we compute $\frac{1-g_x^{(2)}(\delta_0,\tau)}{g^{(2)}(\tau)}$ at a specified $\tau$ at each stage position $\delta_0$ of the Michelson interferometer, indicated by the dotted blue line in **Figure 1.18c**. The relationship between the PCFS interferogram and the $g_x^{(2)}(\delta_0,\tau)$ is shown by the black, red, and green circles for the first, second, and third data points, respectively. For a doublet PL spectrum, the PCFS interferogram will exponentially decay with periodic oscillations related to the energy difference between the fine-structure states (**Figure 1.18d**). The final step is to perform an inverse Fourier transform of the PCFS interferogram to get out the PCFS spectral correlation. The resulting spectral correlation of the doublet is a triplet, with a splitting between the peaks that is related to the fine-structure splitting in the PL spectrum. We will discuss the interpretation of this result in a few paragraphs.

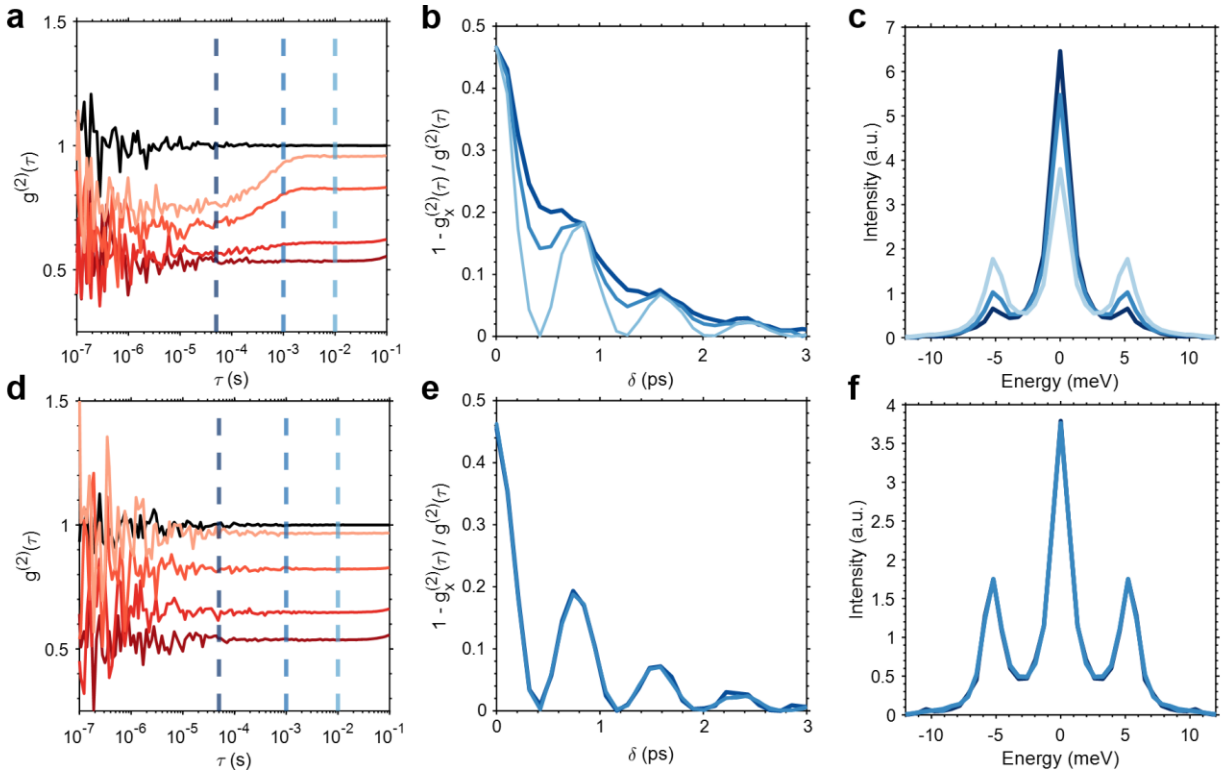


**Figure 1.19. a.** Second-order auto-correlation (black) and second-order cross-correlations (red) for the first three stage positions of a PCFS experiment of a dynamic doublet. Dotted blue lines represent the times in which PCFS interferograms are constructed. **b.** PCFS interferograms of the dynamic doublet system at three values of $\tau$. **c**. PCFS spectral correlations of the dynamic doublet system at three values of $\tau$. **d.** Second-order auto-correlation (black) and second-order cross-correlations (red) for the first three stage positions of a PCFS experiment of a static doublet. Dotted blue lines represent the times in which PCFS interferograms are constructed. **b.** PCFS interferograms of the static doublet system at three values of $\tau$. **c**. PCFS spectral correlations of the static doublet system at three values of $\tau$.

To appreciate the power of PCFS as a spectroscopic tool, let's look at two doublet systems: the dynamic doublet and the static the doublet. The dynamic doublet emits from one fine-structure state for a period of time before switching to emission from the other fine-structure state. The switching frequency is set to 500 $\mu$s in this example system. The static doublet has no switching frequency. Any given emission event has equal probability of emitting from either fine-structure state. We can track the dynamics of these two systems by measuring the photon correlations at difference photon time differences $\tau$. PCFS interferograms and spectral correlations are constructed from the auto- and cross-correlations for the dynamic doublet (**Figure 1.19a-c**) and static doublet (**Figure 1.19d-f**). The dynamic doublet PCFS interferogram decays exponentially at short $\tau$, and is the convolution of an exponential decay with a periodic oscillation at long $\tau$ (**Figure 1.19b**). The static doublet PCFS interferogram is the convolution of an exponential decay with a periodic oscillation at all $\tau$ (**Figure 1.19e**). Taking the Fourier transform of these PCFS interferograms, we observe the dynamic doublet PCFS spectral correlation evolve from mostly singlet character to mostly triplet character from short $\tau$ to long $\tau$ (**Figure 1.19c**). Again, we do not observe a change in the spectral correlation of the static doublet as a function of $\tau$ (**Figure 1.19f**).

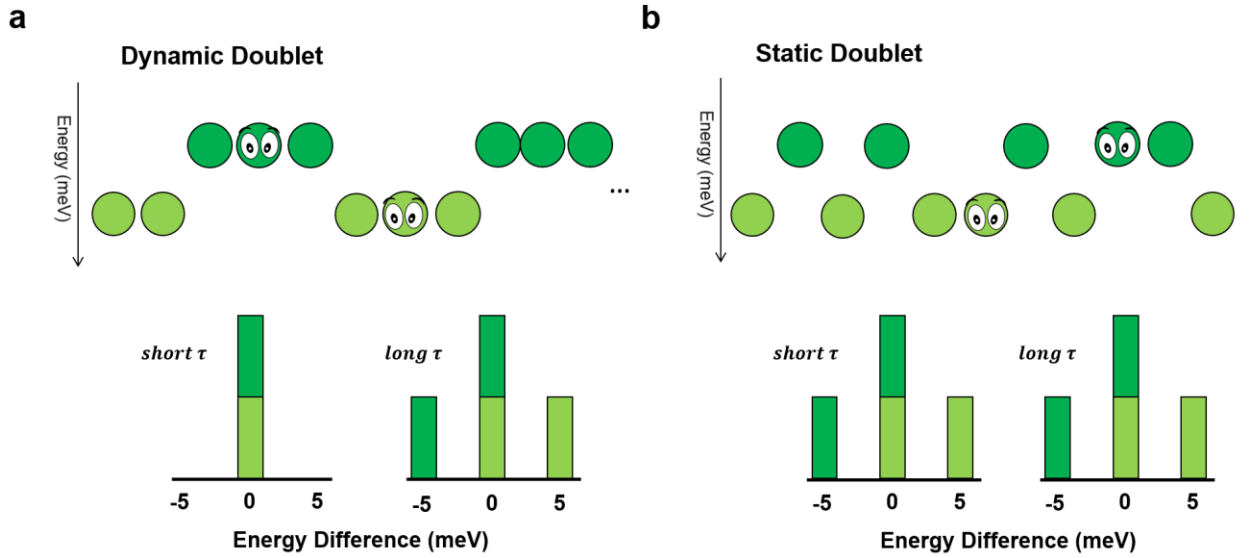


**Figure 1.20.** Illustration of a **a.** dynamic doublet and **b.** static doublet photon stream, and a cartoon construction of the spectral correlation at short and long $\tau$.

A helpful way to interpret the PCFS spectral correlation is to frame it as a histogram of energy differences. I like to think of the spectral correlation by putting myself in the position of a photon in the photon stream and consider what photons I would see close in time to me versus what photons I would see far in time to me. For the dynamic doublet, the photon stream will look like a string of photons emitted from one energy, and then a string of photons from the other energy (**Figure 1.20a**). If I was a lower energy photon (dark green), I would only see similar energy photons close to me (short $\tau$), contributing a count to

the 0 meV peak. Similarly, if I was a higher energy photon, (light green), I would also only see similar energy photons close to me, contributing another count to the 0 meV peak. The resulting spectral correlation at short $\tau$ is a singlet. Now let's consider photons separated further in time (long $\tau$). If I was a low energy photon, I will sometimes see photons with the same energy and sometimes see photons with an energy that is 5 meV higher (meaning the energy difference will be -5 meV). We observe a contribution to the spectral correlation at 0 meV and at -5 meV. Inversely, the high energy photon will see photons separated far in time that are similar in energy and 5 meV lower in energy, contributing counts to the 0 meV peak and the 5 meV peak, respectively. The resulting spectral correlation at long $\tau$ is a triplet. We have successfully constructed the (very cartoonish) spectral correlation for the dynamic doublet. The static doublet will be similar to the dynamic doublet, but in this case, there is no dynamic switching frequency (**Figure 1.20b**). Every emission event has a 50% chance of being a lower energy photon and a 50% chance of being a high energy photon. That means that the spectral correlation will be a triplet across all $\tau$. PCFS is a powerful tool that allows us to probe the dynamic spectral information of NC systems with time resolution well-beyond the capabilities of CCD-based spectroscopic techniques.

The dynamic doublet versus static doublet is one simple example of the power of PCFS. PCFS can probe spectral dynamics including fine-structure switching frequencies and spectral diffusion.[83] Additionally, PCFS can measure spectral line widths with extremely high energy resolution and time resolution, quantifying a lower bound of the exciton coherence time – an important metric for quantum emitter applications.[12,70] PCFS is a foundational technique to the Bawendi lab, mathematically intriguing and an amazing tool to probe the dynamic photophysical properties of NC systems.

### *1.3.6. Average Single NC Correlations in Solution*

Single NC spectroscopy is a powerful tool that is capable of directly probing colloidal NCs systems while avoiding ensemble averaging of the photophysical properties. Single-NC spectroscopy also suffers from user selection bias, where the brightest and most stable NCs are investigated more than the NCs that are dimmer or intermittingly blinking on and off. Using photon correlations, we are able to disentangle correlation contributions from the ensemble – $g^{(2)}_{ensemble}(\tau)$ – and correlation contributions from single NCs – $g^{(2)}_{single}(\tau)$) (**Figure 1.21a**). Colloidal NC diffusion through the excitation focal volume is on the order of single milliseconds. That means that photon pairs that are closer in time than the diffusion time $\tau_D$ of the NC have a nonzero probability of coming from the same NC, contributing to $g^{(2)}_{single}(\tau)$. The lower the concentration of the solution, the higher the ratio of $g^{(2)}_{single}(\tau)$ to $g^{(2)}_{ensemble}(\tau)$ contributions. **Figure 1.21b** shows the second-order cross-correlation of three InP NC solutions with varying concentrations. We

typically refer to the second-order cross-correlation in solution as the "FCS trace", where FCS stands for fluorescence correlation spectroscopy.

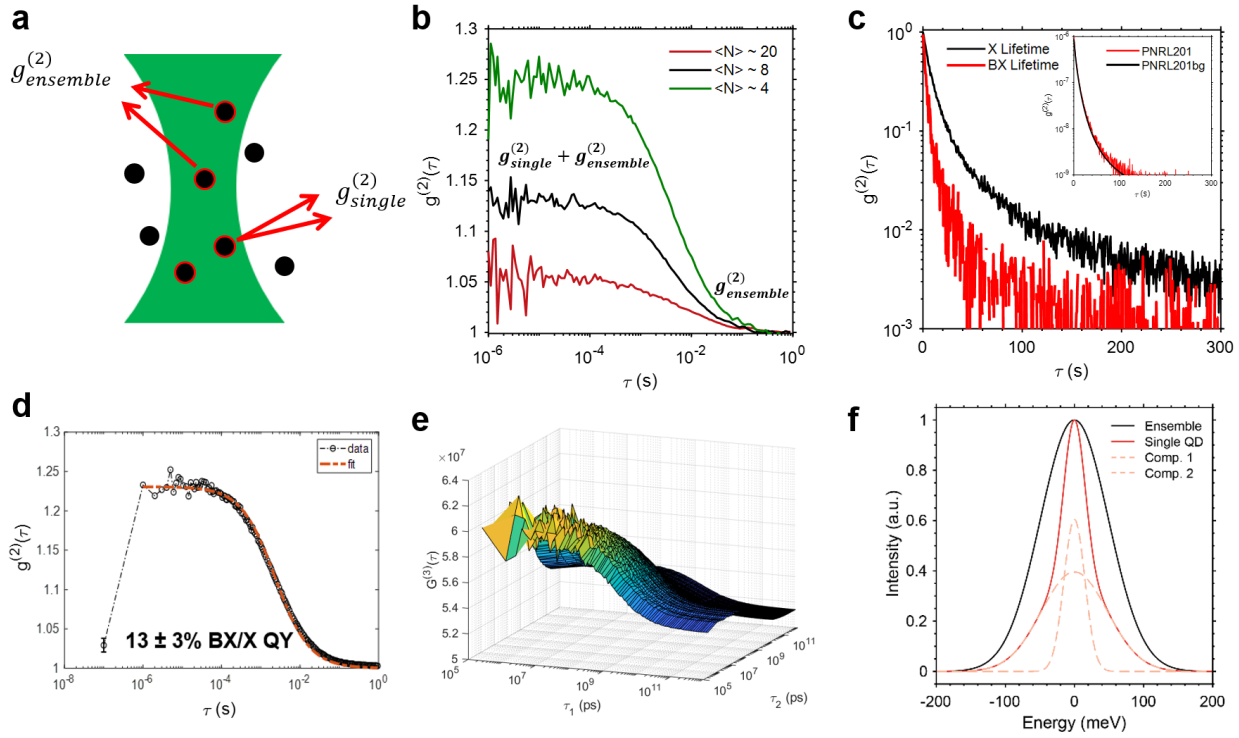


**Figure 1.21. a.** There are two contributions to second-order correlations $g^{(2)}(\tau)$ in solution: ensemble contributions $g^{(2)}_{ensemble}(\tau)$ and single-NC contributions $g^{(2)}_{single}(\tau)$. $g^{(2)}_{ensemble}(\tau)$ contributions occur by taking the photon time difference between two photons emitted by two separate NCs. $g^{(2)}_{single}(\tau)$ contributions occur by taking the photon time difference between two photons emitted by the same NC. **b.** Three solution-$g^{(2)}(\tau)$ of InP solutions at different concentrations $\langle N \rangle$, which is the average NC occupancy. At short $\tau$, the correlations are comprised of both $g^{(2)}_{single}(\tau)$ and $g^{(2)}_{ensemble}(\tau)$ contributions. At long $\tau$, the correlations are comprised of only $g^{(2)}_{ensemble}(\tau)$ contributions. The lower the concentration of the solution sample, the higher $g^{(2)}(\tau)$ will be at short $\tau$ because the $g^{(2)}_{single}(\tau)$ to $g^{(2)}_{ensemble}(\tau)$ will be higher. **c.** Exciton (X) and biexciton (BX) lifetime in solution. Inset shows the $PNRL^{(2,0,1)}(\tau)$ (red) and the ensemble background $PNRL^{(2,0,1)}_{bg}(\tau)$ (black) to isolate the single NC lifetime contributions. **d.** Solution biexciton quantum yield measurement of InP NCs. **e.** Solution triexciton quantum yield measurement of ZnSe NCs. **f.** Solution photon correlation Fourier spectroscopy (sPCFS) measurement of InP NCs showing a narrower average single NC line width (solid red) compare do the ensemble line width (black).

The average occupancy $\langle N \rangle$ can be determined by determining the height of the FCS trace. For instance, the height of the green curve is ~1.25, so we compute the average NC occupancy $\langle N \rangle = \frac{1}{1.25-1} = 4$. The higher the FCS trace, the lower the concentration of the sample, and the less the ensemble signal contributes at short $\tau$. As $\tau$ increases in the FCS traces in **Figure 1.21b**, the correlation slowly approaches a value of 1, meaning the light is uncorrelated. At long $\tau$, we assume that correlation counts are only coming from $g^{(2)}_{ensemble}(\tau)$. In other words, it is extremely unlikely that a NC will emit a photon at some time, diffuse

away, and then one second later, re-enter the focal volume and emit another photon. This assumption is crucial to all of our single NC solution techniques. It allows us to subtract out the $g^{(2)}_{ensemble}(\tau)$ at short $\tau$ because we can isolate $g^{(2)}_{ensemble}(\tau)$ at long $\tau$.

Because correlation experiments compile a photon stream over a long period of time, many NCs contribute to $g^{(2)}_{single}(\tau)$. As a result, the single NC information from a solution correlation experiment is an *average* single NC result. This is advantageous when trying to learn about the sample as a whole, avoiding user selection bias. Additionally, single NC solution techniques are necessary if single NC stability is poor. The Bawendi Lab has developed and uses a number of solution correlation techniques. We are able to perform $PNRL$s in solution, resolving the average single NC biexciton lifetime in solution by subtracting out the ensemble contributions (**Figure 1.21c**), We are able to measure the average single NC biexciton quantum yield (**Figure 1.21d**) and average single NC triexciton quantum yield in solution (**Figure 1.21e**), and we are able to measure the average single NC line width in solution (**Figure 1.21f**). All of these techniques were crucial to my research during my PhD. Detailed explanations for the solution $PNRL$,[84] solution BXQY,[85] solution TXQY (**Chapter 4**), and solution PCFS are given elsewhere.[86]

## 1.4. Experimental Conditions

I want to dedicate some space to my introduction to discuss some of the details of experimental work that do not necessarily get talked about in theses. Many details get passed down through hands-on mentorship, but sometimes that mentorship isn't there. Sometimes certain information gets lost after many years of it getting passed down. I will try my best to write down all the small, and sometimes weird details that were important in my experimental work that hopefully can be helpful to some poor graduate student wondering how the hell they are supposed to do a certain measurement, or why something isn't working. This is not a complete list, but hopefully can be the start of a comprehensive list of tips and tricks for future graduate students to expand on.

### 1.4.1. Sample Preparation

#### *1.4.1.1. Water is Your Worst Enemy*

Water is your worst enemy!!! Before my time, the Bawendi Lab primarily studied CdSe NCs at the single NC level. CdSe NCs are extremely stable and resistant to a lot of atmospheric effects. Single NC samples could be prepared outside of the glovebox! I started my PhD trying to study single InP NCs. I, and many of my lab mates struggled to consistently prepare InP NC samples for long single NC studies. We continued to test sample conditions, prepping all samples in the glovebox. It took a little over a year before we really appreciated how much even the smallest amount of trace water affected InP NCs. We learned that even anhydrous solvents were too hydrated! We began adding molecular sieves to our solutions which

made a major difference in NC stability. Molecular sieves must be activated before adding to solutions. To activate, place a 20 mL vial's worth of molecular sieves into a flask and pull vacuum on it for 24 hours at 70 °C. After 24 hours, turn off the heat and pull vacuum for 48 hours. After 72 hours, pump the sealed flask of molecular sieves into the glovebox, and use as needed.

#### *1.4.1.2. Glovebox Health*

At a similar time as when I was struggling to prepare stable single InP NC samples, we had a major cleanup of the lab space, including the four-hand glovebox where all single NC sample preparation is done. At the same time, other members of the lab were working on preparing single $CsPbBr_3$ and were having similar issues. There were many old samples, solvents, and precursors from past projects. We could identify some of the chemicals from old lab mates that had just graduated, but many of the chemical's origins were unknown. After doing a major cleanout, and adding molecular sieves to our samples, single NC samples immediately started behaving well. Ensuring the glovebox space is well-maintained, removing unnecessary chemicals when possible, is more important than I initially thought.

Other glovebox practices were adopted throughout my time. We now make sure all chemicals are stored in Tupperware, and that chemicals always have electrical tape around the cap to prevent solvent leaks. We also routinely check for leaks in the glovebox, keeping an eye on the $H_2O$ and $O_2$ ppm sensors and the glovebox pressure. If the glovebox pressure is abnormally high or low, it may be the result of a leak somewhere in the glovebox, maybe from the tubing, from a puncture in one of the gloves, or an imperfect seal on one of the antechamber doors.

#### *1.4.1.3. Sample Variation*

There have been moments in lab when single NC sample preparation is going so well. In these moments, we are able to synthesize new NC samples, prepare them for measurements, and routinely get stable single NCs. Then, out of nowhere, the procedure won't work anymore. The same preparation that's been working for months stops working and we can't figure out what has changed. If the glovebox is functioning fine, it may be a result of new chemicals. If we are making NCs in the lab, we end up going through precursor chemicals fast. Each time chemicals are purchased from a company, expect there to be batch-to-batch variation. There may be some impurity introduced into the precursor that poorly affects the NC stability, or some impurity that isn't there anymore that poorly affects the NC stability! Anytime things suddenly stop working, don't be down on yourself, it's probably not you. I wanted to add this little section so anyone who is struggling understands that some of the science around single NC sample preparation is beyond our control. Some of it really is just trial and error. Not all! But some of it.

### 1.4.2. Single Nanocrystal Measurements

#### *1.4.2.1. Cleaning Substrates*

Cleaning substrates is a necessary step to ensuring NC stability on solid substrates. I am going to include the cleaning procedure for glass and quartz substrates below:

Cleaning Glass Substrates:

1. Place glass substrates to be cleaned into a Teflon substrate holder. Place the substrate holder into a beaker.
2. Fill the beaker with toluene just above the point where all the glass substrates are submerged. Place the beaker in the sonicator and sonicate for 10 minutes.
3. Pour out toluene in a liquid waste container. Repeat step 2, replacing toluene with acetone.
4. Pour out acetone in a liquid waste container. Repeat step 2, replacing acetone with isopropyl alcohol.

Cleaning Quartz Substrates:

1. Place quartz substrates to be cleaned into a Teflon substrate holder. Place the substrate holder into a beaker.
2. Fill the beaker with ethyl acetate just above the point where all the glass substrates are submerged. Place the beaker in the sonicator and sonicate for 10 minutes.
3. Pour out ethyl acetate in a liquid waste container. Repeat step 2, replacing ethyl acetate with toluene.
4. Pour out toluene in a liquid waste container. Repeat step 2, replacing toluene with acetone.
5. Pour out acetone in a liquid waste container. Repeat step 2, replacing acetone with isopropyl alcohol.

#### *1.4.2.2. Polymer*

Polymer helps to encapsulate single NC samples, partially preventing air exposure and contact with the substrate. The polymer I have predominantly used is poly(methyl methacrylate) (PMMA). Other polymers include polystyrene and cadmium oleate. Cadmium oleate is not necessarily a polymer but acts somewhat to encapsulate NCs within small cadmium oleate bubbles.

#### *1.4.2.3. Spin Conditions*

The way we prepare single NC samples on glass or quartz substrates is by spin casting a dilute film onto a substrate. In my experience, I have found that more concentrated samples are needed for quartz substrates compared to glass substrates to get a good single NC distribution. Something about the quartz substrate isn't as "sticky" for InP NCs. I also found that using a slow ramp up speed before the fast spin casting speed is helpful for the quartz substrate samples.

### 1.4.3. Solution Measurements

#### *1.4.3.1. Capillaries*

Capillaries are a great way to hold a small amount of dilute NC sample in solution. I have used capillaries from VitroCom (part #5012-50). The path length is 0.1 mm, the width is 2 mm, the wall is 0.1 mm, and the length of the capillary is 50 mm. We have a capillary holder that was custom made by the Machine Shop at MIT designed to hold these particular capillaries.

#### *1.4.3.2. Polymer*

It is sometimes difficult to get the NC sample to diffuse well in solution. You may come across issues where there are very little counts within the capillary except in a very small focal plane of the capillary. I have found that adding polymer to the solution helps solve this issue. I'm not exactly sure what happens in this situation, but it's almost as if all the NCs get stuck to the walls of the capillary.

#### *1.4.3.3. Background Emission*

Background emission is important to remove from any experiment. In solution correlation experiments, it lowers your FCS trace height, making it look like the sample is more concentrated than it really is. The sample will have the same number of single NC correlations, but the signal to noise ratio of the measurement will have to be stronger in order to get a reasonable dataset. Unique to solution measurements, Raman emission from the solvent becomes an issue if the sample is very dilute and the excitation power is relatively high. It's good to perform a baseline scan of the Raman emission of your solvent (including polymer and any other additives) to see if there is any way to filter out the Raman emission through shortpass or longpass filters. For some reason, I have found that PMMA polymer enhances the Raman emission of toluene.

#### *1.4.3.4. Pinhole*

Solution correlation measurements are very particular to the pinhole alignment. The pinhole can be tuned very slightly, such that the counts do not change, but the FCS trace height will change dramatically. When I am touching up the pinhole alignment with a dilute sample, I not only look for what pinhole alignment gives optimal counts, but also which alignment gives the highest fluctuating signal. Fluctuating signal indicates a more dilute solution. If I can find a pinhole position that has optimal counts AND optimal fluctuations, that will give me the best signal to noise ratio to the experiment at.

# Chapter 2

## Narrow Intrinsic Line Widths and Electron-Phonon Coupling of InP Colloidal Nanocrystals

This section is adapted and reproduced from

ǂD. B. Berkinsky, ǂA. H. Proppe, H. Utzat, C. J. Krajewska, W. Sun, T. Šverko, J. J. Yoo, H. Chung, Y. Won, T. Kim, E. Jang, M. G. Bawendi

"Narrow Intrinsic Line Widths and Electron-Phonon Coupling of InP Colloidal Quantum Dots"

*ACS Nano* 2023, 17, 3598-3609



**Author Contributions**

ǂD.B.B and A.H.P contributed equally to this work. D.B.B. and M.G.B. conceived of the study. D.B.B. co-led the study, performed InP measurements, developed the final modelling algorithm, and contributed to analysis and interpretation of all data. A.H.P. co-led the study, performed InP measurements, developed the final modelling algorithm, and contributed to analysis and interpretation of all data. H.U. contributed to an early version of the modeling, and performed CdSe measurements. C.J.K. performed x-ray diffraction, ensemble absorption, and ensemble PL measurements on InP QDs. W.S. contributed to sPCFS technique development. T.S. contributed to InP sample preparation. J.J.Y. performed CdSe synthesis. H.C., Y.W., and E.J. contributed to InP synthesis.

### 2.1. Abstract

InP quantum dots (QDs) are the material of choice for QD display applications and have been used as active layers in QD light-emitting diodes (QDLEDs) with high efficiency and color purity. Optimizing the color purity of QDs requires understanding mechanisms of spectral broadening. While ensemble-level broadening can be minimized by synthetic tuning to yield monodisperse QD sizes, single QD line widths are broadened by exciton−phonon scattering and fine-structure splitting. Here, using photon-correlation Fourier spectroscopy, we extract average single QD line widths of 50 meV at 293 K for red-emitting InP/ZnSe/ZnS QDs, among the narrowest for colloidal QDs. We measure InP/ ZnSe/ZnS single QD emission line shapes at temperatures between 4 and 293 K and model the spectra using a modified independent boson model. We find that inelastic acoustic phonon scattering and fine-structure splitting are

the most prominent broadening mechanisms at low temperatures, whereas pure dephasing from elastic acoustic phonon scattering is the primary broadening mechanism at elevated temperatures, and optical phonon scattering contributes minimally across all temperatures. Conversely for CdSe/CdS/ZnS QDs, we find that optical phonon scattering is a larger contributor to the line shape at elevated temperatures, leading to intrinsically broader single-dot line widths than for InP/ZnSe/ZnS. We are able to reconcile narrow low-temperature line widths and broad room-temperature line widths within a self-consistent model that enables parametrization of line width broadening, for different material classes. This can be used for the rational design of more spectrally narrow materials. Our findings reveal that red-emitting InP/ZnSe/ZnS QDs have intrinsically narrower line widths than typically synthesized CdSe QDs, suggesting that these materials could be used to realize QDLEDs with high color purity.

## 2.2. Background

Colloidal quantum dots (QDs) are solution-processable semiconductor nanocrystals that can exhibit high photoluminescence (PL) quantum yield,[23,51] tunable emission energies,[87,88] and narrow linewidths,[89] making them well suited for light-emitting applications such as biological imaging,[90,91] LEDs,[23,92] and lasers.[93] InP QDs are the material of choice due to their perceived lower environmental toxicity compared to Cd- and Pb-based QDs like CdSe, PbS, and lead halide perovskites.[94,95] Won et al. recently demonstrated the synthesis of highly symmetrical InP/ZnSe/ZnS (core/shell/shell) QDs, using hydrofluoric acid to etch out oxidative surfaces of the InP, yielding near unity photoluminescence quantum yield (PLQY), electroluminescent LEDs with external quantum efficiencies nearing 21.4%, and operating lifetimes of a million hours.[23] These dots also exhibit the narrowest reported full-width at half-maximum (FWHM) for InP QDLEDs of 35 nm (~110 meV), but this remains broader than for well-studied CdSe analogues.[96] For light-emitting applications, narrow emission profiles are desirable to maximize color purity.

The QD emission line shape is broadened at the single dot level and the ensemble level.[71,83] Ensemble broadening typically results from QD size and morphology polydispersity as well as a distribution in local chemical environments, whereas single QD broadening results from phonon scattering[68,74], fine-structure splitting between band-edge states,[75,97,98] and spectral diffusion. Inelastic phonon scattering involves the real emission or absorption of phonons as a result of the exciton coupling to the lattice vibrations, characterized by the Huang-Rhys parameter,[73] and gives rise to phonon sidebands (replicas of the zero-phonon line, ZPL) seen in many QD systems.[73–77,98] Elastic phonon scattering, a mechanism of pure dephasing, involves the virtual emission and absorption of phonons. This process randomizes the phase of the electronic wavefunction, causing a loss of coherence and broadening of the ZPL, but does not change the central emission energy.[78] Fine-structure splitting of the electronic states within the QD occurs as a result of the electron-hole exchange and crystal field and shape anisotropies.[55] Minimizing the spectral

linewidth of QDs requires understanding the contributions of these mechanisms to spectral broadening. Single QD broadening mechanisms are obfuscated at the ensemble level where dot-to-dot variations average out any single QD broadening effects. This can be overcome using nonlinear optical spectroscopy techniques,[99,100] or by studying isolated single QDs.

In this study, we sought to characterize the contributions of fine-structure splitting, phonon scattering, and ensemble broadening on the emission linewidth of InP/ZnSe/ZnS QDs using solution photon-correlation Fourier spectroscopy, temperature-dependent single QD spectroscopy, and simulating the emission spectra with a model that accounts for acoustic and optical phonon inelastic/elastic phonon scattering and fine-structure splitting.

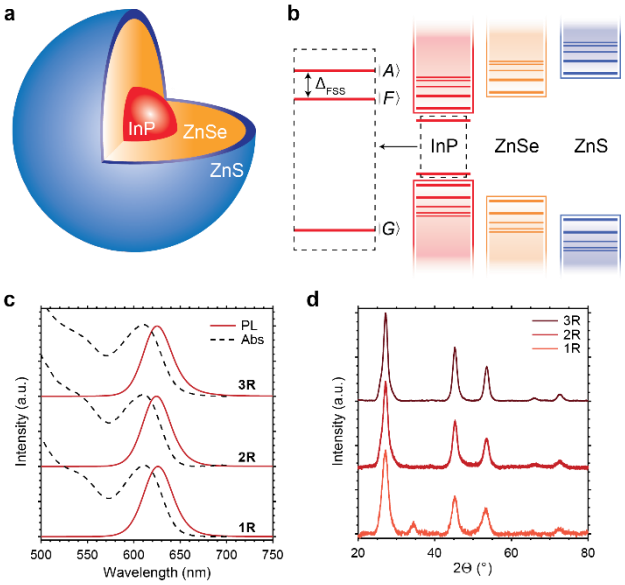


**Figure 2.1.** (**a**) InP/ZnSe/ZnS (core/shell/shell) heterostructure. (**b**) Relative band energies and fine-structure splitting ($\Delta_{FSS}$) in the InP band structure. The states $|G\rangle$, $|F\rangle$, and $|A\rangle$ are ground, forbidden excited ($F = \pm 2$), and allowed excited ($F = \pm 1$), respectively. (**c**) ensemble absorption (dashed black) and emission (solid red) for three InP/ZnSe/ZnS QDs with varying ZnSe shell sizes. The 1R QDs have the thinnest ZnSe shell and the 3R QDs have the thickest shell. (**d**) X-ray diffraction (XRD) patterns of the 1R, 2R, and 3R QDs.

**Figure 2.1.**

The InP/ZnSe/ZnS QDs under investigation (synthesized as described in Won et al.) have a 3.3 nm InP core, varying ZnSe inner shell thicknesses, and a 0.15 nm ZnS outer shell (**Figure 2.1a**).[23] These dots exhibit near unity PLQY, and narrow ensemble PL ($PL_{max}$ of 625 nm, FWHM of 35 nm). Following the naming convention in Won et. al., we refer to QDs with ZnSe shell thicknesses of 1.8, 2.7, and 3.5 nm as 1R, 2R, and 3R, respectively.[23] These QDs are known to exhibit a type-I band alignment.[101] In similar InP/ZnSe systems, it has been shown that the lowest energy exciton state is optically forbidden ($F = \pm 2$), with an optically allowed state ($F = \pm 1$) several meV above (**Figure 2.1b**).[98]

Ensemble PL and absorption spectra are similar for the 1R, 2R, and 3R QDs (**Figure 1c**). Samples were prepared by diluting QDs by a factor of 100 in toluene. Absorption spectra were measured with an Agilent Technologies Cary 5000 UV-VIS-NIR spectrophotometer PL spectra were measured using a HORIBA Jobin Yvon Fluoromax 3 spectrofluorometer. The ensemble PL spectrum is not affected by the varying ZnSe shell sizes, and the PL linewidths are consistent for all three QD sizes — summarized in **Table 2.1**. To investigate any differences in strain or crystal structure between 1R – 3R QDs, we collected X-ray diffraction (XRD) patterns. XRD patterns were obtained using a multipurpose diffractometer (PANalytical X'Pert Pro) equipped with a 1.8 kW Cu-Kα X-ray source aligned in a Bragg-Brentano geometry. For sample preparation, a concentrated solution of QDs was dropcast onto a zero-diffraction plate (MTI Corp., Si crystal, P-type B-doped). The peaks in the XRD patterns for the 1R – 3R QDs are highly similar, showing no obvious shifts or changes in relative amplitude, except for the 1R pattern sometimes exhibiting an additional peak depending on the sample preparation, identified as a ZnO contaminant (**Figure 2.1d**).

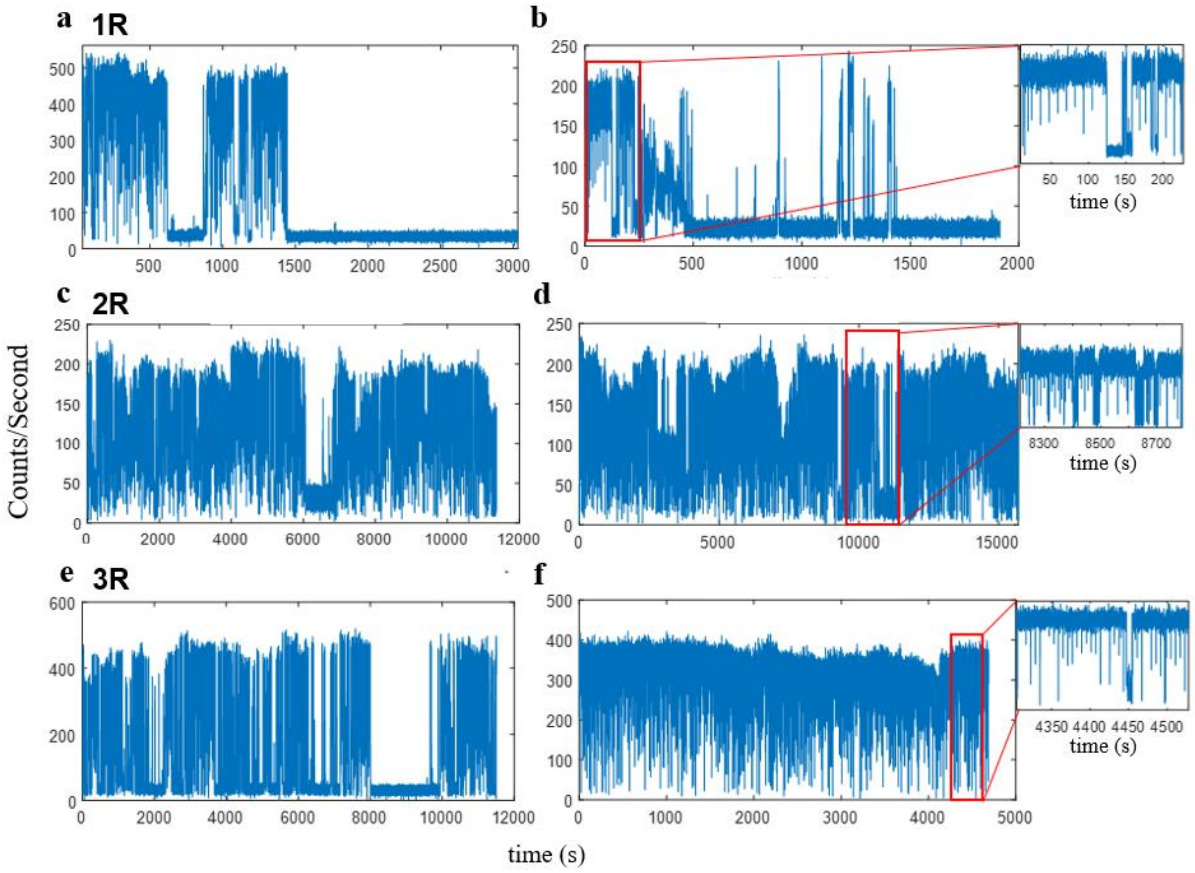


**Figure 2.2.** Room temperature intensity traces of single QDs for the (**a**, **b**) 1R (**c**, **d**) 2R, and (**e**, **f**) 3R. Insets of (**b**, **d**, **f**) expand a smaller region of each intensity trace to show more clearly the on-off times.

This oxidation contaminant was consistent with the fact that the 1R QDs proved to generally be less stable — single QD emission from 1R QDs exhibited more fluorescence intermittency (blinking) compared to 2R and 3R QDs — see **Figure 2.2**.

Since we observed no obvious optical or structural differences between the 1R – 3R QDs, and due to the greater stability of the 3R QDs, the data shown in the main text is for 3R QDs, and similar results from 1R and 2R QDs can be found in the Supporting Information.

## 2.3. Room Temperature Characterization of the InP QD Line Shape

We next assessed the ensemble linewidth and average single QD linewidth using solution photon-correlation Fourier spectroscopy (sPCFS) at room temperature (RT). sPCFS uses interferometric second-order intensity correlations (denoted as $g^{(2)}(\tau)$ and $g^{\times}(\delta,\tau)$ for the auto-correlation and cross-correlation, respectively, where $\tau$ is the difference in arrival times between photon pairs) to draw a relationship between time-correlations, measured by a Hanbury-Brown and Twiss (HBT) interferometer, with the energy-dependent interference from a Michelson interferometer (**Figure 2.3d**).

In this solution-phase experiment, a small number of QDs are probed in the microscope focal volume (typically between 5–20 dots). These QDs will diffuse out of this volume on the order of μs or ms with a characteristic diffusion time $\tau_{diff}$. Photon pairs with $\tau < \tau_{diff}$ have a higher probability of emitting from the same QD. By measuring how $g^{\times}(\delta,\tau)$ changes with respect to $g^{(2)}(\tau)$ as a function of the interferometer stage position (**Figure 2.3a**), an interferogram is constructed. The PCFS interferogram is proportional to the Fourier transform of the autocorrelation of the QD emission spectrum.[102] If we assume two things: (1) there are no single QD contributions to correlations when $\tau >> \tau_{diff}$ and (2) the ensemble correlations are independent of $\tau$, then we can isolate the single QD contributions to the correlations at short $\tau$ by subtracting out the ensemble contributions, which we determine from long $\tau$. In this way, two interferograms are constructed, one for the ensemble component at long $\tau$, and one for the average single QD component at short $\tau$. The single QD interferogram is an average of all QDs diffusing in and out of the focal volume, avoiding user selection bias affecting typical single QD measurements. Detailed explanations of sPCFS are given elsewhere.[68,102]

sPCFS was performed using a home-built confocal microscope. Samples were prepared by diluting QDs by a factor of 20,000 in toluene with poly(methyl methacrylate) (PMMA) (1% wt/wt, Sigma) and trioctylphosphine (TOP) (0.01% v/v, Sigma) and adding the solution to a capillary. The solution sample was excited with a continuous wave laser source (center wavelength 488 nm, Coherent) for sPCFS experiments. The excitation laser was focused onto the solution sample using a water immersion objective (Nikon 60x, NA 1.2), and the sample emission was directed to a 1:1 telescope (8 cm focal length with a

100 µm pinhole), and laser light was filtered using a tunable longpass filter (Semrock Versachrome TLP01-628). The filtered emission was directed to a Michelson interferometer with a 50/50 beamsplitter. The path length difference was controlled by a nanopositioning linear stage (Aerotech). The path length difference was adjusted to discrete stage positions (81 stage positions) using step increments of ~620 nm, and the center stage position being at maximum coherence. At each stage position, the path length difference is dithered with a triangle wave-from over 600 nm with a frequency of 0.05 Hz. Sample photon emission was detected using silicon avalanche photo diodes (APDs) (SPCM CD 3764 H, Excelitas) and recorded using a Time Tagger 20 with a 34 ps jitter (Swabian). We calculated the second-order cross- and auto-correlations using home-built software (MATLAB) at each stage position to determine the ensemble and single QD spectral correlations. We refer to previous publications for detailed descriptions of sPCFS and data analysis.

Experimental sPCFS results for a solution of 3R QDs are shown in **Figure 2.3b**. We observe the single QD interferogram decays at longer interferometer path differences than the ensemble, indicative of a longer coherence time, or narrower linewidth. To fit the experimental interferograms, we assumed the underlying ensemble PL spectrum to be a single Gaussian, whereas the underlying single QD PL spectrum is better fit with the sum of two Gaussians that have the same center emission energy. The ensemble and single QD interferograms are fit to Equations 2.2 and 2.4, respectively. Reconstructed PL spectra, extracted from the interferogram fits, are plotted in **Figure 2.3c**.

The spectral correlation $p(\zeta,\tau)$ is equivalent to the autocorrelation of the QD spectrum in the absence of spectral dynamics. We assume the ensemble PL spectrum fits reasonably to a single Gaussian (Equation 2.1) with a center frequency $\omega_0$, an amplitude $A$, and width $c$. The resulting interferogram (Equation 2.2) is also a single Gaussian related to the ensemble spectrum.

$$Ae^{-\frac{(\omega-\omega_0)^2}{2c^2}} \tag{2.1}$$

$$2\pi A^2 c^2 e^{-4\pi^2 c^2 \delta^2} \tag{2.2}$$

We assume the single QD PL spectrum fits to a sum of two Gaussians (Equation 2.3) with center frequency $\omega_0$, amplitudes $A$ and $B$, and widths $c$ and $d$. The resulting single QD interferogram is the sum of three Gaussians related to the properties of the single QD spectrum.

$$Ae^{-\frac{(\omega-\omega_0)^2}{2c^2}} + Be^{-\frac{(\omega-\omega_0)^2}{2d^2}} \tag{2.3}$$

$$2\pi\left(A^2 c^2 e^{-4\pi^2 c^2 \delta^2} + B^2 d^2 e^{-4\pi^2 d^2 \delta^2} + 2ABcde^{-2\pi^2\delta^2\left(c^2+d^2\right)}\right) \tag{2.4}$$

We can fit the experimental ensemble and single QD interferograms to Equations 2.2 and 2.4, respectively, reconstructing their PL spectra using the parameters from the fit.

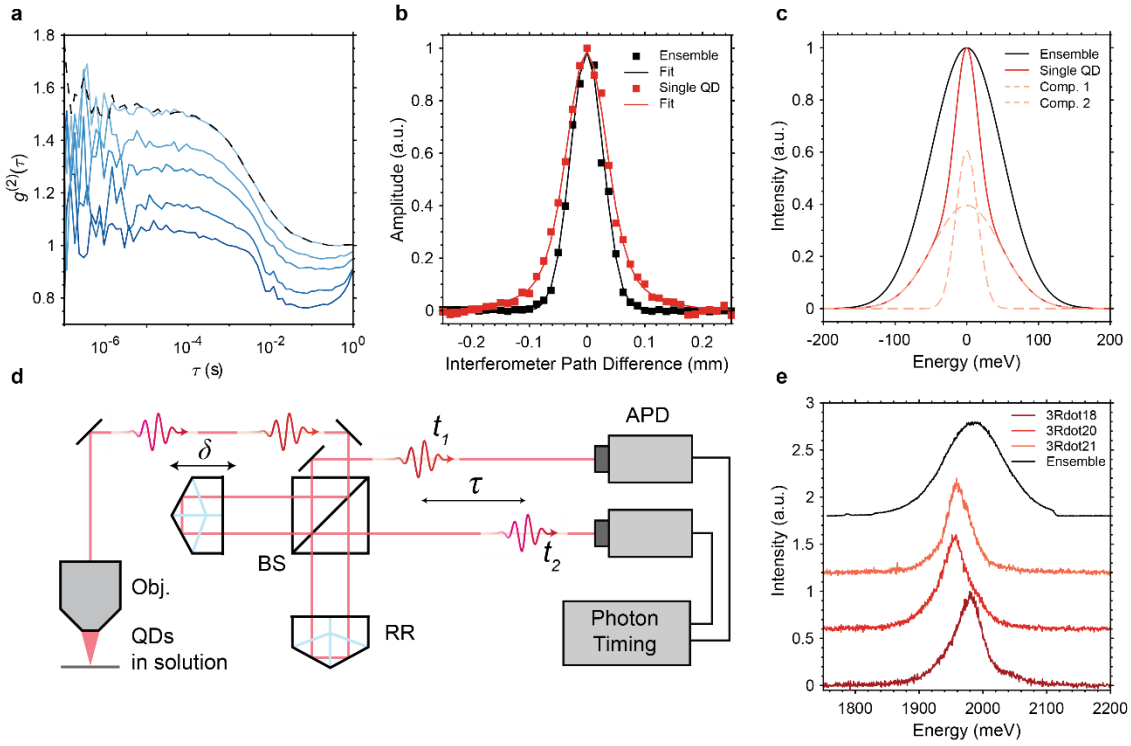


**Figure 2.3.** (**a**) The auto-correlation ($g^{(2)}(\tau)$, dashed black line) and the cross-correlation ($g^{\times}(\delta,\tau)$, solid blue) at different stage positions (dark-to-light blue corresponds to early-to-later stage positions). (**b**) Solution interferogram composed of a series of auto- and cross-correlations at a photon time difference τ=10 μs. The ensemble interferogram fit assumes a single Gaussian for the underlying PL spectrum, and the single QD interferogram fit assumes a sum of two Gaussians. **(c)** Reconstructed spectra for the ensemble (solid black), average single QD (solid red), and components of the single QD fit (Comp. 1 and 2) based on the fit to the experimental interferograms. **(d)** Interferometer schematic. BS = beamsplitter, RR = retroreflector, Obj. = microscope objective. **(e)** Three 3R single QD spectra at room temperature (red) compared to the ensemble spectrum (black).

Interferograms and reconstructed PL spectra for the 1R and 2R QDs are plotted in **Figure 2.11**. Average single QD linewidths are summarized in **Table 2.1**. The ensemble and average single QD linewidths extracted from sPCFS are 115 and 50 meV, respectively ($\tau$ = 10 μs). The observed ensemble FWHM ($\sigma_{obs}$), the single QD FWHM ($\sigma_S$), and the FWHM of the (assumed to be Gaussian) energy distribution due to ensemble broadening ($\sigma_E$) are related by $\sigma_{obs} = \sqrt{{\sigma_E}^2 + {\sigma_S}^2}$, which gives $\sigma_E$ of 104 meV, indicating a wide size and energy distribution of QDs. The 1R and 2R ensemble broadening is summarized in **Table 2.1**. This suggests that optimization of the synthetic procedure to achieve a narrower size distribution can further increase the color purity of InP/ZnSe/ZnS QD devices. Following the production of this work, another study was published suggesting the ensemble broadening can also arise from core-shell interface inhomogeneity. [69]

The narrow average single QD linewidth from sPCFS were corroborated by PL spectra of single QDs. The QDs were highly diluted and spin-coated onto glass coverslips for RT measurements in a protective poly(methyl methacrylate) matrix — see below paragraphs for detailed sample preparation and measurement details. Representative spectra are shown in **Figure 2.3e**, where we measured values of FWHM ranging from 38 - 63 meV. The single QD PL consistently exhibit an additional lower amplitude shoulder at lower energies, resulting in asymmetric line shapes. Single QD PL for 1R and 2R QDs are shown in **Figure 2.12**. These lower amplitude shoulders are consistent with the additional broad base we observe in the spectra generated by fitting the single dot interferogram in sPCFS. Note that the fitted spectra from sPCFS are symmetric, since they are derived from the Fourier transform of the autocorrelation of the single dot spectrum, which is by definition symmetric.

No. 0 coverslips (Goldseal) were cleaned in four steps: (1) coverslips were sonicated for 15 minutes in Hellmanex detergent solution (2% v/v in DI water), (2) sonicated for 15 minutes in pure DI water, (3) sonicated for 15 minutes in acetone, and (4) immersed in boiling isopropanol for 15 minutes and dried under $N_2$ flow before being transferred into an $N_2$ glovebox with <0.1 ppm $H_2O$ and $O_2$. In the same glovebox, InP/ZnSe/ZnS QDs were diluted 50,000-fold in anhydrous toluene (Sigma) with PMMA (1% wt/wt, Sigma) and TOP (0.1% v/v, Sigma). 40 µL of the diluted sample was spin-coated at 8,000-rpm with 1000 rpm/s acceleration for 60s onto previously mentioned clean No. 0 coverslips. The spun samples were then encapsulated against 25x75x1 mm microscope slides using epoxy (Devcon 5-minute epoxy, VWR). The encapsulated coverslips were allowed to cure for at least 2 hours before removed from the glovebox, ready for experiments.

Room temperature single QD spectroscopy was performed using a home-built confocal microscope. A pulsed laser source (center wavelength 532nm, repetition rate 1 MHz, 100 ps pulse duration, Picoquant LDH-P-F-A-530-B) was directed into an oil-immersion objective (Nikon 100x, NA 1.45) and the sample emission was directed to a 1:1 telescope (8 cm focal length with a 100 µm pinhole), and laser light was filtered using a tunable longpass filter (Versachrome TLP01-628, Semrock). The sample was mounted below the objective, and the galvo mirror angles were adjusted electronically for confocal raster scans. For intensity trace measurements, the filtered sample emission was directed to a 50:50 plate beamsplitter (BSW10, Thorlabs), and each output is reflected off a cold mirror with a cut-off above 700 nm (M254C00, Thorlabs) before being focused onto two APDs (SPCM CD 3764 H, Excelitas). Photon arrival times were then recorded using a Time Tagger 20 with a 34 ps jitter (Swabian). For single QD spectrum measurements, the filtered sample emission was directed to a spectrometer setup where a monochromator (sp2500i with a 150 g/mm grating, Princeton Instruments) diffracts the light. Spectra were recorded with a CCD camera (ProEM512B, Princeton Instruments).

## 2.4. Temperature-Dependent InP Line Shape

It is challenging to identify which line shape broadening mechanisms contribute to the asymmetry in the single QD line shape at RT, as there are several mechanisms that convolve with one another at elevated temperatures. To gain insight into the asymmetry and single QD broadening contributions to the emission line shape, we measured the PL spectra of several single InP/ZnSe/ZnS QDs at temperatures ranging from 4K to 293K. The PL spectra for 3 different single 3R QDs from 4K – 220K are shown in **Figure 2.4a-c**. Low temperature spectra from 4K – 30K for the 1R – 3R QDs are shown in **Figure 2.4d-f** to show the fine-structure splitting more clearly.

Quartz substrates (MTI corp, optical grade) were cleaned in a similar process as the No. 0 coverslips for room temperature single QD sample preparation. Samples were diluted 50,000-fold in anhydrous toluene (Sigma) with PMMA (5% wt/wt, Sigma) and TOP (0.1% v/v, Sigma). 20 µL of the diluted sample was spin-coated in a three-spin speed process: (1) 500-rpm with 100 rpm/s acceleration for 5s, (2) 1,000-rpm with 200 rpm/s acceleration for 5s, and (3) 6,000-rpm with 1000 rpm/s for 60s. To avoid extended exposure to atmosphere, the samples were quickly transferred from an inert atmosphere container onto the platform of a 4K closed cycle liquid helium cryostat (Cryostation, Montana Instruments), which was immediately placed under vacuum.

Cryogenic temperature single QD spectroscopy was performed using a home-built confocal microscope. A continuous wave laser source was used (center wavelength 532nm, Laser Quantum Ventus-MPC6000) for single QD spectrum measurements and a pulsed laser source (center wavelength 532nm, repetition rate 0.125 MHz, 100 ps pulse duration, Picoquant LDH-P-FA-530B) for PL lifetime measurements. Excitation laser was focused onto the sample using an air-immersion objective (Zeiss Epiplan-Neofluar 100x, NA 0.90) and the sample emission was directed to a 1:1 telescope (8 cm focal length with a 50 µm pinhole), and laser light was filtered using a tunable longpass filter (Versachrome TLP01-628, Semrock). For single QD spectra, filtered single QD emission was directed to a spectrometer setup were a monochromator (spi2500i with a 300g/mm grating, Princeton Instruments) diffracts the light. Spectra were recorded with an EMCCD camera (ProEM512B, Princeton Instruments). Resolution of the spectrometer-camera setup was 0.9 meV. For single QD PL lifetimes, filtered single QD emission was directed to a Michelson interferometer where the variable path was set beyond the coherence length of the emitter to ensure interference would not affect the measurement. Photon streams were detected by two APDs (AQRH-16, Excelitas) and recorded in a time-tagged mode (T3 mode) using a HydraHarp400 (Picoquant).

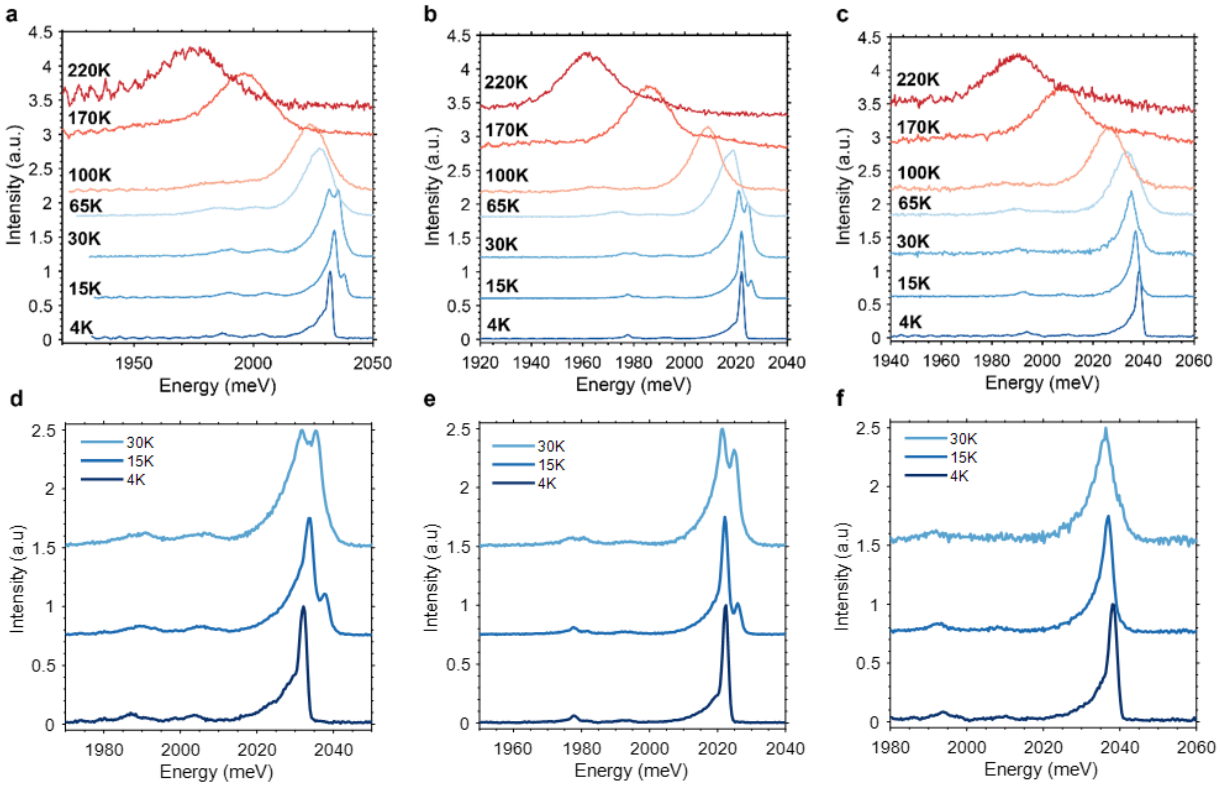


**Figure 2.4.** (**a-c**) Three single 3R QD spectra from 4K – 220K. The higher energy peak growing in at 15K and 30K is identified as the allowed state transition. Fringes on the lower energy side of the spectra (between ~1920 and 1970 meV) result from EM gain applied across the CCD camera used to collect the spectra. (**d-f**) 4K – 30K spectra expanded for the 3R QDs to show fine-structure more clearly.

At 4K, these spectra show a sharp zero-phonon line (ZPL) accompanied by a pronounced lower energy shoulder, which is identified as the acoustic phonon sideband from the inelastic acoustic phonon scattering occurring due to the deformation potential;[73,103] similar line shapes have been observed in other QD systems.[77,104–108] PL spectra as a function of temperature for 1R and 2R QDs are shown in **Figure 2.16.** Similar measurements were performed for CdSe/CdS/ZnS QDs in **Figure 2.18**. Contributions from the acoustic phonon sideband extend out to ~20 meV from the ZPL in some QDs. The broader and lower amplitude peaks ~42 meV and ~39 meV lower in energy than the ZPL corresponds to the inelastic scattering of the exciton with two optical phonon modes: the longitudinal optical (LO) and transverse optical (TO) phonons of the InP core.[74] We assign the remaining peak centered ~28 meV lower in energy than the ZPL to the inelastic scattering of the LO and TO ZnSe phonons. Inelastic optical phonon scattering is attributed to the Fröhlich coupling mechanism, where an LO phonon creates an electric field that the atoms within the crystal lattice respond to. The more polar the nature of the lattice, the stronger the Fröhlich coupling.[109,110] The optical deformation potential is another coupling mechanism responsible for the smaller TO phonon sideband in InP QDs.[111] However, we will focus our discussions on the Fröhlich coupling mechanism as the LO phonons contribute more significantly to the inelastic optical phonon scattering. The phonon replicas

take the shape of the ZPL, with an intensity that reflects the strength of the exciton-phonon coupling (Huang-Rhys parameter) and the phonon occupation number at the given temperature.

Inelastic scattering of phonons involves the real emission or absorption of phonons, resulting in a phonon sideband on the lower energy side of the ZPL (phonon emission) or the higher energy side of the ZPL (phonon absorption).[73] In the case of phonon emission, the exciton gives some of its energy to the lattice, emitting a phonon, leaving the radiative recombination of the exciton at a lower energy than the ZPL. In phonon absorption, an existing phonon within the QD interacts with the exciton promoting the exciton to a higher vibrational state. The exciton radiatively recombines in this higher vibrational state meaning the emission is at a higher energy than the ZPL. At 4K, the acoustic phonon sideband is only visible on the lower energy side of the ZPL, corresponding to the real emission of acoustic phonons during radiative recombination. There is a small probability of phonon occupation of these modes at low temperatures, and so phonon absorption is suppressed, causing the higher energy side of the ZPL to instead be narrow. With increasing temperature, we observe a growth of the higher energy shoulder of the ZPL, consistent with increasing acoustic phonon occupation and phonon absorption. As the temperature increases above 30K, the ZPL and phonon replicas broaden and overlap as a result of elastic phonon scattering (pure dephasing). As the temperature increases, so does the phonon occupation and therefore the elastic scattering processes which leads to a broadening of the ZPL and phonon replicas.

## 2.5. Fine Structure

At 4K, single 3R QD emission proved to be spectrally stable, exhibiting minimal blinking and spectral diffusion over many minutes (**Figure 2.5a**), suggesting that spectral diffusion on the seconds to minutes timescale contributes minimally to the observed linewidths. Spectral diffusion contributions on faster timescales (sub-ms) can be investigated using single QD PCFS, and will be the subject of future studies — see Chapter 3. The PL of the 1R QDs was more likely to diffuse or blink off entirely under excitation, suggesting the additional ZnSe shell thickness of the 2R and 3R helps to increase emissive and spectral stability (**Figure 2.14**).

Upon increasing the temperature to 15K and 30K, a second peak grows in at higher energy, which we identified as the $F = \pm 1$ allowed state (*A*), indicating the ZPL at 4K arises from the $F = \pm 2$ forbidden state (*F*). The higher energy peak grows in intensity with higher temperatures as *A* becomes thermally populated. This direct observation of both the *A* and *F* states has been observed previously for CdSe QDs at similar temperatures.[97]

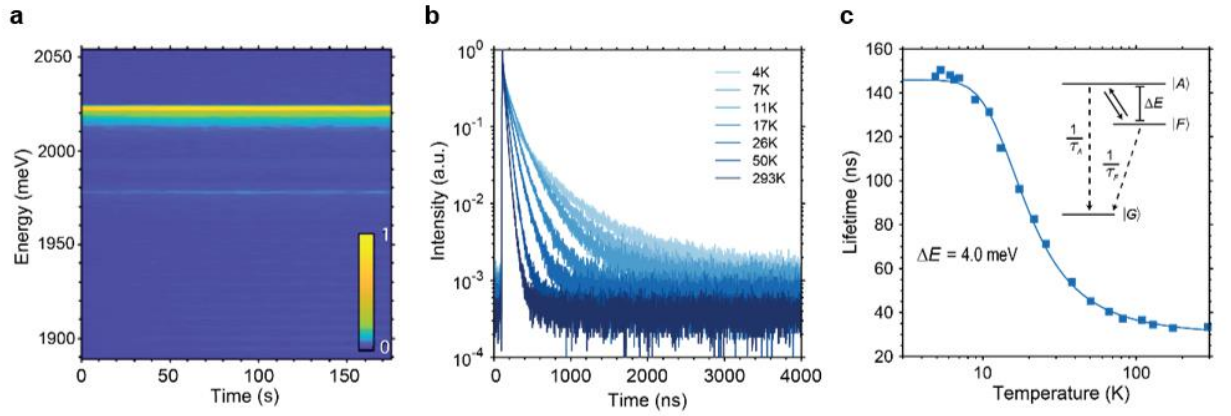


**Figure 2.5.** (**a**) Spectral stability of the ZPL at 4K as a function of time. (**b**) Temperature-dependent lifetimes in a dilute film of QDs. (**c**) Long component of the lifetimes in (**b**) as a function of temperature fit to Eq. 2.5 to extract the average fine-structure state energy splitting.

These observations suggest a band-edge electronic structure highly similar to that of CdSe QDs, a 3-level system (**Figure 2.5c** inset) wherein above bandgap excitation creates an exciton that can thermalize into the *A* or *F* state. Excitons in the *A* state can undergo allowed radiative recombination into the ground state, or enter the *F* state. The *A* state can be thermally repopulated from *F*, introducing a set of coupled rate equations that can be rearranged to express the overall temperature-dependent PL lifetime as:

$$\Gamma_{tot} = \frac{1}{\tau_{tot}} = \frac{1}{\tau_F}\left(\frac{1}{1+e^{\frac{-\Delta E}{k_B T}}}\right) + \frac{1}{\tau_A}\left(\frac{1}{1+e^{\frac{\Delta E}{k_B T}}}\right) \tag{2.5}$$

where $\tau_F$ and $\tau_A$ are the lifetimes of the forbidden and allowed state, respectively, $\Delta E$ is the energy splitting between the two states, $k_B$ is the Boltzmann constant, $\tau_{tot}$ is the long component of the measured lifetime, and $\Gamma_{tot}$ is the decay rate of the system. Such a 3-level model has been verified by Brodu et al. for InP/ZnSe QDs using the above equation.[98] We perform a similar analysis here, at the ensemble level, for the InP/ZnSe/ZnS QDs. Ensemble PL lifetimes from thin films of QDs at 4K – 293K were measured (**Figure 2.5b**) and fit (**Figure 2.5c**) to Equation 2.5, yielding average fine-structure splitting energies of 4 meV for the 3R QDs. Similar measurements were performed on the 1R and 2R QDs (Fig. S7). Results are summarized in **Table 2.1**. This energy splitting is consistent with the energy splitting we observe in single QD low temperature PL spectra, which supports our assignment of the higher energy ZPL as the allowed $F = \pm 1$ state.

## 2.6. Independent Boson Model

From these spectra, we can identify several mechanism that contribute to broadening of the single QD line shape: pure dephasing from elastic phonon scattering that gives rise to a Lorentzian ZPL; spectral diffusion that adds Gaussian broadening to the ZPL;[112] fine-structure splitting; and inelastic scattering with acoustic and optical phonons. We sought to model the emission line shapes in order to characterize the

magnitude of each single QD broadening contribution to the overall linewidth as a function of temperature. The influence of phonons on the absorption and emission line shapes of chromophores can be described in the time- or frequency-domain by assuming a model for the two-time correlation function that describes the fluctuations of the electronic energy gap – typically a correlation function corresponding to a phonon bath comprised of a discrete set of a harmonic oscillators.[112] Through the fluctuation-dissipation theorem, this can be cast into a frequency-domain spectral density, $J(\omega)$, which describes the coupling strength between the optical transition and a given phonon mode of frequency $\omega_i$.

In order to account for phonon scattering in the spectral lineshape, we model the PL spectra in the frequency-domain using a modified independent boson model (IBM) [73]. IBMs have been used previously to describe acoustic phonon coupling in QD systems,[77,105,106] and we extend the model here to also account for coupling to optical phonons and both the *A* and *F* fine-structure states simultaneously. To ensure the generality of our model to other QD systems, we additionally measured temperature-dependent single QD spectra for CdSe/CdS/ZnS (core/shell/shell) QDs.

While analytical solutions of the emission line shape in the frequency domain are typically intractable for a given $J(\omega)$, we can instead discretize $J(\omega)$ and treat the acoustic phonon sideband and optical phonon sideband as a series of replicas of the ZPL, whose coupling strengths (i.e. the amplitudes of these replicas in the spectrum) are determined by $J(\omega)$. We use the following spectral densities $J(\omega)$:

$$J(\omega)_{InP} = J_{a_1}(\omega) + J_{a_2}(\omega) + J_{InP-LO}(\omega) + J_{InP-TO}(\omega) + J_{ZnSe-LO/TO}(\omega) \tag{2.6}$$

$$J(\omega)_{CdSe} = J_{a_3}(\omega) + +J_{CdSe-LO/TO}(\omega) + J_{CdS-LO/TO}(\omega) \tag{2.7}$$

The InP/ZnSe/ZnS total spectral density is described by two acoustic spectral densities — $J_{a_1}(\omega)$ and $J_{a_2}(\omega)$ — and by three optical spectral densities — $J_{InP-LO}(\omega)$, $J_{InP-TO}(\omega)$, $J_{ZnSe-LO/TO}(\omega)$ corresponding to the InP longitudinal optical (LO) phonon, the InP transverse optical (TO) phonon, and the ZnSe LO/TO phonon modes, respectively. The CdSe/CdS/ZnS total spectral density is described by one acoustic spectral density —$J_{a_3}(\omega)$ — and two optical spectral densities —$J_{CdSe-LO/TO}(\omega)$, $J_{CdS-LO/TO}(\omega)$ corresponding to the CdSe LO/TO phonon modes and the CdS LO/TO phonon modes, respectively. The acoustic spectral densities are described by Equation 2.8

$$J_{a_j}(\omega) = \sum_{i=1}^{N} \delta(\omega_i - \omega)\, \lambda_j \omega_i e^{-\omega_i/\omega_{c_j}} \tag{2.8}$$

where $\lambda_j$ and $\omega_{c_j}$ are the coupling strength and the cutoff frequency of the $j^{th}$ acoustic spectral density. The InP/ZnSe/ZnS QDs the acoustic phonon sideband is fit to two spectral densities since, in contrast to other QD systems,[73] we found that one spectral density alone could not account for the entire acoustic band. The InP acoustic spectral density is broad and contains many phonon modes that can add or subtract from one

another to create even more phonon modes.[113] The CdSe/CdS/ZnS acoustic phonon sidebands were fit to a single spectral density. We found Ohmic spectral densities to be suitable to obtain good fits to our data.[114]

In the InP/ZnSe/ZnS QD spectra, we observe that the optical phonon replicas are broader than the ZPL, suggesting a distribution of the optical phonon energies, which has been observed in GaAs single QDs.[115] To account for this, we modelled the optical phonons for the InP/ZnSe/ZnS and CdSe/CdS/ZnS QDs as Gaussian distributions, rather than as single discrete ZPL replicas, using the following form:

$$J_o(\omega) = \sum_{i=1}^{N} \delta(\omega_i - \omega)\, S_o e^{-\frac{(\omega_i - \omega_o)^2}{\sigma_o}} \tag{2.9}$$

where $S_o$, $\omega_o$, and $\sigma_o$ are the coupling strength (Huang-Rhys parameter), phonon energy, and the Gaussian FWHM of optical phonon $o$, respectively. We use three different phonon modes in the model for InP/ZnSe/ZnS: InP-LO at 42 meV, InP-TO at 38.5 meV, and a single peak to account for the mixed ZnSe-LO and ZnSe-TO phonons at 28 meV. We use two different optical modes in the model for CdSe/CdS/ZnS: CdSe-LO/TO at 26 meV, CdS-LO/TO at 36 meV.

Using a discretized vector of frequencies $\omega$ that spans ±60 meV, the IBM model creates phonon replicas (initially as delta functions) at each frequency whose amplitudes are determined by $J(\omega)$ and weighted by Bose-Einstein statistics that account for phonon occupation and phonon number (multi-phonon processes) (eq. M8), creating the asymmetry between higher and lower energy replicas around the ZPL, corresponding to phonon absorption and emission.

$$W_{p,i} = \left(\frac{n_i+1}{n_i}\right)^{\frac{p}{2}} e^{-J_i(2n+1)} I_p\left[2J_i\sqrt{n_i(n_i+1)}\right] \tag{2.10}$$

where $n_i = \left[e^{\frac{\hbar\omega_i}{k_b T}} - 1\right]^{-1}$ is the Bose-Einstein distribution and $I_p[z]$ is the imaginary argument Bessel function. The *A* and *F* ZPLs are then generated as Voigt lineshapes[116] – a product of a Lorentzian to account for pure dephasing from elastic phonon scattering, and a Gaussian to account for any spectral diffusion – where the amplitude of the higher energy *A* state is also weighted by a temperature-dependent Bose-Einstein distribution. Both ZPLs are convolved with their own acoustic phonon sidebands, and then finally convolved with their own optical phonon sidebands to obtain the spectrum (Equation 2.11)

$$\sum_{p_1 \ldots p_2}^{\infty} W_{p_1} \ldots W_{p_N} \delta(h\nu - E_0 + p_1\hbar\omega_1 + \cdots + p_N\hbar\omega_N) \tag{2.11}$$

We measured emission spectra as a function of temperature and fit the line shapes to the modified IBM using a gradient-descent least-squares fitting algorithm. We first fit the spectra at 4K using floating parameters for $\lambda_j$ and $\omega_{c_j}$ of the acoustic phonons, and for $S_o$ and $\sigma_o$ of the optical phonons. The parameters are then tightly constrained except for the Lorentzian linewidth of the ZPL, assuming no temperature

dependence in the Huang-Rhys parameters for the acoustic and optical phonons. The remaining temperature-dependent growth of the acoustic and optical phonon sidebands in the fit enters only through Bose-Einstein statistics (Equation 2.10).

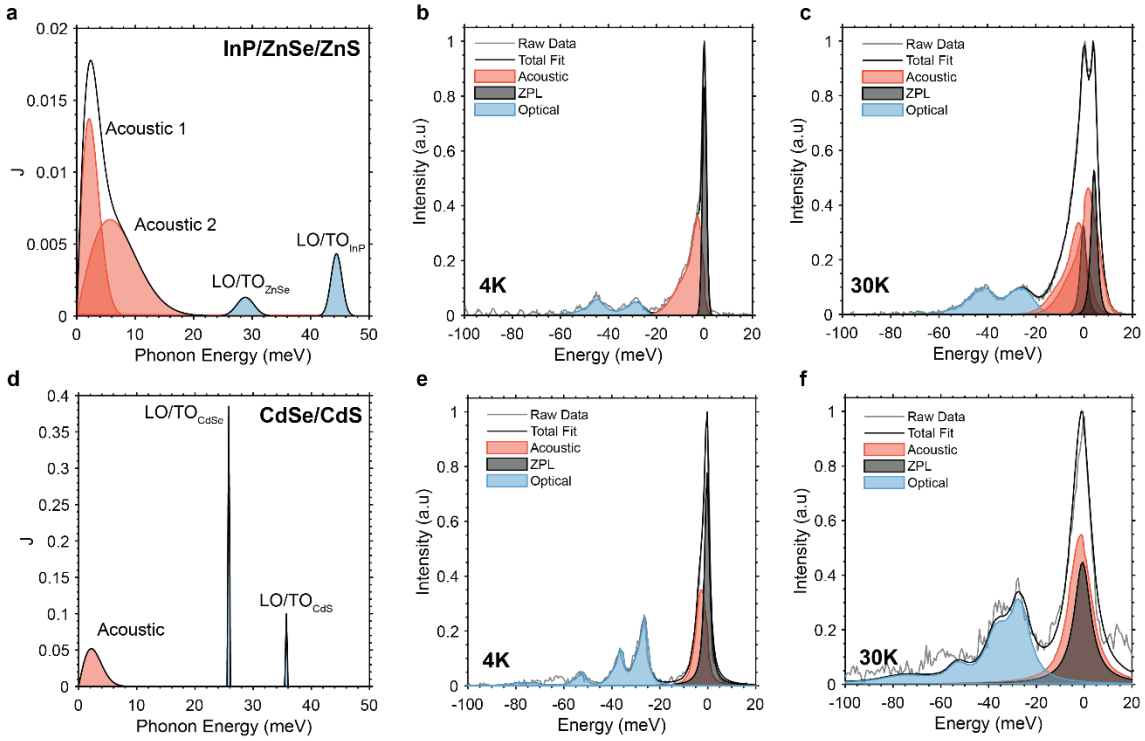


**Figure 2.6.** (**a, d**) Spectral density of phonon modes for representative InP/ZnSe/ZnS and CdSe/CdS/ZnS single QDs, respectively. The acoustic (red) and optical (blue) phonon modes can be summed together into an overall spectral density $J(\omega)$ (black line). (**b, e**) Single QD PL spectra for the same QDs and fits from the IBM separated into the individual components contributing to the overall line shape at 4K and **(c, f)** 30K.

Examples of $J(\omega)$ generated from fits to spectra of single InP/ZnSe/ZnS and CdSe/CdS/ZnS QDs are shown in **Figure 2.6a,d**, highlighting the individual constituent spectral densities for the acoustic and optical phonons. The Huang-Rhys parameter is calculated as the overall integrated area for each spectral density. Since our modified IBM separately generates each component of the emission lineshape, we can isolate each contribution to the total FWHM including the forbidden and allowed state ZPLs, their respective acoustic phonon sidebands, the optical phonon sidebands, and contributions from pure dephasing. The overall PL spectra, the isolated ZPL, acoustic sideband, and optical phonon components of a single 3R InP QD and a CdSe/CdS/ZnS QD are shown in **Figure 2.6b,c** and **Figure 2.6e,f** at 4K and 30K, respectively. We can clearly resolve the individual components of both *F* and *A* states in the InP 3R QD (**Figure 2.6c**), but only see one ZPL in the CdSe/CdS/ZnS QD (**Figure 2.6e,f**). The fine-structure splitting is expected to be similar for similarly sized InP and CdSe cores since the II-VI and III-V electronic structure is the same.[55] We posit that the lack of fine structure in CdSe/CdS/ZnS QD emission indicates we are observing emission from the trion state, which has no exchange interaction to split the excited state.[117,118]

## 2.7. Deconvoluting the Temperature Dependent InP QD Line Shape

Spectra at temperatures ranging from 4K to 220K, and fits using the modified IBM, are shown in **Figure 2.7e,f**. Single 1R, 2R, and 3R QD spectra with fits are plotted in **Figure 2.16**, and single CdSe/CdS/ZnS QD spectra with fits are plotted in **Figure 2.18**. We find that our model is able to generate excellent fits to the spectra across the entire temperature range, and we track the contributions to the full FWHM from the acoustic phonon sideband, the fine-structure splitting, the optical phonon sideband, and the ZPL as a function of *T* (**Figure 2.8a-d**).

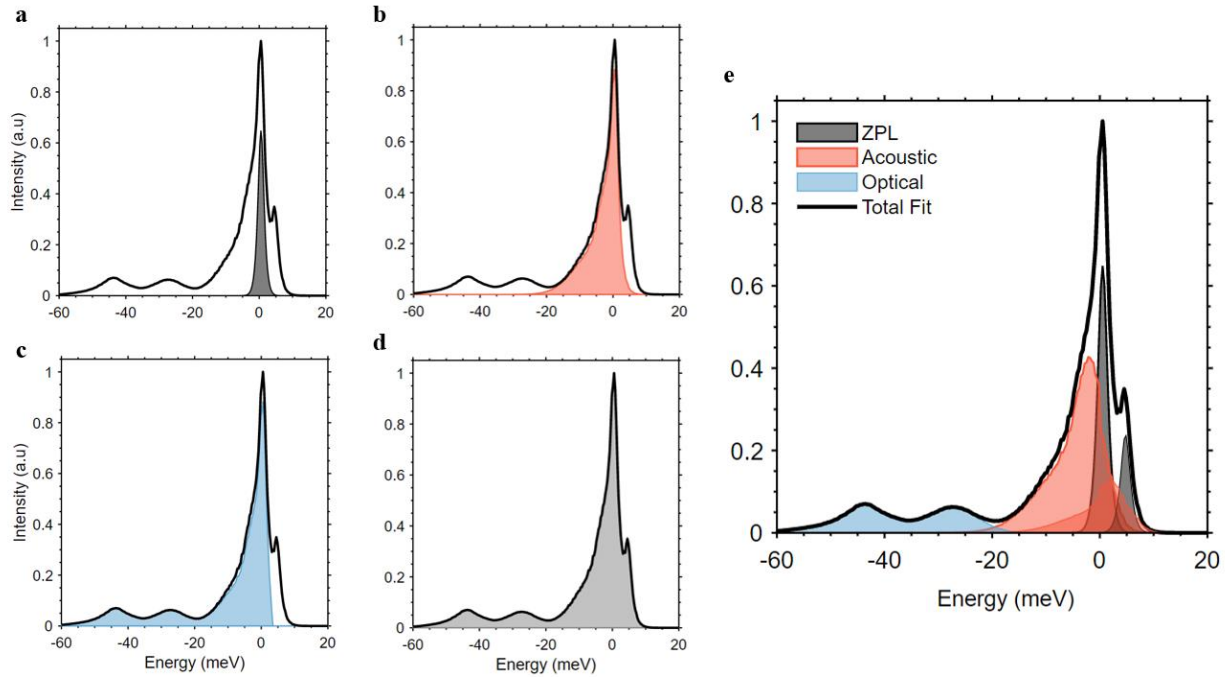


**Figure 2.7.** Line shape of a 3R QD at 15K separated into the individual components. (**a**) contribution from the forbidden F state ZPL (shaded black). (**b**) contribution from the forbidden F state ZPL and acoustic phonon sideband (PSB) (shaded red). (**c**) contribution from the forbidden F state ZPL, acoustic PSB, and the optical PSB (shaded blue). (**d**) contribution from the forbidden F state ZPL, acoustic PSB, optical PSB, and the allowed A state ZPL, acoustic PSB, and optical PSB. (**e**) Overall line shape at 15K broken down into all the individual components from the F and A states.

We chose to quantify the contributions from each individual component of the line shape in an iterative process. First, we calculated the FWHM of the forbidden *F* state ($FWHM_{ZPL}$) in **Figure 2.7a**. Next, we calculated the FWHM of the *F* state acoustic phonon sideband (PSB) convolved with the ZPL ($FWHM_{ZPL+Ac}$) in **Figure 2.7b**. Next, we calculated the FWHM of the *F* state acoustic PSB and optical PSB convolved with the ZPL ($FWHM_{ZPL+Ac+Op}$) in **Figure 2.7c**. Finally, we calculate the FWHM of the *F* state acoustic PSB and optical PSB convolved with the ZPL plus the allowed *A* state acoustic PSB and optical PSB convolved with the ZPL, or in other words, the full line shape FWM ($FWHM_{full}$) in **Figure**

**2.7d**. We assigned the contributions to the overall line shape from the pure dephasing, the acoustic PSB, the optical PSB, and fine structure in equations (2.12)-(2.15):

$$Pure\ Dephasing = FWHM_{ZPL} \tag{2.12}$$

$$Acoustic\ PSB = FWHM_{ZPL+Ac} - FWHM_{ZPL} \tag{2.13}$$

$$Optical\ PSB = FWHM_{ZPL+Ac+Op} - FWHM_{ZPL+Ac} \tag{2.14}$$

$$Fine\ Strucure\ Splitting = FWHM_{full} - FWHM_{ZPL+Ac+Op} \tag{2.15}$$

We note the FWHM of the ZPL at 4K is limited by the resolution of the spectrometer (~0.9 meV). For the 3R InP QD, inelastic acoustic phonon scattering, fine-structure splitting, and the ZPL contribute similar amounts to the linewidth at low temperature (**Figure 2.8a,b**). Inelastic acoustic phonon scattering contributions to the linewidth increase and saturate at 65K, contributing less than 5 meV to the linewidth at elevated temperatures. A sudden jump in the overall linewidth around 15K to 30K can be attributed to the growth of the *A* fine-structure state. There is negligible contribution from inelastic optical phonon scattering across all temperatures, likely a result of the type-I heterostructure of InP/ZnSe/ZnS and the less polar nature of the III-V InP. Elastic phonon scattering contributions to the linewidth increases with temperature according to Equation 2.16

$$\Gamma(T) = \Gamma_0 + \gamma\left(e^{\hbar\omega_c/k_bT} - 1\right)^{-1} \tag{2.16}$$

where $\Gamma_0$ is the zero-temperature linewidth, $\omega_c$ is the energy of the phonon mode, and $\gamma$ is the coupling strength to the phonon mode. The ZPL is the largest contributor to the spectral linewidth in the 3R QDs at elevated temperatures, and since Equation 2.16 fits well to the ZPL linewidth as a function of temperature, we conclude that elastic phonon scattering is the dominant line broadening mechanism for the 3R QDs at elevated temperatures.[119] The energy of the phonon mode contributing to elastic phonon scattering in the QD in **Figure 2.8a** is $\omega_c = 2.3$ meV suggesting pure dephasing of the ZPL occurs only through acoustic phonons. The $LO/TO_{InP}$ phonons are high in energy and therefore require higher temperatures for the elastic optical phonon scattering process to become thermally active. Additional 1R, 2R, and 3R QD FWHM vs. temperature plots are shown in **Figure 2.17**. The strength of the inelastic phonon scattering is determined by the Huang-Rhys parameter, $S$, which for our discretized spectral densities is simply calculated by summing over the spectral densities for each component, $S = \sum_{i=1}^{N} J_i$. For this representative 3R dot, we observe the acoustic phonons have higher inelastic scattering strengths than the optical phonons with $S$ = 0.96, 0.11, and 0.06 for the acoustic phonons, $LO/TO_{InP}$, and $LO/TO_{ZnSe}$, respectively. Values of $S$ are summarized for the 1R, 2R, and 3R QDs in **Table 2.2**. From these extracted values, we observe some small

differences between the 1R, 2R, and 3R QDs, where the 1R QDs appear to have the strongest coupling to phonons.

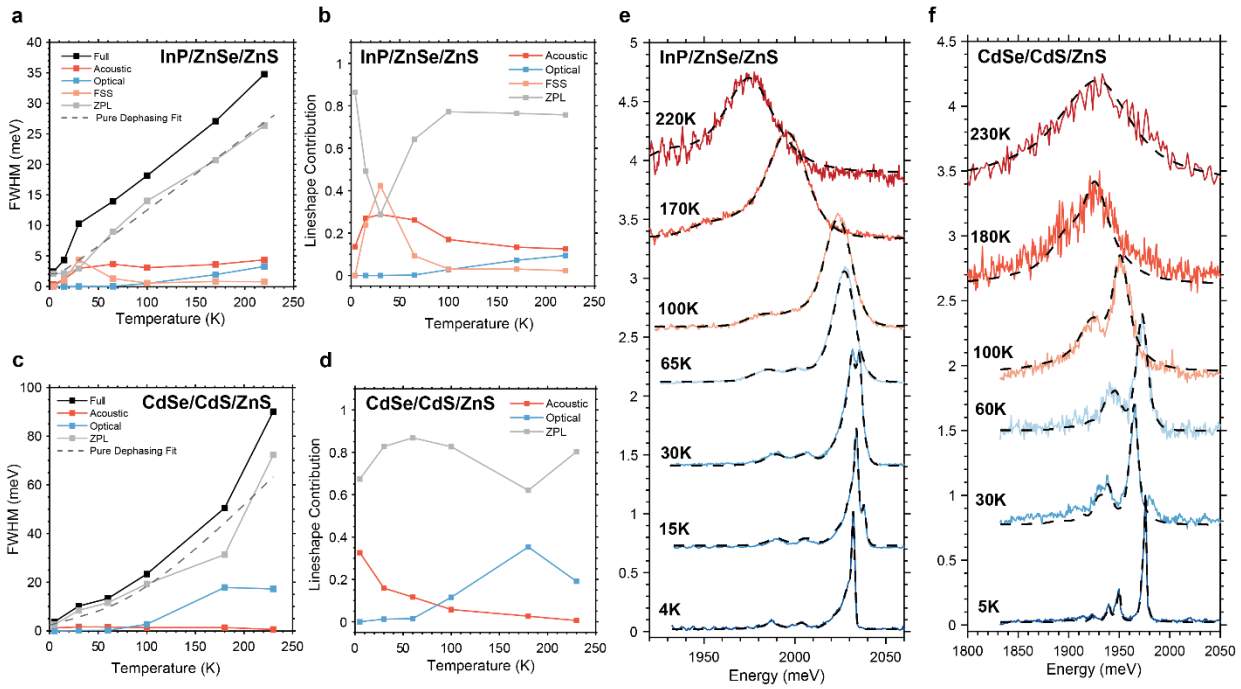


**Figure 2.8.** FWHM as a function of temperature of (**a**) 3R and (**b**) CdSe/CdS/ZnS single QDs separated into the contributions from inelastic acoustic phonon coupling, inelastic optical phonon coupling, fine-structure splitting (FSS), ZPL and the fit to the pure dephasing within the ZPL– (**a**) $\gamma = 3.2$, $\omega_c = 2.3$, $\Gamma_0 = 2.05$ (**b**) $\gamma_1 = 0.67$, $\omega_{c_1} = 0.5$, $\gamma_2 = 100.0$, $\omega_2 = 26.9$, $\Gamma_0 = 2.55$. Fraction of the full line shape contributed from acoustic phonons, optical phonons, and the ZPL of a (**c**) 3R and (**d**) CdSe/CdS/ZnS QD. Single QD PL spectra (solid lines) as a function of temperature with IBM fits (dotted black) for a (**e**) 3R QD and (**f**) CdSe/CdS/ZnS QD.

Tracking the line shape of CdSe/CdS/ZnS as a function of temperature, the ZPL linewidth dominates across all temperatures. The largest difference between InP/ZnSe/ZnS and CdSe/CdS/ZnS QDs comes from the optical phonon scattering: for the CdSe/CdS/ZnS QDs, optical phonons contributes significantly through both inelastic and elastic scattering (**Figure 2.8c,d,f**). Additional CdSe FWHM vs. temperature plots are shown in **Figure 2.19**. The larger optical phonon scattering due to the more polar nature of CdSe and the quasi-Type II heterostructure in CdSe/CdS/ZnS causes the inelastic optical phonon sideband to contribute ~20 meV to the overall linewidth at elevated temperatures. We posit that the sharp increase in the ZPL component of the linewidth at 180K results from elastic scattering of the $LO/TO_{CdSe}$ phonons, whose occupation numbers are sufficiently high at these temperatures, in addition to the elastic scattering of acoustic phonons that arises at lower temperatures.[120]

For this representative CdSe/CdS/ZnS dot, we observe the inelastic phonon scattering of the acoustic and optical phonons are similar with $S = 0.63$, 0.39, and 0.10 for the acoustic phonons, $LO/TO_{CdSe}$, and $LO/TO_{CdS}$, respectively. The $LO/TO_{CdSe}$ and $LO/TO_{CdS}$ phonon sidebands are similar to those observed

in other studies of CdSe/CdS QDs.[121,122] Compared to $S$ extracted from the InP dot, we observe that the inelastic scattering strength for acoustic phonons is ~0.5x lower in CdSe, whereas for optical phonons it is ~1.6 - 3.5x stronger (by comparing $LO/TO_{CdSe}$ and $LO/TO_{CdS}$ with $LO/TO_{InP}$ and $LO/TO_{ZnSe}$). Overall, the less polar nature of III-V InP QDs compared to CdSe, and the lesser electron-hole wavefunction spatial difference in the Type-I InP/ZnSe/ZnS QDs compared to the quasi-type II CdSe/CdS/ZnS QDs, results in less inelastic optical phonon scattering via Fröhlich coupling. This makes InP/ZnSe/ZnS the material of choice for light-emitting applications with narrow emission linewidths. The difference in acoustic coupling strength between these two materials is still under investigation and will be the topic of future works.

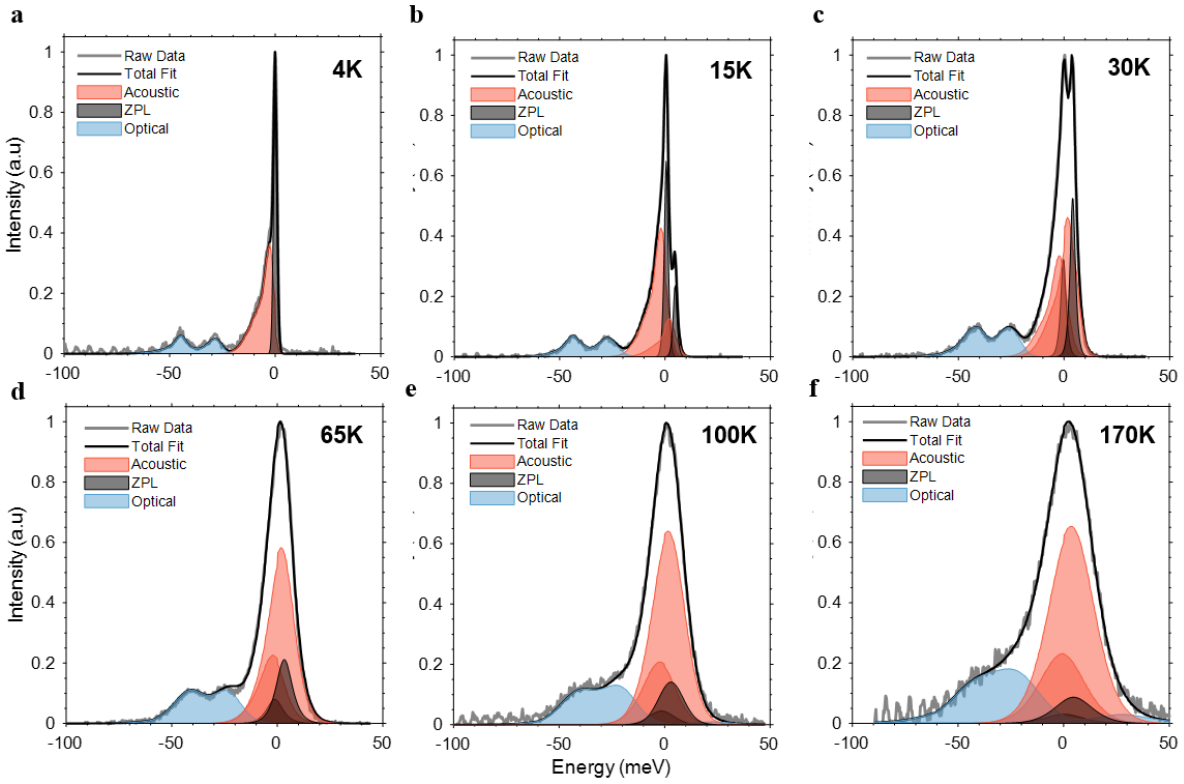


**Figure 2.9.** PL spectra of 3Rdot1 as a function of temperature. The spectra are separated into its individual components including the ZPL, the acoustic phonon side band, and the optical phonon side band and for temperatures of (**a**) 4K, (b) 15K (**c**) 30K, (**d**) 65K, (**e**) 100K, and (**f**) 170K

For both the InP/ZnSe/ZnS QD in **Figure 2.9** and the CdSe/CdS/ZnS QD in **Figure 2.10**, emission is dominated by the inelastic scattering of acoustic and optical phonons at elevated temperatures. It is important to note that although emission is dominated by inelastic phonon scattering, the linewidth is dominated by elastic phonon scattering. If there was minimal elastic phonon scattering, then the linewidth would be effectively limited by the energy of the phonon. For instance, the CdSe and CdS optical phonons are roughly 30 meV away from the ZPL. As the temperature increases so does the phonon occupation number. As long as the ZPL stays relatively narrow — under the assumption of minimal elastic phonon

scattering — the phonon sidebands will also remain relatively narrow because they are phonon *replicas* of the ZPL. When we observe a broadening phonon sideband like we see in both the InP and CdSe systems at elevated temperatures in **Figure 2.9** and **Figure 2.10**, we should interpret the broadening as the ZPL itself broadening and the phonon sidebands reacting accordingly.

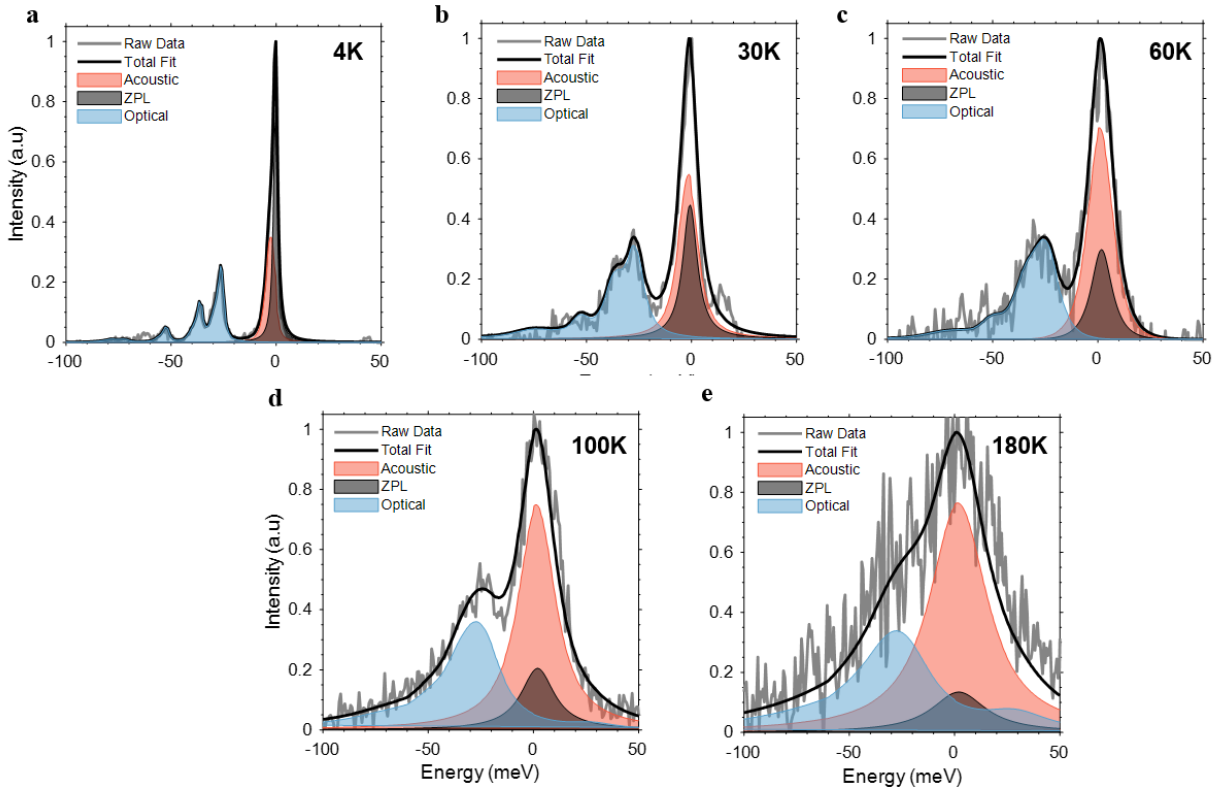


**Figure 2.10.** PL spectra of CdSe/CdS DotI as a function of temperature. The spectra are separated into its individual components including the ZPL, the acoustic phonon side band, and the optical phonon side band and for temperatures of (**a**) 4K, (**b**) 30K, (**c**) 60K, (**d**) 100K, and (**e**) 180K.

In CdSe systems, strain engineering has been used to synthesize QDs with RT single dot linewidths of ~36 meV for biaxially strained QDs,[123] and as low as ~20 meV for asymmetrically compressed cores in CdSe/$Cd_xZn_{1-x}Se$ QDs.[124] In both cases, straining the emissive cores of these QDs modifies the fine-structure of the excitonic band-edge and reduces exciton-phonon interactions to yield a narrower linewidth. Our results demonstrate that InP-based QDs do not require additional strain engineering in order to achieve comparably narrow linewidths, and suggests that a similar growth technique applied to these systems could further reduce single QD broadening by possibly reducing phonon interactions, and reducing fine-structure splitting between *F* and *A* states.

## 2.8. Conclusions

In conclusion, we examined the sources of broad ensemble emission linewidths and narrow single QD linewidths in InP/ZnSe/ZnS QDs. Single InP/ZnSe/ZnS QD linewidths were measured to be as narrow

as 38 meV at RT. Using sPCFS, we find an average single QD linewidth of ~50 meV in solution, compared to an ensemble linewidth of 115 meV, indicating a large QD size polydispersity that results in an energy distribution of 104 meV. Additionally, we have developed a self-consistent model that allows us to reconcile low temperature to RT single QD linewidths for different material classes. We show that pure dephasing of the ZPL from elastic acoustic phonon scattering is the dominant contributor to the FWHM of the single QD lineshape of InP/ZnSe/ZnS QDs at elevated temperatures, with minor contributions from fine-structure splitting, inelastic acoustic phonon scattering, and inelastic/elastic optical phonon scattering. Average fine-structure splitting energies were 4 meV between the forbidden $F = \pm 2$ state and the allowed $F = \pm 1$ state. We further find that for CdSe/CdS/ZnS QDs pure dephasing also dominates the single QD linewidth, however contributions from both optical and acoustic phonon scattering contribute to pure dephasing in this QD system. We also find the more polar nature of CdSe/CdS/ZnS compared to InP/ZnSe/ZnS leads to significant contributions from inelastic optical phonon scattering to the linewidth. Our results indicate that highly luminescent InP/ZnSe/ZnS QDs can exhibit narrow single QD linewidths without requiring strain engineering strategies that mitigate contributions from phonons or fine-structure splitting, further exemplifying them as ideal QD materials for light-emitting display applications. Optimization of synthetic conditions to reduce size polydispersity can further reduce the emission lineshape FWHM at the ensemble level. Exploring similar strain engineering strategies as used for CdSe QDs could possibly yield InP QDs with even narrower single QD spectra, making them exemplary color-pure light emitters.

## 2.9. Acknowledgements

D.B.B and A.H.P acknowledge support from the Samsung Advanced Institute of Technology (SAIT). C.J.K., W.S., and T.S. acknowledge support from the US Department of Energy, Office of Basic Energy Sciences, Division of Materials Sciences and Engineering (under award no. DE-SC0021650). H.H acknowledges support from the US Department of Energy, Office of Basic Energy Sciences, Division of Materials Sciences and Engineering (under award no. DE-FG02-07ER46454). J.J.Y. acknowledges support from the Institute for Soldier Nanotechnology (ISN) grant W911NF-13-D0001. We thank J. Cui and K. Ridderbeek for helpful discussions on sPCFS data analysis.

## 2.10. Supplementary Information

| | $\Gamma_{ensemble}$ (meV) | $\Gamma_{single}$ (meV) | $\sigma_E$ (meV) | FSS (meV) |
|---|---|---|---|---|
| **1R** | 122 | 47 | 111 | 3.6 |
| **2R** | 119 | 50 | 108 | 3.7 |
| **3R** | 115 | 50 | 104 | 4.0 |

**Table 2.1.** Ensemble FWHM, average single QD FWHM, ensemble broadening, and fine-structure splitting (FSS) of the 1R, 2R, and 3R InP QDs.

| | Acoustic HRP | Core Optical HRP | Shell Optical HRP | A1 $\lambda$ | A1 $\omega_c$ (meV) | A2 $\lambda$ | A2 $\omega_c$ (meV) | O1 $\sigma$ (meV) | O2 $\sigma$ (meV) | O3 $\sigma$ (meV) |
|---|---|---|---|---|---|---|---|---|---|---|
| **1R** | 1.33 ± 0.49 | 0.11 ± 0.04 | 0.06 ± 0.04 | 0.0048 ± 0.0013 | 9.69 ± 0.59 | 0.033 ± 0.011 | 3.41 ± 0.36 | 1.54 ± 0.34 | 0.98 ± 0.43 | 1.91 ± 0.53 |
| **2R** | 0.91 ± 0.26 | 0.09 ± 0.02 | 0.05 ± 0.02 | 0.0040 ± 0.0013 | 8.96 ± 0.59 | 0.028 ± 0.011 | 3.20 ± 0.36 | 1.92 ± 0.34 | 1.05 ± 0.43 | 1.71 ± 0.53 |
| **3R** | 0.96 ± 0.47 | 0.11 ± 0.04 | 0.06 ± 0.04 | 0.0037 ± 0.0013 | 9.23 ± 0.59 | 0.024 ± 0.011 | 3.53 ± 0.36 | 1.34 ± 0.34 | 1.04 ± 0.43 | 1.72 ± 0.53 |
| **CdSe/CdS dotI** | 0.63 | 0.39 | 0.10 | 0.0039 ± 0.0013 | 3.10 ± 0.59 | - | - | 0.01 ± 0.34 | 0.01 ± 0.43 | - |
| | | | | | | | | | | |
| | **O1 $\lambda$ (InP-LO/ CdSe)** | **O1 $\omega_c$ (meV)** | **O2 $\lambda$ (InP-TO/ CdS)** | **O2 $\omega_c$ (meV)** | **O3 $\lambda$ (ZnSe)** | **O3 $\omega_c$ (meV)** | **Dephasing Rate ($\mu$eV/K)** | | | |
| **1R** | 0.010 ± 0.0007 | 43.79 ± 0.24 | 0.0019 ± 0.0009 | 39.15 ± 0.37 | 0.0042 ± 0.003 | 27.77 ± 0.09 | 131 ± 16 | | | |
| **2R** | 0.0056 ± 0.0007 | 43.91 ± 0.24 | 0.001 ± 0.0009 | 39.02 ± 0.37 | 0.0032 ± 0.003 | 28.72 ± 0.09 | 98 ± 5 | | | |
| **3R** | 0.012 ± 0.0007 | 44.19 ± 0.24 | 0.0022 ± 0.0009 | 38.99 ± 0.37 | 0.0044 ± 0.003 | 28.91 ± 0.09 | 102 ± 14 | | | |
| **CdSe/CdS dotI** | 0.25 ± 0.015 | 25.9 ± 0.24 | 0.073 ± 0.009 | 36.0 ± 0.37 | - | - | - | | | |

**Table 2.2.** Acoustic phonon sideband (PSB) Huang Rhys Parameter (HRP), the core material (InP or CdSe) optical PSB HRP, the shell material (ZnSe or CdS) optical PSB HRP, acoustic spectral density intensity $\lambda$, acoustic phonon energy $\omega_c$, optical phonon gaussian broadening $\boldsymbol{\sigma}$, optical phonon spectral density intensity $\lambda$, optical phonon energy $\omega_c$, and dephasing rate of the ZPL for the 1R, 2R, 3R QDs and CdSe/CdS dotI.

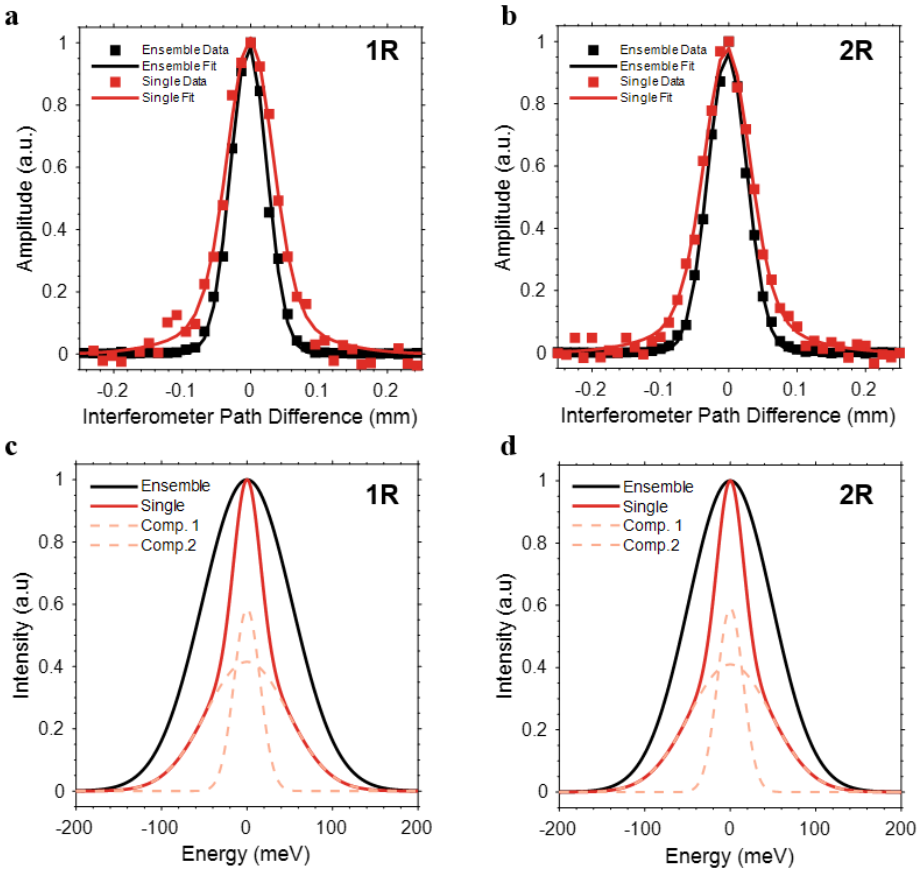


**Figure 2.11.** (**a**),(**b**) Solution interferograms composed of a series of auto- and cross-correlations at a photon time difference τ=10 μs for the 1R (left) and 2R (right) QDs. Ensemble interferogram fit assumes a single Gaussian underlying PL spectrum and the single QD interferogram fit assumes a sum of two Gaussians underlying PL spectrum. (**c**),(**d**) Reconstructed spectra for the ensemble (solid black) and average single QD (solid red) based on the fit to the experimental interferograms for the 1R (left) and 2R (right) QDs. Linewidths are summarized in table

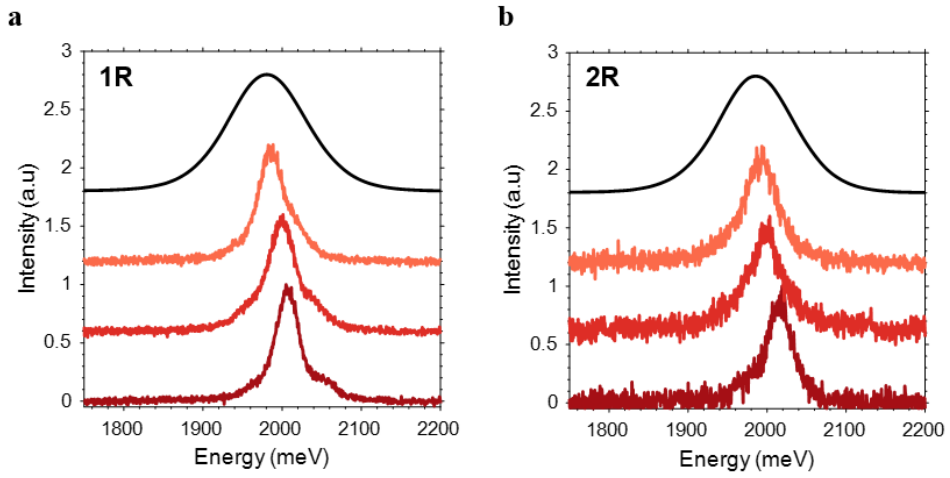


**Figure 2.12.** Three single QD spectra at room temperature (red) compared to the ensemble spectrum (black) for the (**a**) 1R QDs and (**b**) 2R QDs.

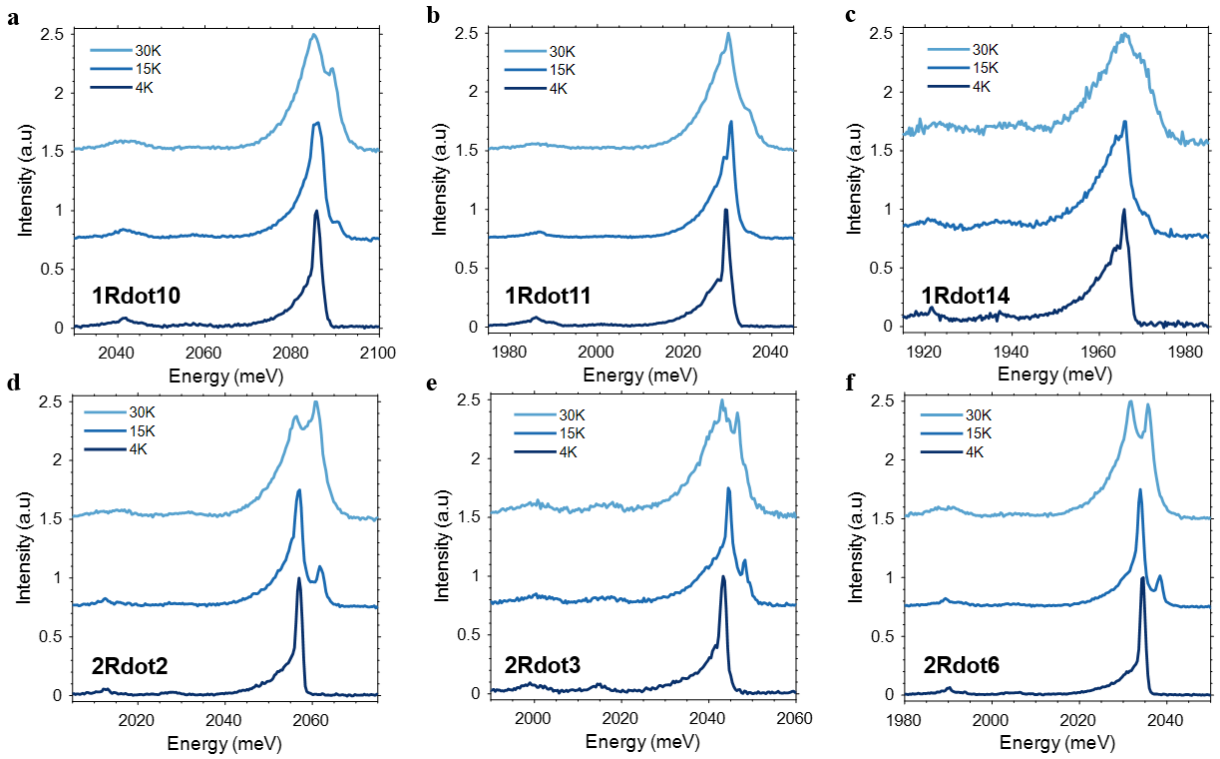


**Figure 2.13.** Three single QD spectra at 4K, 15K, and 30K for the (**a**)-(**c**) 1R QDs and (**d**)-(**f**) 2R QDs, and (**g**)-(**i**) 3R QDs

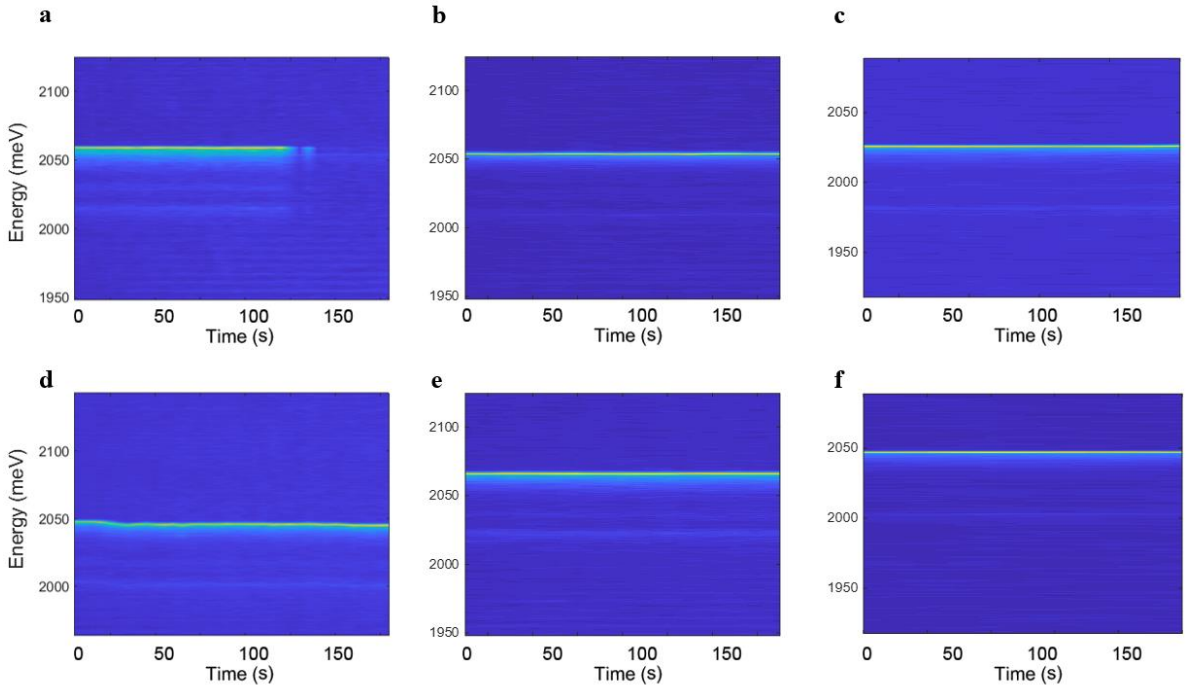


**Figure 2.14.** Spectral stability of the ZPL as a function of time for the (**a**),(**d**) 1R QDs, (**b**),(**e**) 2R QDs, and (**c**),(**f**) 3R QDs.

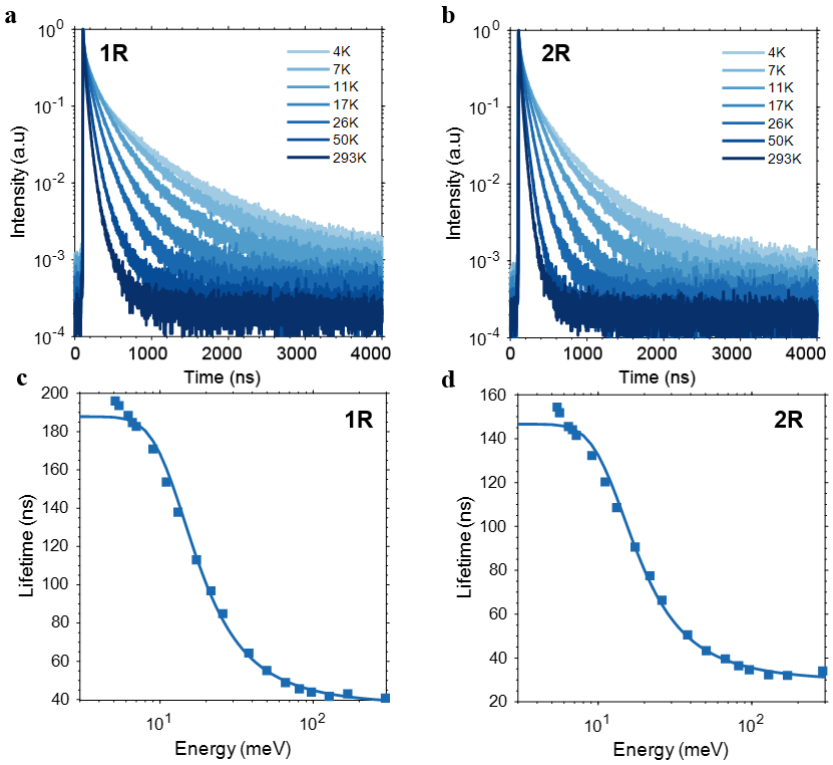


**Figure 2.15.** Temperature-dependent lifetimes in a dilute film of (**a**) 1R QDs and (**b**) 2R QDs. Long component of the lifetimes in (**a**), (**b**) as a function of temperature fit to eq. 1 to extract the average fine-structure state energy splitting for the (**c**) 1R QDs and (**d**) 2R QDs.

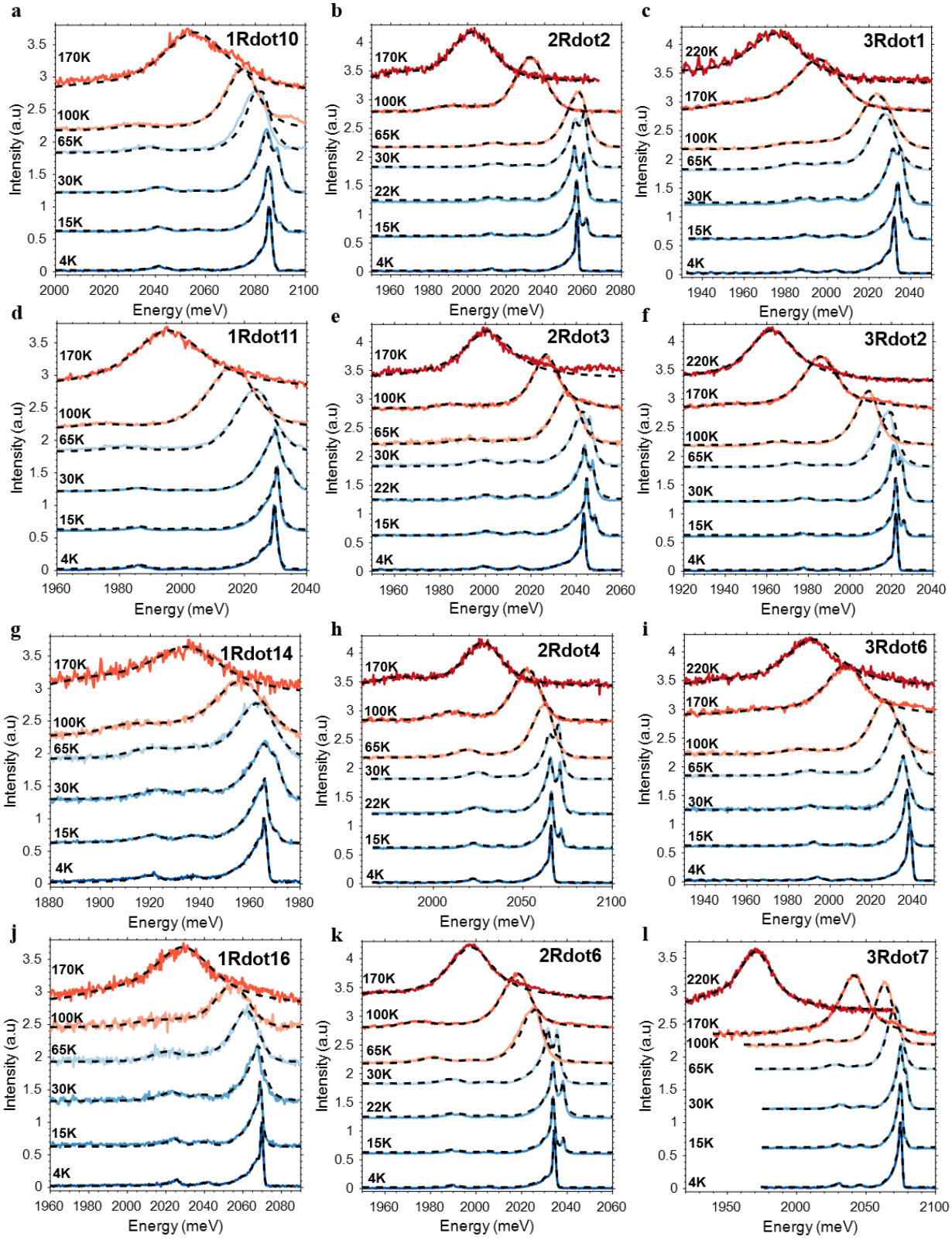


**Figure 2.16.** Single QD PL spectra (solid lines) as a function of temperature with IBM fits (dotted black) overlaid for (**a**),(**d**),(**g**),(**j**) 1R QDs, (**b**),(**e**),(**h**),(**k**) 2R QDs, and (**c**),(**f**),(**i**),(**l**) 3R QDs.

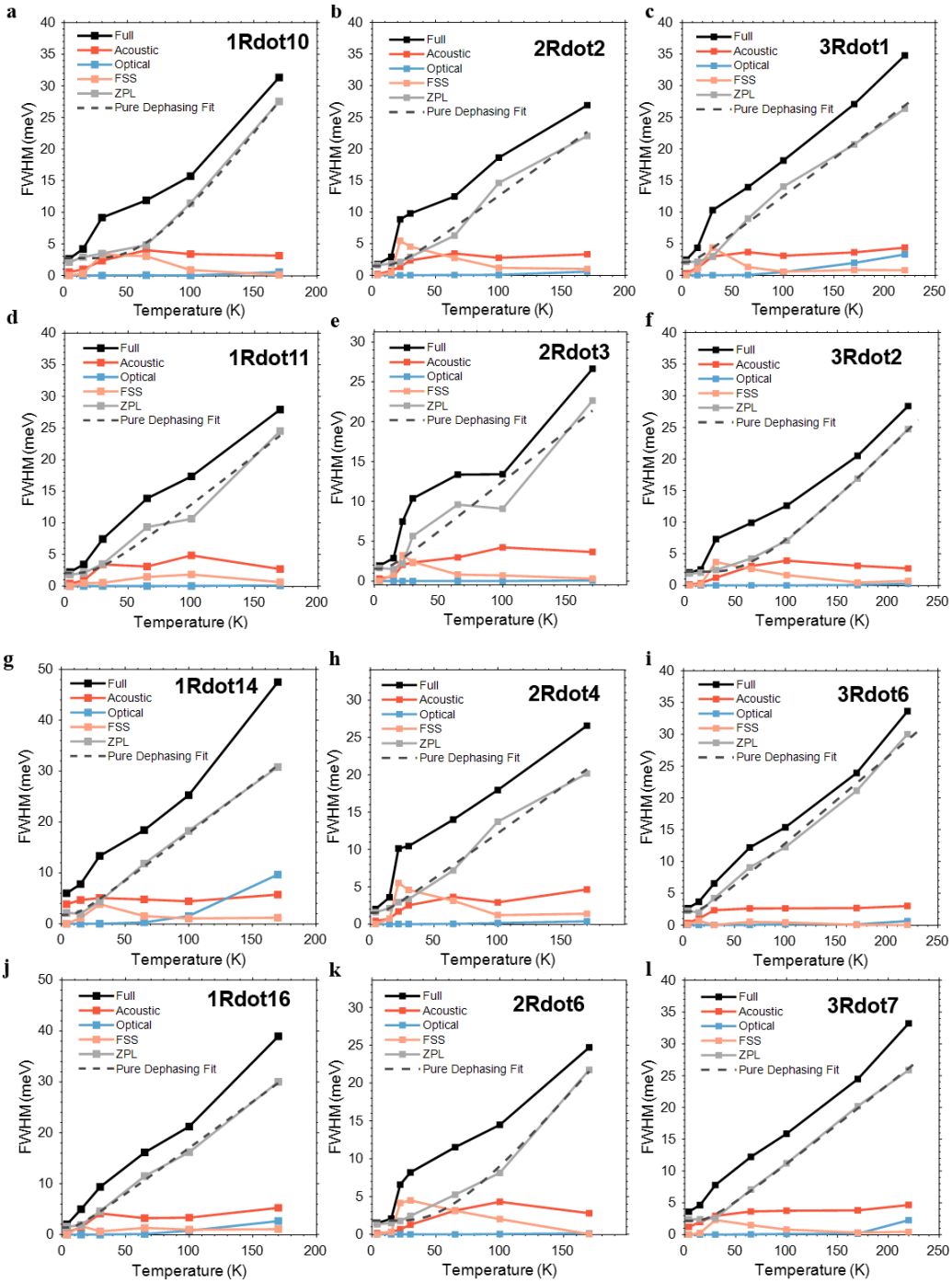


**Figure 2.17.** Single QD FWHM as a function of temperature broken down into the contributions from the acoustic phonon sideband, optical phonon sideband, the fine-structure splitting (FSS), the zero-phonon line (ZPL), and the pure dephasing fit to the ZPL. (**a**) 1Rdot10: $\gamma = 61.0$, $\omega_c = 18.2$, $\Gamma_0 = 2.7$ (**b**) 2Rdot2: $\gamma = 7.9$, $\omega_c = 4.6$, $\Gamma_0 = 1.5$ (**c**) 3Rdot1 $\gamma = 3.2$, $\omega_c = 2.3$, $\Gamma_0 = 2.1$ (**d**) 1Rdot11: $\gamma = 11.6$, $\omega_c = 6.3$, $\Gamma_0 = 2.1$ (**e**) 2Rdot3: $\gamma = 3.8$, $\omega_c = 2.6$, $\Gamma_0 = 1.5$ (**f**) 3Rdot2: $\gamma = 33.4$, $\omega_c = 17.3$, $\Gamma_0 = 2.2$ (**g**) 1Rdot14: $\gamma = 6.3$, $\omega_c = 2.9$, $\Gamma_0 = 1.8$ (**h**) 2Rdot4: $\gamma = 3.4$, $\omega_c = 2.4$, $\Gamma_0 = 1.5$ (**i**) 3Rdot6: $\gamma = 6.3$, $\omega_c = 4.0$, $\Gamma_0 = 2.1$ (**j**) 1Rdot16: $\gamma = 5.7$, $\omega_c = 2.7$, $\Gamma_0 = 1.4$ (**k**) 2Rdot6: $\gamma = 3.4$, $\omega_c = 2.4$, $\Gamma_0 = 1.5$ (**l**) 3Rdot7 $\gamma = 8.5$, $\omega_c = 5.7$, $\Gamma_0 = 2.2$.

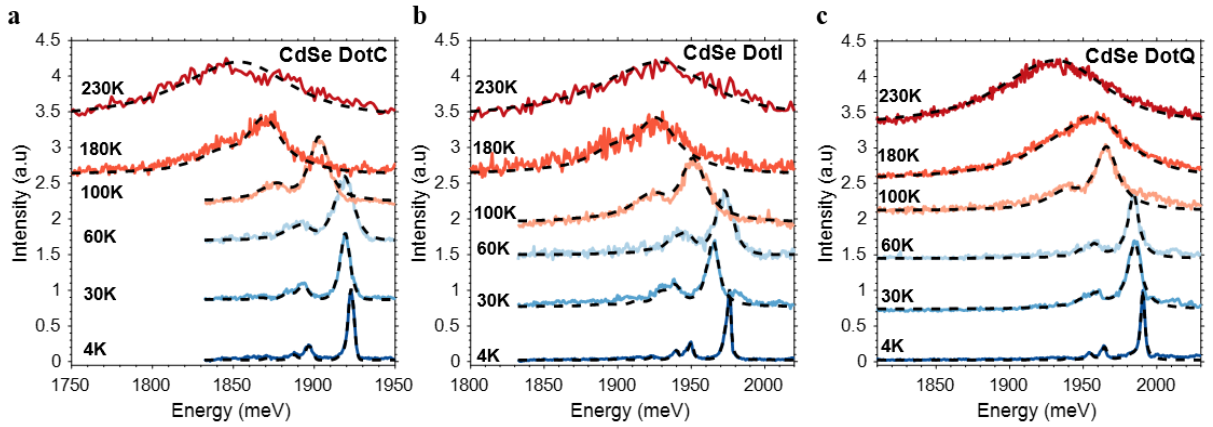


**Figure 2.18.** Single CdSe/CdS/ZnS QD PL spectra (solid lines) as a function of temperature with IBM fits (dotted black) superimposed for (**a**) CdSe DotC, (**b**) CdSe DotI, (**c**) CdSe DotQ.

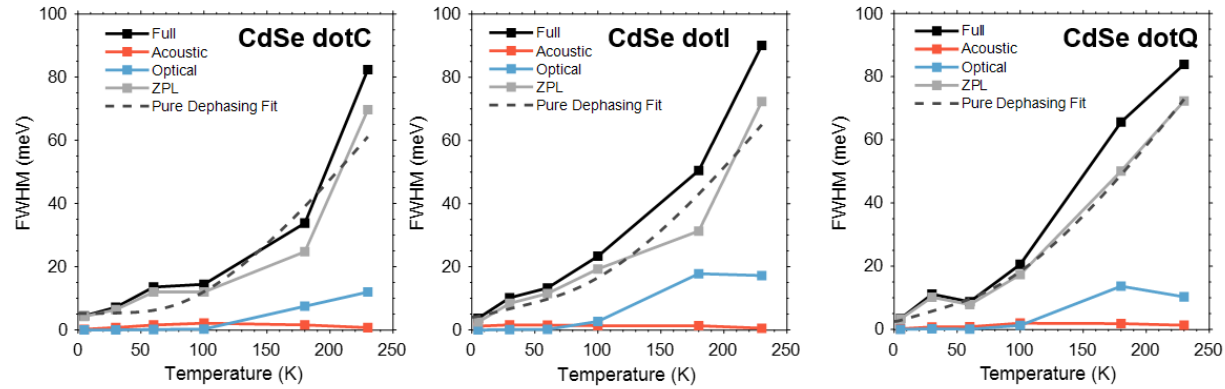


**Figure 2.19.** Single QD FWHM as a function of temperature broken down into the contributions from the acoustic phonon sideband, optical phonon sideband, the fine-structure splitting (FSS), the zero-phonon line (ZPL), and the pure dephasing fit to the ZPL. (**a**) CdSe dotC: $\gamma_1 = 0.5$, $\omega_{c_1} = 4.0$, $\gamma_2 = 192.2$, $\omega_2 = 30.0$, $\Gamma_0 = 5.2$ (**b**) CdSe dotI: $\gamma_1 = 0.67$, $\omega_{c_1} = 0.5$, $\gamma_2 = 100.0$, $\omega_2 = 26.9$, $\Gamma_0 = 2.55$ (**c**) CdSe dotQ: $\gamma_1 = 0.7$, $\omega_{c_1} = 0.5$, $\gamma_2 = 176.2$, $\omega_2 = 32.1$, $\Gamma_0 = 2.6$.

# Chapter 3

## Highly Stable and Pure Single-Photon Emission with 250 ps Optical Coherence Times in InP Colloidal Nanocrystals

This section is adapted and reproduced from

ǂA. H. Proppe, ǂD. B. Berkinsky, H. Zhu, T. Šverko, H. Chung, A. E. K. Kaplan, J. R. Horowitz, T. Kim, H. Chung, S. Jun, M. G. Bawendi

"Highly stable and pure single-photon emission with 250 ps optical coherence times in InP colloidal quantum dots"

*Nature Nanotechnology* 2023, 18, 993-999



**Author Contributions**

ǂD.B.B and A.H.P contributed equally to this work. A. H. P. and D. B. B. contributed equally to this work. A. H. P acquired all experimental data, performed all data fitting, analysis, and fitting algorithm design. D. B. B. assisted in acquiring all experimental data and data analysis. T. S assisted with sample preparation and the optical setup. A. E. K. K. assisted with optical setup. J. R. H assisted with data collection of quantum dot radiative lifetimes. H. Z. provided the CdSe/CdS/ZnS QDs and their TEM images. T. K. and H.C. provided the InP/ZnSe/ZnS dots and their TEM images. M. G. B. and S. J. supervised the project. All authors read and commented on the manuscript.

### 3.1. Abstract

Quantum photonic technologies like quantum communication, sensing, or computation require efficient, stable, and pure single-photon sources. Epitaxial quantum dots (QDs) have been made capable of on-demand photon generation with high purity, indistinguishability, and brightness – but require precise fabrication and face challenges in scalability. In contrast, colloidal QDs are batch synthesized in solution but typically have broader linewidths, low single-photon purities, and unstable emission. Here, we demonstrate spectrally stable, pure, and narrow linewidth single-photon emission from InP/ZnSe/ZnS colloidal QDs. Using photon correlation Fourier spectroscopy, we observe single dot linewidths as narrow as ~5 μeV at 4K, giving a lower-bounded optical coherence time, $T_2$, of ~250 ps. These dots exhibit minimal spectral diffusion on timescales of μs to minutes, and narrow linewidths are maintained on timescales up to 50 ms, orders of magnitude longer than other colloidal systems. Moreover, these InP/ZnSe/ZnS dots have

single-photon purities $g^{(2)}(\tau = 0)$ of 0.077 – 0.086 in the absence of spectral filtering. This work demonstrates the potential of heavy-metal-free InP-based QDs as spectrally stable sources of single-photons.

## 3.2. Background

Quantum photonic technologies use quantum light – single-photons – to enable applications like quantum communication,[125] quantum sensing,[126] or quantum computation.[127,128] The most widely used sources of single-photons are spontaneous parametric down conversion and four-wave mixing, but these nonlinear processes are probabilistic. Solid-state single-photon emitters (SPEs) are a promising platform for deterministic quantum light generation, combining atom-like optical properties with scalable and mature fabrication technologies.[129] Among solid-state SPEs – including crystal color centres and quantum defects in 2D materials[130–133] – self-assembled semiconductor quantum dots (QDs) are particularly outstanding, capable of on-demand photon generation with near-unity indistinguishability and single-photon purity.[134,135] QDs embedded in photonic structures can be manipulated by electrical contacts, and electrically-driven single- and entangled-photon emission has been demonstrated.[135,136]

Indistinguishable single-photons are generated when the SPE's optical coherence time, $T_2$, is equal to twice the radiative lifetime, $T_1$, in the transform-limit of $T_2 = 2T_1$. Narrow emission linewidths correspond to longer coherence times by the relation $T_2 = 2\pi/\Gamma$, where Γ is the full width at half maximum (FWHM) of the (Lorentzian) emission peak. In solid-state emitters like QDs, the exciton couples to its surrounding environment, and coherence of the excited state is deteriorated by interactions with phonons, spin-noise,[137] and charge-noise, which may increase Γ and reduce $T_2$.[70] Epitaxial QDs attain photon indistinguishability using photonic cavity structures that decrease $T_1$ to several hundred ps,[138–140] and longer $T_2$ times are enabled by well-optimized QD growth conditions. These strict and precise fabrication methods pose challenges for scalability and reproducibility of epitaxial QD SPEs.

In comparison, colloidal QDs have been less explored for quantum photonic applications, as they exhibit long $T_1$ due to dark lowest energy excited states[62,141,142] and short $T_2$ due to broader linewidths resulting from charge noise: spectral diffusion due to local field fluctuations randomly shifts the optical transitions on the order of 10s of μeV to several meV.[143–145] For epitaxial dots, charge noise broadening can be as small as sub-μeV.[139,146]

The discovery of fast radiative recombination ($T_1 \approx 200$ ps) for $CsPbBr_3$ perovskite QDs at 4K prompted interest in colloidal QDs as single-photon sources.[147] Subsequent work by Utzat et al. on the same materials measured $T_2 = 78$ ps ($\Gamma = 17$ μeV) and a $T_2/2T_1$ ratio of ~0.19, far exceeding any other colloidal QD.[70] More recently, Hong-Ou-Mandel (HOM) two-photon interference was demonstrated for $CsPbBr_3$ nanocrystals with visibilities up to 0.55.[12] These results highlight the as-yet untapped potential application

of colloidal QDs as solid-state quantum emitters. Recently, Won et al. reported the synthesis of core/shell/shell InP/ZnSe/ZnS QDs with unity quantum yield, and used these dots to fabricate QD light-emitting diodes with optimal external quantum efficiency and million hour operating lifetimes.[148] Free of heavy metals, InP-based QDs are ideal for scalable light-emission applications. So far, InP/ZnSe/ZnS QDs have remained unexplored for quantum light generation, and herein we examine their single-photon emission properties.

## 3.3. Structure and Emission Spectra of InP/ZnSe/ZnS QDs and CdSe/CdS/ZnS QDs

A schematic illustration and TEM image of the InP/ZnSe/ZnS QDs are shown in **Figure 3.1a,b**. A 3.3 nm diameter InP core is surrounded by a 3.5 nm shell of ZnSe, over which is grown another thin (0.2 nm) shell of ZnS. Hexanoic acid (OA) ligands bind to the dot surface, enabling colloidal stability in solution.[148] Conduction and valence band offsets between the InP core and ZnSe shell depend on the degree of quantum confinement and interfacial strain, with reported values widely varying: 0.5 – 1.0 eV for valence band offsets,[149] and 0.41 – 0.8 eV for the conduction band.[150,151] We have previously used effective mass approximations to calculate a conduction band offset of ~0.8 eV between InP and ZnSe, which would impose a type-I band alignment (**Figure 3.1c**) and localize the electron to the InP core.[101,152] This contrasts CdSe/CdS QDs, which form a type-II band alignment that delocalizes the electron wavefunction over the CdS shell (**Figure 3.2**).

InP/ZnSe/ZnS QDs were synthesized according to Won et. al. [148]. Regarding CdSe synthesis, First, CdSe core QDs were synthesized by a hot-injection method as previously reported.[21] The synthesis of CdSe/CdS/ZnS core-shell QDs was based on similar procedures with minor modifications.[153] Briefly, 200 nmol of CdSe cores were loaded into a 250 mL 3-neck flask with a solvent mixture of 1 mL ODE and 1 mL OAm. The reaction mixture was degassed under vacuum at room temperature for 1 hour and 120 °C for 10 min. Then the reaction mixture was heated to 310 °C under nitrogen for shell growth. When temperature reached 240 °C, a desired amount of Cd-oleate (0.1 M in ODE) and 1.2 equivalent of 1-octanethiol (0.12 M in ODE) were injected slowly into the reaction mixture simultaneously using a syringe pump with a rate of two monolayers of CdS shell per hour. 1 mL of OLA was injected every hour during growth. After the desired shell thickness has been reached (4ML CdS shell), The reaction was stopped by removing the heating mantle and cooling down to room temperature. The synthesized CdSe/CdS QDs were purified by three rounds of precipitation and redispersion using acetone/methanol and hexane. The purified CdSe/CdS QDs were then used to further grow ZnS shell. The ZnS shell growth follows the similar procedure as previous discussed, except the growth temperature was raised to 330 °C, and Zn-oleate (0.1 M in ODE) and 1-dodecanethiol (0.1 M in ODE) were used as precursors. After the desired shell thickness

has been reached (4ML ZnS shell), the synthesized CdSe/CdS/ZnS QDs were purified by three rounds of precipitation and redispersion using acetone/methanol and hexane.

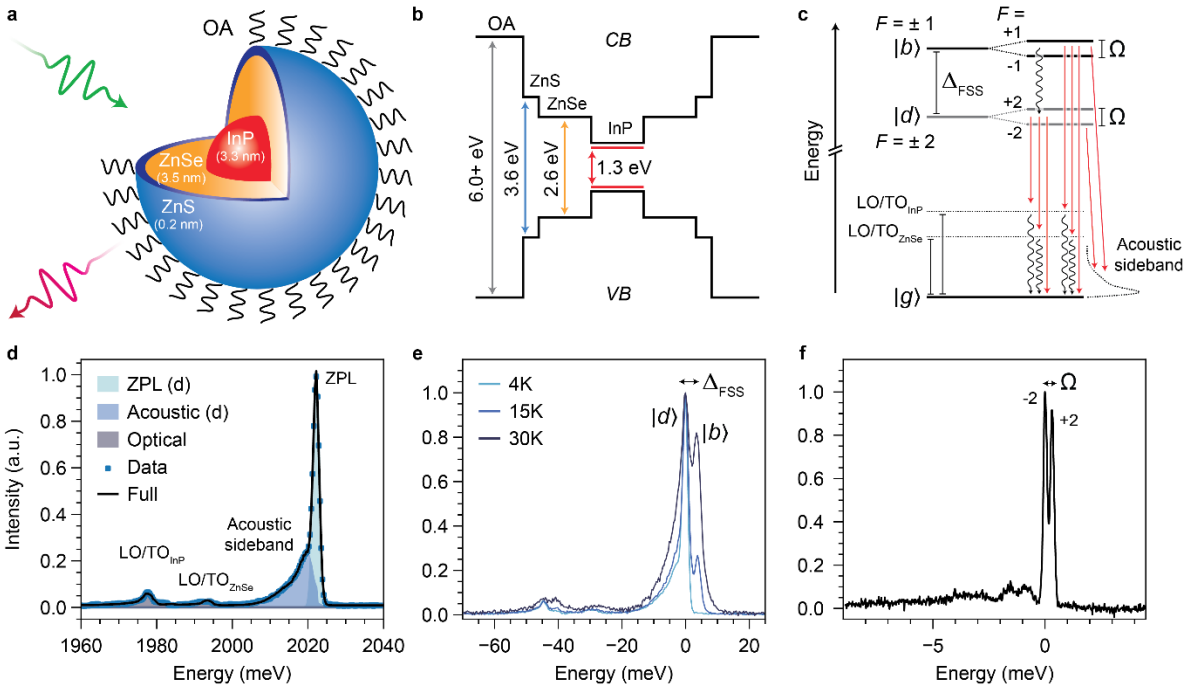


**Figure 3.1.** InP/ZnSe/ZnS QD structure and energy levels. **(a)** Schematic structure and **(b)** TEM image of colloidal InP/ZnSe/ZnS QDs with hexanoic acid (HA) surface ligands. **(c)** Band diagram of the core, shells, and surface ligands, illustrating the type-I band alignment in these heterostructures. Note the bandgaps of InP, ZnSe, and ZnS used here (from ref [148]) are values for bulk semiconductors. The HOMO-LUMO gap for HA was taken from ref [154]. CB: conduction band, VB: valence band **(d)** Jablonski diagram for emission from the band-edge exciton of the InP core. Red (wavy) arrows represent radiative (nonradiative) transitions between states. LO/TO: longitudinal optical and torsional optical phonons, $\Delta$: splitting between $|d\rangle$ and $|b\rangle$ states, $\Omega$: splitting between $|X\rangle$ and $|Y\rangle$ state. **(e)** Spectrum of an InP QD at 4K and fit from an independent boson model (see Chapter 2.6).[47] ZPL: zero-phonon line. **(f)** Spectra of the same QD at 4, 15, and 30K, showing the emergence of the bright $F = \pm 1$ state via thermal population. The spectra are shifted by their maxima to line up at 0 meV for clarity. **(g)** High resolution spectrum of a QD at 4K that shows the further splitting of $|d\rangle$ into superpositions $|X\rangle$ and $|Y\rangle$ of its $\pm 2$ transitions. Unless otherwise stated, dots were photoexcited with a 532 nm CW laser with a power density of 50 - 100 W/cm$^2$.

**Figure 3.1d** illustrates the exciton fine-structure. Electron-hole exchange separates the band-edge exciton states by their total angular momentum projection, $F$, along the nanocrystal axis. The lowest energy states are the dark ($|d\rangle$) $F = \pm 2$ and bright ($|b\rangle$) $F = \pm 1$ states.[47] The energy separation, $\Delta$, of ~4 meV between states $|b\rangle$ and $|d\rangle$ is referred to as the fine-structure splitting. The degeneracy of these two states can be further lifted due to crystal field splitting and shape anisotropy,[62] resulting in two states $|X\rangle$ and $|Y\rangle$ that are superpositions of the $F = \pm 1$ or $\pm 2$ states, separated by $\Omega$.

The emission spectrum of a single InP/ZnSe/ZnS QD at 4K is shown in **Figure 3.1e**. Excitons in these QDs have weak coupling to optical phonons, evidenced by two small amplitude peaks ~25 and ~45 meV lower in energy than the zero-phonon line (ZPL).[155] Coupling to acoustic phonons is much stronger, evidenced by the broad acoustic sideband that extends ~20 meV away from the ZPL. $\gamma_0$ is the spin-flip

relaxation rate from $|b\rangle$ to $|d\rangle$, and $\gamma_{\mathrm{th}}$ is the thermalization rate between these states, mediated by emission or absorption of acoustic phonons.[156] Thermalization from $|d\rangle$ to $|b\rangle$ by absorption of acoustic phonons is observed with increasing temperature, whereby a second ZPL corresponding to state $|b\rangle$ grows in (**Figure 3.1f**). Similar spectra for four other QDs are shown in **Figure 3.10**. A higher resolution spectrum of a different QD at 4K is shown in **Figure 3.1g**, showing further splitting of $|d\rangle$ into $|X\rangle$ and $|Y\rangle$. We attribute this splitting to shape anisotropy of the QD (**Figure 3.1b**).

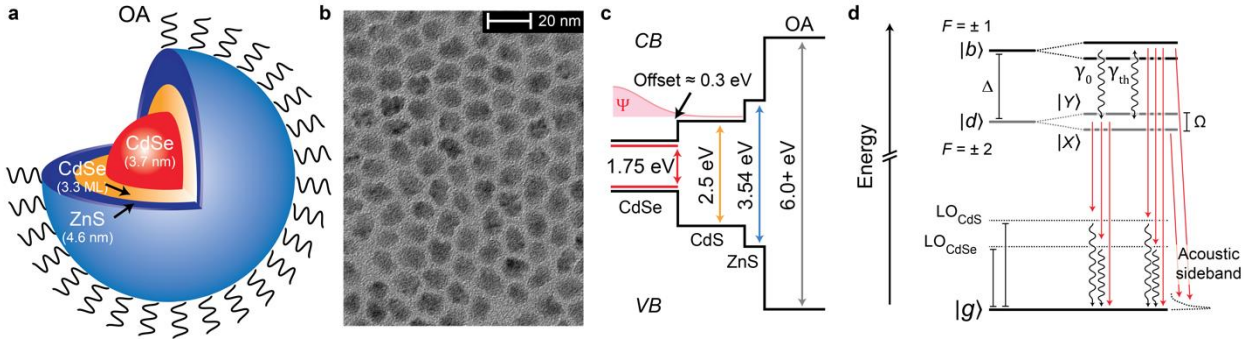


**Figure 3.2.** Band-structure and fine-structure of CdSe/CdS/ZnS QDs. **(a)** Schematic structure and **(b)** TEM image of colloidal CdSe/CdS/ZnS QDs with oleic acid (OA) surface ligands. **(c)** Band diagram of the core, shells, and surface ligands, illustrating the type-II band alignment in these heterostructures. The bandgaps of CdSe, CdS, and ZnS are taken from ref [157]. The HOMO-LUMO gap for OA was taken from ref [154]. CB: conduction band, VB: valence band **(d)** Jablonski diagram for emission from the band-edge exciton of the CdSe core. Red (wavy) arrows represent radiative (nonradiative) transitions between states. LO: longitudinal optical phonons, $\Delta$: splitting between $|d\rangle$ and $|b\rangle$ states, $\Omega$: splitting between $|X\rangle$ and $|Y\rangle$ state.

## 3.4. Spectral Stability on Timescales of Seconds-Minutes

We first assessed the spectral stability of single QDs by collecting sequences of photoluminescence emission spectra. Figure 2a shows a series of 600 spectra with a 1s acquisition time and a spectral resolution of ~1.1 meV. The emission remains stable without any significant shifting or fluorescence intermittency (blinking). **Figure 3.3b** and **Figure 3.3c** show series of higher resolution spectra (1s each, 60 frames) with a spectral resolution of ~0.08 meV, where only sub-meV shifting can be observed. We also collected intensity traces of the total number of single-photon counts emitted from single QDs on a pair of single-photon avalanche diodes (SPADs), showing stable, blinking-free emission over a period of 10 minutes in **Figure 3.3d**, and no apparent fluctuations on a smaller time interval of 10s (**Figure 3.3d** inset). Similar intensity plots for other dots are shown in **Figure 3.11**. These results show that on the timescale of seconds – minutes, there is minimal spectral diffusion of the emission line shape.

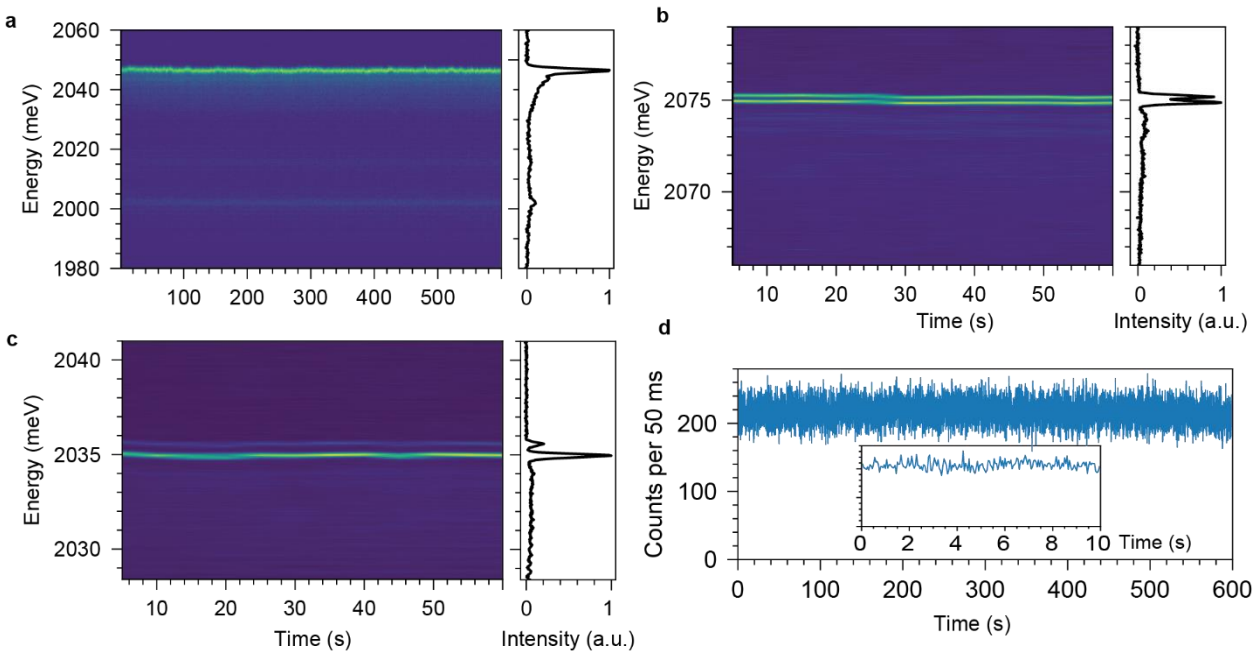


**Figure 3.3.** Tracking spectral stability on a timescale of seconds – minutes. **(a)** (left) Sequentially collected spectra of a single InP/ZnSe/ZnS QD using a 300gr/mm grating with a 0.5m spectrometer (spectral resolution ~1.1 meV). The acquisition time for each frame was 1s with a total of 600 frames. (right) The sum of all collected spectra with normalized intensity. **(b, c)** Spectral trajectory for two different QDs using a 2400gr/mm grating (spectral resolution ~0.08 meV). **(d)** Intensity trace of total counts in 50 ms bins over a period of 600s and (inset) 10s.

Despite this spectral stability and lack of reversible blinking, the dots were prone to apparent photobleaching, irreversibly entering an 'off' state even under mild excitation conditions. A subsequent series of spectra for the same dot as in **Figure 3.3a** is shown in **Figure 3.4**, where after another ~300s of illumination, the dot turns off and does not recover. This limitation in photostability often resulted in us being unable to perform multiple different measurements on the same dot. While some QDs were able to survive up to 3 hours of continuous excitation without blinking, many dots turned off after 5 – 10 minutes. Consequently, many of the different measurements shown below do not correspond to the same set of QDs.

InP/ZnSe QDs are known to be especially prone to water-induced oxidation of the oxyphilic InP surface.[158] The synthesis developed by Won et al. used HF to etch oxidative sites on the InP core during growth of the ZnSe shell and achieved PLQYs of 100%, suggesting oxidation-free interfaces. However, other reports, for example by Cossairt et al. have found that thoroughly degassed synthesis of InP/Zn(Se,S) QDs still resulted in up to 85% phosphorous oxidation.[159] Vikram et al. found that aminolytic reactions between oleylamine and carboxylates used in QD synthesis introduce oxidative defects during the shelling process, and note that carboxylic acids (like hexanoic acid, our QD ligand) promotes oxidation by the formation of water as a ketonization reaction byproduct.

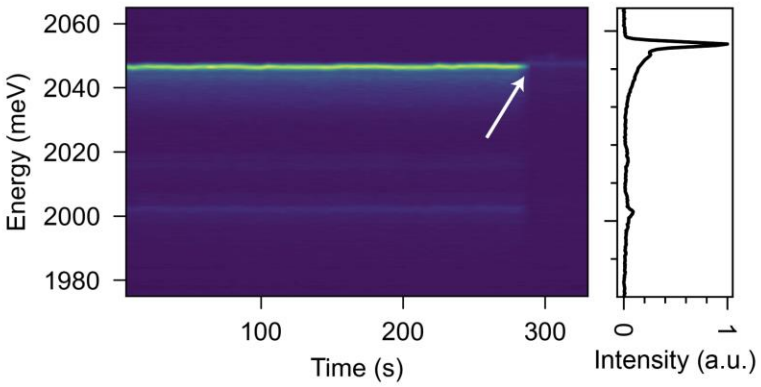


**Figure 3.4.** Sequential spectra (left) and sum (right) collected over a period of ~300s for the same QD as shown in Fig. 2a. The acquisition time for each frame was 5s. The white arrow indicates where the dot irreversibly entered an off state.

Given the above reports, and the fact that our dots used a carboxylic acid as ligands, we speculate that a low density of oxidative defects may still be present in the QDs that can lead to charge trapping and ultimately irreversible photobleaching. Though we thoroughly dried our solvents, PMMA solutions, and baked our quartz slides for preparing single dot cryostat samples, there is an unavoidable exposure to air when we transfer the samples to the cold platform before pumping down. In other experiments on room-temperature single InP/ZnSe/ZnS dot experiments, we have observed that baking cover slips in a nitrogen glovebox before spin-coating and encapsulating samples can result in better photostability of the dots, which supports our hypothesis.

Finally, it is likely that the combination of shape anisotropy, size polydispersity, and thin (~0.2 nm) ZnS results in a large variety of surface conditions from dot-to-dot, which would also point to an oxidative degradation process that originates at the dot surface.

It is also noted that these same QDs exhibited exceptional stability in the QD-LED devices reported by Won et al.[148] The key differences are the excitation flux and the ligands. In single dot experiments, we typically employ laser powers that do not exceed a ~0.10 probability of generating an exciton per pulse. At the ensemble level in electrically-driven LEDs, the average excitation flux experienced by any given QD is much lower. In the QD-LEDs reported by Won et al., the dots undergo a ligand exchange with thiol ligands, removing the potentially oxidative hexanoic acid.

## 3.5. Spectral Stability on Timescales of Microseconds-Milliseconds

To observe spectral diffusion on sub-ms timescales, we used photon correlation Fourier spectroscopy (PCFS). Single photons were transmitted through a Michelson interferometer onto two SPADs, and second-order photon correlation ($g^{(2)}(\tau)$) functions are measured for different interferometer delay times, $\delta$. The $g^{(2)}(\tau)$ provides temporal resolution, whereas scanning the interferometer across $\delta$

provides energetic resolution, and the resulting interferogram is a function of both $\tau$ and $\delta$. The Fourier transform of the interferogram for a given $\tau$ yields the spectral correlation, $p(\zeta,\tau)$, which is the autocorrelation of the emission spectrum. $p(\zeta,\tau)$ is a function of $\zeta$, the energy differences between the photon pairs that comprise the $g^{(2)}(\tau)$, and of $\tau$. A detailed explanation of this technique can be found in references [70,160,161].

Interferograms and $p(\zeta,\tau)$ for three different InP/ZnSe/ZnS QDs and one CdSe/CdS/ZnS QD (hereafter named dots InP-1, InP-2, InP-3, and CdSe-1, respectively) are shown in **Figure 3.5a,d,g,j**. We show interferograms for $\tau$ spanning three different windows: $\tau_{0\to1}$ = 0.1 – 0.5 ms, $\tau_{2\to3}$ = 1 – 5 ms, and $\tau_{4\to5}$ = 10 – 50 ms. For the InP dots, we observe clear beating patterns in the interferograms, consistent with emission from a doublet. For CdSe-1, no beating is observed, consistent with a single emission peak as observed in previous PCFS measurements on low-temperature CdSe QDs.[162] Fourier transformation of these interferograms into $p(\zeta,\tau)$ reveals the triplet for dots InP-1-3 (which corresponds to doublet emission spectra) and a singlet for CdSe-1. The splittings Ω between the $F = \pm2$ superposition states for these InP dots are ~150, 310, and 840 μeV, which results in the different oscillation periods of the interferograms.

The decay of these interferograms is determined by the linewidth of the emission spectra: narrower (broader) peaks correspond to longer (shorter) coherence times, $T_2$. We fit these interferograms by generating a spectrum consisting of a 1 or 2 Lorentzian peaks with an acoustic sideband (Equation 3.1), and taking its autocorrelation and Fourier transform.

$$s(\omega) = a_1 \frac{\frac{1}{2}\Gamma}{(\omega)^2+\left(\frac{1}{2}\Gamma\right)^2} + a_2 \frac{\frac{1}{2}\Gamma}{(\omega-\Omega)^2+\left(\frac{1}{2}\Gamma\right)^2} + \lambda\omega^p e^{-\omega/\omega_c} + y_0 \tag{3.1}$$

The first two terms correspond to the Lorentzian peaks with amplitudes $a_1$ and $a_2$ and with the same Γ, and Ω is the energy separation between them. The third term is a spectral density used to approximate the acoustic sideband, where $\lambda$ is the coupling strength (i.e. amplitude), $p$ is the power acting on $\omega$ to create an Ohmic ($p$=1), sub-Ohmic ($p < 1$) or super-Ohmic ($p > 1$) spectral density, and $\omega_c$ is the cut-off frequency.[115,163] $y_0$ is a constant to account for a broad, flat background in the spectra. To perform the fits, the equation is used to generate a spectrum, $s(\omega)$, which is autocorrelated to make $p(\zeta,\tau)$ and finally Fourier transformed into an interferogram.

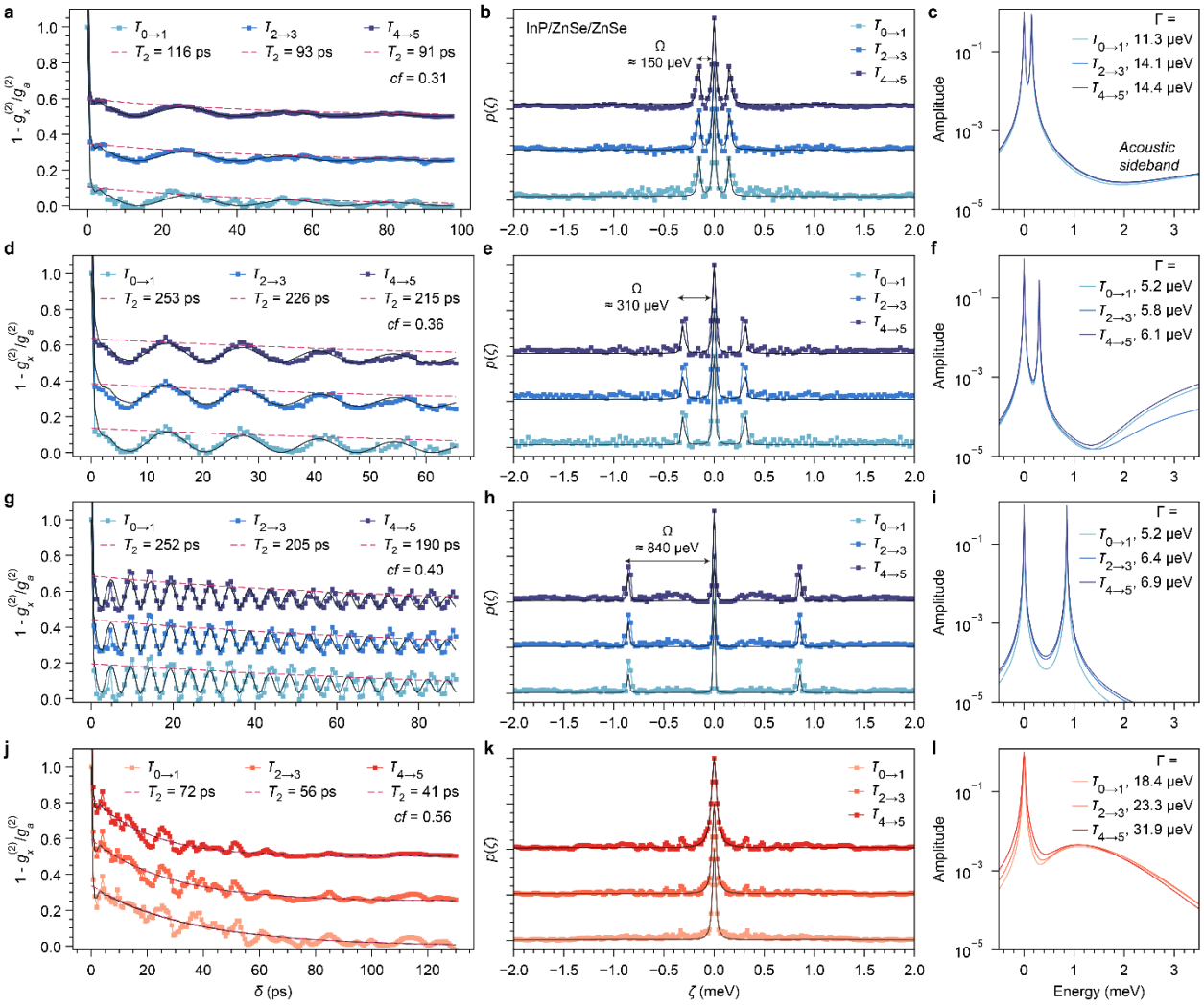


**Figure 3.5.** Using PCFS to track spectral diffusion on μs – ms timescales. (**a**) Interferograms built from photon pairs with time separations $\tau$ between $\tau_{0\to1}$ = 0.1 – 0.5 μs, $\tau_{2\to3}$ = 1 – 5 ms, and $\tau_{4\to5}$ = 10 – 50 ms. For clarity, the interferograms are normalized to a maximum of 1 and given an offset. The oscillatory-like features for dot CdSe-1 result from QD blinking, which affects the underlying $g^{(2)}(\tau)$ at these stage positions. Fourier transforming these interferograms gives (**b**) the spectral correlations, $p(\zeta,\tau)$. (**c**) Spectra, $s(\omega)$ generated using optimized parameters to fit the interferograms. (**a – c**) are fitted interferograms, $p(\zeta,\tau)$, and spectra for InP/ZnSe/ZnS dots InP-1, (**d-f**) InP-2, (**g-i**) InP-3, and (**j-l**) CdSe/CdS/ZnS dot CdSe-1. The values of $T_2$ shown with the interferogram fits are calculated from the FWHM of the Lorentzian spectra, $T_2 = 2\pi/\Gamma$. The fitted exponential coherence decay follows $e^{-2/T_2\delta}$, where the factor of 2 arises due to the autocorrelation of the Lorentzian spectrum. Uncertainties are omitted for clarity. cf = coherent fraction.

This model assumes a purely Lorentzian line shape for the emission peaks from these QDs. We found that this approach, which was used for PCFS interferograms of $CsPbBr_3$ QDs by Utzat,[70] yielded good fits to the interferograms. A more appropriate model would be to generate transform-limited Lorentzian peaks whose spectral correlation is convolved with a Gaussian peak that has a $\tau$-dependent FWHM, which simulates Wiener or Poisson spectral diffusion.[162] In our case, we found that this approach hardly affected the fits, and so did not pursue it. Our gradient descent algorithm uses Python's SciPy

package[164] with Powell's conjugate direction method[165] and does not output uncertainties; instead, we performed each fit 20 times starting with randomized initial guesses for each parameter (within user defined bounds) to obtain means ($\mu$) and standard deviations ($\sigma$), which are given in **Table 3.1**.

Fits are plotted with the raw interferograms in **Figure 3.5**, along with the corresponding $p(\zeta,\tau)$ and underlying $s(\omega)$. We extract mean values of Γ and $T_2$ for InP-1 - 3, which range from as narrow as ~5.1 (±0.14) μeV and as broad as 14.4 (±0.49) μeV. These are among the narrowest linewidths reported for colloidal QD materials, with corresponding values of $T_2$ that exceed the best reported for $CsPbBr_3$ QDs and commensurate with epitaxial QDs.[65,166–168] Moreover, we obtain these $T_2$ values for $\tau$ as high as 50 ms. As a comparison, $T_2$ values of 35 – 78 ps reported for $CsPbBr_3$ QDs were evaluated for photons within <100 μs of each other,[64,70] meaning these InP/ZnSe/ZnS dots maintain narrower linewidths over two orders of magnitude longer timescales. Fitted interferograms, $p(\zeta,\tau)$, and $s(\omega)$ for two more dots are shown in **Figure 3.12,** which also show limited spectral diffusion.

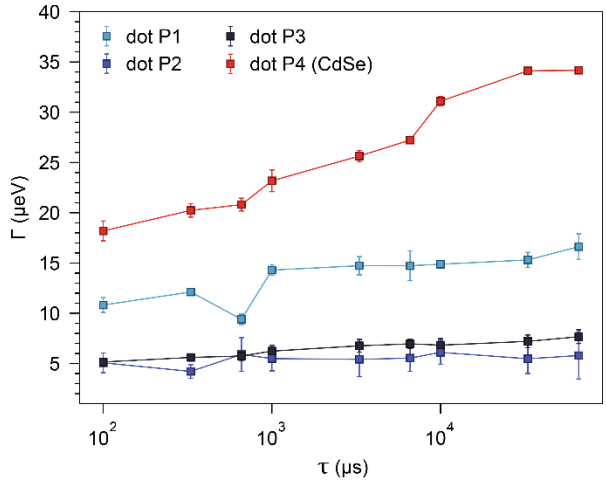


**Figure 3.6.** $\Gamma$ extracted from interferogram fits at different $\tau$ for dots InP-1 – 3 and CdSe-1. The values of $\Gamma$ shown above correspond to the mean ($\mu$) and one standard deviation ($\sigma$) which are generated from 20 different fits for each point, with randomized and bounded initial guesses. These values are given in **Table 3.2**.

Similar spectral stability has been observed in some CdSe/CdS QDs, with linewidths as low as 5 μeV at short $\tau$ that broaden to >10 μeV on ms timescales;[160,169] whereas other reports found linewidths that exceed 100 μeV.[162] We measured a PCFS interferogram for a single CdSe/CdS/ZnS QD, and found the emission to be more unstable than for the InP QDs, exhibiting blinking and larger degree greater spectral diffusion, with a fitted Γ that increases from an initial 18.4 μeV to 32.4 μeV. **Figure 3.6** shows a comparison of the evolution of $\Gamma(\tau)$, demonstrating both the smaller linewidths of these InP/ZnSe/ZnS dots compared to CdSe, and the lesser extent of spectral diffusion.

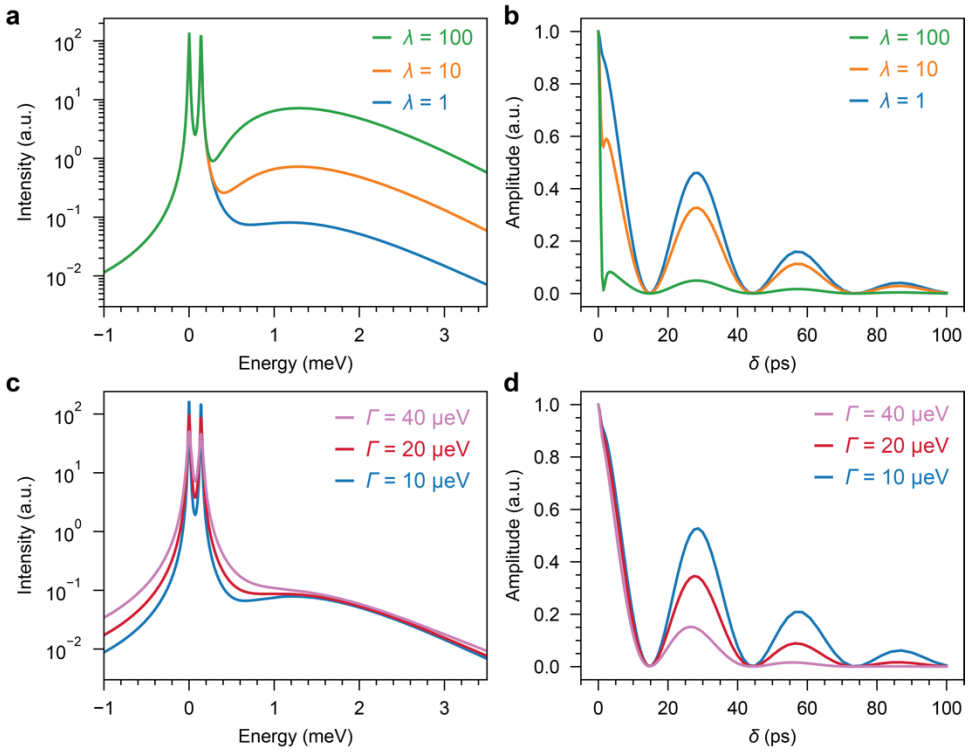


**Figure 3.7.** Influence of exciton-phonon coupling on PCFS interferograms. (**a**) Increasing parameter $\lambda$ (the coupling strength between the exciton and acoustic phonons) gives higher amplitude phonon sidebands, which when auto-correlated and Fourier transformed into an interferogram (**b**) results in a reduced coherent fraction. (**c**) Increasing parameter $\Gamma$, the Lorentzian FWHM, results in lower coherence lengths for corresponding interferograms shown in (**d**), but does not reduce the coherent fraction.

Taken together, these results indicate that, compared to other colloidal QD materials, excitons in InP/ZnSe/ZnS QDs can be highly robust against spectral diffusion. We posit that low defect densities afforded by HF etching and high reaction temperatures during ZnSe shell growth,[148] combined with a type-I band alignment that localizes the exciton to the InP core, helps protect the exciton against spectral diffusion and decoherence. For well-engineered CdSe/CdS dots, low defect densities can be achieved, but type-II band alignment facilitates surface interactions which will lead to spectral diffusion.[170,171] To achieve instead a type-I band alignment, CdSe/CdS/ZnS structures can be used, but strain due to lattice mismatch can create dangling bonds at the interface, which could be deleterious to both spectral stability and quantum yield.[157] Such a compromise between interfacial defects and type-I band alignment is not necessary for InP/ZnSe/ZnS QDs, highlighting another intrinsic advantage of this material over Cd-based QDs for quantum light-emission. $CsPbBr_3$ dots have no shell,[172] and so greater coupling of the exciton with the surrounding environment is expected, leading to spectral diffusion. Other solid-state quantum emitters like defects in two-dimensional hexagonal boron nitride (hBN) flakes also suffer from strong coupling to their environment, experiencing spectral diffusion that broadens the ZPL up to 50 μeV on similar timescales as in our experiments,[131] and up to 1 meV in steady-state.[130]

PCFS interferograms also measure the coherent fraction of the emission. Phonon sidebands arising from inelastic (real) exciton-phonon coupling lowers the coherent fraction, whereas elastic (virtual) exciton-phonon scattering causes dephasing of the excited state, lowering $T_2$ (**Figure 3.7**). The initial rapid drop-off in interference amplitudes due to loss of coherence are more clearly shown in **Figure 3.8**. We observe coherent fractions of 0.31, 0.36, and 0.40 for dots InP-1-3, attributed to the large acoustic sideband (Fig. 1d).

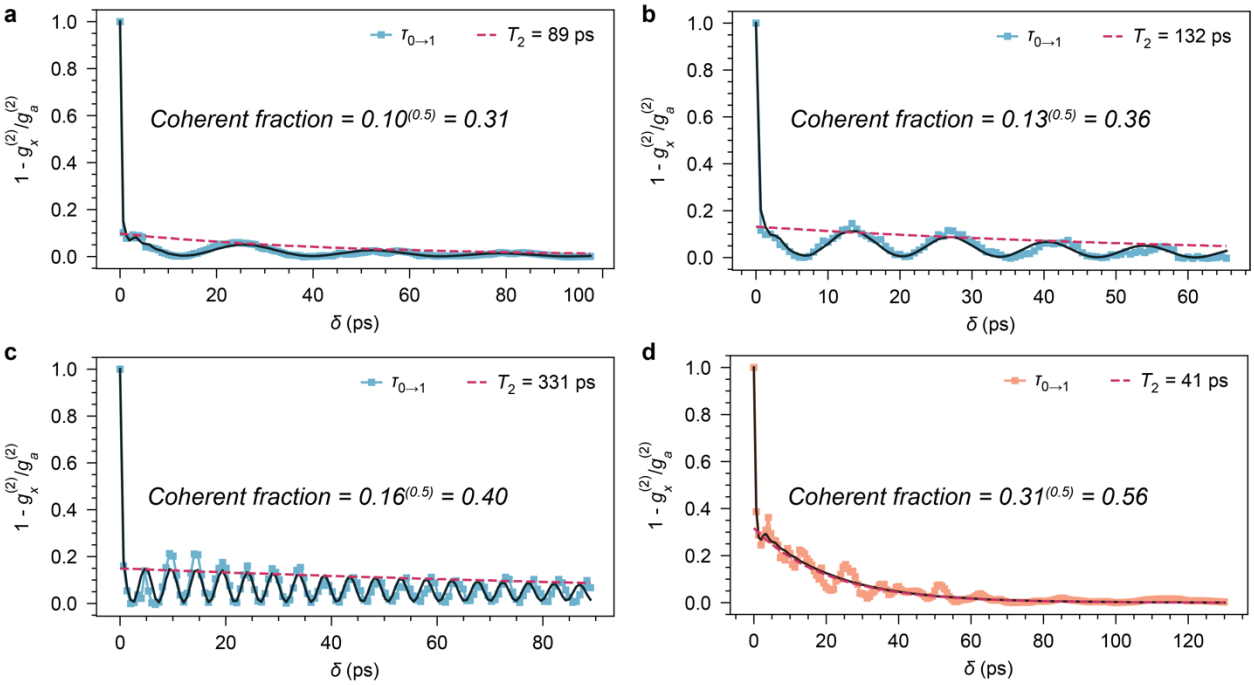


**Figure 3.8.** Full interferograms that show the rapid initial drop-off in coherence for **(a-d)** dots P1 – P4, respectively. Coherent fractions are calculated as the square-root of the value of the fitted exponential coherence decay at $\delta = 0$.

## 3.6. Radiative Lifetime and Single-Photon Purity

Lastly, we characterize the single-photon lifetime and purity. The photoluminescence lifetime for dot InP-4 is shown in **Figure 3.9a,b**, which was fit using biexponential decays. Lifetimes and fits for two other dots are shown in **Figure 3.13** and **Table 3.3**, which show similar amplitudes and lifetimes. The observed lifetimes are consistent with other II-VI semiconductor QDs at 4K – including CdSe/ZnS, which exhibits highly similar fine-structure.[62,142] At 4K, carriers that are photogenerated above the band-edge will rapidly relax to the lowest energy excited states. Excitons in state $|b\rangle$ will rapidly relax to $|d\rangle$ with rate $\gamma_0$, which accounts for the fast lifetime component $\tau_1$, and the slow component $\tau_2$ arises from phonon-assisted radiative recombination from state $|d\rangle$ with rate $\Gamma_d$. Emission from $|b\rangle$ with rate $\Gamma_b$ accounts for a negligible percentage of the emission, owing to the faster relaxation rate $\gamma_0$.

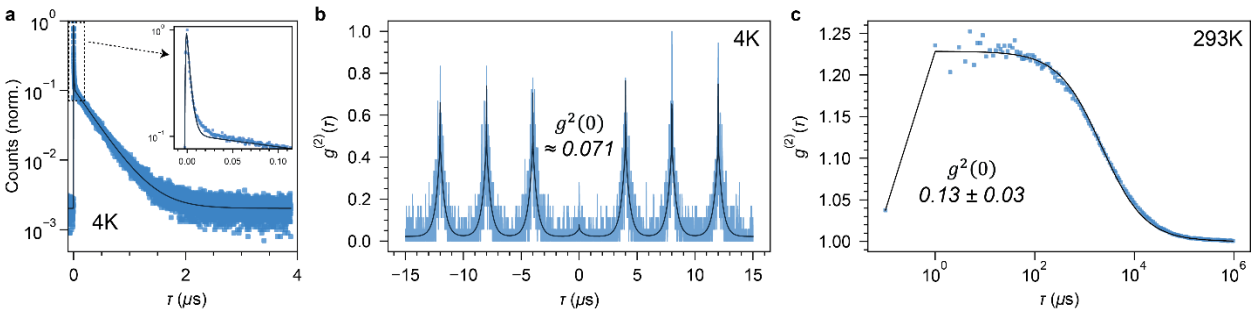


**Figure 3.9.** Single-photon emission properties of colloidal InP/ZnSe/ZnS QDs. **(a)** Lifetime plotted on a linear time axis. Inset of **a** shows a zoomed-in look at the fast component of the lifetime. **(b)** $g^{(2)}(\tau)$ of a single QD (dot InP-4). Periods of 4 μs between laser pulses were required to allow QDs to fully decay to the ground state in between excitation events. This resulted in low counts rates and noisy $g^{(2)}(\tau)$ functions whose acquisition time was limited by the photostability of the QDs. We performed fits following the methodology of reference [173] using a Poisson likelihood for the data.[174] **(c)** Solution $g^{(2)}(\tau)$ measurement, fit, and ensemble-averaged $g^{(2)}(0)$.

Following the methodology of Labeau et al., we fit temperature-dependent lifetimes of an ensemble of InP/ZnSe/ZnS QDs between 4 – 295K using the three-level system depicted (see **Section 2.5**). We obtain values of Δ on the order of 4 meV (similar to Brodu et al.),[155] and estimate the radiative rate of the bright state, $\Gamma_b$ = 0.06 ns$^{-1}$, corresponding to a lifetime of 16.7 ns. These values are similar to $\Gamma_b$ = 0.1 ns$^{-1}$ for CdSe/ZnS QDs.[156]

Single-photon purity is evaluated from the normalized value of $g^{(2)}(0)$, fit with a maximum likelihood estimation (MLE) method.[134,173,175] MLE with normal and Poisson likelihoods was implemented with SciPy library for Python using scipy.optimize.minimize. For MLE with a normal likelihood, Powell's conjugate direction method (previously determined to be the most well-suited subroutine for this problem)[174] is used as the optimization subroutine to minimize the following objective function:

$$\frac{1}{2}\sum_i \big(n_i - y_i(\theta)\big)^2 \tag{3.2}$$

Where $n_i$ and $y_i(\theta)$ are the values of the data and the reconstruction at time bin $i$, respectively, and $\theta$ is the array of variables used to parameterize $y$. For MLE with a Poisson likelihood, Cortes et al. showed that the following objective function can be used:[174]

$$\sum_i \big(n_i \log y_i(\theta) - y_i(\theta)\big) \tag{3.3}$$

Randomized initial guesses for each parameter were drawn from within the bounds in Supplementary Table 1, and the same bounds were used to constrain the fitting.

The $g^{(2)}(\tau)$ for the same dot InP-4 is shown in **Figure 3.9b**, where a biexponential fit[173] gives 0.071 for $g^{(2)}(0)$. These single-photon purities are obtained without any spectral filtering, in contrast to $CsPbBr_3$ QDs which have near unity $g^{(2)}(\tau = 0)$ at 4K and require significant filtering to remove BX

emission and observe antibunching.[70] This is consistent with the small (~3.3 nm) and strongly-confined InP core, whose exciton Bohr radius is 10 nm,[176] which leads to increased spatial overlap of the exciton wavefunctions to favor Auger recombination of multiexcitons.[101,177,178] In contrast, large (~14-15 nm edge length) weakly-confined $CsPbBr_3$ nanocrystals with faster radiative lifetimes favor efficient emission from multiexciton states.

At room-temperature in solution, the ensemble-average single-photon purity can be evaluated by collecting the same $g^{(2)}(\tau)$ for a highly dilute solution of QDs in a fluorescence correlation spectroscopy (FCS) experiment. We used a pulsed excitation source in a Hanbury-Brown-Twiss setup to collect the QD emission. This technique is also known as Fluorescence Correlation Spectroscopy (FCS). In a dilute solution of QDs, photon pairs close in time to one another (short τ) are more likely to emit from the same QD giving rise to a higher degree of correlation in the $g^{(2)}(\tau)$. Photon pairs far apart in time to one another (long τ) are highly unlikely to arise from the same QD resulting in low degree of correlation in the $g^{(2)}(\tau)$ at τ. Photon pairs within the same pulse (τ = 0) either are a result of biexciton emission from the same QD or exciton emission from two different QDs in the focal volume. We can calculate the BX/X QY by taking the ratio of the center to side peak subtracted by the ensemble background: $\frac{g^{(2)}(0)-1}{g^{(2)}(\tau_{rep})-1}$, where $\tau_{rep}$ is the repetition rate of the laser. The side peak, $g^{(2)}(\tau_{rep})$, is determined by fitting correlations across all timescales to a diffusion model (Equation 3.4). Measurements were performed under low excitation flux ($\langle n \rangle \ll 1$) to ensure negligible correlation contributions from higher order excitons. We also use a repetition rate of the laser that is well beyond the lifetime of the emitter.

To fit the FCS traces, we used the following equation:

$$\left(1+\frac{1}{N}\right)\left[\frac{\left(1-B*\tau^{2-m}\right)}{\left(1+\frac{\tau}{\tau_D}\right)}\right] \tag{3.4}$$

Where $N$ is the average number of particles being probed in the confocal volume, $B$ and $m$ are a coefficient and exponent, respectively, that describe the power-law distribution of on- and off-times for blinking dots (this accounts for the tilt of the $g^{(2)}(\tau)$ at early $\tau$),[179] and $\tau_D$ is the diffusion time of the particles. Similar fitting equations for FCS curves often include a term to account for antibunching – we omit this term here, since the spacing between pulses $\tau_{rep}$ exceeds the antibunching time. We perform this measurement for the InP/ZnSe/ZnS QDs and fit the FCS curve (**Figure 3.9c**), measuring an average $g^{(2)}(0)$ of 0.13±0.03, in agreement with our low-temperature single dot measurements.

## 3.7. Conclusions

We have shown that colloidal InP/ZnSe/ZnS can exhibit linewidths as narrow as 5 - 15 μeV, and undergo minimal spectral diffusion over timescales as long as 50 ms. This spectral stability is on par with or superior to CdSe/CdS QD systems, and orders of magnitude longer than for $CsPbBr_3$ perovskite dots. The demonstrated spectral stability and single-photon purity of these InP/ZnSe/ZnS dots make them potential candidates as solid-state SPEs, exhibiting narrower linewidths and higher single-photon purities than all other colloidal QD systems and quantum defect emitters in 2D hBN and TMDCs.[130,131,133] See Table S5 for a comparison of $g^{(2)}(0)$, $T_1$, and $T_2$ for different material SPE systems.

To leverage these promising quantum optical properties and use InP/ZnSe/ZnS dots as solid-state SPEs, they could be integrated in a cavity structure that, via Purcell enhancement, would decrease $T_1$ and increase the fraction of photons emitted into the ZPL. An 880-fold enhancement of $T_1$ for CdSe/ZnS QDs has been demonstrated using plasmonic nanoantennas.[180] Increasing the radiative rate of the bright state, $\Gamma_b$, would be required to outcompete the bright-to-dark relaxation. Given the bright state lifetime on the order of 15 ns for these InP/ZnSe/ZnS QDs, an enhancement of 120 would result in $T_1$ of ~125 ps. With a $T_2$ of ~250 ps, this would achieve transform-limited emission. PCFS measures an upper-bound for $T_2$ at a given photon separation time $\tau$, and this value will only further increase with decreasing $\tau$, e.g. for 2 ns pulse separations commonly used in Hong-Ou-Mandel experiments for single QDs. Spectral filtering could then be used to further diminish photons emitted from phonon sidebands and multiexciton recombination,[101] increasing single-photon purity. Synthetic strategies may also be used to reduce electron-phonon coupling via strain engineering, as has been done for CdSe/CdS[123] and alloyed CdSe/$Cd_xZn_{1-x}Se$ dots,[124] and to tune Auger rates to reduce biexciton quantum yield.[101,177] Asymmetrically strained CdSe/$Cd_xZn_{1-x}Se$ dots have also been shown to emit six times more light from the bright exciton state.[181] Altering surface ligands to rigidify the shell surface could reduce acoustic phonon coupling, further improving the coherent fraction. Implementation of these strategies could help realize InP/ZnSe/ZnS QDs as a scalable material for coherent and stable single-photon generation.

## 3.8. Acknowledgements

A. H. P., D. B. B., T. S, A. E. E. K., and J. R. H. were supported by the Samsung Advanced Institute of Technology (SAIT). H. Z. was supported by the National Science Foundation (Award No. CHE-2108357). A. H. P. was additionally supported by a Postdoctoral Fellowship from the Natural Sciences and Engineering Research Council of Canada (NSERC). This work was supported by SAIT, Samsung Electronics Co., Ltd.

## 3.9. Supplementary Information

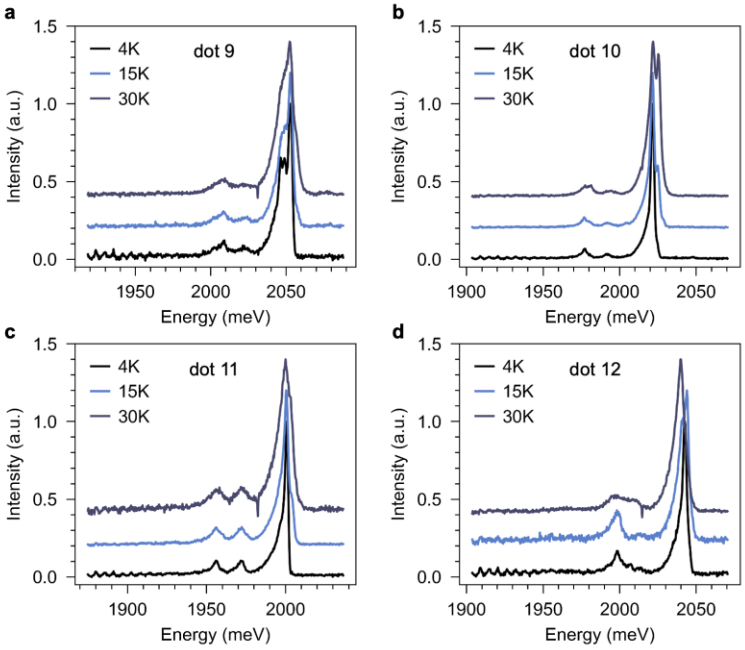


**Figure 3.10.** Temperature-dependent spectra for four different InP/ZnSe/ZnS QDs, which shows the population of the bright $F = \pm 1$ state with increasing temperature. The visibility of the higher energy bright ZPL peak depends on its energy separation from the dark ZPL; for dot10, a second peak is clearly visible, whereas for dot12, the second peak is more overlapped with the dark ZPL. Oscillations at lower energies (~1850 – 1925 meV), and the sharp dip at ~1980 meV, are a result of the Electron-Multiplying (EM) gain applied across the CCD camera and imperfect background subtraction.

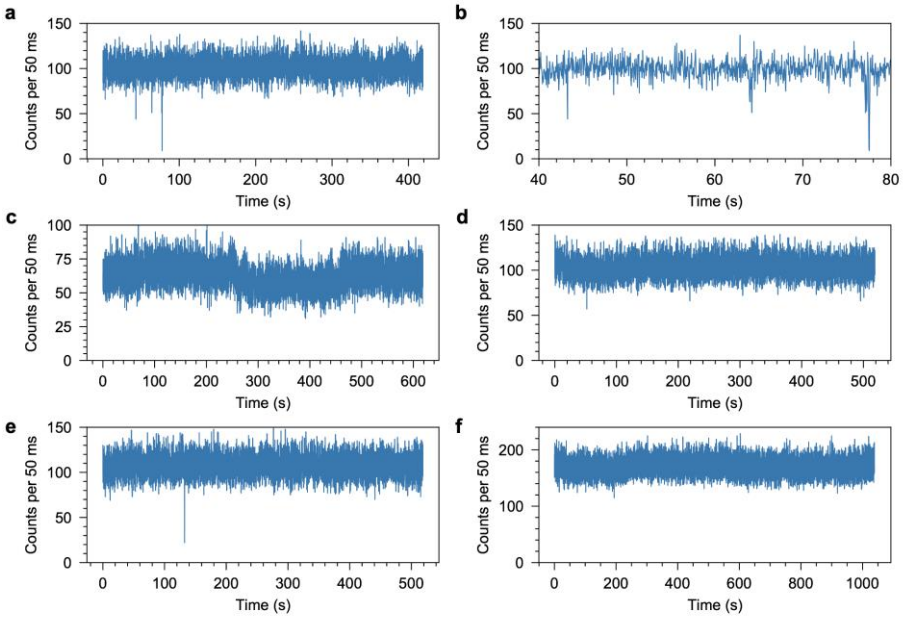


**Figure 3.11.** Intensity traces for 5 different InP/ZnSe/ZnS dots. Panels **a** and **b** are for the same dot, with panel **b** zoomed in on 40 – 80s to more clearly observe blinking.

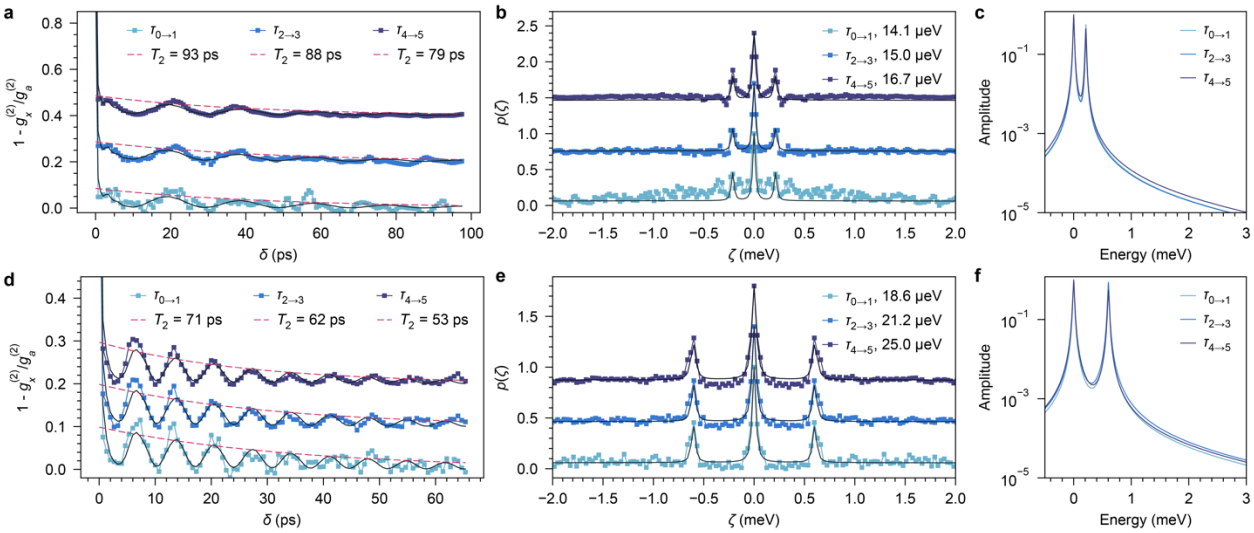


**Figure 3.12.** Fitted interferograms, spectral correlations, and spectra for two more dots, P5 (**a-c**) and P6 (**d-f**).

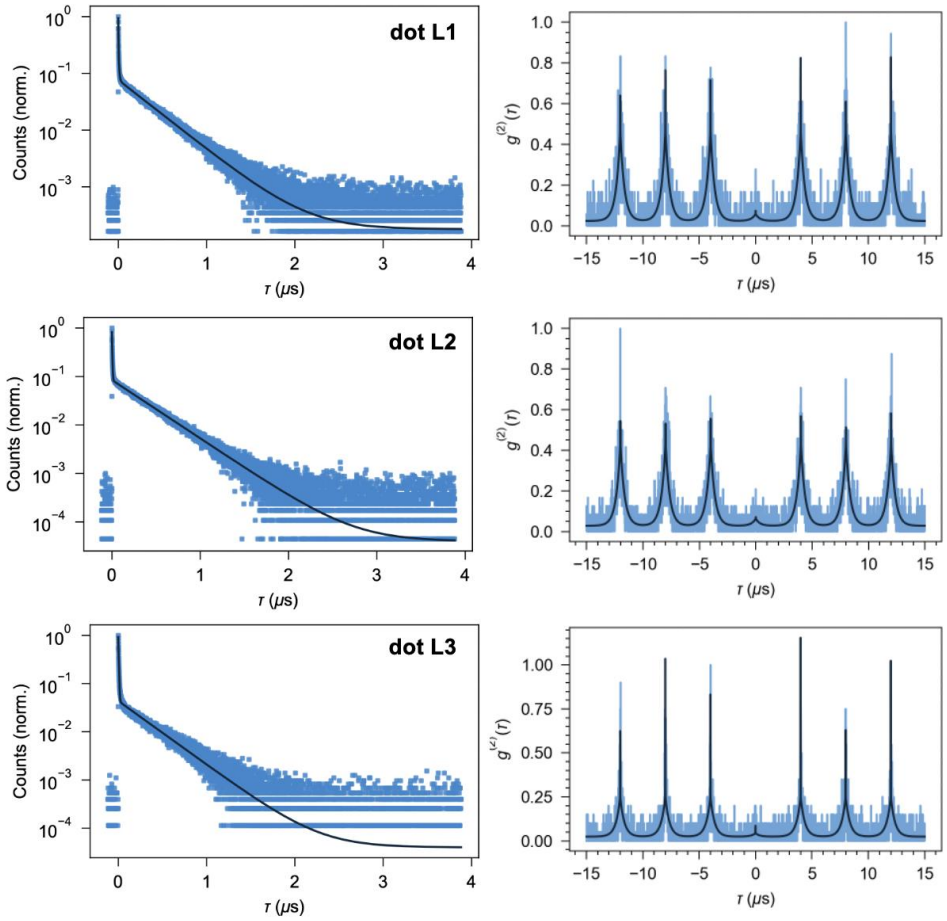


**Figure 3.13.** Fitted lifetimes and $g^{(2)}(\tau)$ functions for dots L1 – L3. Fitted parameters are in **Table 3.3** and **Table 3.4**.

| | $\tau$ | $\Gamma$ (μeV) | $\omega_c$ (meV) | $a_1$ | $a_2$ | $\lambda$ (meV) | Ω (meV) | $p$ | $y_0$ |
|---|---|---|---|---|---|---|---|---|---|
| P1 $\mu$ | $\tau_{0\to1}$ | 11.321 | 2.881 | 1.005 | 0.852 | 8.1E-04 | 0.151 | 3.018 | 0.783 |
| | $\tau_{2\to3}$ | 14.064 | 2.880 | 1.009 | 0.850 | 8.1E-04 | 0.156 | 3.000 | 0.833 |
| | $\tau_{4\to5}$ | 14.428 | 2.880 | 1.010 | 0.850 | 8.1E-04 | 0.156 | 3.000 | 0.838 |
| P1 $\sigma$ | $\tau_{0\to1}$ | 0.700 | 0.002 | 0.007 | 0.002 | 2.9E-15 | 0.002 | 0.053 | 0.012 |
| | $\tau_{2\to3}$ | 0.711 | 0.000 | 0.002 | 0.000 | 4.5E-09 | 0.000 | 0.000 | 0.004 |
| | $\tau_{4\to5}$ | 0.489 | 0.000 | 0.001 | 0.000 | 5.5E-10 | 0.000 | 0.000 | 0.007 |
| P2 $\mu$ | $\tau_{0\to1}$ | 5.232 | 0.765 | 1.005 | 0.214 | 8.1E-04 | 0.304 | 6.869 | 0.237 |
| | $\tau_{2\to3}$ | 5.807 | 0.749 | 1.004 | 0.245 | 8.4E-04 | 0.305 | 6.772 | 0.234 |
| | $\tau_{4\to5}$ | 6.105 | 0.770 | 0.996 | 0.232 | 9.1E-04 | 0.306 | 6.375 | 0.235 |
| P2 $\sigma$ | $\tau_{0\to1}$ | 1.232 | 0.109 | 0.008 | 0.029 | 1.2E-04 | 0.002 | 1.315 | 0.026 |
| | $\tau_{2\to3}$ | 1.375 | 0.082 | 0.007 | 0.030 | 1.2E-04 | 0.003 | 0.800 | 0.027 |
| | $\tau_{4\to5}$ | 1.017 | 0.094 | 0.008 | 0.036 | 7.2E-05 | 0.003 | 0.571 | 0.022 |
| P3 $\mu$ | $\tau_{0\to1}$ | 5.216 | 0.354 | 1.010 | 0.853 | 5.6E-05 | 0.856 | 3.600 | 0.501 |
| | $\tau_{2\to3}$ | 6.418 | 0.366 | 0.994 | 0.906 | 1.4E-04 | 0.856 | 3.600 | 0.516 |
| | $\tau_{4\to5}$ | 6.918 | 0.368 | 0.994 | 0.913 | 5.4E-05 | 0.855 | 3.600 | 0.524 |
| P3 $\sigma$ | $\tau_{0\to1}$ | 0.136 | 0.008 | 0.000 | 0.004 | 6.8E-14 | 0.000 | 0.000 | 0.003 |
| | $\tau_{2\to3}$ | 0.608 | 0.008 | 0.008 | 0.023 | 2.7E-04 | 0.001 | 0.000 | 0.020 |
| | $\tau_{4\to5}$ | 0.810 | 0.006 | 0.008 | 0.021 | 6.8E-06 | 0.001 | 0.000 | 0.021 |
| P4 (CdSe) $\mu$ | $\tau_{0\to1}$ | 18.359 | 0.299 | 1.008 | 0.000 | 9.5E+00 | 0.154 | 3.689 | 0.120 |
| | $\tau_{2\to3}$ | 23.314 | 0.292 | 1.000 | 0.000 | 9.1E+00 | 0.154 | 3.809 | 0.117 |
| | $\tau_{4\to5}$ | 31.944 | 0.292 | 0.999 | 0.000 | 9.0E+00 | 0.154 | 3.771 | 0.121 |
| P4 (CdSe) $\sigma$ | $\tau_{0\to1}$ | 0.649 | 0.010 | 0.002 | 0.000 | 3.2E-01 | 0.000 | 0.139 | 0.005 |
| | $\tau_{2\to3}$ | 0.604 | 0.011 | 0.006 | 0.000 | 5.5E-01 | 0.000 | 0.084 | 0.006 |
| | $\tau_{4\to5}$ | 0.801 | 0.007 | 0.007 | 0.000 | 4.0E-01 | 0.000 | 0.036 | 0.004 |

**Table 3.1.** Fitted parameters for PCFS interferograms. $\tau_{0\to1}$ corresponds to photons arriving with time difference $\tau$ between 100 – 500 μs; $\tau_{2\to3}$ for 1 – 5 ms; and $\tau_{4\to5}$ for 10 – 50 ms. Mean values and standard deviations were obtained by performing each fit 20 times starting with randomized (within user defined bounds) initial guesses.

| | dot P1 | dot P2 | dot P3 | dot P4 |
|---|---|---|---|---|
| $\tau$ (ms) | $\mu \pm \sigma$ | $\mu \pm \sigma$ | $\mu \pm \sigma$ | $\mu \pm \sigma$ |
| 0.1 - 0.33 | 10.8 ± 0.7 | 5.1 ± 1.0 | 5.2 ± 0.3 | 18.2 ± 1.0 |
| 0.33 - 0.66 | 12.1 ± 0.2 | 4.2 ± 0.7 | 5.6 ± 0.4 | 20.2 ± 0.7 |
| 0.66 - 0.99 | 9.4 ± 0.5 | 5.9 ± 1.7 | 5.8 ± 0.4 | 20.8 ± 0.6 |
| 1 - 3.3 | 14.3 ± 0.5 | 5.5 ± 1.2 | 6.2 ± 0.6 | 23.2 ± 1.1 |
| 3.3 - 6.6 | 14.7 ± 0.9 | 5.4 ± 1.7 | 6.8 ± 0.6 | 25.6 ± 0.6 |
| 6.6 - 9.9 | 14.7 ± 1.5 | 5.5 ± 1.3 | 7.0 ± 0.5 | 27.2 ± 0.3 |
| 10 - 33 | 14.9 ± 0.3 | 6.1 ± 1.2 | 6.8 ± 0.7 | 31.1 ± 0.4 |
| 33 - 66 | 15.3 ± 0.8 | 5.5 ± 1.5 | 7.2 ± 0.6 | 34.1 ± 0.1 |
| 66 - 99 | 16.6 ± 1.3 | 5.8 ± 2.3 | 7.7 ± 0.7 | 34.2 ± 0.0 |

**Table 3.2.** Means $\mu$ and standard deviations $\sigma$ of the value of $\Gamma$ for fitted interferograms at different $\tau$ windows spanning 100 μs to ~100 ms.

| **Variable** | $a_1$ | $\tau_1$ ($\mu$s) | $\alpha_2$ | $\tau_2$ ($\mu$s) | $y_0$ |
|---|---|---|---|---|---|
| **dot L1** | 0.91 | 3.2e-3 | 0.09 | 0.36 | 2.0e-3 |
| **dot L2** | 0.92 | 2.6e-3 | 0.08 | 0.36 | 2.3e-3 |
| **dot L3** | 0.95 | 4.5e-3 | 0.05 | 0.32 | 1.4-3 |

**Table 3.3.** Fitted parameters for lifetimes of dots L1 – L3. The fitted amplitudes are scaled to sum to 1, i.e. $a_1/(a_1 + a_2)$ and $a_2/(a_1 + a_2)$.

| **Variable** | $a_1$ | $\tau_1$ ($\mu$s) | $\alpha_2$ | $\tau_2$ ($\mu$s) | $R$ | $y_0$ | $\Lambda$ ($\mu$s) |
|---|---|---|---|---|---|---|---|
| **dot L1** | 0.43 | 3.5e-3 | 0.45 | 0.39 | 0.077 | 2.3e-2 | 4.0 |
| **dot L2** | 0.18 | 3.5e-3 | 0.41 | 0.37 | 0.087 | 2.8e-2 | 4.0 |
| **dot L3** | 1.04 | 3.5e-3 | 0.22 | 0.37 | 0.086 | 2.4e-2 | 4.0 |

**Table 3.4.** Fitted parameters for $g^{(2)}(\tau)$ of dots L1 – L3.

| Material system | $\lambda$ (nm) | Linewidth ($\mu$eV) | $g^2(0)$ | $T_1$ (ns) | Ref. |
|---|---|---|---|---|---|
| CdSe/CdS QD (colloidal) | 585 | 6.5 for $\tau$ < 20 μs, 10 for $\tau$ > 1 ms | 0.60 | $\tau_b$ = 10,[182] $\tau_d$ = 150[169] | [169,182] |
| | 626 | ~10 μeV (at 2K) | 0.8 – 1.0 | $\tau_1$ = 1, $\tau_2$ = 18, $\tau_3$ = 220 | [162,183] |
| $CsPbBr_3$ QD (colloidal) | 530 | 17 - 27 for $\tau$ < 100 μs | 1 (unfiltered) 0 (filtered) | 0.21 – 0.27 | [70] |
| | 510 - 520 | 20.8 for $\tau$ < 100 ms | - | 0.19 – 0.24 | [19] |
| 2D hBN defect | 573 – 821 | 45 | 0.41 - 0.42 | -[(c)] | |
| | 575 | 5 for $\tau < 10$ μs, 50 for $\tau > 10$ ms | 0.35 ± 0.05 | 1.7 ± 0.2 | [131] |
| 2D $WSe_2$ defect | 730 | 130 | 0.14 – 0.21 | 1.79 | [133] |
| 2D $MoS_2$ defect | 700 | 248 | 0.23 | 1730 ± 150 | [184] |
| InGaAs (epitaxial)[(a)] | 925 | Lifetime-limited[(b)] | 0.024 – 0.047 | 0.15 | [138] |
| | 915 | 1.25[(b)] | 0.021 | 0.05 | [185] |
| **InP/ZnSe/ZnS QD (colloidal)** | **610** | **5 for $\tau$ = 100 – 500 μs 7 for $\tau$ = 10 – 50 ms** | **0.071 – 0.086** | **$\tau_b$ = 16.7[47] $\tau_d$ = 360** | **This work** |

**Table 3.5.** Comparison of center wavelength, linewidth, and unfiltered $g^{(2)}(\tau = 0)$ for various solid-state single-photon emitter systems. PL = photoluminescence, μ-PL = micro-photoluminescence. [(a)] = dot in cavity structure, [(b)] = radiatively limited linewidth, [(c)] = value not found in reference.

# Chapter 4

# Third-Order Photon Correlation Technique Reveals High Average Multiexciton Quantum Yields in ZnSe Nanocrystals

## 4.1. Abstract

Colloidal nanocrystals (NCs) are used in several high excitation flux applications such as the active layer in light-emitting diodes. One property that makes them particularly good for high flux applications is their ability to hold multiple excitons at once enabling higher photon output compared to molecular systems. However, nonradiative Auger recombination can severely hinder the multiexciton quantum efficiency in many colloidal NCs. Here, we use a second-order cross-correlation technique to show ZnSe/ZnS NCs have a high average biexciton quantum yield ratio of $84\% \pm 2\%$, making these NCs a great candidate for high flux optical applications. To generalize the multiexciton properties, we advance the correlation technique to the third-order to measure the average triexciton quantum yield ratio. Additionally, we extend the photon number resolved lifetime analytical method to determine the triexciton lifetime in addition to the biexciton lifetime of these ZnSe/ZnS NCs in solution. We find the biexciton lifetime to be 2.4 ns and the triexciton lifetime to be 1.9 ns. The faster triexciton lifetime suggests a lower triexciton quantum yield ratio compared to the biexciton quantum yield ratio. Our findings show that the multiexciton efficiency and dynamics of colloidal NCs can be routinely probed in solution, and that ZnSe/ZnS NCs are a promising material for high flux optical applications.

## 4.2. Background

Colloidal nanocrystals (NCs) are a material of interest in several high excitation flux applications such as lasing,[186] light-emitting diodes (LEDs),[92,148] and quantum emission for quantum information sciences.[12,58] Colloidal NCs are solution-processable and have been proven to exhibit high photoluminescence (PL) quantum yields (QYs),[148,171] narrow linewidths,[47,89,124] and tunable emission energies.[87,88] For materials that can only hold a single exciton at once, light output is limited by the PL lifetime. NC emission output is limited by the exciton lifetime, but can partially overcome this limitation by sustaining multiple excitons at once. Multiexciton efficiency becomes a more significant factor in overall efficiency of NCs in high flux applications, and is known to be primarily reduced by nonradiative Auger recombination where the energy from recombination of an electron-hole pair transfers to another electron or hole, promoting the charge to a higher energetic state, rather than emitting as a photon.

Multiexciton and Auger recombination have been studied using primarily two spectroscopic methods: ultrafast spectroscopy and single-NC spectroscopy. Ultrafast techniques such as transient absorption and transient photoluminescence have the power to measure average multiexciton and Auger lifetimes on the ensemble level.[101,187] However, these ultrafast techniques require high excitation fluxes, limiting control over the number of excitons generated,[188] and require precise modelling of the NC system to extract significant physical properties. Single-NC spectroscopy avoids ensemble averaging of the interrogated system which allows for greater control of the number of excitons generated and straightforward interpretation of the emission properties. Biexciton dynamics and QY have been investigated at the single-NC level in several systems including CdSe,[80,82,189] InP,[58] $CsPbBr_3$,[12,70,190] and InAs[191] by measuring second-order photon correlations, $g^{(2)}(\tau)$, using a Hanbury Brown and Twiss configuration.[192] Low excitation fluxes were used in all of these studies to ensure higher-order multiexciton generation ($n \geq 3$) was negligible. Shulenberger et al. extended the single-NC correlation technique by measuring third-order photon correlations, $g^{(3)}(\tau_1, \tau_2)$, in a modified Hanbury Brown and Twiss configuration to resolve the triexciton dynamics and QY of single CdSe NCs.[82,193]

Single-NC photon correlation spectroscopy can unambiguously measure fundamental properties of colloidal NCs important for high flux optical applications, however these measurements are time intensive making it challenging to gather statistically significant numbers on the material of interest. Single-NC spectroscopy also suffers from user selection bias, where the brightest and most stable NCs are investigated more than the NCs that are dimmer or intermittingly blinking on and off. Beyler et al.[85] and Bischof et al.[84] acknowledged a need to adapt the single-NC $g^{(2)}(\tau)$ technique to measure average single-NC biexciton QYs and lifetimes in an ensemble of NCs.[84,85] This solution-phase $g^{(2)}(\tau)$ technique combines the useful information from single-NC measurements with the increased stability and consistency of ensemble-level measurements, and has been used for routine characterization of many colloidal NC materials.[24,25,29,58,194,195] An analogous solution-phase $g^{(3)}(\tau_1, \tau_2)$ technique must be developed to measure triexciton properties with statistical significance.

In this study, we develop a solution-phase $g^{(3)}(\tau_1, \tau_2)$ technique to characterize the average single-NC triexciton dynamics and QY in colloidal NC systems, gaining statistically significant quantities and avoiding user selection bias. We extend the solution-phase $g^{(2)}(\tau)$ theory to incorporate triexction emission and create a series of Monte Carlo simulations to corroborate the theory. Finally, we measure ZnSe QDs demonstrating their high multiexciton QYs and their efficient multiexciton radiative recombination dynamics.

## 4.3. High Exciton and Average Biexciton Quantum Yield in ZnSe/ZnS QDs

The ZnSe/ZnS NCs under investigation have an 8 nm ZnSe core and a 1 nm ZnS outer shell. The surface of the inorganic heterostructure is capped with oleic acid (OA) organic ligand to promote colloidal stability in solution. A schematic illustration and transmission electron microscopy image with energy dispersive X-ray analysis (TEM-EDX) of the ZnSe/ZnS NCs is shown **Figure 4.1a,b**, respectively. These NCs have near-unity PLQY and narrow ensemble PL with a $PL_{max}$ of ~442 nm and a full-width at half-maximum of 11 nm (**Figure 4.1c**). ZnSe NCs are within the II-VI semiconductor group exhibiting similar electronic structure as CdSe NCs.[62] ZnSe/ZnS NCs have shown to exhibit both Type I and quasi-Type II heterostructure behavior. Depending on the study, ZnSe NCs optical properties indicate confinement of the electron wavefunction within the ZnSe core (Type I), or a delocalization of the electron wavefunction into the ZnS shell (quasi-Type II).[196–200]

We measured the average biexciton quantum yield to exciton quantum yield ratio of these ZnSe NCs in solution using a second-order cross-correlation $g^{(2)}(\tau)$ technique where $\tau$ is the time difference between NC photon emission times.[84] By exciting a dilute solution of ZnSe NCs with a pulsed excitation source, we can measure the combination of single NC correlation contributions $g^{(2)}_{single}(\tau)$ and ensemble correlation contributions $g^{(2)}_{ensemble}(\tau)$ at short $\tau$, and ensemble correlation contributions at long $\tau$. If we assume ensemble contributions are consistent across all $\tau$, we can subtract the ensemble contributions out at short $\tau$ to isolate the single NC correlation contributions. The biexciton quantum yield to exciton quantum yield ratio is determined by measuring the ratio of the ensemble subtracted correlations occurring within the same excitation pulse $g^{(2)}(0)$ and the correlations occurring one pulse separated $g^{(2)}(T_{rep})$ (**Equation 4.1**).

$$\frac{QY_{BX}}{QY_X} = \frac{g^{(2)}(0)-1}{g^{(2)}(T_{rep})-1} \tag{4.1}$$

We measure an average $\frac{QY_{BX}}{QY_X}$ of $86\% \pm 2\%$. This high biexciton quantum yield ratio suggests a very slow Auger recombination rate, potentially a result of the large volume of the ZnSe NC and a gradient-like interface between the ZnSe core and the ZnS shell.[201]

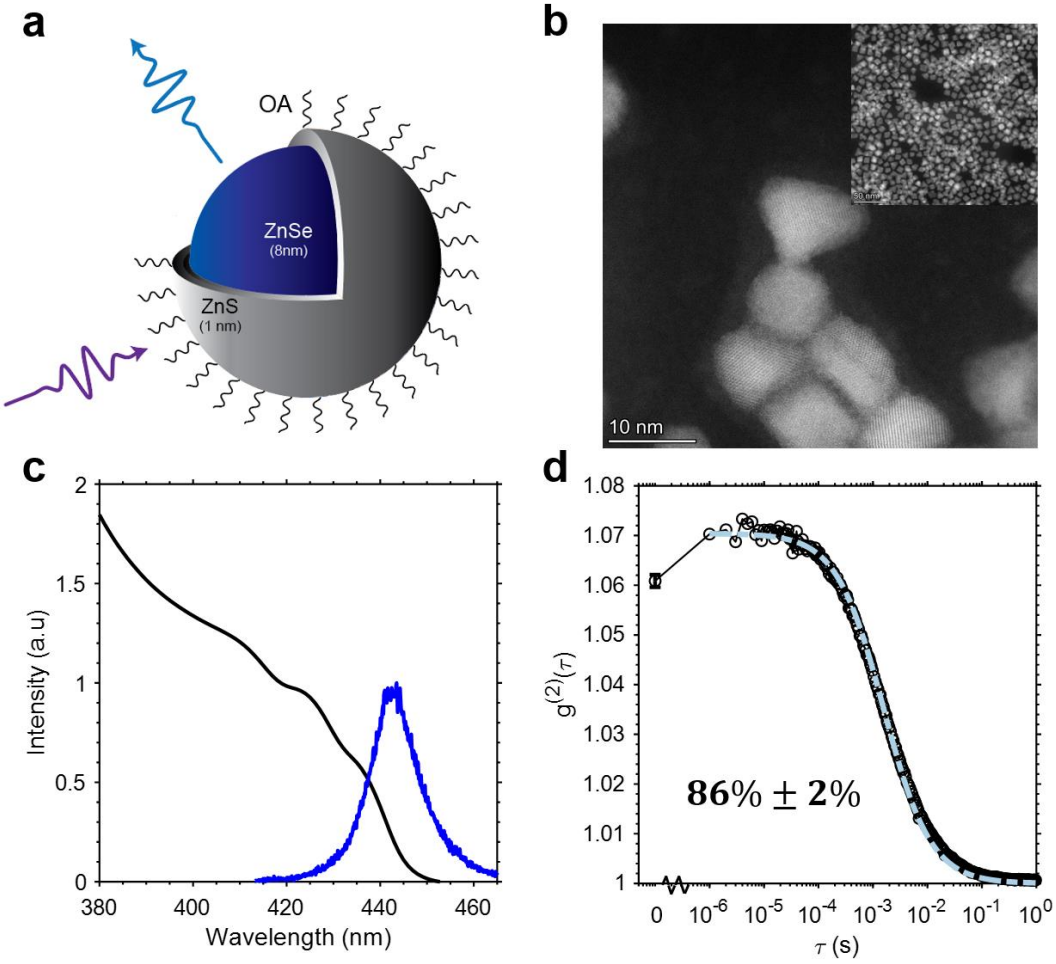


**Figure 4.1**. **a.** ZnSe/ZnS (core/shell) heterostructure schematic**. b**. ZnSe/ZnS NC TEM images. Inset shows a larger window TEM image with a 50 nm scale bar. **c**. Ensemble ZnSe/ZnS absorption (black) and emission (blue). **d.** Solution $g^{(2)}(\tau)$ measurement, fitting, and ensemble-averaged biexciton quantum yield ratio.

Measuring the biexciton efficiency is not sufficient to generalize multiexciton behavior in when considering ZnSe/ZnS NCs for high flux optical applications as many higher order multiexcitons are generated. We propose an analogous solution third-order cross-correlation $g^{(3)}(\tau_1, \tau_2)$ technique to measure average triexciton quantum yield ratio of these ZnSe NCs. Additionally, we propose to extend the photon number resolved lifetime ($PNRL$) analysis to measure the biexciton and triexciton lifetimes in solution. By extending these solution multiexciton techniques to the triexciton, we attempt to begin to generalize the multiexciton behavior in ZnSe/ZnS NCs.

## 4.4. Derivation of Solution Third-Order Correlation Technique

We start the derivation by defining all necessary terms and important assumptions necessary to work through the mathematical framework. We develop the relationship between the third-order cross-

correlations and the triexciton quantum yield (TXQY) through a series of cases: (1) A single-stationary dot, (2) a single-diffusing dot, (3) $N_0$ diffusing QDs, and (4) Poisson distribution of diffusing particles.

***Definitions***

- $a$ : the absorption cross-section, assumed to be constant in time and the same for all transitions from the ($n$-1)X to $n$X excitonic state
- $\gamma_n(t)$ : the time-dependent quantum yield of the $n$X excitonic state radiatively relaxing to the ($n$-1)X state. For simplicity, we will write $\gamma_n(t)$ simply as $\gamma_n$
- $p(t)$ : rate of excitation, which depends on the particle's absorption cross-section $a$ and its position within the reference volume, as well as laser intensity
- $\tau_D$ : characteristic diffusion time of emissive particle as governed by Brownian motion
- $T_{\text{rep}}$ : the period of the pulsed laser excitation
- $V_0$ : an arbitrarily large reference volume containing the focal volume
- $N_0$ : the number of particles within $V_0$ at a given point in time
- $\text{Poi}(m, p)$ : a Poisson distribution with average value $p$, evaluated for some integer $m$
- $P(n, p(t))$ : the probability of exactly $n$ photon emissions following a laser pulse, originating from a single QD with a time-dependent excitation flux $p(t)$
- $P_T(n, N_0, \{p_i(t)\})$ : the total probability of exactly $n$ photon emissions arising from $N_0$ QDs with time-dependent excitation fluxes $\{p_i(t)\}$ following an excitation pulse
- $G^{(3)}(\tau_1, \tau_2, t)$ : instantaneous probability at time $t$ of a correlation count at $(\tau_1, \tau_2)$ for a single particle
- $G^{(3)}(\tau_1, \tau_2, t)$ : probability of a correlation count at $(\tau_1, \tau_2)$ averaged over the course of the experiment, for a single particle
- $G^{(3)}(\tau_1, \tau_2, N_0)$ : probability of a correlation count at $(\tau_1, \tau_2)$ averaged over the course of the experiment for $N_0$ particles
- $\langle \cdots \rangle$ : time average over the experiment's integration time

***Starting Assumptions***

1. **Low excitation flux:** We assume that the excitation flux is sufficiently small such that, under Poisson absorption statistics, we are generating a negligible number of fourth-order excitations, both in an individual QD and across the ensemble of QDs. This assumption greatly simplifies the following derivation.

2. **Uniform and constant absorption cross-sections:** We assume that all *n*X excitonic states have the same absorption cross section. This approximation should hold given that the laser excitation is well above the material's band gap. Moreover, for convenience we assume that the absorption cross-section is constant over the course of the experiment. Although it is challenging to rigorously verify this claim, a similar assumption was made in Beyler *et al*.[85] and did not apparently lead to any issues in the solution $G^{(2)}$ experiment.

3. **Pulsed laser period is significantly longer than emitter lifetime:** This assumption ensures that emission events are binned properly. If emission events from one excitation pulse overlaps with emission events from another excitation pulse, the measured multiexciton QYs would be artificially inflated.

4. **Focal volume population obeys Poisson statistics:** For convenience we assume that, when we have a large number of freely diffusing QDs, the occupation number of the focal volume follows a Poisson distribution. For a solution of QDs, this assumption should hold true unless we have significant sample aggregation. In this case, the diffusion of distinct emitters is correlated, invalidating this assumption. Fortunately, the presence of aggregation can be inferred experimentally through the shape of the FCS and solution conditions can be optimized to favor Poisson behavior.

***Derivation***

This derivation is an extension of the solution BXQY derivation found in Beyler *et al*.[85] The key difference in this derivation is the assumption that third-order terms contribute significantly to the overall emission, allowing us to track triexciton emission statistics. The derivation will be broken into a set of cases of increasing complexity. We will build up the relevant equations from the case of a single, stationary QD to the "real-life" scenario of a fluctuating number of unique QDs freely diffusing in and out of the focal volume. Ultimately, we will identify analytical expressions for key points in the $G^{(3)}(\tau_1, \tau_2)$ correlation function, the experimental observable.

Case 1: A single, stationary QD

We'll first consider the case of a single, static QD experiencing a time-independent excitation rate $p(t) = p$. Under the assumption that all excitonic states have the same absorption cross-section, we can reasonably model absorption statistics with a Poisson distribution, with an average probability of absorbing

a photon given by the excitation rate $p$. In other words, the probability of a single QD absorbing $m$ photons, is given by

$$\mathrm{Poi}(m,p) = \frac{p^m e^{-p}}{m!} = \frac{p^m}{m!}\left(1 - p + \frac{p^2}{2!} - \frac{p^3}{3!} + \cdots\right). \tag{4.2}$$

As a result, the probability of a single QD emitting $n$ photons is

$$P(n,p) = \sum_{m=0}^{\infty} \mathrm{Poi}(m,p) \times E(n,m)\,, \tag{4.3}$$

where $E(n,m)$ describes the probability of the QD, having absorbed $m$ photons, emitting $n$. As such, $E(n,m)$ can be written exclusively in terms of the QD's quantum yields for the relevant excitonic states. For example, the probability of a QD to emit 0 photons after absorbing 1 photon is

$$E(0,1) = 1 - \gamma_1 \tag{4.4}$$

Expanding the Poisson distributions, substituting in appropriate expressions for the $E(n,m)$, and truncating to the third order in $p$ yields

$$\begin{aligned} P(0,p) \approx 1 - \gamma_1 \times p + \frac{1}{2}(\gamma_1 - \gamma_2 + \gamma_1\gamma_2) \times p^2 \\ + \frac{1}{6}(-\gamma_1 + 2\gamma_2 - 2\gamma_1\gamma_2 - \gamma_3 + \gamma_1\gamma_3 + \gamma_2\gamma_3 - \gamma_1\gamma_2\gamma_3) \times p^3 \end{aligned} \tag{4.5}$$

$$\begin{aligned} P(1,p) \approx \gamma_1 \times p + \frac{1}{2}(-\gamma_1 + \gamma_2 - 2\gamma_1\gamma_2) \times p^2 \\ + \frac{1}{2}(\gamma_1 + \gamma_3 - 2\gamma_1\gamma_3 - 2\gamma_2\gamma_3 + 3\gamma_1\gamma_2\gamma_3) \times p^3 \end{aligned} \tag{4.6}$$

$$P(2,p) \approx \frac{1}{2}\gamma_1\gamma_2 \times p^2 + \frac{1}{6}(-2\gamma_1\gamma_2 + \gamma_1\gamma_3 + \gamma_2\gamma_3 - 3\gamma_1\gamma_2\gamma_3) \times p^3 \tag{4.7}$$

$$P(3,p) \approx \frac{1}{6}\gamma_1\gamma_2\gamma_3 \times p^3 \tag{4.8}$$

Lastly, under our assumptions we set

$$P(n \geq 4, p) = 0 \tag{4.9}$$

These probabilities are not directly measured, however. Instead, we record third-order cross-correlations, $G^{(3)}$. The next step is to write the $G^{(3)}$ in terms of emission probabilities.

First, we have to account for the fact that when multiple emissions occur within the same excitation pulse, $G^{(3)}$counts may arise from either "positive" or "negative" time separations. To account for the additional opportunities for contributions to a given $G^{(3)}$ peak when emissions occur in the same excitation pulse, we add pre-factors to obtain proper values of $G^{(3)}(\tau_1, \tau_2, t)$. For three simultaneous events there is a multiplicity of 6, for two simultaneous events a multiplicity of 2, and for a single event a multiplicity of 1. Therefore

$$G^{(3)}(0,0,t) = 6P(3,p) = \gamma_1\,\gamma_2\,\gamma_3 \times p^3, \tag{4.10}$$

$$\begin{aligned} G^{(3)}\left(0, T_{\text{rep}}, t\right) &= 2P(2,p)P(1,p) \\ &= \gamma_1^2\,\gamma_2 \times p^3, \end{aligned} \tag{4.11}$$

$$G^{(3)}\left(T_{\text{rep}}, T_{\text{rep}}, t\right) = P(1,p)^3 = \gamma_1^3 \times p^3. \tag{4.12}$$

Thus, when we average the $G^{(3)}$ over the full course of the experiment, we obtain

$$G^{(3)}(0,0) = \langle \gamma_1 \gamma_2 \gamma_3 \rangle \times p^3 \tag{4.13}$$

$$G^{(3)}\left(0, T_{\text{rep}}\right) = \langle \gamma_1^2 \gamma_2 \rangle \times p^3 \tag{4.14}$$

$$G^{(3)}\left(T_{\text{rep}}, T_{\text{rep}}\right) = \langle \gamma_1^3 \rangle \times p^3 \tag{4.15}$$

Note that, in the case where the quantum yields change negligibly over time, the ratio of the center peak to the on-axis side peak yields the relative TXQY of a single particle:

$$\frac{G^{(3)}(0,0)}{G^{(3)}\left(0,T_{\text{rep}}\right)} = \frac{\gamma_3}{\gamma_1} \tag{4.16}$$

This is the result obtained for the single-QD $G^{(3)}$ measurement derived in Shulenberger *et al.*,[13] verifying our treatment up to this point.

Case 2: A single, diffusing QD

Now consider a single particle which freely diffuses within an arbitrarily large reference volume $V_0$. The identity of the particle may change, but the occupation of $V_0$ is always one. Due to QD diffusion, the excitation rate $p(t)$ felt by the particle changes with time. Since these changes are uncorrelated with time-dependent variations in quantum yields $\{\gamma_n(t)\}$, we now have that

$$G^{(3)}(0,0) = 6\langle P(3,p(t))\rangle = \langle \gamma_1\gamma_2\gamma_3\rangle \times \langle p(t)^3\rangle \tag{4.17}$$

$$G^{(3)}\left(0,T_{\text{rep}}\right) = 2\langle P(2,p(t))P(1,p,t)\rangle = \langle \gamma_1^2\gamma_2\rangle \times \langle p(t)^3\rangle \tag{4.18}$$

$$G^{(3)}\left(T_{\text{rep}},T_{\text{rep}}\right) = \langle P(1,p(t))^3\rangle = \langle \gamma_1^3\rangle \times \langle p(t)^3\rangle \tag{4.19}$$

Implicit in these equations is the assumption that the QD does not feel a difference in the excitation rate between one excitation pulse and the subsequent pulse, or $p(t) \approx p\left(t + T_{\text{rep}}\right)$.

Case 3: $N_0$ diffusing QDs

Now assume that there are exactly $N_0$ diffusing particles in the reference volume at all times, although their identities may change. We allow each particle *i* to have its own $\{\gamma_n\}_i$ and $p_i(t)$. Since we now have multiple dots potentially emitting during the same excitation pulse, our probabilities will reflect the possibility of photon emission from multiple dots. Consequently,

$$P_T(0,N_0,\{p_i(t)\}) = \prod_{i=1}^{N_0} P_i\left(0,p_i(t)\right), \tag{4.20}$$

$$P_T(1, N_0, \{p_i(t)\}) = \sum_{i=1}^{N_0} P_i\big(1, p_i(t)\big) \prod_{j\neq i}^{N_0} P_j\left(0, p_j(t)\right), \tag{4.21}$$

$$\begin{aligned} &P_T(2, N_0, \{p_i(t)\}) \\ &\quad = \sum_{i=1}^{N_0} P_i\big(2, p_i(t)\big) \prod_{j\neq i}^{N_0} P_j\left(0, p_j(t)\right) \\ &\quad + \sum_{i=1}^{N_0-1} \sum_{j=i+1}^{N_0} P_i\big(1, p_i(t)\big)\, P_j\left(1, p_j(t)\right) \prod_{k\neq i,j}^{N_0} P_k\big(0, p_k(t)\big), \end{aligned} \tag{4.22}$$

$$\begin{aligned} &P_T(3, N_0, \{p_i(t)\}) \\ &= \sum_{i=1}^{N_0} P_i\big(3, p_i(t)\big) \prod_{j\neq i}^{N_0} P_j\left(0, p_j(t)\right) \\ &+ \sum_{i=1}^{N_0} \sum_{j\neq i}^{N_0} P_i\big(2, p_i(t)\big)\, P_j\left(1, p_j(t)\right) \prod_{k\neq i,j}^{N_0} P_k\big(0, p_k(t)\big) \\ &+ \sum_{i=1}^{N_0-2} \sum_{j=i+1}^{N_0-1} \sum_{k=j+1}^{N_0} P_i\big(1, p_i(t)\big) P_j\left(1, p_j(t)\right) P_k\big(1, p_k(t)\big) \prod_{l\neq i,j,k}^{N_0} P_l\big(0, p_l(t)\big). \end{aligned} \tag{4.23}$$

Now we use these probabilities to write expressions for correlation peaks. This requires simplifying the products of the above probabilities and applying a time average. For the center peak we obtain

$$G^{(3)}(0,0,N_0) = 6 \times \langle P_T(3, N_0, \{p_i(t)\})\rangle. \tag{4.24}$$

We next apply the time average, bearing in mind that emissions from separate particles are uncorrelated. Therefore

$$
\begin{aligned}
G^{(3)}(0,0,N_0) = 6\sum_{i=1}^{N_0}\langle P\big(3,p(t)\big)\rangle\prod_{j\neq i}^{N_0}\langle P\big(0,p(t)\big)\rangle \\
+ 6\sum_{i=1}^{N_0}\sum_{j\neq i}^{N_0}\langle P\big(2,p(t)\big)\rangle\,\langle P\big(1,p(t)\big)\rangle\prod_{k\neq i,j}^{N_0}\langle P\big(0,p(t)\big)\rangle \\
+ 6\sum_{i=1}^{N_0-2}\sum_{j=i+1}^{N_0-1}\sum_{k=j+1}^{N_0}\langle P\big(1,p(t)\big)\rangle^3\prod_{l\neq i,j,k}^{N_0}\langle P\big(0,p(t)\big)\rangle \\
= 6N_0\times\langle P\big(3,p(t)\big)\rangle\langle P\big(0,p(t)\big)\rangle^{N_0-1} \\
+ 6N_0(N_0-1)\times\langle P\big(2,p(t)\big)\rangle\langle P\big(1,p(t)\big)\rangle\langle P\big(0,p(t)\big)\rangle^{N_0-2} \\
+ N_0(N_0-1)(N_0-2)\times\langle P\big(1,p(t)\big)\rangle^3\langle P\big(0,p(t)\big)\rangle^{N_0-3}. \qquad (4.25)
\end{aligned}
$$

For the on-axis side peak,

$$
G^{(3)}\big(0,T_{rep},N_0\big) = 2\times\langle P_T(2,N_0,\{p_i(t)\})\times P_T(1,N_0,\{p_i(t)\})\rangle. \qquad (4.26)
$$

We next simplify the sum products and apply the time average

$$
\begin{aligned}
&G^{(3)}\big(0, T_{rep}, N_0\big) \\
&= 2\sum_{i=1}^{N_0}\langle P\big(2,p(t)\big)P\big(1,p(t)\big)\rangle\prod_{j\neq i}^{N_0}\langle P\big(0,p(t)\big)^2\rangle \\
&+ 2\sum_{i=1}^{N_0}\sum_{j\neq i}^{N_0}\langle P\big(2,p(t)\big)P\big(0,p(t)\big)\rangle\langle P\big(1,p(t)\big)P\big(0,p(t)\big)\rangle\prod_{k\neq i,j}^{N_0}\langle P\big(0,p(t)\big)^2\rangle \\
&+ 2\sum_{i=1}^{N_0}\sum_{j\neq i}^{N_0}\langle P\big(1,p(t)\big)^2\rangle\langle P\big(1,p(t)\big)P\big(0,p(t)\big)\rangle\prod_{k\neq i,j}^{N_0}\langle P\big(0,p(t)\big)^2\rangle \\
&+ 6\sum_{i=1}^{N_0-2}\sum_{j=i+1}^{N_0-1}\sum_{k=j+1}^{N_0}\langle P\big(1,p(t)\big)P\big(0,p(t)\big)\rangle^3\prod_{l\neq i,j,k}^{N_0}\langle P\big(0,p(t)\big)^2\rangle \\
&= 2N_0\times\langle P\big(2,p(t)\big)P\big(1,p(t)\big)\rangle\langle P\big(0,p(t)\big)^2\rangle^{N_0-1} \\
&+ 2N_0(N_0-1) \\
&\times\langle P\big(2,p(t)\big)P\big(0,p(t)\big)\rangle\langle P\big(1,p(t)\big)P\big(0,p(t)\big)\rangle\langle P\big(0,p(t)\big)^2\rangle^{N_0-2} \\
&+ 2N_0(N_0-1)\times\langle P\big(1,p(t)\big)^2\rangle\langle P\big(1,p(t)\big)P\big(0,p(t)\big)\rangle\langle P\big(0,p(t)\big)^2\rangle^{N_0-2} \\
&+ N_0(N_0-1)(N_0-2)\times\langle P\big(1,p(t)\big)P\big(0,p(t)\big)\rangle^3\langle P\big(0,p(t)\big)^2\rangle^{N_0-3}.
\end{aligned}
\tag{4.27}
$$

Similarly for the diagonal side peak,

$$
G^{(3)}\big(T_{\text{rep}}, T_{\text{rep}}, N_0\big) = \langle P_T(1, N_0, \{p_i(t)\})^3\rangle. \tag{4.28}
$$

Then

$$
\begin{aligned}
&G^{(3)}\left(T_{\text{rep}}, T_{\text{rep}}, N_0\right) \\
&= \sum_{i=1}^{N_0} \langle P\left(1, p(t)\right)^3 \rangle \prod_{j \neq i}^{N_0} \langle P\left(0, p(t)\right)^3 \rangle \\
&+ 3 \sum_{i=1}^{N_0} \sum_{j \neq i}^{N_0} \langle P\left(1, p(t)\right)^2 P\left(0, p(t)\right) \rangle \langle P\left(1, p(t)\right) P\left(0, p(t)\right)^2 \rangle \prod_{k \neq i,j}^{N_0} \langle P\left(0, p(t)\right)^3 \rangle \\
&+ 6 \sum_{i=1}^{N_0-2} \sum_{j=i+1}^{N_0-1} \sum_{k=j+1}^{N_0} \langle P\left(1, p(t)\right) P\left(0, p(t)\right)^2 \rangle^3 \prod_{l \neq i,j,k}^{N_0} \langle P\left(0, p(t)\right)^3 \rangle \\
&= N_0 \times \langle P\left(1, p(t)\right)^3 \rangle \langle P\left(0, p(t)\right)^3 \rangle^{N_0-1} \\
&+ 3N_0(N_0 - 1) \\
&\times \langle P\left(1, p(t)\right)^2 P\left(0, p(t)\right) \rangle \langle P\left(1, p(t)\right) P\left(0, p(t)\right)^2 \rangle \langle P\left(0, p(t)\right)^3 \rangle^{N_0-2} \\
&+ N_0(N_0 - 1)(N_0 - 2) \times \langle P\left(1, p(t)\right) P\left(0, p(t)\right)^2 \rangle^3 \langle P\left(0, p(t)\right)^3 \rangle^{N_0-3}.
\end{aligned} \tag{4.29}
$$

The expressions above now contain terms originating from single QDs as well as multiple QDs ("the ensemble"). In order to determine the average TXQY, a single-dot property, we will need to subtract out these ensemble terms. To this end, we will derive expressions for correlation peaks at long-time separations such that we can safely assume that they exclusively originate from distinct particles. As we will see, these peaks will correspond to ensemble terms above, allowing us to recover single-particle information from an ensemble solution measurement.

To begin, we make the reasonable assumption that, in the limit of infinitely long-time separations, the likelihoods of emission events are uncorrelated. In other words,

$$
\begin{aligned}
&G^{(3)}(\tau_1 \to \infty, \tau_2 \to \infty, N_0) \\
&\qquad = \langle \lim_{\tau_1, \tau_2 \to \infty} I(t, N_0) I(t + \tau_1, N_0) I(t + \tau_1 + \tau_2, N_0) \rangle, \\
&\qquad = \langle I(t, N_0) \rangle^3
\end{aligned} \tag{4.30}
$$

$$
\begin{aligned}
G^{(3)}(0, \tau_2 \to \infty, N_0) &= \langle \lim_{\tau_2 \to \infty} I(t, N_0) I(t, N_0) I(t + \tau_2, N_0) \rangle \\
&= \langle I(t, N_0) \rangle \times G^{(2)}(0, N_0)
\end{aligned} \tag{4.31}
$$

$$= \langle I(t, N_0)\rangle \times [2N_0 \times \langle P(2, p(t))\rangle \langle P(0, p(t))\rangle^{N_0-1} + N_0(N_0 - 1)\langle P(1, p(t))\rangle^2 \langle P(0, p(t))\rangle^{N_0-2}],$$

and

$$G^{(3)}\left(T_{\text{rep}}, \tau_2 \to \infty, N_0\right) = \langle \lim_{\tau_2 \to \infty} I(t, N_0) I(t + T_{\text{rep}}, N_0) I(t + \tau_2, N_0)\rangle$$
$$= \langle I(t, N_0)\rangle \times G^{(2)}\left(T_{\text{rep}}, N_0\right)$$
$$= \langle I(t, N_0)\rangle \times [N_0 \times \langle P(1, p(t))^2\rangle \langle P(0, p(t))^2\rangle^{N_0-1} + N_0(N_0 - 1)\langle P(1, p(t))P(0, p(t))\rangle^2 \langle P(0, p(t))^2\rangle^{N_0-2}]. \quad (4.32)$$

Here, $\langle I(t, N_0)\rangle$ gives the average number of photon counts at a point in time. It can be expressed as

$$\langle I(t, N_0)\rangle = \langle 1 \times P_T(1, N_0, \{p_i(t)\}) + 2 \times P_T(2, N_0, \{p_i(t)\}) + 3 \times P_T(3, N_0, \{p_i(t)\}) + \cdots \rangle. \quad (4.33)$$

Derivations for $G^{(2)}(0, N_0)$ and $G^{(2)}\left(T_{\text{rep}}, N_0\right)$, which also appear above, may be found in Beyler *et al.*[14]

Case 4: Poisson Distribution of Diffusing Particles

Finally, we reach the "real-world" case, in which we let the number of particles in the reference volume vary according to a Poisson distribution centered on some average occupancy $\langle N_0\rangle$. For the $G^{(3)}$ peaks at short $\tau$, we make the reasonable approximation that the occupation number doesn't significantly change on the timescale of the laser period. Consequently, when $\tau_1, \tau_2 \ll \tau_D$

$$G^{(3)}(\tau_1, \tau_2, \langle N_0\rangle) = \sum_{n=0}^{\infty} \text{Poi}(n, \langle N_0\rangle) \times G^{(3)}(\tau_1, \tau_2, n). \quad (4.34)$$

Then by simplifying, substituting in previously determined values for $\langle P\left(n, p(t)\right)\rangle$, and truncating at third order in $p$, we find that

$$G^{(3)}(0,0,\langle N_0\rangle) = \sum_{n=0}^{\infty} \mathrm{Poi}(n,\langle N_0\rangle) \times G^{(3)}(0,0,n)$$
$$= \sum_{n=0}^{\infty} \frac{\langle N_0\rangle^n e^{-\langle N_0\rangle}}{n!} G^{(3)}(0,0,n). \tag{4.35}$$

We can rearrange the above expression to obtain

$$G^{(3)}(0,0,\langle N_0\rangle)$$
$$= 6\langle N_0\rangle\langle P\big(3,p(t)\big)\rangle e^{-\langle N_0\rangle} \sum_{n=1}^{\infty} \frac{\langle N_0\rangle^{n-1}\langle P\big(0,p(t)\big)\rangle^{n-1}}{(n-1)!}$$
$$+ 6\langle N_0\rangle^2\langle P\big(2,p(t)\big)\rangle\langle P\big(1,p(t)\big)\rangle e^{-\langle N_0\rangle} \sum_{n=2}^{\infty} \frac{\langle N_0\rangle^{n-2}\langle P\big(0,p(t)\big)\rangle^{n-2}}{(n-2)!}$$
$$+ \langle N_0\rangle^3\langle P\big(1,p(t)\big)\rangle^3 e^{-\langle N_0\rangle} \sum_{n=3}^{\infty} \frac{\langle N_0\rangle^{n-3}\langle P\big(0,p(t)\big)\rangle^{n-3}}{(n-3)!}. \tag{4.36}$$

Note that the sum factors are simply Taylor expansions of an exponential. Thus

$$G^{(3)}(0,0,\langle N_0\rangle) = [6\langle N_0\rangle\langle P(3,p(t))\rangle + 6\langle N_0\rangle^2\langle P(2,p(t))\rangle\langle P(1,p(t))\rangle + \langle N_0\rangle^3\langle P(1,p(t))\rangle^3] \times e^{(\langle P(0,p(t))-1\rangle\langle N_0\rangle}. \tag{4.37}$$

Finally, truncating at third order in $p$ we find

$$G^{(3)}(0,0,\langle N_0\rangle) \approx \langle N_0\rangle\langle\gamma_1\gamma_2\gamma_3\rangle\langle p(t)^3\rangle + 3\langle N_0\rangle^2\langle\gamma_1\gamma_2\rangle\langle\gamma_1\rangle\langle p(t)^3\rangle\langle p(t)\rangle + \langle N_0\rangle^3\langle\gamma_1\rangle^3\langle p(t)\rangle^3. \tag{4.38}$$

Intuitively, the first term in the above expression corresponds to the probability of a TX event, the second term corresponds to one QD emitting a BX and another QD emitting an X, and the final term corresponds to the emission of three Xs from three separate QDs. By a similar process, it can be shown that

$$
\begin{aligned}
&G^{(3)}\left(0, T_{\text{rep}}, \langle N_0 \rangle\right) \\
&\quad = \Big[2\langle N_0\rangle\langle P\left(2,p(t)\right)P\left(1,p(t)\right)\rangle \\
&\quad + 2\langle N_0\rangle^2\langle P\left(2,p(t)\right)P\left(0,p(t)\right)\rangle\langle P\left(1,p(t)\right)P\left(0,p(t)\right)\rangle \\
&\quad + 2\langle N_0\rangle^2 \left\langle P\left(1,p(t)\right)^2\right\rangle \langle P\left(1,p(t)\right)P\left(0,p(t)\right)\rangle \\
&\quad + \langle N_0\rangle^3\langle P\left(1,p(t)\right)P\left(0,p(t)\right)\rangle^3\Big] \times e^{\left(\langle P\left(0,p(t)\right)^2\rangle - 1\right)\langle N_0\rangle} \\
&\quad \approx \langle N_0\rangle\langle {\gamma_1}^2\gamma_2\rangle\langle p(t)^3\rangle + \langle N_0\rangle^2\langle\gamma_1\gamma_2\rangle\langle\gamma_1\rangle\langle p(t)^2\rangle\langle p(t)\rangle \\
&\quad + 2\langle N_0\rangle^2\langle {\gamma_1}^2\rangle\langle\gamma_1\rangle\langle p(t)^2\rangle\langle p(t)\rangle + \langle N_0\rangle^3\langle\gamma_1\rangle^3\langle p(t)\rangle^3. \qquad (4.39)
\end{aligned}
$$

Now the first term in the above equation describes the probability of a single QD emitting a BX followed by an X; the second term describes the probability of one QD emitting a BX followed by another QD emitting an X; the third term describes the probability of two X emissions from two separate QDs within a single excitation pulse, followed by another X from one of the QDs that emitted an X in the previous excitation pulse; and the fourth term describes the probability of, again, three separate X emissions from three separate QDs. The difference in the fourth term in Equation 37 compared to the third term in Equation 36 is that the three separate X emissions occur between two separate excitation pulses in Equation 37. The three separate X emissions all occur within the same excitation pulse in Equation 36. Likewise,

$$
\begin{aligned}
&G^{(3)}\left(T_{\text{rep}}, T_{\text{rep}}, \langle N_0 \rangle\right) \\
&\quad = [\langle N_0\rangle\langle P(1,p(t))^3\rangle \\
&\quad + 3\langle N_0\rangle^2\langle P(1,p(t))^2P(0,p(t))\rangle\langle P(1,p(t))P(0,p(t))^2\rangle \\
&\quad + \langle N_0\rangle^3 \langle P(1,p(t))P(0,p(t))^2\rangle^3] \times e^{\left(\langle P(0,p(t))^3\rangle - 1\right)\langle N_0\rangle} \\
&\quad \approx \langle\gamma_1^3\rangle\langle p(t)^3\rangle\langle N_0\rangle + 3\langle\gamma_1^2\rangle\langle\gamma_1\rangle\langle p(t)^2\rangle\langle p(t)\rangle\langle {N_0}^2\rangle \\
&\quad + \langle\gamma_1\rangle^3\langle p(t)\rangle^3\langle {N_0}^3\rangle. \qquad (4.40)
\end{aligned}
$$

Conceptually, the first term gives the likelihood of a single QD emitting three Xs after three sequential excitation pulses, the second that of a single QD emitting two Xs followed by a second QD emitting a third X after three sequential excitation pulses, and the third that of three QDs emitting three Xs after three sequential excitation pulses.

When the time interval separating emission events is long relative to the diffusion time $\tau_D$, the occupancy of the reference volume is liable to change in between these events. Therefore, for probabilities spaced at long time separations, we must apply separate Poisson distributions. In other words,

$$G^{(3)}(\tau_1 \to \infty, \tau_2 \to \infty, \langle N_0 \rangle) = \left[\sum_{n=0}^{\infty} \mathrm{Poi}(n, \langle N_0 \rangle) \times \langle I(t,n) \rangle\right]^3 \tag{4.41}$$

Plugging in our expression for $\langle I(t,n) \rangle$ and factoring out the resulting exponential Taylor expansion, we arrive at

$$\begin{aligned} &G^{(3)}(\tau_1 \to \infty, \tau_2 \to \infty, \langle N_0 \rangle) \\ &\qquad \approx \langle N_0 \rangle^3 \langle P\big(1, p(t)\big) \rangle^3 e^{-3\langle N_0 \rangle \left(P\left(0, p(t)\right)-1\right)} \approx \langle N_0 \rangle^3 \langle \gamma_1 \rangle^3 \langle p(t) \rangle^3. \end{aligned} \tag{4.42}$$

Next, we have that

$$\begin{aligned} &G^{(3)}(0, \tau_2 \to \infty, \langle N_0 \rangle) \\ &\qquad = \left[\sum_{n=0}^{\infty} \mathrm{Poi}(n, \langle N_0 \rangle)[2n \times \langle P(2, p(t)) \rangle \langle P(0, p(t)) \rangle^{n-1} \right. \\ &\qquad \left. + n(n-1) \langle P(1, p(t)) \rangle^2 \langle P(0, p(t)) \rangle^{n-2}]\right] \\ &\qquad \times \left[\sum_{n=0}^{\infty} \mathrm{Poi}(n, \langle N_0 \rangle) \times \langle I(t,n) \rangle\right], \end{aligned} \tag{4.43}$$

and simplifying yields

$$\begin{aligned} &G^{(3)}(0, \tau_2 \to \infty, \langle N_0 \rangle) \\ &\qquad \approx \left[2\langle N_0 \rangle^2 \langle P\big(2, p(t)\big) \rangle \langle P\big(1, p(t)\big) \rangle + \langle N_0 \rangle^3 \langle P\big(1, p(t)\big) \rangle^3\right] \\ &\qquad \times e^{2\langle N_0 \rangle \left(\langle P\left(0, p(t)\right) \rangle - 1\right)} \\ &\qquad \approx \langle N_0 \rangle^2 \langle \gamma_1 \gamma_2 \rangle \langle \gamma_1 \rangle \langle p(t)^2 \rangle \langle p(t) \rangle + \langle N_0 \rangle^3 \langle \gamma_1 \rangle^3 \langle p(t) \rangle^3. \end{aligned} \tag{4.44}$$

Applying the same process to $G^{(3)}\big(T_{\mathrm{rep}}, \tau_2 \to \infty, \langle N_0 \rangle\big)$ gives us that

$$
\begin{aligned}
&G^{(3)}\left(T_{\text{rep}}, \tau_2 \to \infty, \langle N_0 \rangle\right) \\
&\quad = \left[\sum_{n=0}^{\infty} \text{Poi}(n, \langle N_0 \rangle)[n \times \langle P(1,p(t))^2 \rangle \langle P(0,p(t))^2 \rangle^{n-1} \right. \\
&\quad \left. + n(n-1)\langle P(1,p(t))P(0,p(t)) \rangle^2 \langle P(0,p(t))^2 \rangle^{n-2}]\right] \\
&\quad \times \left[\sum_{n=0}^{\infty} \text{Poi}(n, \langle N_0 \rangle) \times \langle I(t,n) \rangle\right] \\
&\quad \approx \left[\langle N_0 \rangle^2 \langle P\left(1,p(t)\right)^2 \rangle \langle P\left(1,p(t)\right) \rangle \right. \\
&\quad \left. + \langle N_0 \rangle^3 \langle P\left(1,p(t)\right)P\left(0,p(t)\right) \rangle^2 \langle P\left(1,p(t)\right) \rangle\right] \\
&\quad \times e^{\langle N_0 \rangle \left(\langle P\left(0,p(t)\right) \rangle + \langle P\left(0,p(t)\right)^2 \rangle - 2\right)} \\
&\quad \approx \langle N_0 \rangle^2 \langle {\gamma_1}^2 \rangle \langle \gamma_1 \rangle \langle p(t)^2 \rangle \langle p(t) \rangle + \langle N_0 \rangle^3 \langle \gamma_1 \rangle^3 \langle p(t) \rangle^3. \qquad (4.45)
\end{aligned}
$$

At last, we have obtained analytical expressions for a sufficient set of peaks in the $G^{(3)}$ function to back out physically meaningful single-particle information.

***Determining multiexciton quantum yields***

With the above values of $G^{(3)}(\tau_1 \to \infty, \tau_2 \to \infty, \langle N_0 \rangle)$, we may subtract the "ensemble" contributions from the center and on-axis side peak and take their ratio:

$$
\frac{G^{(3)}(0,0,\langle N_0 \rangle) - 3G^{(3)}(0, \tau_2 \to \infty, \langle N_0 \rangle) + 2G^{(3)}(\tau_1 \to \infty, \tau_2 \to \infty, \langle N_0 \rangle)}{G^{(3)}\left(0, T_{\text{rep}}, \langle N_0 \rangle\right) - G^{(3)}(0, \tau_2 \to \infty, \langle N_0 \rangle) - 2G^{(3)}\left(T_{\text{rep}}, \tau_2 \to \infty, \langle N_0 \rangle\right) + 2G^{(3)}(\tau_1 \to \infty, \tau_2 \to \infty, \langle N_0 \rangle)} = \frac{\langle \gamma_1 \gamma_2 \gamma_3 \rangle}{\langle {\gamma_1}^2 \gamma_2 \rangle}. \qquad (4.46)
$$

We interpret this quantity as the TXQY relative to the XQY, averaged across the sample and weighted by the brightness of individual emitters. We can also verify our $G^{(3)}$ measurement by using it to calculate the relative, brightness-weighted BXQY:

$$
\frac{G^{(3)}\left(0, T_{\text{rep}}, \langle N_0 \rangle\right) - G^{(3)}(0, \tau_2 \to \infty, \langle N_0 \rangle) - 2G^{(3)}\left(T_{\text{rep}}, \tau_2 \to \infty, \langle N_0 \rangle\right) + 2G^{(3)}(\tau_1 \to \infty, \tau_2 \to \infty, \langle N_0 \rangle)}{G^{(3)}\left(T_{\text{rep}}, T_{\text{rep}}, \langle N_0 \rangle\right) - G^{(3)}\left(T_{\text{rep}}, \tau_2 \to \infty, \langle N_0 \rangle\right) + 2G^{(3)}(\tau_1 \to \infty, \tau_2 \to \infty, \langle N_0 \rangle)} = \frac{\langle {\gamma_1}^2 \gamma_2 \rangle}{\langle {\gamma_1}^3 \rangle}. \qquad (4.47)
$$

To measure the third-order correlations, we modify the HBT configuration to split the photon stream into four paths. The modified HBT in **Figure 4.2a** shows a pulsed excitation source excite a solution NC sample. The emission is sent to 50:50 beamsplitter where it has a 50% chance to travel towards detectors 1 and 2 or towards detectors 3 and 4. After the NC emission travels through the first beamsplitter, it will

continue to another beamsplitter, making it such that there is a 25% of the NC emission to travel to any of the detectors. The third-order cross-correlations are computed by recording the histogram of all photon time differences $\tau_1$ of photons at Detector A with photons at Detector B, while simultaneously recording the histogram of all photon time differences $\tau_2$ of photons at Detector B with photons at Detector C (**Figure 4.2b**).

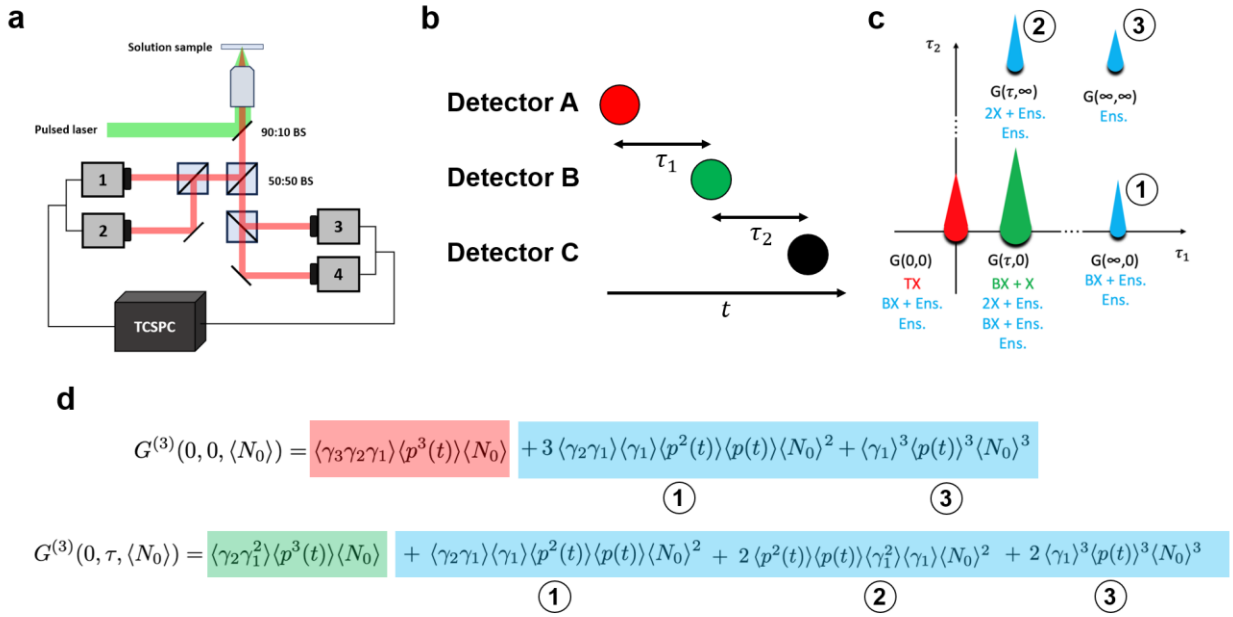


**Figure 4.2**. **a.** Modified Hanbury Brown and Twiss (HBT) setup to measure third-order cross-correlations $g^{(3)}(\tau_1,\tau_2)$ **b.** $g^{(3)}(\tau_1,\tau_2)$ between Detector A, Detector B, and Detector C. **c.** Single NC (red, green) and ensemble (blue) contributions to $g^{(3)}(\tau_1,\tau_2)$. **d.** Center peak contributions $G^{(3)}(0,0)$ (top equation) and side peak contributions to $G^{(3)}(0,T_{rep})$ (bottom equation). Numbered ensemble contributions highlighted in blue correspond to ensemble correlation peaks in **c**.

To verify the validity of the above derivation, we simulated the third-order correlation experiment with varying biexciton and triexciton quantum yields in the next section.

## 4.5. Monte Carlo Simulations of Third-Order Correlation Experiment

Monte Carlo (MC) simulations of the solution triexciton quantum yield experiment is developed through three steps: (1) modelling the Brownian motion of diffusing NCs, (2) modelling the Poisson nature of photon emission, and (3) performing the third-order cross-correlation analysis and photon number resolved lifetime analysis on simulated photon streams.

### 4.5.1. Modelling Brownian Motion of Diffusing Nanocrystals

We begin by modelling the diffusion of individual NCs in solution. We use a Brownian diffusion model that tracks the movement of a NC in the $x$-, $y$-, and $z$-direction every excitation pulse. For instance,

if the repetition rate of the excitation source is 1 MHz, the NC position will be stored every 1000 ns. The magnitude of the displacement of the NC in all directions is determined by the diffusion constant

$$D = \frac{k_B T}{6\pi\eta a} \tag{4.48}$$

where $k_B$ is the Boltzmann constant, $T$ is temperature, $\eta$ is the viscosity of the solvent, and $a$ is the NC radius. The diffusion constant $D$ is scaled by a constant $k$ in order to consider the dimension $d$ of the Brownian motion and the step size in time $\tau$.

$$k = D * d * \tau \tag{4.49}$$

We show the three-dimensional Brownian motion of 50 NCs in solution in **Figure 4.3a**. Diffusion is modelled at room temperature ($T = 293$ K) in toluene ($\eta = 5.54 \times 10^{-4}$ Pascal·seconds), and the NC radius $a$ is set to 5 nm. The black sphere in **Figure 4.3a,b** represents the focal volume of the laser excitation. The focal volume is modelled using a point spread function (**Equation 4.48**) to appropriately simulate the Gaussian excitation volume (**Figure 4.3c**). Only NC position and time data within the focal volume is stored for photon stream generation. (**Figure 4.3b**).

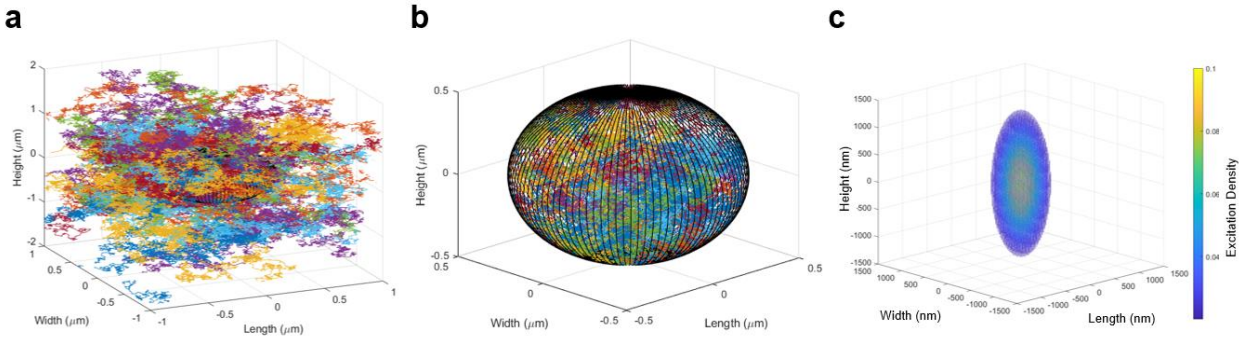


**Figure 4.3**. **a.** Simulated Brownian motion of 50 NCs in a 1 $\mu m$ × 1 $\mu m$ × 2 $\mu m$ box. **b.** NC diffusion (colored traces) within the excitation focal volume (black sphere). **c**. Point spread function representing the distribution of excitation densities following **Equation 4.48**.

$$PSF(x, y, z) = e^{-\frac{2r^2}{w_{xy}^2}} e^{-\frac{2z^2}{w_z^2}} \tag{4.50}$$

### 4.5.2. Modelling Photon Emission

We now have a dataset of NC excitation times. The next step is to generate the photon stream from these NCs. To do this, we model the absorption process, the emission process, and the optical path each photon travels to a single photon detector.

We model the absorption process using a Poisson model. For any NC excitation event, there is some probability for the NC to absorb 0, 1, 2, …, $m$ photons, given an excitation density $\langle n \rangle$.

$$Poi(m, \langle n \rangle) = \frac{\langle n \rangle^m e^{-\langle n \rangle}}{m!} \tag{4.51}$$

**Figure 4.4** shows the probability of an NC to absorb $m$ photons with an excitation density $\langle n \rangle$ = 0.1, 0.5, 1, 5, 10. The higher the excitation density, the higher the probability of the NC to absorb several photons at once. Necessary to the assumptions of these solution multiexciton experiments, we operate at a low excitation density ($\langle n \rangle \leq 0.1$) so that there are negligible contributions from absorption processes of $m \geq 4$.

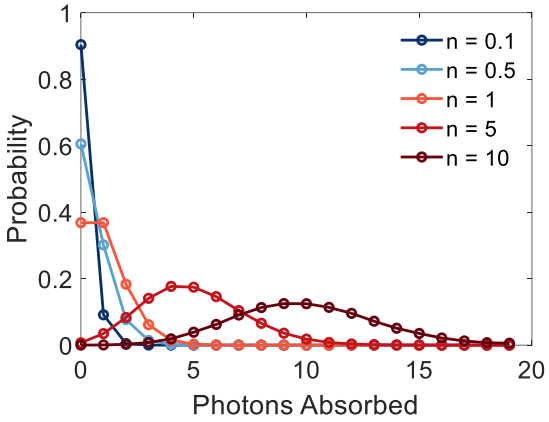


**Figure 4.4.** Poisson distribution describing the probability of absorbing $m$ photons given a particular excitation density $\langle n \rangle$.

Successful photon emission is determined by the randomly generating a number and comparing it to exciton, biexciton, or triexciton quantum yield. For instance, let's say three photons were absorbed in an excitation event, and the exciton, biexciton, and triexciton quantum yields are 100%, 50%, and 20%, respectively. We first generate a random number from 0 to 1 for the triexciton. If the number is between 0 and 0.2, we say the triexciton radiatively recombines. Otherwise, it nonradiatively recombines and we remove the triexciton from the photon stream. Similarly, we generate random numbers from 0 to 1 for the biexciton and exciton. If the random number for the biexciton is between 0 and 0.5, the biexciton radiatively recombines. If the random number for the exciton is between 0 and 1, the exciton radiatively recombines. For successful radiative recombination events, we store the excitation time for further processing of the photon stream.

To determine the arrival time of the photon, we must simulate the lifetime of the exciton, biexciton, or triexciton. Let's continue with our example of the three-photon absorption event, and say that the exciton, biexciton, and triexciton all successfully radiatively recombine. Let's also say that the exciton radiative lifetime is 30 ns, and the biexciton and triexciton radiative lifetimes are both 7.5 ns. We randomly generate

exponential decay numbers related to the exciton, biexciton, or triexciton lifetime, add that number to the excitation time, and store it in the array of photon arrival times.

The final step is to simulate the detector number for each photon arrival time. Each photon has a 25% chance of arriving at one of the four detectors in the modified HBT setup. We have taken into account the dead time of detectors, so two photons cannot arrive at the same detector within the same pulse. If the triexciton photon arrives at detector 1 and then the biexciton photon also arrives at detector 1, the biexciton photon will be discarded from the photon stream.

### 4.5.3. Third-Order Cross-Correlation and Photon Number Resolved Lifetime Analysis

We extend the correlation algorithm developed to compute fast second-order correlations to now correlate in the third-order.[202] To do so, we first compute the second-order cross-correlation at Detector B with photons at Detector C. However, we do not compute the cumulative correlation of every photon, but instead store the correlation of every individual photon at Detector B with photons at Detector C. **Figure 4.5** shows an example of how the first two photon correlations in the Detector B photon stream are stored. Then, we compute the *cumulative* correlation of the photons at Detector A with photons at Detector B. **Figure 4.**6 demonstrates how the first two Detector B second-order correlations are stored within the columns of the first Detector A photon third-order correlation. The final step is to normalize the total number of counts according to the bin width. The reason the bin widths exponentially increase is to speed up the algorithm.

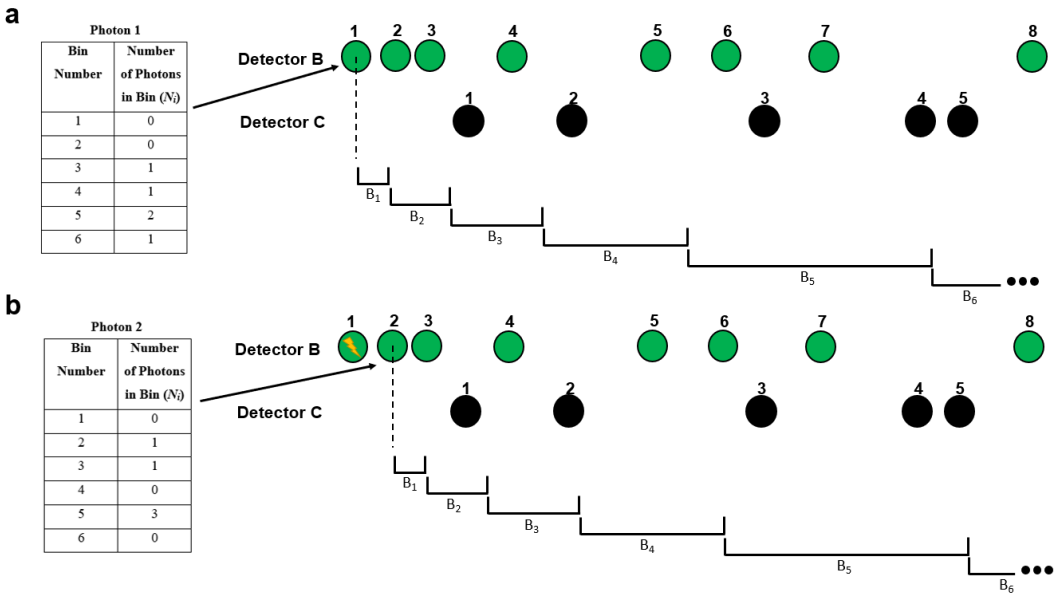


**Figure 4.5.** Individual photon second-order cross-correlations for the **a.** first photon and **b.** second photon in the Detector B photon stream

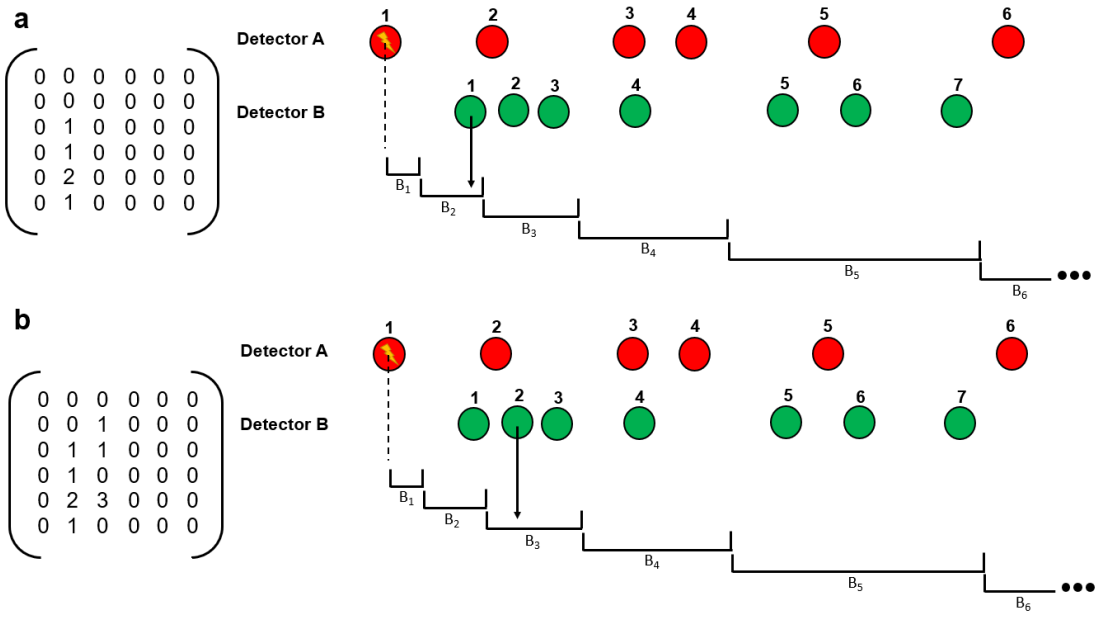


**Figure 4.6.** Frist two Detector B photon second-order cross-correlations added to the column of the first Detector A photon third-order cross-correlation. The column the correlation is added to depends on which bin the Detector B photon sits within.

Regarding the $PNRLs$, we measure the arrival time of the first photon in a two-photon event $PNRL^{(2,0,1)}(\tau)$ to determine the biexciton lifetime, and the first photon in a three-photon event $PNRL^{(3,0,1)}(\tau)$ to determine the triexciton lifetime. Since we are in solution, we have to consider a number of ensemble emission events that can contribute to the $PNRL^{(2,0,1)}(\tau)$ and $PNRL^{(3,0,1)}(\tau)$. The dominant ensemble background emission event that affects the $PNRL^{(2,0,1)}(\tau)$ is the detection of two excitons from two separate NCs (**Equation 4.52**). The two dominant ensemble background emission events that affect the $PNRL^{(3,0,1)}(\tau)$ are the detection of three excitons from three separate NCs and the detection of a biexciton from one NC and an exciton from another NC (**Equation 4.53**).

$$PNRL_{bkg}^{(2,0,1)}(\tau) = \left(\frac{d-1}{d}\right) g^{(1)}(\tau) \left(\int_0^{T_{rep}} g^{(1)}(t)dt\right) \tag{4.52}$$

$$PNRL_{bkg}^{(3,0,1)}(\tau) = \left(\frac{d-1}{d}\right)\left(\frac{d-2}{d}\right)\left[g^{(1)}(\tau)\left(\int_{\tau}^{T_{rep}}\int_{t_1}^{T_{rep}} g^{(1)}(t_2)dt_2dt_1\right) + PNRL^{(2,0,1)}(\tau)\left(\int_0^{T_{rep}} g^{(1)}(t)dt\right)\right] \tag{4.53}$$

The biexciton lifetime and triexciton lifetimes are therefore

$$BX(\tau) = PNRL^{(2,0,1)}(\tau) - PNRL_{bg}^{(2,0,1)}(\tau) \tag{4.54}$$

$$TX(\tau) = PNRL^{(3,0,1)}(\tau) - PNRL_{bg}^{(3,0,1)}(\tau). \quad (4.55)$$

To perform the analysis, we uploaded the photon streams to the MIT SuperCloud and parallelized the code to speed up the computations.

### 4.5.4. Monte Carlo Simulation Results

To validate the triexciton quantum yield derivation in **Section 4.4**, we sought to quantify the average single NC triexciton quantum yield of a series of Monte Carlo simulations. Each simulation consisted of the following parameters:

- Number of NCs $\boldsymbol{NC} = 10000$
- Box dimensions $\boldsymbol{L} \times \boldsymbol{W} \times \boldsymbol{H} = 19\ \mu m \times 19\ \mu m \times 19\ \mu m$
- Duration of experiment $\boldsymbol{Time} = 3600\ s$
- NC radius $\boldsymbol{a} = 5\ nm$
- Solvent viscosity $\boldsymbol{\eta} = 5.54 \times 10^{-4} Pa * s$
- Temperature $\boldsymbol{T} = 293\ K$
- Repetition Rate $\boldsymbol{reprate} = 1\ MHz$
- Excitation focal volume dimensions $\boldsymbol{w_z} = 1500\ nm$ and $\boldsymbol{w_{xy}} = 500\ nm$
- Exciton lifetime $\boldsymbol{\tau_X} = 30\ ns$
- Biexciton lifetime $\boldsymbol{\tau_{BX}} = 7.5\ ns$
- Triexciton lifetime $\boldsymbol{\tau_{TX}} = 30\ ns$ and $\boldsymbol{\tau_{TX}} = 7.5\ ns$
- Exciton quantum yield $\boldsymbol{QY_X} = 100\%$

Prior to running our newly developed third-order cross-correlation analysis on the MC datasets, we tested the physical reasonability of the simulations by measuring the second-order cross-correlation, used to determine the biexciton quantum yield. **Figure 4.7a** shows the second-order cross-correlation of a MC simulation with 75% biexciton quantum yield. We determined the shape and values to be reasonable, within 1% of the expected biexciton quantum yield value. Additionally, we ran an MC simulation of NCs diffusing in two-dimensions, rather than three-dimensions, and measured the second-order cross-correlation (**Figure 4.7b**). The value of the biexciton quantum yield is within 2% of the expected value, however the shape of the correlation at short tau does not plateau.

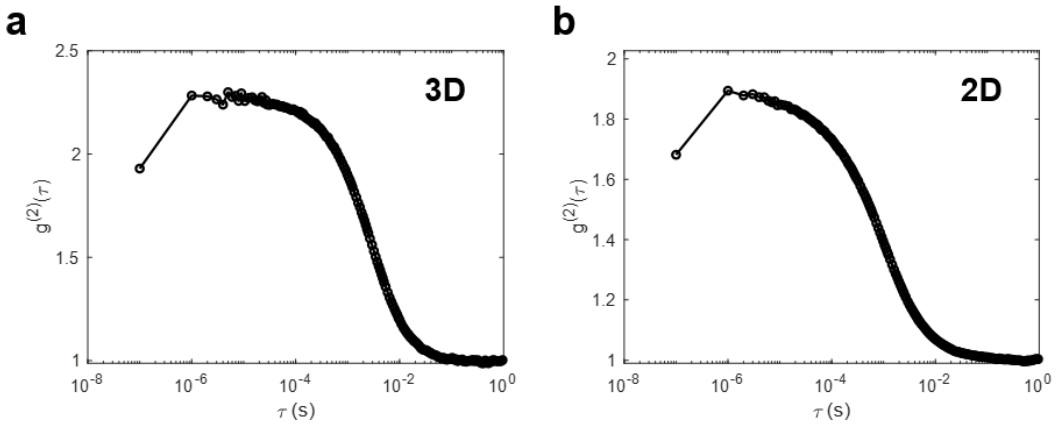


**Figure 4.7**. Second-order cross-correlation of MC simulation in **a.** 3D and **b.** 2D.

**Figure 4.9** shows the results of the 15 third-order cross-correlation Monte Carlo simulations. The biexciton and triexciton quantum yields ranged from 5% to 100%. Qualitatively, we observe a dip in the center peak of the third-order cross-correlation as the triexciton quantum yield decreases. Additionally, the trace of the third-order cross-correlation where $\tau_1$ or $\tau_2$ is equal to 0 dips as the biexciton quantum yield decreases. Quantitatively, we find the analysis of the third-order cross-correlations in **Figure 4.9** using **Equation 4.46** are in good agreement with the set parameters of the simulations (**Figure 4.8**)

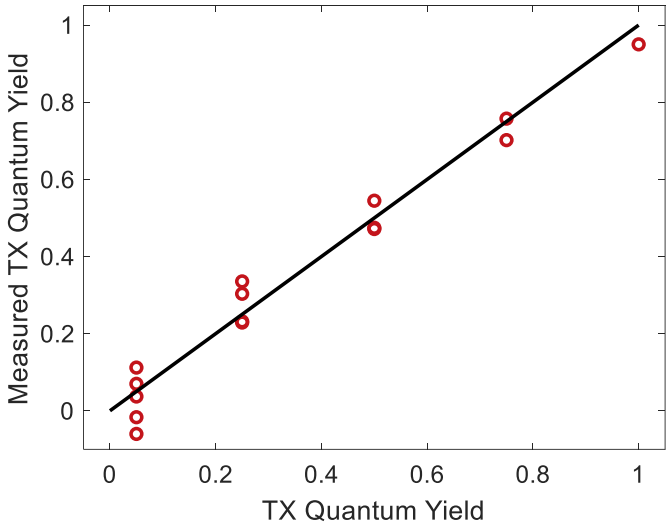


**Figure 4.8. Figure 4.8.** Measured triexciton quantum yield compared to the set triexciton quantum yield in MC simulations in **Figure 4.9**.

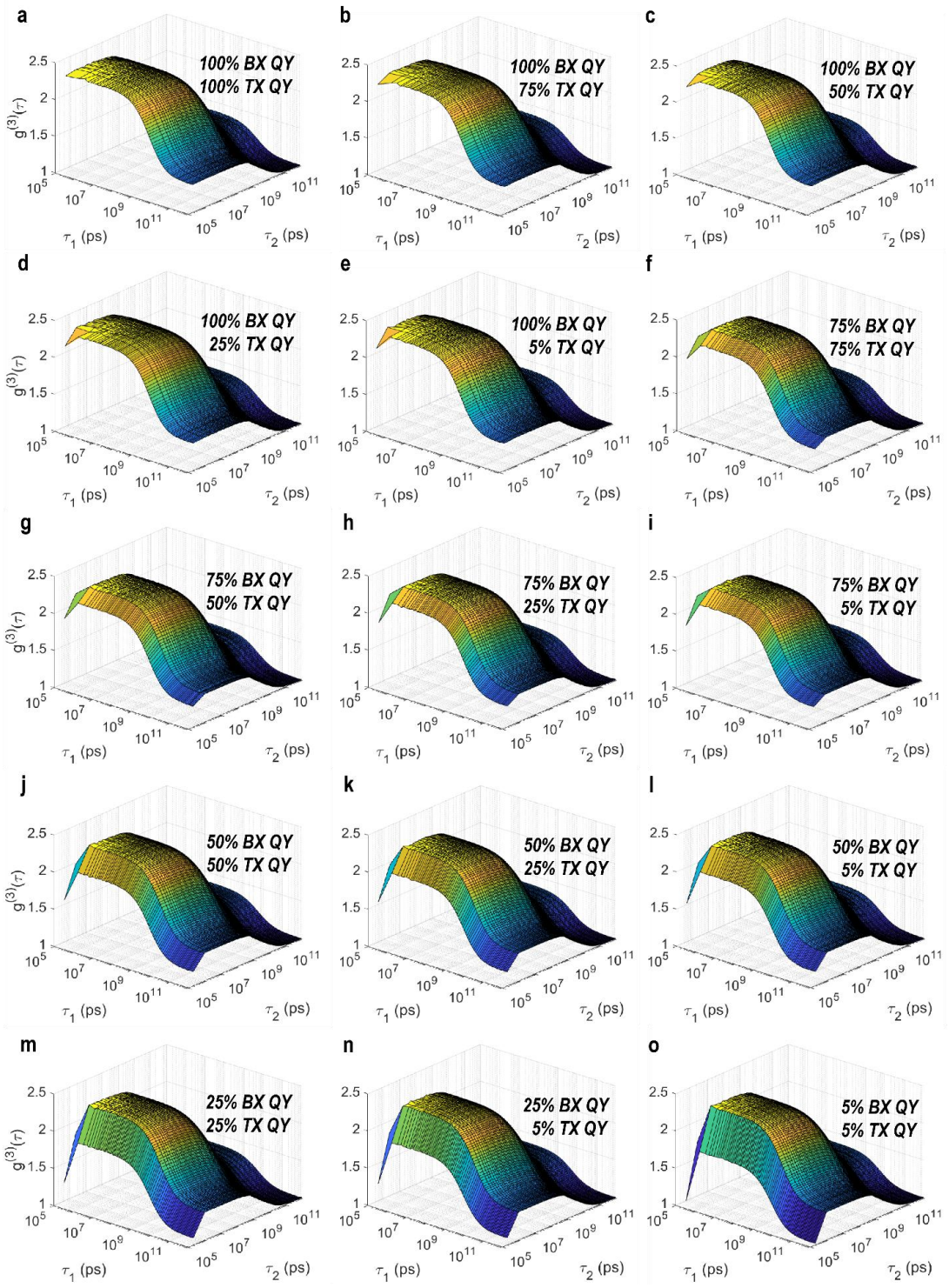


**Figure 4.9.** Monte Carlo Simulations of the 10,000 QDs diffusing in a $19\ \mu m \times 19\ \mu m \times 19\ \mu m$ box for 3600 seconds. The QDs have a 30 ns exciton lifetime, a 7.5 ns biexciton lifetime, and a 7.5 ns triexciton lifetime The exciton quantum yield was set to 100% for all experiments, and the BX/TXQYs varied depending on the experiment. The QDs were excited by a 1 MHz repetition laser at a 0.1 excitation density, and the focal volume shape was set such that $w_z = 3w_{xy}$. **a-o**. BX and TX quantum yields vary depending on the simulation, specified within the figure.

To test the $PNRL$ method and background subtraction, we simulated two potentially physical systems. The first one is a system where the statistical scaling of the triexciton is set to 1 compared to the exciton lifetime. This would occur in a system where the triexciton solely recombines through p-state emission (CITE). The second system has a statistical scaling factor of the triexciton set to 4 compared to the exciton lifetime. This would occur in a system where the triexciton solely recombines through s-state emission and behaves similarly to the biexciton. **Figure 4.10a** shows the system with a statistical scaling factor of 1 for the triexciton. We find that the method reasonably isolates the biexciton and triexciton emission from the background ensemble for the biexciton and triexciton lifetimes (**Figure 4.10b,c**). Similarly, **Figure 4.10d** shows the system with a statistical scaling factor of 4 for the triexciton. We find again that the method reasonably isolates the biexciton and triexciton lifetimes from the ensemble background (**Figure 4.10e,f**).

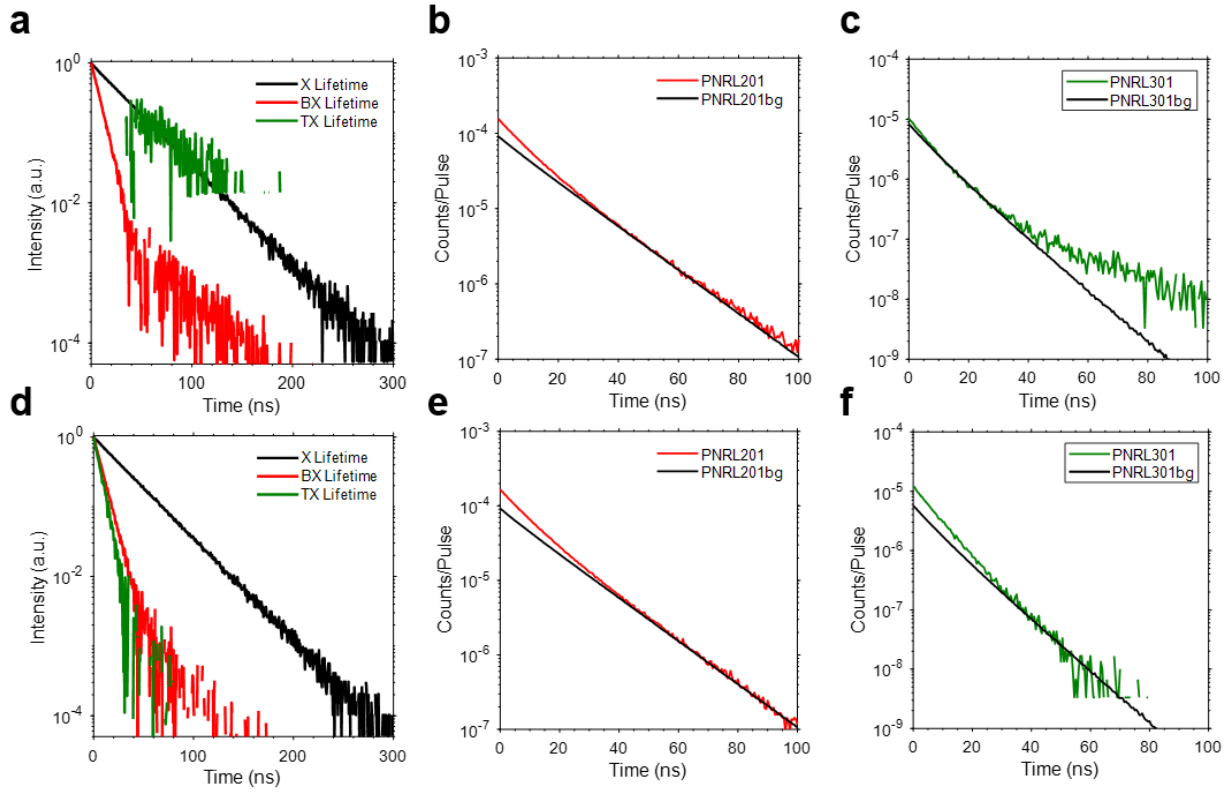


**Figure 4.10. a.** Exciton (black), biexciton (red), and triexciton lifetime extracted from the $PNRLs$ of a Monte Carlo simulated dataset where the triexciton lifetime was set to be equal to the exciton lifetime (statistical scaling = 1). **b.** $PNRL^{(2,0,1)}(\tau)$ and $PNRL_{bg}^{(2,0,1)}(\tau)$ calculated to determine the biexciton lifetime in **a**. **c.** $PNRL^{(3,0,1)}(\tau)$ and $PNRL_{bg}^{(3,0,1)}(\tau)$ calculated to determine the triexciton lifetime in **a**. **d.** Exciton (black), biexciton (red), and triexciton lifetime extracted from the $PNRLs$ of a Monte Carlo simulated dataset where the triexciton lifetime was set to be four times faster than the exciton lifetime (statistical scaling = 4). **c.** $PNRL^{(2,0,1)}(\tau)$ and $PNRL_{bg}^{(2,0,1)}(\tau)$ calculated to determine the biexciton lifetime in **d**. **f.** $PNRL^{(3,0,1)}(\tau)$ and $PNRL_{bg}^{(3,0,1)}(\tau)$ calculated to determine the triexciton lifetime in **d**.

Now that we have validated the merits of the triexciton lifetime and quantum yield analysis, we look at experimental ZnSe/ZnS NC data.

## 4.6. Measuring Average Triexciton Quantum Yield and Triexciton Lifetime of ZnSe/ZnS QDs

We perform the third-order cross-correlation method on a series of ZnSe/ZnS NC solution samples and find that the experimental data qualitatively resembles the simulated data (**Figure 4.11**). However, we are running into issues extracting the triexciton quantum yield using **Equation 4.46**. The correlations systematically have an abnormally low side peak relative to the center peak, indicating a potential issue in the analysis code or the experimental setup that will give rise to errors in the quantitative analysis. We plan to investigate this issue prior to publishing this data.

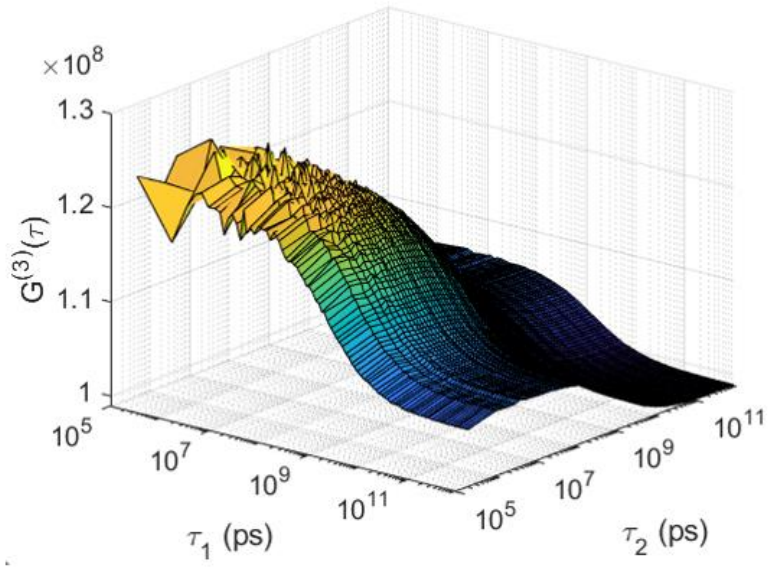


**Figure 4.11.** Experimental ZnSe/ZnS NC $g^{(3)}(\tau_1, \tau_2)$ from a series of solution measurements.

Additionally, we perform the $PNRL$ method on the ZnSe/ZnS NC solution samples and find the analysis gives rise to reasonable biexciton and triexciton lifetime in **Figure 4.12a**. The biexciton and triexciton lifetime are fit to monoexponential decay functions and are 2.4 ns and 1.8 ns, respectively (**Figure 4.12cd**). Meanwhile, the exciton lifetime is fit to a biexponential decay function and has lifetime parameters of 5.7 ns and 30.5 ns for $\tau_1$ and $\tau_2$, respectively with amplitudes of 0.8 and 0.2 for $A_1$ and $A_2$, respectively. Given the high biexciton quantum yield, the value of 2.4 ns seems reasonable given a statistical scaling factor of 4 for the biexciton lifetime. The slightly faster triexciton lifetime suggests the triexciton quantum

yield is slightly lower, potentially a result of the greater Auger recombination rate due to the greater exciton overlap when there are three excitons in the NC compared to two in the biexciton system.

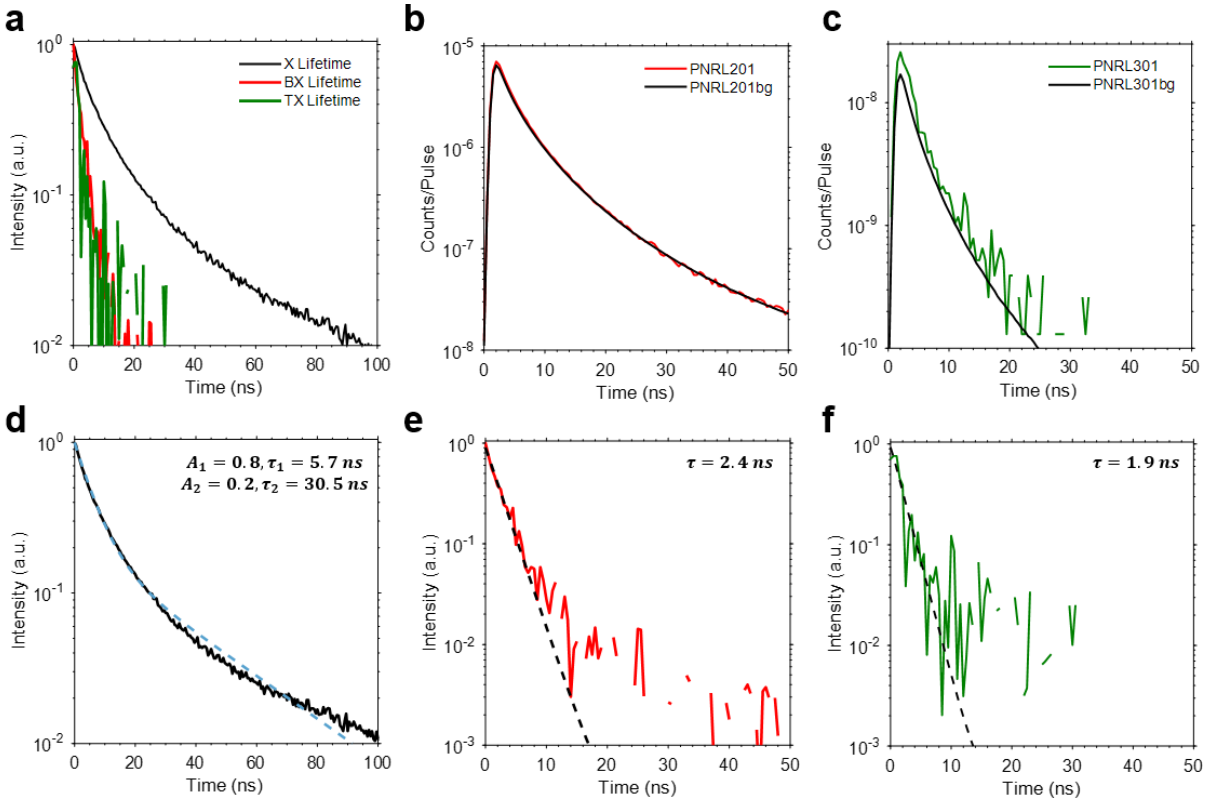


**Figure 4.12. a.** Exciton (black), biexciton (red), and triexciton lifetime extracted from the $PNRLs$ of a solution ZnSe/ZnS NC experimental dataset. **b.** $PNRL^{(2,0,1)}(\tau)$ and $PNRL_{bg}^{(2,0,1)}(\tau)$ calculated to determine the biexciton lifetime in **a**. **c.** $PNRL^{(3,0,1)}(\tau)$ and $PNRL_{bg}^{(3,0,1)}(\tau)$ calculated to determine the triexciton lifetime in **a**. **d.** Exciton lifetime (black) fit to a biexponential decay (dotted blue) with constants in the top right of the figure. **e.** Biexciton lifetime (red) fit to a monoexponential decay (dotted black) with the lifetime displayed in the top right of the figure. **f.** Triexciton lifetime (green) fit to a monoexponential decay (dotted black) with the lifetime displayed in the top right of the figure.

## 4.7. Conclusions

We have shown that colloidal ZnSe/ZnS NCs have a high biexciton quantum yield ratio of $86\% \pm 2\%$ in solution. This high biexciton quantum efficiency is amongst the highest in colloidal NC systems without intentional optimization of the NC structure for minimal Auger recombination, making these NCs promising candidates for high flux optical applications.

To begin to generalize the multiexciton behavior in these ZnSe/ZnS NCs, we developed a third-order cross-correlation technique and derived the necessary mathematical framework to quantify the average triexciton quantum yield ratio in solution. The derivation was validated by a series of Monte Carlo simulations.

Additionally, we extend the photon number resolved lifetime analytical method to measure the triexciton lifetime in solution, and validate the extension using Monte Carlo simulations. We show that the biexciton lifetime is 2.4 ns and the triexciton lifetime is 1.9 ns, suggesting the triexciton quantum yield ratio might be slightly lower than the biexciton quantum yield ratio. Regardless, we have shown that these ZnSe/ZnS NCs have high multiexciton efficiencies and should be incorporated into device structures for high flux optical applications.

The next step is to continue to process the third-order cross-correlations to quantify the average triexciton quantum yield ratio.

## 4.8. Acknowledgements

I want to thank Jonah Horowitz for completing this work with me. Working together at the beginning of Jonah's time during his PhD has been a blessing. It has been amazing to watch Jonah quickly catch on to the concepts, the experimental work, and the pace of research. It was amazing to get to work with you and I am thankful to call you a friend. I know you are going to continue developing into an amazing scientist and look forward to seeing your PhD defense in a few years.

I also want to acknowledge the help of a dear friend, Harry Bendekgey who has helped me develop the higher order correlation code. He has been integral to the advancement of the higher order correlation algorithm development.

We acknowledge the MIT SuperCloud and Lincoln Laboratory Supercomputing Center for providing HPC resources that have contributed to the research results reported within this paper/report.

# Chapter 5

# Future Directions

I will use this section to discuss two projects that I have explored in my PhD work, and wish I had more time to work on.

The first project is on developing a fourth-order correlation technique to resolve asymmetric line shape information with similar energy and time resolution as PCFS. I will expand on Andrew Beyler's Future Direction **Section 9.3** on this topic. I make amendments to the derivation and I show Monte Carlo simulation results that work towards achieving the correct results, but are not quite there yet.

The second project is a Monte Carlo photon correlation toolkit. I used Monte Carlo simulations in a lot of my work. I found them to be extremely helpful for gaining intuition of the photon correlations used in the Bawendi Lab. They were also helpful testing code, making sure there were no errors in my analysis before applying it to experimental data. I propose the development of a toolkit that would be made available to the public to make the photon correlation techniques we use in the Bawendi Lab more accessible around the world.

## 5.1. Resolving Asymmetric Line Shapes with High Time and Energy Resolution using Absolute Photon Energy Correlation Spectroscopy

### 5.1.1. Introduction

Photon-correlation Fourier spectroscopy (PCFS) is a powerful tool to gain insight into the energetic distribution of NC photon emission with greater time and energy resolution than a standard CCD-based spectrometer.[203] One drawback of the technique is its inability to determine asymmetric information in the emitter's PL spectrum. The spectral correlation will always be symmetric no matter the line shape $s(\omega)$. Andrew Beyler has a great, succinct explanation for why the spectral correlation is always symmetric in **Section 3.7** of his thesis.[81] To recap:

$$F[p(\zeta, \tau \to 0)]_\delta = F[s(\omega) \circ s(\omega)]_\delta \tag{5.1}$$

$$= F[s(\omega)]^*_\delta F[s(\omega)]_\delta \tag{5.2}$$

$$= |F[s(\omega)]_\delta|^2 \tag{5.3}$$

When we take the square root of a Fourier transform to isolate $s(\omega)$, we get the expression

$$s(\omega) = F^{-1}\left[(a(\delta) + b(\delta)i)\sqrt{F[p(\zeta, \tau \to 0)]_\delta}\right] \tag{5.4}$$

which is true spectral line shape for any real $a(\delta)$ and $b(\delta)$ that result in a physically reasonable line shape. Values for $a(\delta)$ and $b(\delta)$ must also satisfy $a(\delta)^2 + b(\delta)^2 = 1$. We lose all phase information in **Equation 5.3**. As a result, there are many spectral line shapes that can produce the same spectral correlation. This is a fundamental limit of using second-order correlations. When we use PCFS to probe photophysical properties of NC systems, we are careful to discuss the spectral information in relation to the *line width*, not the line shape. We can identify fine-structure splitting in NC systems at low temperature, but we do not have the insight on how each fine-structure state behaves. We have no ability to identify if one fine-structure state is more susceptible to spectral diffusion or another, or if one fine-structure state dominates the emission.

Andrew Beyler proposed in **Section 9.3** of his thesis a fourth-order correlation technique that is capable of resolving asymmetric information, and at the same time, maintain the high time and energy resolution of PCFS. Andrew Beyler referred to this technique as "Heterodyne-Detection Photon-Correlation Fourier Spectroscopy". I am going to refer to this technique as Absolute Photon Energy Correlation Spectroscopy (APECS). APECS requires the correlation of sample emission, similar to PCFS, but additionally requires the correlation of that sample emission with a reference light source with a known energy. For now, we will say that the known light source is the excitation laser.

**Figure 5.1a** shows the optical setup for APECS. A continuous wave laser reflects off a 90:10 beamsplitter (90% transmission, 10% reflection) to excite the NC sample. Typically, the laser light is filtered out of the optical setup, but we choose to keep it as the reference light source. Both the laser and sample light enter a 50:50 beamsplitter, splitting the path into two Michelson interferometers. Each Michelson interferometer has an independently controlled stage that can change the path length difference $\delta$. At the end of each Michelson interferometer are to single photon detectors, where one detector filters to accept only sample light and the other filters to accept only laser light. Overall, the single photon arrival times are recorded in four photon streams. Detector A and Detector C accept sample light and Detector B, and Detector D accept laser light.

Let's say we have a NC spectrum that is a asymmetric doublet with a fine-structure splitting of 0.6 meV (**Figure 5.1b**). We can excite the NC sample with a laser that is 0.5 meV away from the higher energy fine-structure state, and send the collective light through the APECS setup in **Figure 5.1a.** We can correlate the laser light with the sample light twice. Once at the first Michelson interferometer and another time at the second Michelson interferometer. These isolated correlations are effectively the spectral correlation that we observe in a PCFS experiment. However, since the system involves two interacting Michelson interferometers, we can also correlate these two spectral correlations – a product of two correlations. We refer to this two-dimensional spectral correlation as the APECS spectrum (**Figure 5.1c**), where we can see

the asymmetric information of the spectrum in the third quadrant of the figure. The energy values correspond to the energy difference between the fine-structure state and the reference laser light. Since we know the energy of the laser, we can simply add that value to **Figure 5.1c** to determine the absolute energy of the spectrum. In a PCFS or APECS experiment, we cannot directly measure the spectral correlation or the APECS spectrum, but the interferogram. We can take the double cosine transform of the APECS spectrum to visualize how the APECS interferogram looks (**Figure 5.1d**). We can see the APECS interferogram has a complex oscillatory motion in both dimensions, and decays according to the coherence time (or line width) of the NC emission.

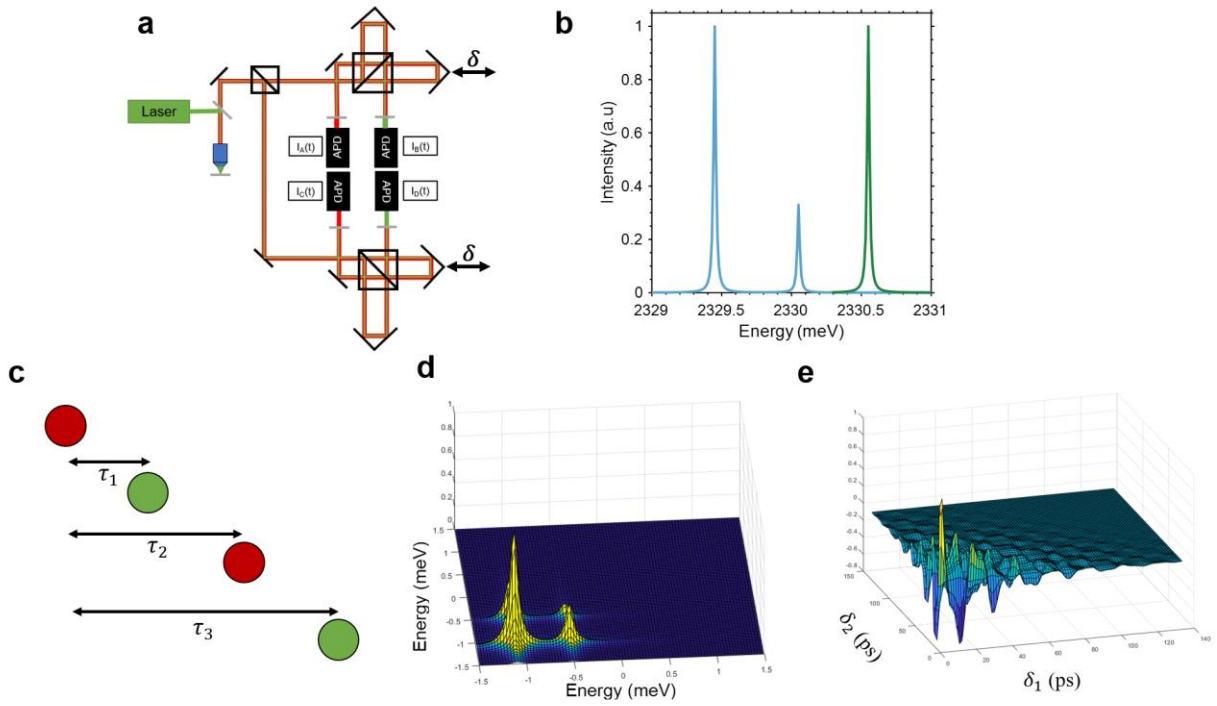


**Figure 5.1.** APECS optical setup. **b.** Asymmetric doublet NC sample spectrum (blue) and reference laser spectrum (green). **c**. Fourth-order cross-correlation is constructed by the photon time differences of the photons at Channel A with photons at Channel B ($\tau_1$), Channel C ($\tau_2$), and Channel D ($\tau_3$) **d.** Theoretical APECS interferogram of the system in **b. e.** Theoretical APECS spectral correlation displaying asymmetric doublet spectrum.

The goal of this project is to develop the mathematical framework to measure the APECS spectrum. Additionally, I sought to validate the APECS derivation by developing a Monte Carlo model that simulates this experiment to reproduce **Figure 5.1d,e**.

### 5.1.2. Derivation

We will begin by restating **Equations**. (**9.36-9.40**) of Andrew Beyler's (AB's) thesis. We have 2 laser channels and 2 sample channels whose intensity is given by

$$I_A(\delta_1(t), t) = I(t)(1 + F_{cos}[s(\omega, t)]_{\delta_1(t)}) \tag{5.1}$$

$$I_B(\delta_1(t), t) = I_L(t)\big(1 - \cos\big(\omega_L \delta_1(t)\big)\big) \tag{5.2}$$

$$I_C(\delta_2(t), t) = I(t)(1 + F_{cos}[s(\omega, t)]_{\delta_2(t)}) \tag{5.3}$$

$$I_D(\delta_2(t), t) = I_L(t)\big(1 - \cos\big(\omega_L \delta_2(t)\big)\big) \tag{5.4}$$

where $I(t)$ is the total intensity of the sample signal, $I_L(t)$is the total intensity of the laser signal, $s(\omega, t)$ is the normalized sample spectrum, and $\omega_L$ is the laser energy.

We then want to operate on the fourth-order cross-correlation function

$$\begin{aligned} &g^{(4)}_{ABCD}(\delta_{01}, \delta_{02}, \tau_1, \tau_2, \tau_3) \\ &= \frac{\langle I_A(\delta_1(t), t)\, I_B(\delta_1(t+\tau_1), t+\tau_1)\, I_C(\delta_2(t+\tau_2), t+\tau_2)\, I_D(\delta_2(t+\tau_3), t+\tau_3)\rangle}{\langle I_A(\delta_1(t), t)\rangle\langle\, I_B(\delta_1(t+\tau_1), t+\tau_1)\rangle\langle\, I_C(\delta_2(t+\tau_2), t+\tau_2)\rangle\langle\, I_D(\delta_2(t+\tau_3), t+\tau_3)\rangle} \end{aligned} \tag{5.5}$$

Assuming the spectral and intensity fluctuations are independent, we can expand each intensity and separate out terms, writing

$$\begin{aligned} &g^{(4)}_{ABCD}(\delta_{01}, \delta_{02}, \tau_1, \tau_2, \tau_3) \\ &= \frac{\langle I(t)\, I_L(t+\tau_1)\, I(t+\tau_2) I_L(t+\tau_3)\rangle}{\langle I(t)\rangle\langle I_L(t+\tau_1)\rangle\langle I(t+\tau_2)\rangle\langle I_L(t+\tau_3)\rangle} \\ &\times \frac{\langle\big(1 + F_{cos}[s(\omega, t)]_{\delta_1(t)}\big)\big(1 - \cos\big(\omega_L \delta_1(t)\big)\big)\big(1 + F_{cos}[s(\omega, t)]_{\delta_1(t)}\big)\big(1 - \cos\big(\omega_L \delta_2(t)\big)\big)\rangle}{\langle 1 + F_{cos}[s(\omega, t)]_{\delta_1(t)}\rangle\langle 1 - \cos\big(\omega_L \delta_1(t)\big)\rangle\langle 1 + F_{cos}[s(\omega, t)]_{\delta_1(t)}\rangle\langle 1 - \cos\big(\omega_L \delta_2(t)\big)\rangle} \end{aligned} \tag{5.6}$$

AB's thesis notes that the "time-dependence of the path-length difference, given by the dither form… has been chosen to average equally over the interference fringes of the time-averaged spectrum." This is equivalent to saying

$$\langle I_A(t)\rangle = \langle I_C(t)\rangle = \langle I(t)\rangle \tag{5.7}$$

$$\langle I_B(t)\rangle = \langle I_D(t)\rangle = \langle I_L(t)\rangle \tag{5.8}$$

Which is a clearly desirable property for our choice of dither.

Assuming the laser intensity does not drift over time, we can cancel it out as a constant, noting the intensity term in **Equation 5.6** is simply the second-order auto-correlation of the sample $g^{(2)}(\tau_2)$. Expanding the numerator of **Equation 5.6**, we obtain **Equation 9.44** of AB's thesis.

$$\begin{aligned} &g^{(4)}_{ABCD}(\delta_{01}, \delta_{02}, \tau_1, \tau_2, \tau_3) = \\ &\quad g^{(2)}(\tau_2)\,\langle 1 - \cos\big(\omega_L \delta(t+\tau_1)\big)\, F_{cos}[s(\omega, t)]_{\delta_1(t)} + F_{cos}[s(\omega, t)]_{\delta_1(t)} F_{cos}[s(\omega, t+\tau_2)]_{\delta_2(t+\tau_2)} \end{aligned} \tag{5.9}$$

$$
\begin{aligned}
&-\cos\left(\omega_L\delta_2(t+\tau_3)\right)F_{cos}[s(\omega,t)]_{\delta_1(t)}-\cos\left(w_L\delta_1(t+\tau_1)\right)F_{cos}[s(\omega,t+\tau_2)]_{\delta_2(t+\tau_2)}\\
&+\cos\left(\omega_L\delta_1(t+\tau_1)\right)\cos\left(\omega_L\delta_2(t+\tau_3)\right)-\cos\left(\omega_L\delta_2(t+\tau_3)\right)F_{cos}[s(\omega,t)]_{\delta_2(t+\tau_2)}\\
&+\cos\left(\omega_L\delta_1(t+\tau_1)\right)\cos\left(\omega_L\delta_2(t+\tau_3)\right)F_{cos}[s(\omega,t)]_{\delta_1(t)}F_{cos}[s(\omega,t+\tau_2)]_{\delta_2(t+\tau_2)}\rangle
\end{aligned}
$$

Note that the expression is missing all terms in the expansion of **Equation 5.6** which contain an odd number of spectral products. Based on the discussion in **Equations 5.7** and **5.8**, and if we assume spectral fluctuations are independent of intensity fluctuations, it is clear why terms with a single Fourier transform average to 0, e.g.

$$
\langle F_{cos}[s(\omega,t)]_{\delta_1(t)}\rangle=0 \tag{5.10}
$$

However, it is less clear on what assumption is required to ensure that third-order terms average to 0, e.g.

$$
\langle F_{cos}[s(\omega,t)]_{\delta_1(t)}\cos\left(\omega_L\delta_1(t+\tau_1)\right)\ F_{cos}\left[s(\omega,t+\tau_2)\right]_{\delta_2(t+\tau_2)}\rangle=0 \tag{5.11}
$$

For now, we will assume that we **<u>cannot</u>** say third-order terms go to zero. We incorporate third order terms into **Equation 5.9**,

$$
\begin{aligned}
&g^{(4)}_{ABCD}(\delta_{01},\delta_{02},\tau_1,\tau_2,\tau_3)=\\
&\quad g^{(2)}(\tau_2)\,\langle 1-F_{cos}[s(\omega,t)]_{\delta_1(t)}\cos\left(\omega_L\delta(t+\tau_1)\right)+F_{cos}[s(\omega,t)]_{\delta_1(t)}F_{cos}[s(\omega,t+\tau_2)]_{\delta_2(t+\tau_2)}\\
&\qquad -F_{cos}[s(\omega,t)]_{\delta_1(t)}\cos\left(\omega_L\delta_2(t+\tau_3)\right)-F_{cos}[s(\omega,t+\tau_2)]_{\delta_2(t+\tau_2)}\cos\left(\omega_L\delta_1(t+\tau_1)\right)\\
&\qquad +\cos\left(w_L\delta_1(t+\tau_1)\right)\cos\left(\omega_L\delta_2(t+\tau_3)\right)-F_{cos}[s(\omega,t+\tau_2)]_{\delta_2(t+\tau_2)}\cos\left(\omega_L\delta_2(t+\tau_3)\right)\\
&\qquad\qquad -F_{cos}[s(\omega,t)]_{\delta_1(t)}F_{cos}[s(\omega,t+\tau_2)]_{\delta_2(t+\tau_2)}\cos\left(\omega_L\delta_1(t+\tau_1)\right)\\
&\qquad\qquad -F_{cos}[s(\omega,t)]_{\delta_1(t)}F_{cos}[s(\omega,t+\tau_2)]_{\delta_2(t+\tau_2)}\cos\left(\omega_L\delta_2(t+\tau_3)\right)\\
&\qquad\qquad +F_{cos}[s(\omega,t)]_{\delta_1(t)}\cos\left(\omega_L\delta_1(t+\tau_1)\right)\cos\left(\omega_L\delta_2(t+\tau_3)\right)\\
&\qquad\qquad +F_{cos}[s(\omega,t+\tau_2)]_{\delta_2(t+\tau_2)}\cos\left(\omega_L\delta_1(t+\tau_1)\right)\cos\left(\omega_L\delta_2(t+\tau_3)\right)\\
&\qquad +\cos\left(\omega_L\delta_1(t+\tau_1)\right)\cos\left(\omega_L\delta_2(t+\tau_3)\right)F_{cos}[s(\omega,t)]_{\delta_1(t)}F_{cos}[s(\omega,t+\tau_2)]_{\delta_2(t+\tau_2)}\rangle
\end{aligned} \tag{5.12}
$$

We can re-transform each second-order product back into correlations through a similar process used in Section 3.1. of AB's thesis. To walk through 2 examples:

$$
g^{(2)}_{AB}(\delta_{01},\tau_1)=\frac{\langle I_A(t)I_B(t+\tau_1)\rangle}{\langle I_A(t)\rangle\langle I_B(t+\tau_1)\rangle} \tag{5.13}
$$

$$= \frac{\langle I(t)\rangle\langle I_L(t+\tau_1))\rangle\langle\left(1+F_{cos}[s(\omega,t)]_{\delta_1(t)}\right)\left(1-\cos\left(\omega_L\delta_1(t+\tau_1)\right)\right)\rangle}{\langle I(t)\rangle\langle I_L(t+\tau_1))\rangle\langle\left(1+F_{cos}[s(\omega,t)]_{\delta_1(t)}\right)\rangle\langle\left(1-\cos\left(\omega_L\delta_1(t+\tau_1)\right)\right)\rangle}$$

$$= \langle\left(1+F_{cos}[s(\omega,t)]_{\delta_1(t)}\right)\left(1-\cos\left(\omega_L\delta_1(t+\tau_1)\right)\right)\rangle$$

$$= 1-\langle F_{cos}[s(\omega,t)]_{\delta_1(t)}\cos\left(\omega_L\delta_1(t+\tau_1)\right)\rangle$$

Thus, we can replace

$$-\langle F_{cos}[s(\omega,t)]_{\delta_1(t)}\cos\left(\omega_L\delta_1(t+\tau_1)\right)\rangle \tag{5.14}$$

In **Equation 5.12** with

$$g^{(2)}_{AB}(\delta_{01},\tau_1)-1 \tag{5.15}$$

We can do a similar transformation to a positive term, e.g.

$$g^{(2)}_{BD}(\delta_{01},\delta_{02},\tau_3-\tau_1) = \frac{\langle I_B(t+\tau_1)I_D(t+\tau_3)\rangle}{\langle I_B(t+\tau_1)\rangle\langle I_D(t+\tau_3)\rangle}$$

$$= \frac{\langle I(t+\tau_1)\rangle\langle I_L(t+\tau_3))\rangle\langle\left(1-\cos\left(\omega_L\delta_1(t+\tau_1)\right)\right)\left(1-\cos\left(\omega_L\delta_2(t+\tau_3)\right)\right)\rangle}{\langle I(t+\tau_1)\rangle\langle I_L(t+\tau_3))\rangle\langle\left(1-\cos\left(\omega_L\delta_1(t+\tau_1)\right)\right)\rangle\langle\left(1-\cos\left(\omega_L\delta_2(t+\tau_3)\right)\right)\rangle}$$

$$= \langle\left(1-\cos\left(\omega_L\delta_1(t+\tau_1)\right)\right)\left(1-\cos\left(\omega_L\delta_2(t+\tau_3)\right)\right)\rangle$$

$$g^{(2)}_{BD}(\delta_{01},\delta_{02},\tau_3-\tau_1) = 1+\langle\cos\left(\omega_L\delta_1(t+\tau_1)\right)\cos\left(\omega_L\delta_2(t+\tau_3)\right)\rangle \tag{5.16}$$

Thus, we can similarly replace the product of cosines with $g^{(2)}_{BD}(\delta_{01},\delta_{02},\tau_3-\tau_1)-1$.

We can do similar transformations to the third-order products. For instance,

$$g^{(3)}_{ABC}(\delta_{01},\delta_{02},\tau_1,\tau_2) = \frac{\langle I_A(t)I_B(t+\tau_1)I_C(t+\tau_2)\rangle}{\langle I_A(t)\rangle\langle I_B(t+\tau_1)\rangle\langle I_C(t+\tau_2)\rangle}$$

$$= \frac{\langle I_L(t+\tau_1))\rangle\langle I(t)I(t+\tau_2))\rangle}{\langle I(t)\rangle\langle I_L(t+\tau_1))\rangle\langle I(t+\tau_2)\rangle} \tag{5.17}$$

$$\times \frac{\langle \left(1 + F_{cos}[s(\omega,t)]_{\delta_1(t)}\right)\left(1 - \cos\left(\omega_L \delta_1(t+\tau_1)\right)\right)\left(1 + F_{cos}[s(\omega,t+\tau_2)]_{\delta_2(t+\tau_2)}\right)\rangle}{\langle \left(1 + F_{cos}[s(\omega,t)]_{\delta_1(t)}\right)\rangle\langle \left(1 - \cos\left(\omega_L \delta_1(t+\tau_1)\right)\right)\rangle\langle \left(1 + F_{cos}[s(\omega,t+\tau_2)]_{\delta_2(t+\tau_2)}\right)\rangle}$$

$$= \frac{\langle I(t)I(t+\tau_2))\rangle}{\langle I(t)\rangle\langle I(t+\tau_2)\rangle}\left(1 + \left\langle F_{cos}[s(\omega,t)]_{\delta_1(t)} F_{cos}[s(\omega,t+\tau_2)]_{\delta_2(t+\tau_2)}\right.\right.$$
$$- F_{cos}[s(\omega,t)]_{\delta_1(t)} \cos\left(\omega_L \delta_1(t+\tau_1)\right) - F_{cos}[s(\omega,t+\tau_2)]_{\delta_2(t+\tau_2)} \cos\left(\omega_L \delta_1(t+\tau_1)\right)$$
$$\left.\left. - F_{cos}[s(\omega,t)]_{\delta_1(t)} F_{cos}[s(\omega,t+\tau_2)]_{\delta_2(t+\tau_2)} \cos\left(\omega_L \delta_1(t+\tau_1)\right)\right\rangle\right)$$

We recall from earlier transformations that we can rephrase second-order products in terms of various second-order cross-correlations

$$\langle F_{cos}[s(\omega,t)]_{\delta_1(t)} F_{cos}[s(\omega,t+\tau_2)]_{\delta_2(t+\tau_2)}\rangle = \frac{g_{AC}^{(2)}(\delta_{01},\delta_{02},\tau_2)}{g^{(2)}(\tau_2)} - 1 \tag{5.18}$$

$$\langle F_{cos}[s(\omega,t)]_{\delta_1(t)} \cos\left(\omega_L \delta_1(t+\tau_1)\right)\rangle = 1 - g_{AB}^{(2)}(\delta_{01},\tau_1) \tag{5.19}$$

$$\langle F_{cos}[s(\omega,t+\tau_2)]_{\delta_2(t+\tau_2)} \cos\left(\omega_L \delta_1(t+\tau_1)\right)\rangle = 1 - g_{BC}^{(2)}(\delta_{01},\delta_{02},\tau_2-\tau_1) \tag{5.20}$$

Inserting **Equations 5.18-5.20** into **Equation 5.17**, we get

$$g_{ABC}^{(3)}(\delta_{01},\delta_{02},\tau_1,\tau_2)$$
$$= g^{(2)}(\tau_2)\left(-2 + g_{AB}^{(2)}(\delta_{01},\tau_1) + \frac{g_{AC}^{(2)}(\delta_{01},\delta_{02},\tau_2)}{g^{(2)}(\tau_2)} + g_{BC}^{(2)}(\delta_{01},\delta_{02},\tau_2-\tau_1) - \langle T.O.T_{ABC}\rangle\right) \tag{5.21}$$

where

$$\langle T.O.T_{ABC}\rangle = \langle F_{cos}[s(\omega,t)]_{\delta_1(t)} F_{cos}[s(\omega,t+\tau_2)]_{\delta_2(t+\tau_2)} \cos\left(\omega_L \delta_1(t+\tau_1)\right)\rangle \tag{5.22}$$

Isolating for the third-order term $T.O.T_{ABC}$

$$T.O.T_{ABC} = -\frac{g_{ABC}^{(3)}(\delta_{01},\delta_{02},\tau_1,\tau_2)}{g^{(2)}(\tau_2)} + g_{AB}^{(2)}(\delta_{01},\tau_1) + \frac{g_{AC}^{(2)}(\delta_{01},\delta_{02},\tau_2)}{g^{(2)}(\tau_2)} + g_{BC}^{(2)}(\delta_{01},\delta_{02},\tau_2-\tau_1) - 2 \tag{5.23}$$

Similarly,

$$T.O.T_{ABD} = g_{ABD}^{(3)}(\delta_{01},\delta_{02},\tau_1,\tau_3) - g_{AB}^{(2)}(\delta_{01},\tau_1) - g_{AD}^{(2)}(\delta_{01},\delta_{02},\tau_3) - g_{BD}^{(2)}(\delta_{01},\delta_{02},\tau_3-\tau_1) + 2 \tag{5.24}$$

$$T.O.T_{ACD} = -\frac{g^{(3)}_{ACD}(\delta_{01},\delta_{02},\tau_1,\tau_2)}{g^{(2)}(\tau_2)} + \frac{g^{(2)}_{AC}(\delta_{01},\delta_{02},\tau_2)}{g^{(2)}(\tau_2)} + g^{(2)}_{AD}(\delta_{01},\delta_{02},\tau_3) + g^{(2)}_{CD}(\delta_{02},\tau_3-\tau_2) - 2 \quad (5.25)$$

$$T.O.T_{BCD} = g^{(3)}_{BCD}(\delta_{01},\delta_{02},\tau_1,\tau_2) - g^{(2)}_{BD}(\delta_{01},\delta_{02},\tau_3-\tau_1) - g^{(2)}_{BC}(\delta_{01},\delta_{02},\tau_2-\tau_1) - g^{(2)}_{CD}(\delta_{02},\tau_3-\tau_2) + 2 \quad (5.26)$$

Putting transformation of second-order and third-order products into **Equation 5.12.4**, we obtain

$$\begin{aligned} & g^{(4)}_{ABCD}(\delta_{01},\delta_{02},\tau_1,\tau_2,\tau_3) \\ & = g^{(2)}(\tau_2)\Bigg\langle F.O.T_{ABCD} + \frac{g^{(3)}_{ABC}(\delta_{01},\delta_{02},\tau_1,\tau_2)}{g^{(2)}(\tau_2)} + \frac{g^{(3)}_{ACD}(\delta_{01},\delta_{02},\tau_1,\tau_2)}{g^{(2)}(\tau_2)} + g^{(3)}_{ABD}(\delta_{01},\delta_{02},\tau_1,\tau_3) \\ & \quad + g^{(3)}_{BCD}(\delta_{01},\delta_{02},\tau_1,\tau_2) - g^{(2)}_{AB}(\delta_{01},\tau_1) - \frac{g^{(2)}_{AC}(\delta_{01},\delta_{02},\tau_2)}{g^{(2)}(\tau_2)} - g^{(2)}_{AD}(\delta_{01},\delta_{02},\tau_3) \\ & \quad - g^{(2)}_{BC}(\delta_{01},\delta_{02},\tau_2-\tau_1) - g^{(2)}_{BD}(\delta_{01},\delta_{02},\tau_3-\tau_1) - g^{(2)}_{CD}(\delta_{02},\tau_3-\tau_2) + 3\Bigg\rangle \end{aligned} \quad (5.27)$$

Note that this result differs from **Equation 9.45** in AB's thesis in three ways: we have included third-order cross-correlations, all signs are negative on the second-order cross correlations, and the constant at the end is a 3 instead of a 1.

Now we want to simplify the fourth-order term $F.O.T_{ABCD}$, which we write

$$\begin{aligned} F.O.T_{ABCD} = & \langle F_{cos}[L(\omega_L-\omega)]_{\delta_1(t+\tau_1)} F_{cos}[s(\omega,t)]_{\delta_1(t)}\rangle \\ & \times \langle F_{cos}[L(\omega_L-\omega)]_{\delta_2(t+\tau_3)} F_{cos}[s(\omega,t+\tau_2)]_{\delta_2(t+\tau_2)}\rangle \end{aligned} \quad (5.28)$$

This is a simple restatement of **Equation 9.46** of AB's thesis. The cosine transform of cosine terms are rephrased as cosine transforms of Dirac delta functions $L(\omega_L-\omega)$. AB notes that the synchronized dither of the two stages force the dependence between the correlation terms in **Equation 5.28**. We operate on each pair of terms as in **Chapter 3** (al la **Equation 3.30**) of AB's thesis.

$$\begin{aligned} F.O.T_{ABCD} = & \Bigg\langle \frac{1}{2}\Bigg( F_{cos}\left[\int_{-\infty}^{\infty} L(\omega_L-\omega)s(\omega+\zeta,t)\cos\big(\omega x(t)-(\omega+\zeta)x(t+\tau_1)\big)\,d\omega\right]_{\delta_{01}} \\ & + F_{cos}\left[\int_{-\infty}^{\infty} L(\omega_L-\omega)s(\omega-\zeta,t)\cos\big(\omega x(t)+(\omega-\zeta)x(t+\tau_1)\big)\,d\omega\right]_{\delta_{01}} \\ & + F_{sin}\left[\int_{-\infty}^{\infty} L(\omega_L-\omega)s(\omega+\zeta,t)\sin\big(\omega x(t)-(\omega+\zeta)x(t+\tau_1)\big)\,d\omega\right]_{\delta_{01}} \\ & - F_{sin}\left[\int_{-\infty}^{\infty} L(\omega_L-\omega)s(\omega-\zeta,t)\sin\big(\omega x(t)+(\omega-\zeta)x(t+\tau_1)\big)\,d\omega\right]_{\delta_{01}}\Bigg) \end{aligned} \quad (5.29)$$

$$\times \frac{1}{2}\Bigg(F_{cos}\left[\int_{-\infty}^{\infty} L(\omega_L-\omega)s(\omega+\zeta,t+\tau_2)\cos\big(\omega x(t+\tau_2)-(\omega+\zeta)x(t+\tau_3)\big)\,d\omega\right]_{\delta_{02}}$$
$$+F_{cos}\left[\int_{-\infty}^{\infty} L(\omega_L-\omega)s(\omega-\zeta,t+\tau_2)\cos\big(\omega x(t+\tau_2)+(\omega-\zeta)x(t+\tau_3)\big)\,d\omega\right]_{\delta_{02}}$$
$$+F_{sin}\left[\int_{-\infty}^{\infty} L(\omega_L-\omega)s(\omega+\zeta,t+\tau_2)\sin\big(\omega x(t+\tau_2)-(\omega+\zeta)x(t+\tau_3)\big)\,d\omega\right]_{\delta_{02}}$$
$$-F_{sin}\left[\int_{-\infty}^{\infty} L(\omega_L-\omega)s(\omega-\zeta,t+\tau_2)\sin\big(\omega x(t+\tau_2)+(\omega-\zeta)x(t+\tau_3)\big)\,d\omega\right]_{\delta_{02}}\Bigg)\Bigg\rangle$$

Every odd line contains the spectral correlation terms that we're interested in, and the even lines describe spectral convolutions.

The next steps are not fully clear to me. The next step is to distribute the time average to each term in the sum; unfortunately, we cannot do that here. The outer-most operation in this time average is a product, and we cannot pass the average through it. This differs from the regime in **Chapter 3** in AB's thesis, where we are operating on a single pair of spectral terms, not four.

**Equation 9.47** of AB's thesis claims that the convolution terms are dithered away, but it seems to me additional assumptions are necessary for that to be the case, as we cannot apply the results of **Chapter 3** of AB's thesis directly. What ensures that *products of convolution terms with correlation terms/other convolution terms* time average to 0?

Assuming we do get to drop these terms, we obtain the fourth-order spectral correlation term

$$F.O.T_{ABCD}=\Bigg\langle\frac{1}{2}\Bigg(F_{cos}\left[\int_{-\infty}^{\infty} L(\omega_L-\omega)s(\omega+\zeta,t)\cos\big(\omega x(t)-(\omega+\zeta)x(t+\tau_1)\big)\,d\omega\right]_{\delta_{01}}$$
$$+F_{sin}\left[\int_{-\infty}^{\infty} L(\omega_L-\omega)s(\omega+\zeta,t)\sin\big(\omega x(t)-(\omega+\zeta)x(t+\tau_1)\big)\,d\omega\right]_{\delta_{01}}\Bigg)$$
$$\times \frac{1}{2}\Bigg(F_{cos}\left[\int_{-\infty}^{\infty} L(\omega_L-\omega)s(\omega+\zeta,t+\tau_2)\cos\big(\omega x(t+\tau_2)-(\omega+\zeta)x(t+\tau_3)\big)\,d\omega\right]_{\delta_{02}}$$
$$+F_{sin}\left[\int_{-\infty}^{\infty} L(\omega_L-\omega)s(\omega+\zeta,t+\tau_2)\sin\big(\omega x(t+\tau_2)-(\omega+\zeta)x(t+\tau_3)\big)\,d\omega\right]_{\delta_{02}}\Bigg)\Bigg\rangle \tag{5.30}$$

The derivation then argues that the cosine terms reduce to unity and sine terms vanish as they do in **Section 3.2.2** of AB's thesis. However, this is achieved in **Section 3.2.2** by pulling in the time average (and then using the independence of intensity and spectral fluctuations to have low-level time averages of

*only* cosine and sine terms). Similar to how the convolutions are discarded, I am confused by the applicability of these assumptions. If we do drop those terms, we obtain

$$\begin{aligned} F.O.T_{ABCD} &= \left\langle \frac{1}{2}\left( F_{cos}\left[\int_{-\infty}^{\infty} L(\omega_L-\omega)s(\omega+\zeta,t)d\omega\right]_{\delta_{01}}\right.\right. \\ &\qquad \left.\left. \times F_{cos}\left[\int_{-\infty}^{\infty} L(\omega_L-\omega)s(\omega+\zeta,t+\tau_2)d\omega\right]_{\delta_{02}}\right)\right\rangle \\ &= \left\langle \frac{1}{2} F_{cos}\left[L(\omega_L-\omega)\circ s(\omega,t)\right]_{\delta_{01}} F_{cos}\left[L(\omega_L-\omega)\circ s(\omega,t+\tau_2)\right]_{\delta_{02}}\right. \\ &= \int_{-\infty}^{\infty}\int_{-\infty}^{\infty} \langle p_L(\zeta_1,t)p_L(\zeta_2,t+\tau_2)\rangle \cos(\zeta_1\delta_{01})\cos(\zeta_2\delta_{02})\, d\zeta_1 d\zeta_2 \end{aligned} \tag{5.31}$$

where $p_L(\zeta_1,t)$ represents the spectral correlation of each sample photon on Detector A with laser photons on Detector B, $p_L(\zeta_2,t+\tau_2)$ represents the spectral correlation of each signal photon on Detector C with laser photons on channel D, for all signal photons that arrived $\tau_2$ *after* the corresponding count on Detector A. **Equation 5.31** is the double cosine transform of the APECS spectrum

$$p_{APECS}(\zeta_1,\zeta_2,\tau_2) = p_L(\zeta_1,t)p_L(\zeta_2,t+\tau_2) \tag{5.32}$$

which is the probability distribution function for a pair of sample photons with temporal spacing $\tau_2$. The energy difference $\zeta_1$ is the energy difference between the first photon and the laser photon, and $\zeta_1$ is the energy difference between the second photon and the laser photon. The APECS spectrum is two-dimensional and provides us with absolute energy information on timescales down to reasonable signal to noise in the correlations at $\tau_2$.

The heavy lifting of the mathematical framework was completed by Andrew Beyler, with some minor tweaks and comments added in this section. The next step is to verify the derivation is correct. Before we jump straight to building the setup in the Bawendi Lab, we can simulate a NC system and hopefully gain insights and intuition for how this technique should be built and what kind of interesting physical questions we can probe with this technique.

### 5.1.3. APECS Monte Carlo Simulations

Monte Carlo (MC) simulations of the APECS experiment is developed through four steps: (1) generation of photon stream of sample and laser photons, (2) energy assignments for each photon in the

photon stream, (3) determining which detector each photon arrives at, and (4) performing the fourth-order cross-correlation analysis on simulated photon streams.

The APECS experiment consists of a series of short photon streams. The number of photon streams is determined by the number of stage positions in the experiment, and the photon stream length is determined by the number of seconds set per stage position.

#### *5.1.3.1. Photon Stream Generation*

APECS MC simulations begin by simulating the photon stream arrival times. Inputs for photon stream time generate are laser power, absorption probability, NC quantum yield, NC lifetime, and number of seconds per stage position. The laser photon times are generated by a random flat distribution with an intensity determined by the laser power. Next, a random number is generated for each laser photon time and referenced off of the absorption probability to determine if the laser photon resulted in a successful NC absorption. Then, a random number is generated for each successful absorption event and referenced off of the NC quantum yield to determine if the successful absorption results in the emission of a sample photon. If an emission event is successful, the emission time is set by randomly generating the lifetime of the NC exciton, shifting the emission time such that the emission time is equal to the excitation time plus the lifetime. A photon stream containing laser photons and sample photons is generated for each stage position in the APECS experiment. A filter is applied to the laser photon stream to set the laser photon stream approximately to the same length as the sample photon stream. This is simply to reduce the computational time. In theory, a large laser photon stream is beneficial for signal to noise reasons.

#### *5.1.3.2. Photon Stream Energy Assignments – Asymmetric Doublet*

The next step in the APECS MC simulations is to assign a photon energy to each photon such that we have a Lorentzian laser spectrum and an asymmetric doublet sample spectrum that is comprised of two Lorentzian spectra (**Figure 5.1b**). For the laser spectrum, we randomly generate Lorentzian numbers centered around 2330.52994 meV (532 nm) for each laser photon with a narrow line width. For the sample spectrum, we randomly generate a number for each sample photon to determine which fine-structure state it emits from. Similar to the laser spectrum, we then generate Lorentzian numbers centered around its fine-structure state energy.

#### *5.1.3.3. Detector Determination*

The last step in generating the photon streams for the four single photon detectors is to determine the path of each photon through the optical setup (**Figure 5.1a**). To start, we generate random numbers for each photon (laser and sample photon) to determine which Michelson interferometer the photon travels to (50/50 probability). Then we need to determine how each photon travels through the Michelson

interferometer. Depending on the stage position $\delta_0$ and the dither position $\delta(t)$, each photon will have some probability $p_{int}(t)$ of traveling through one path of the interferometer and probability $1 - p_{int}(t)$ of traveling through the other path of the interferometer.

$$p_{int}(t) = 0.5 + 0.5e^{\frac{-\Delta(t)}{T_2}} \sin(2\pi\Delta(t)\nu) \tag{5.33}$$

where $\Delta(t) = \delta_0 + \delta(t)$, $T_2$ is the coherence time, and $\nu$ is the photon emission frequency. Once the probability is assigned to each photon, a random number is generated to determine which detector in the interferometer the photon goes to. Finally, depending on the photon energy, the photon time will be assigned to the detector or will be filtered out (removed from the photon stream).

#### *5.1.3.4. Fourth-Order Cross-Correlation Analysis*

We developed an algorithm to compute fourth-order cross-correlations across many orders of magnitude in time, extending the method in Laurence et al.[202] and the method discussed in **Section 4.5.3** to compute third-order cross-correlations. The main difference between the algorithm for the third-order and the fourth-order correlations is the addition of an extra photon stream. In the case of the fourth-order correlations, individual second-order cross-correlations and individual third-order cross-correlations are stored for every photon, and only the cumulative sum of the fourth-order cross-correlations are computed.

One thing I will note that might unfortunately throw a wrench in folks understanding of this technique is that I switched the Channel A and Channel B filters. The mathematical framework is set up such that Channel A filters to only accept sample photons and Channel B filters to only accept laser photons. I switched them early on in my work because I had a misunderstanding of how the correlation algorithm would work and I did not have a chance to switch it back. In the next steps of this investigation, I plan to switch it back to the original framework to make the simulations more consistent with the math.

### 5.1.4. APECS Monte Carlo Simulation Results

The goal of the Monte Carlo simulations is to show that we have built up the mathematical foundation and analysis methodology to get a similar APECS interferogram and APECS spectrum that we have shown is possible in **Figure 5.1d,e**. I have run the simulations with the following inputs:

- $Stage\ Positions = 99 \times 100 = 4950$
    - I only measure the upper triangular and reflect it across the lower triangular, similar to reflecting the PCFS interferogram across the white-fringe in single NC PCFS experiments
- $Maximum\ Stage\ Distance = 20\ mm$
- $Time\ per\ Stage\ Position = 40\ seconds$
- $Absorption\ Probability = 0.1$

- $Quantum\ Yield = 100\%$
- $Dither\ Amplitude = 500\ nm$
- $Number\ of\ Dither\ Cycles = 4$
- $Fine\ structure\ state\ \#1\ Wavelength = 532.11416\ nm$
- $Fine\ structure\ state\ \#2\ Wavelength = 532.2471\ nm$
- $Laser\ Wavelength = 532\ nm$
- $Line\ Width = 50\ \mu eV$

**Figure 5.2** shows the results of the Monte Carlo simulations using the above inputs. The APECS interferogram in **Figure 5.2a** has a significantly reduced coherence time compared the one in **Figure 5.1d**. Taking the double inverse cosine transform, the resulting APECS spectrum appears to have multiple peaks at seemingly random energy differences relative to the laser. The data is inconclusive and should just be considered noise. At this point in time as I am writing my thesis, this project is unfortunately not finished and will require more work to investigate the source of the inconclusive data. To start, we can take a look at all the individual second-order, third-order, and fourth-order cross-correlations, interferograms, and spectral correlations to hopefully begin to get insight into where the simulations are going wrong. For all correlations, I plot the first stage position correlations. For all interferograms, I extract the average value of the correlations across stage positions from approximately $\tau_1, \tau_2, \tau_3 = 10^9 - 10^{10}\ ps$. For all spectral correlations, I performed the double inverse cosine transform of the interferogram. This is strictly necessary for the APECS term, but I am not sure if it is strictly necessary for the other terms below.

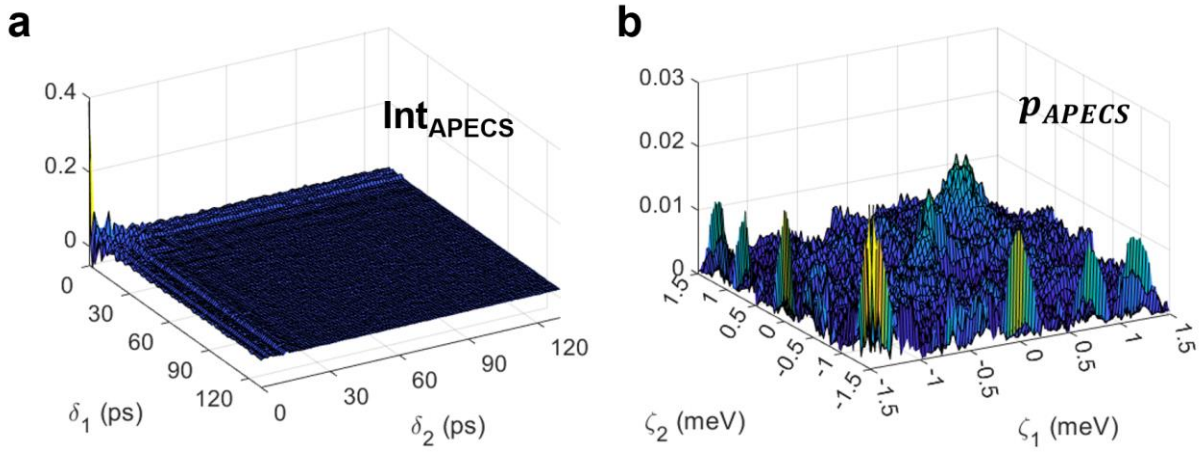


**Figure 5.2.** Monte Carlo Simulation results of the **a.** APECS interferogram and **b.** APECS spectrum.

#### *5.1.4.1. Second-Order Correlations, Interferograms, and Spectral Correlations*

Let's begin by looking at all the individual second-order cross-correlations. I have plotted the correlations for the first stage position in **Figure 5.3**. In order to add and subtract second-order cross-correlations from the fourth-order cross-correlation, we must broadcast the second-order cross-correlation into multiple dimensions. For instance, $g_{AB}^{(2)}(\tau_1)$ is a one-dimensional function with respect to $\tau_1$. We therefore, have to broadcast it into the $\tau_2$ and $\tau_3$ dimension to allow it to interact with the three-dimensional fourth-order cross-correlation. This is similar as multiplying a constant to a multi-dimensional array. I'll also note that all these correlation figures only show two dimensions, even though the overall correlation is three dimensions. We can't really visualize the plots in three dimensions so we just have to be aware which dimensions we are plotting in.

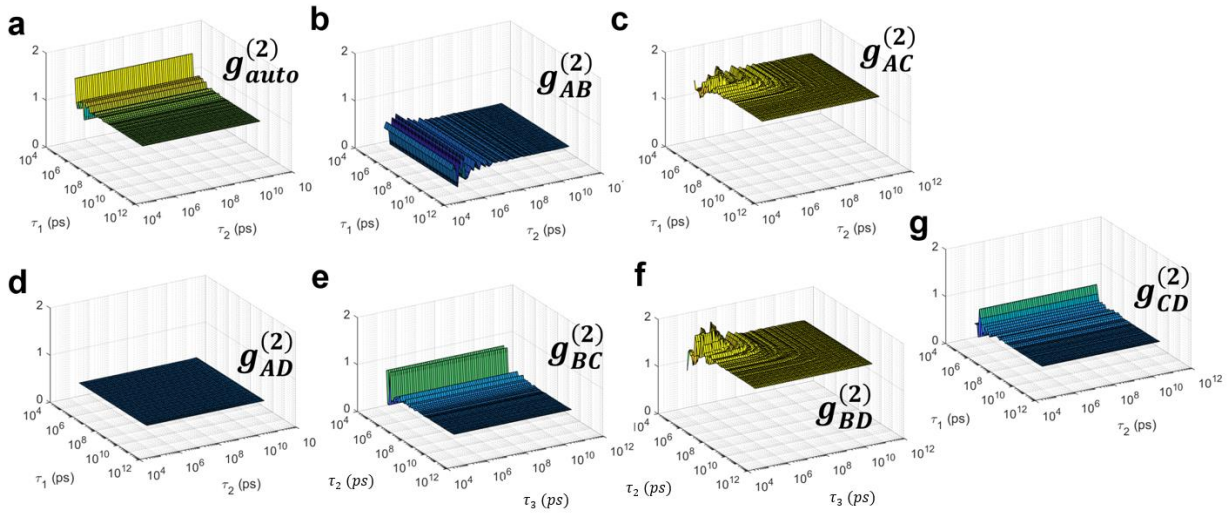


**Figure 5.3.** Monte Carlo Simulation results for the second-order cross-correlations including **a.** $g_{auto}^{(2)}$, **b.** $g_{AB}^{(2)}$, **c.** $g_{AC}^{(2)}$, **d.** $g_{AD}^{(2)}$, **e.** $g_{BC}^{(2)}$, **f.** $g_{BD}^{(2)}$, and **g.** $g_{CD}^{(2)}$. Note that $g_{BD}^{(2)}$ and $g_{CD}^{(2)}$ are projected in the $\tau_2$ and the $\tau_3$ dimensions while the rest of the correlations are projected in the $\tau_1$ and the $\tau_2$ dimensions.

The second-order cross-correlations appear as expected. Because some of the correlations are a function of multiple dimensions, they are broadcasted diagonally across two dimensions (**Figure 5.3c,f**) or three dimensions (**Figure 5.3d**)

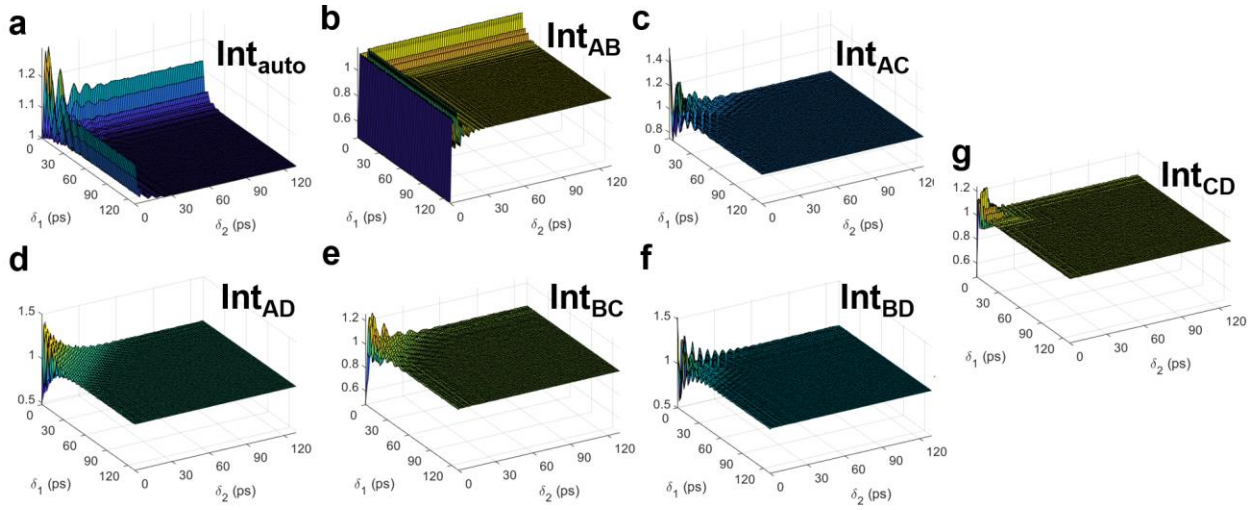


**Figure 5.4.** Monte Carlo Simulation results for the second-order interferograms including **a.** $Int_{auto}$,**b.** $Int_{AB}$, **c.** $Int_{AC}$, **d.** $Int_{AD}$, **e.** $Int_{BC}$, **f.** $Int_{BD}$, and **g.** $Int_{CD}$.

As a whole, the second-order interferograms appear to behave appropriately. I will note that it appears that $Int_{CD}$ in **Figure 5.4g** looks like it has a lower coherence time than the other second-order interferograms which is interesting. There theoretically should be no difference in the interactions between the sample and laser photons at Channels A and B and the interactions between sample and laser photons at Channels C and D.

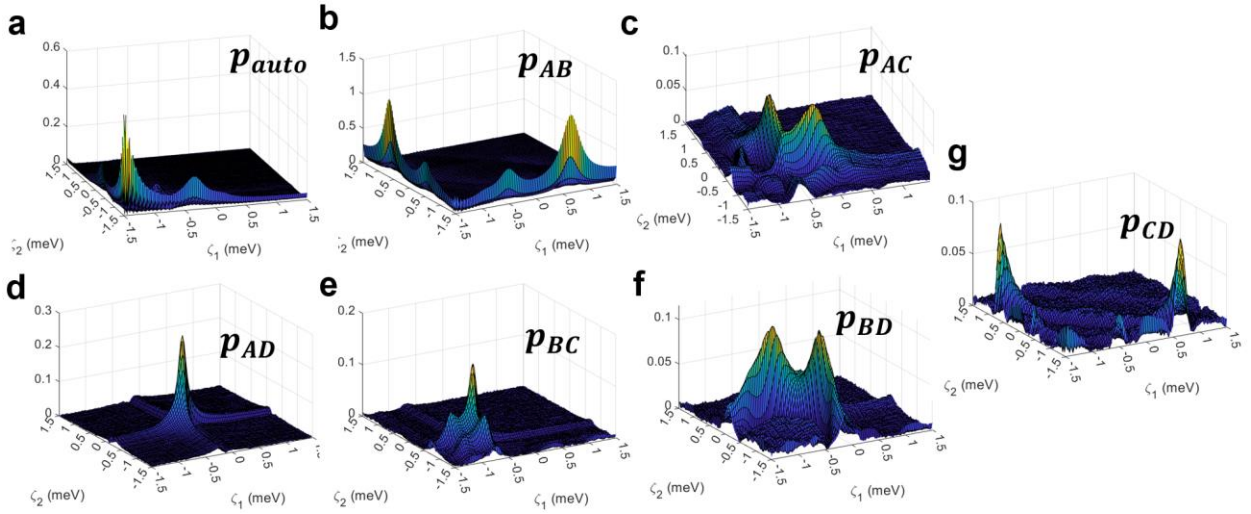


**Figure 5.5.** Monte Carlo Simulation results for the second-order spectral correlations including **a.** $p_{auto}$,**b.** $p_{AB}$, **c.** $p_{AC}$, **d.** $p_{AD}$, **e.** $p_{BC}$, **f.** $p_{BD}$, and **g.** $p_{CD}$.

The spectral correlations are definitely interesting and a little hard to interpret initially when broadcasting the second order correlations into multiple dimensions. First off, I don't think there is much to draw from the auto-correlation in **Figure 5.5a**. What's interesting in the correlations of Channel A and

Channel B, we can see the proper energy difference of the sample photons with the laser, however one of the doublet states has a positive difference and one of them has a negative difference (**Figure 5.5b**). Spectral correlations of Channel A and Channel D (laser-laser correlations) is expectedly a singlet centered around 0 meV (**Figure 5.5d**). Some of the spectral correlations like $p_{AC}$ and $p_{BD}$ are a little harder to interpret what is going on. Maybe this is because we are correlating sample to laser correlations across multiple interferometers. One more observation I want to make is that I would have expected $p_{AB}$ and $p_{CD}$ to be similar, but this does not seem to be the case. This may be an indication that something is still wrong in my simulations.

#### *5.1.4.2. Third-Order Correlations, Interferograms, and Spectral Correlations*

For the third-order correlations, I will look at both the raw correlations and the *total* third-order correlations that are defined in **Equations 5.23-5.26**.

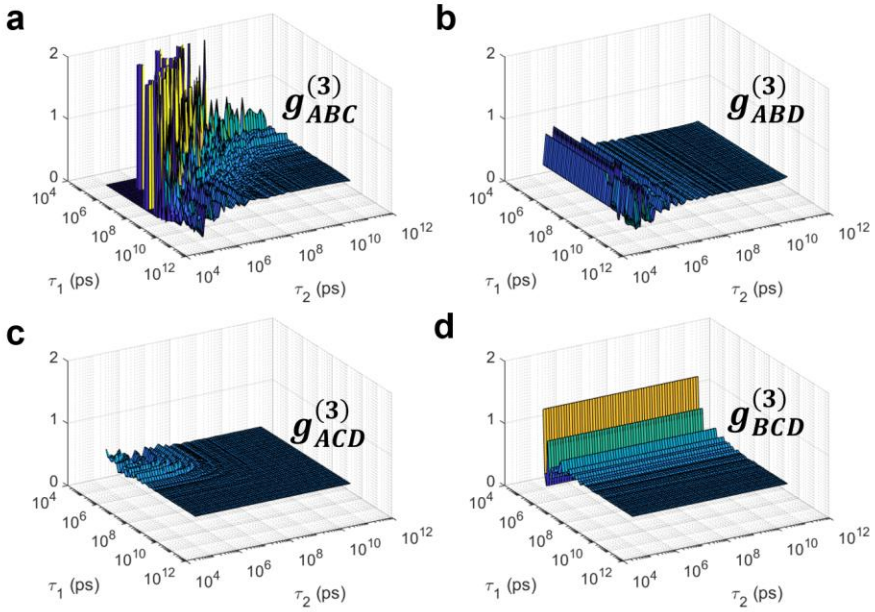


**Figure 5.6.** Monte Carlo Simulation results for the third-order cross-correlations including **a.** $g^{(3)}_{ABC}$, **b.** $g^{(3)}_{ABD}$, **c.** $g^{(3)}_{ACD}$, **d.** $g^{(3)}_{BCD}$.

Nothing seems out of the norm for the third-order correlations in **Figure 5.6**. The difference in noise of the various third-order cross-correlations does not make a ton of sense to me.

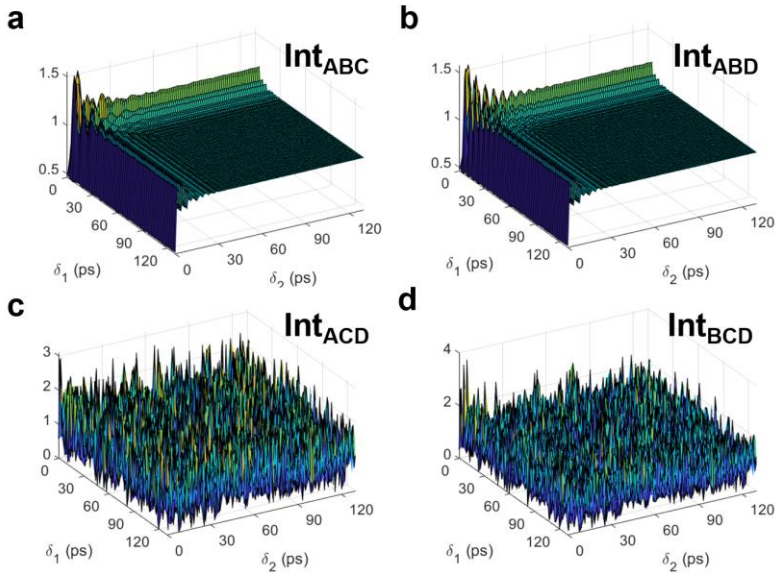


**Figure 5.7.** Monte Carlo Simulation results for the third-order interferograms including **a.** $Int_{ABC}$, **b.** $Int_{ABD}$, **c.** $Int_{ACD}$, **d.** $Int_{BCD}$.

Looking at the third-order interferograms is where things go obviously wrong. $Int_{ACD}$ and $Int_{BCD}$ in **Figure 5.7c,d** appear to just be noise. There may be an issue with the Channel C-Channel D correlations that are affecting the overall results.

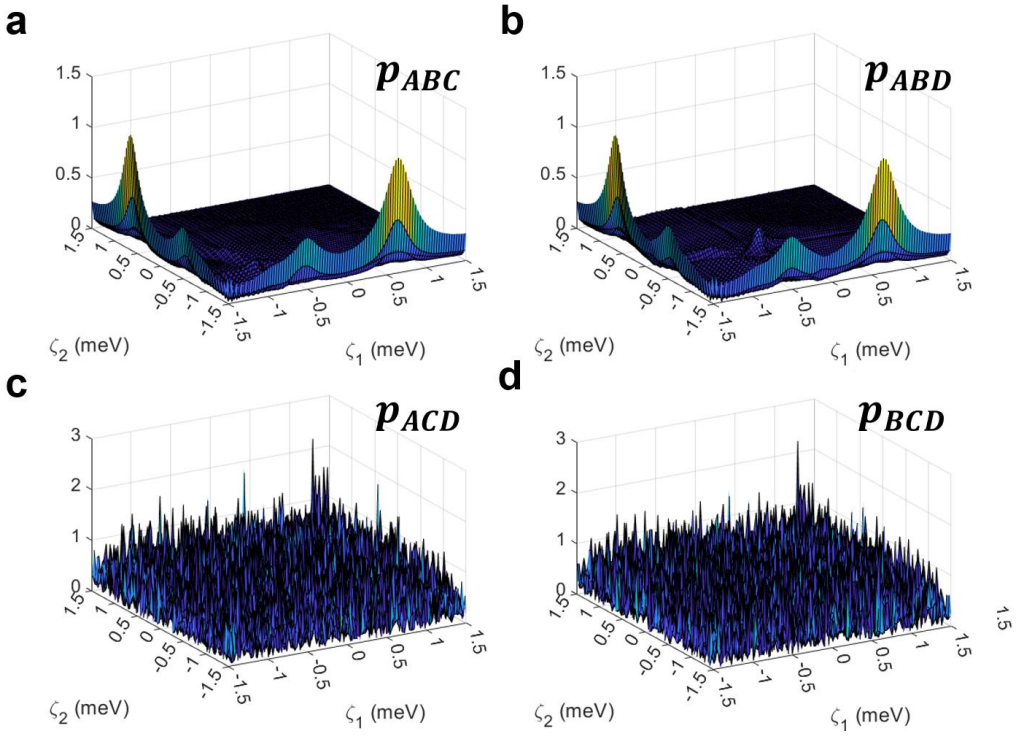

**Figure 5.8.** Monte Carlo Simulation results for the third-order spectral correlations including **a.** $p_{ABC}$, **b.** $p_{ABD}$, **c.** $p_{ACD}$, **d.** $p_{BCD}$.

Looking at the spectral correlations of the third-order correlations, we see potential signatures of the asymmetric doublet again in $p_{ABC}$ and $p_{ABD}$ in **Figure 5.8ab**. We also see that the noise interferograms transform into noise spectral correlations for $p_{ACD}$ and $p_{BCD}$ in **Figure 5.8c,d**.

I am particularly interested in the total third-order cross-correlations because Andrew Beyler claims these should average to zero and therefore do not have to take them into account. Looking at the interferograms for the total third-order cross-correlations in **Figure 5.9**, it appears that might not be the case. Interestingly, the coherence of these interferograms drops to zero very sharply everywhere except along the axes where one of the stages remains at the white fringe where the interference is the most intense.Taking the double inverse cosine transform, we see seemingly random peaks in the spectral correlations (**Figure 1.11**). I'll note that these peaks are extremely low in magnitude and should just be considered noise.

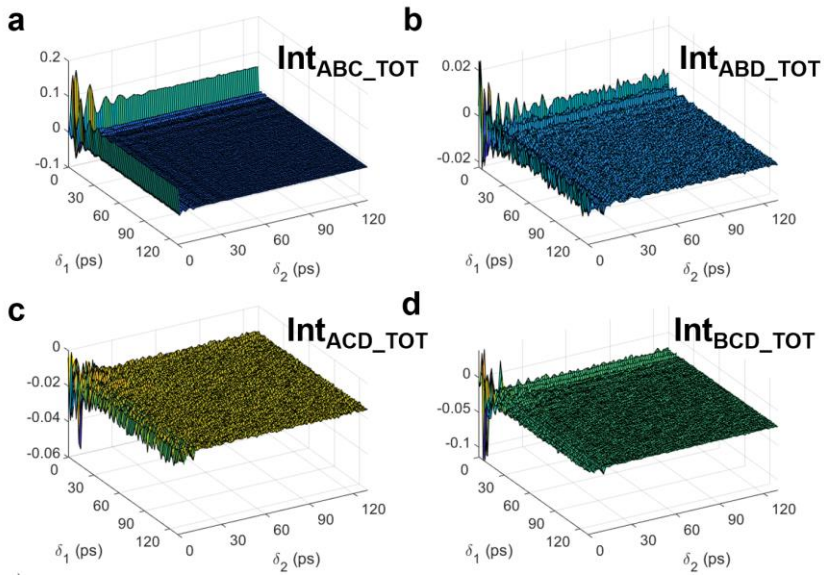


**Figure 5.9.** Monte Carlo Simulation results for the total third-order interferograms including **a.** $Int_{ABC\_TOT}$, **b.** $Int_{ABD\_TOT}$, **c.** $Int_{ACD\_TOT}$, **d.** $Int_{BCD\_TOT}$.

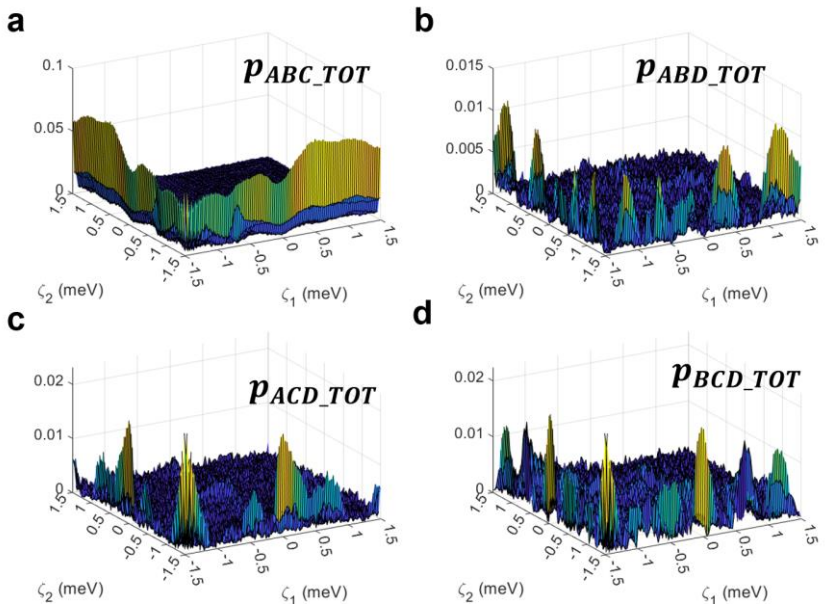


**Figure 5.10.** Monte Carlo Simulation results for the third-order spectral correlations including **a.** $p_{ABC\_TOT}$, **b.** $p_{ABD\_TOT}$, **c.** $p_{ACD\_TOT}$ , **d.** $p_{BCD\_TOT}$.

### *5.1.4.3. Fourth-Order Correlations, Interferograms, and Spectral Correlations*

Finally, nothing particularly stands out as abnormal in the fourth-order correlations, interferograms or spectral correlations in **Figure 5.11**. The coherence of the interferogram seems reasonable in **Figure 5.11b**. The spectral correlation has the same potential asymmetric signature as the third order spectral correlation $p_{ABC}$ and $p_{ABD}$ (**Figure 5.11c**). Additionally, the spectral correlation has additional peaks that are more within the two-dimensional plots, however they are small and hard to resolve. It's possible these are the features we are interested in, and that the axis features are the ones that are supposed to be subtracted out to isolate the APECS spectrum.

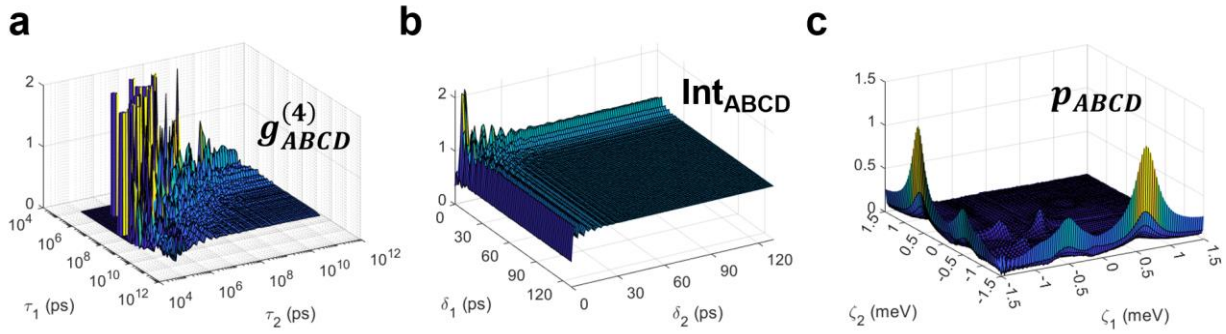


**Figure 5.11.** Monte Carlo Simulation results for the fourth-order **a.** cross-correlation $g^{(4)}_{ABCD}$, **b.** interferogram $Int_{ABCD}$, and **c**. spectral correlation $p_{ABCD}$

### 5.1.5. Conclusions

There is still much that is unclear about these simulations. What is clear is that I will need to revisit the simulations to ensure that the correlations between C and D are behaving normally. I also might try to switch Channels A and B so that sample photons arrive at Channel A and laser photons arrive at Channel B to make it more consistent with the derivation. There is more work to do, and likely many more simulations to run, but its becoming more clear that the asymmetric information is there, but the question remains how to precisely extract it from the fourth-order correlations.

### 5.1.6. Acknowledgements

I also want to acknowledge the help of a dear friend, Harry Bendekgey who has been integral to this work. Harry and I went to Pomona College together and have remained the closest of friends as I have worked on my PhD at MIT and he has worked on his PhD at UC Irvine in Computer Science. It has been amazing to be able to find ways to still work together on projects, across our disciplines, while also working on our main respective projects. There were so many times I felt like I was hitting a dead end with this work, only to work through the problem with Harry. Thank you so much for your enthusiasm to work on a project unrelated to your PhD research and thank you for your support as a close friend all of these years.

We acknowledge the MIT SuperCloud and Lincoln Laboratory Supercomputing Center for providing HPC resources that have contributed to the research results reported within this paper/report.

## 5.2. Photon Correlation Monte Carlo Simulations as a Learning Tool

### 5.2.1. Introduction

The Bawendi Lab has been at the forefront of the colloidal NC spectroscopy field for several decades contributing to single NC spectroscopic studies of many materials including CdSe,[68,82,162,193] InP,[47,58] $CsPbBr_3$,[58,63,64,70,72] InAs[191], and hexagonal boron nitride.[204] The group has contributed to significant experimental discoveries including electric field dependent single NC measurements[144] and the first observation of Hong-Ou-Mandel (HOM) interference in a colloidal NC system.[12] Additionally, the Bawendi Lab has contributed to the field by developing novel spectroscopic techniques such as photon correlation techniques that can extract average single NC information in solution,[84,86,205] photon number resolved techniques to extract multiexciton dynamics,[82,84,193] and a photon correlation technique that extracts the single NC emission line width with high time and energy resolution known as photon correlation Fourier spectroscopy (PCFS).[203]

The Bawendi Lab has a large bank of knowledge that allows new graduate students to build off of past discoveries, pushing the envelope on what is possible with something as simple as a photon stream. Unfortunately, these techniques are omitted from undergraduate and even graduate coursework because of their complex nature. Our objective is to provide the scientific community with an easy-to-use toolkit to explore fundamental photophysical questions and to aid spectroscopic technique development. We propose to develop a series of photon correlation Monte Carlo (PCMC) simulations to explore prominent correlation techniques in the NC spectroscopy field. The PCMC toolkit will be open-access and will aim to fill educational gaps and provide the research community with a database of analytical tools that would encourage a wider audience to engage with photon correlation spectroscopy.

### 5.2.2. Toolkit Simulations

The PCMC toolkit will consist of a series of simulations that will allow members of the NC spectroscopic community to interact with simulated NC system photon streams. Simulated photon streams will exist for pulsed excitation and continuous wave excitation experiments. The PCMC toolkit will also include analysis code, built by the Bawendi Lab to aid the user to understand how to work up the photon streams. Experiments and analysis code will be included for the following systems:

1. Single NC pulsed-$g^{(2)}(\tau)$ to quantify the biexciton quantum yield – **Figure 5.12a**
2. Single NC pulsed-$g^{(3)}(\tau_1, \tau_2)$ to quantify the triexciton quantum yield – **Figure 5.12b**
3. Solution NC pulsed-$g^{(2)}(\tau)$ to quantify the average biexciton quantum yield – **Figure 5.12c**
4. Solution NC pulsed-$g^{(3)}(\tau_1, \tau_2)$ to quantify the average triexciton quantum yield – **Figure 5.12d**

5. Photon number resolved lifetime (PNRL) analysis code to measure multiexciton lifetimes of single NCs and solutions of NCs – **Figure 5.12e**
6. Single NC photon correlation Fourier spectroscopy (PCFS) to extract spectral dynamics and line widths – **Figure 5.13a-c**
7. Solution NC photon correlation Fourier spectroscopy (PCFS) to extract average single NC line widths in an ensemble sample – **Figure 5.13d-f**

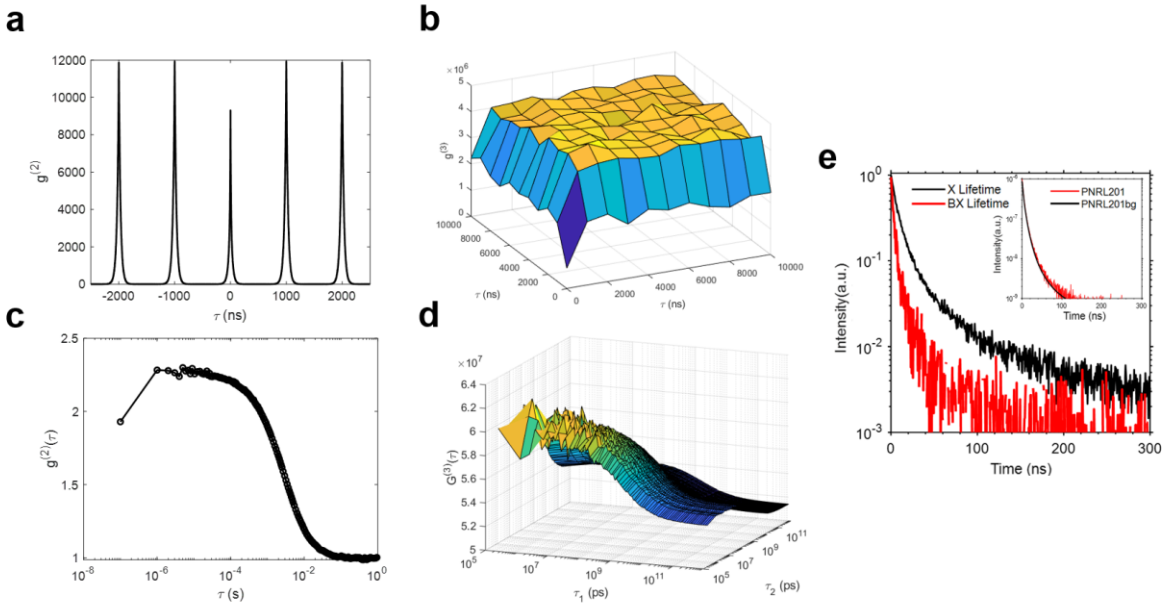


**Figure 5.12.** Monte Carlo simulations of pulsed correlation experiments to understand the multiexciton dynamics and efficiency of emissive systems. Techniques include the **a.** single NC pulsed-$g^{(2)}(\tau)$, **b.** single NC pulsed-$g^{(3)}(\tau_1, \tau_2)$, **c**. solution NC pulsed-$g^{(2)}(\tau)$, **d**. solution NC pulsed-$g^{(3)}(\tau_1, \tau_2)$, and **e.** photon number resolved lifetime experiments.

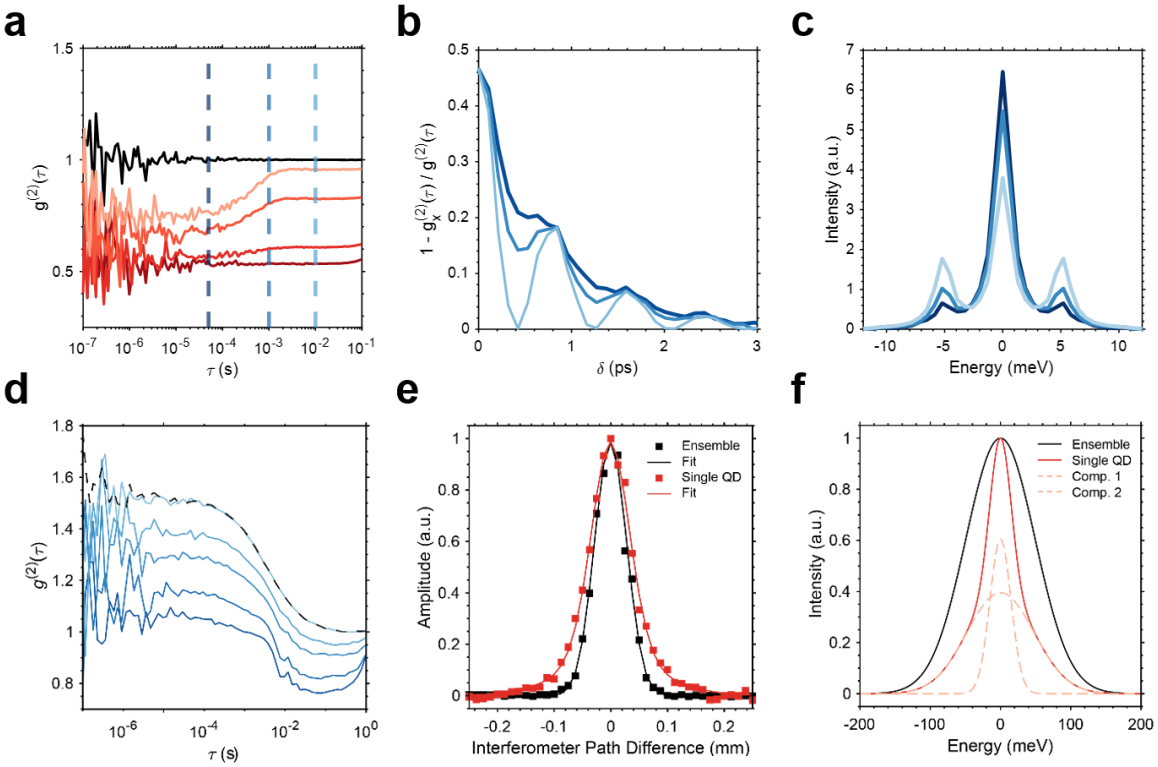


**Figure 5.13.** Monte Carlo simulations of **a-c.** single NC photon correlation Fourier spectroscopy and **d-f.** solution NC photon correlation Fourier spectroscopy experiments. Note that the solution figures in **d-f** are real measurements, not Monte Carlo simulations of InP NCs in solution. These Monte Carlo simulations have not been developed yet. **a,d** show the second order auto- and cross-correlations, **b,e** show the interferograms, and **c,f** show the spectral correlations.

# References


1. Atikur Rahman, Md. A Review on Semiconductors Including Applications and Temperature Effects in Semiconductors. *Am. Sci. Res. J. Eng. Technol. Sci.* **7**, 50–70 (2014).
2. Rossetti, R. & Brus, L. Electron-hole recombination emission as a probe of surface chemistry in aqueous cadmium sulfide colloids. *J. Phys. Chem.* **86**, 4470–4472 (1982).
3. Hoekzema, D., Berg, E. V. D., Schooten, G. & Dijk, L. V. The particle/wave-in-a-box model in Dutch secondary schools. *Phys. Educ.* **42**, 391–398 (2007).
4. Brus, L. E. Electron–electron and electron-hole interactions in small semiconductor crystallites: The size dependence of the lowest excited electronic state. *J. Chem. Phys.* **80**, 4403–4409 (1984).
5. Harry, S. T. & Adekanmbi, M. A. CONFINEMENT ENERGY OF QUANTUM DOTS AND THE BRUS EQUATION. *Int. J. Res. -GRANTHAALAYAH* **8**, 318–323 (2020).
6. Kayanuma, Y. Quantum-size effects of interacting electrons and holes in semiconductor microcrystals with spherical shape. *Phys. Rev. B* **38**, 9797–9805 (1988).
7. Aubert, T. *et al.* General Expression for the Size-Dependent Optical Properties of Quantum Dots. *Nano Lett.* **22**, 1778–1785 (2022).
8. Murray, C. B., Norris, D. J. & Bawendi, M. G. Synthesis and characterization of nearly monodisperse CdE (E = sulfur, selenium, tellurium) semiconductor nanocrystallites. *J. Am. Chem. Soc.* **115**, 8706–8715 (1993).
9. LaMer, V. K. & Dinegar, R. H. Theory, Production and Mechanism of Formation of Monodispersed Hydrosols. *J. Am. Chem. Soc.* **72**, 4847–4854 (1950).
10. Jang, E. Environmentally Friendly Quantum Dots for Display Applications. in *2018 IEEE International Electron Devices Meeting (IEDM)* 38.2.1-38.2.4 (IEEE, San Francisco, CA, 2018). doi:10.1109/IEDM.2018.8614647.
11. Bruns, O. T. *et al.* Next-generation in vivo optical imaging with short-wave infrared quantum dots. *Nat. Biomed. Eng.* **1**, 0056 (2017).
12. Kaplan, A. E. K. *et al.* Hong-Ou-Mandel Interference in Colloidal CsPbBr3 Perovskite Nanocrystals. *Nat. Photonics* (2023).
13. Shang, Y. & Ning, Z. Colloidal quantum-dots surface and device structure engineering for high-performance light-emitting diodes. *Natl. Sci. Rev.* **4**, 170–183 (2017).

14. Kirkwood, N. *et al.* Finding and Fixing Traps in II–VI and III–V Colloidal Quantum Dots: The Importance of Z-Type Ligand Passivation. *J. Am. Chem. Soc.* **140**, 15712–15723 (2018).

15. Wang, R. *et al.* Colloidal quantum dot ligand engineering for high performance solar cells. *Energy Environ. Sci.* **9**, 1130–1143 (2016).

16. Karakoti, A. S., Shukla, R., Shanker, R. & Singh, S. Surface functionalization of quantum dots for biological applications. *Adv. Colloid Interface Sci.* **215**, 28–45 (2015).

17. Xu, F. *et al.* Quantum size effect and surface defect passivation in size-controlled CsPbBr3 quantum dots. *J. Alloys Compd.* **831**, 154834 (2020).

18. Fischer, S. A., Crotty, A. M., Kilina, S. V., Ivanov, S. A. & Tretiak, S. Passivating ligand and solvent contributions to the electronic properties of semiconductor nanocrystals. *Nanoscale* **4**, 904–914 (2012).

19. Ginterseder, M. *et al.* Lead Halide Perovskite Nanocrystals with Low Inhomogeneous Broadening and High Coherent Fraction through Dicationic Ligand Engineering. *Nano Lett.* (2023) doi:10.1021/acs.nanolett.2c03354.

20. Hines, M. A. & Guyot-Sionnest, P. Synthesis and Characterization of Strongly Luminescing ZnS-Capped CdSe Nanocrystals. *J. Phys. Chem.* **100**, 468–471 (1996).

21. Chen, O. *et al.* Compact high-quality CdSe–CdS core–shell nanocrystals with narrow emission linewidths and suppressed blinking. *Nat. Mater.* **12**, 445–451 (2013).

22. Hopfield, J. J. Exciton States and Band Structure in CdS and CdSe. *J. Appl. Phys.* **32**, 2277–2281 (1961).

23. Won, Y.-H. *et al.* Highly efficient and stable InP/ZnSe/ZnS quantum dot light-emitting diodes. *Nature* **575**, 634–638 (2019).

24. Cassidy, J. *et al.* Quantum Shells Boost the Optical Gain of Lasing Media. *ACS Nano* **16**, 3017–3026 (2022).

25. Harankahage, D. *et al.* Quantum Shell in a Shell: Engineering Colloidal Nanocrystals for a High-Intensity Excitation Regime. *J. Am. Chem. Soc.* **145**, 13326–13334 (2023).

26. Ithurria, S. & Dubertret, B. Quasi 2D Colloidal CdSe Platelets with Thicknesses Controlled at the Atomic Level. *J. Am. Chem. Soc.* **130**, 16504–16505 (2008).

27. Krajewska, C. J. *et al.* Controlled Assembly and Anomalous Thermal Expansion of Ultrathin Cesium Lead Bromide Nanoplatelets. *Nano Lett.* **23**, 2148–2157 (2023).

28. Krajewska, C. J. *et al.* A-Site Cation Influence on the Structural and Optical Evolution of Ultrathin Lead Halide Perovskite Nanoplatelets. *ACS Nano* acsnano.3c12286 (2024) doi:10.1021/acsnano.3c12286.

29. Zhu, H. *et al.* One-Dimensional Highly-Confined $CsPbBr_3$ Nanorods with Enhanced Stability: Synthesis and Spectroscopy. *Nano Lett.* **22**, 8355–8362 (2022).

30. Wang, W., Banerjee, S., Jia, S., Steigerwald, M. L. & Herman, I. P. Ligand Control of Growth, Morphology, and Capping Structure of Colloidal CdSe Nanorods. *Chem. Mater.* **19**, 2573–2580 (2007).

31. Zhu, H. *et al.* Synthesis of Zwitterionic $CsPbBr_3$ Nanocrystals with Controlled Anisotropy using Surface-Selective Ligand Pairs. *Adv. Mater.* **35**, 2304069 (2023).

32. Ondry, J. C., Gupta, A., Zhou, Z., Chang, J. H. & Talapin, D. V. Synthesis of Ternary and Quaternary Group III-Arsenide Colloidal Quantum Dots via High-Temperature Cation Exchange in Molten Salts: The Importance of Molten Salt Speciation. *ACS Nano* **18**, 858–873 (2024).

33. Pan, D. *et al.* Semiconductor "Nano-Onions" with Multifold Alternating CdS/CdSe or CdSe/CdS Structure. *Chem. Mater.* **18**, 4253–4258 (2006).

34. Kim, Y. *et al.* Tailored growth of single-crystalline InP tetrapods. *Nat. Commun.* **12**, 4454 (2021).

35. Weisskopf, V. Probleme der neueren Quantentheorie des Elektrons. *Naturwissenschaften* **23**, 631–637 (1935).

36. Yu, P. *et al.* Absorption Cross-Section and Related Optical Properties of Colloidal InAs Quantum Dots. *J. Phys. Chem. B* **109**, 7084–7087 (2005).

37. Leistikow, M. D., Johansen, J., Kettelarij, A. J., Lodahl, P. & Vos, W. L. Size-dependent oscillator strength and quantum efficiency of CdSe quantum dots controlled via the local density of states. *Phys. Rev. B* **79**, 045301 (2009).

38. Stobbe, S., Hvam, J. M. & Lodahl, P. On the interpretation of wave function overlaps in quantum dots. *Phys. Status Solidi B* **248**, 855–858 (2011).

39. Burdov, V. A. & Vasilevskiy, M. I. Exciton-Photon Interactions in Semiconductor Nanocrystals: Radiative Transitions, Non-Radiative Processes and Environment Effects. *Appl. Sci.* **11**, 497 (2021).

40. Nirmal, M. *et al.* Fluorescence intermittency in single cadmium selenide nanocrystals. *Nature* **383**, 802–804 (1996).

41. Efros, A. L. & Nesbitt, D. J. Origin and control of blinking in quantum dots. *Nat. Nanotechnol.* **11**, 661–671 (2016).

42. Kuno, M., Fromm, D. P., Hamann, H. F., Gallagher, A. & Nesbitt, D. J. “On”/“off” fluorescence intermittency of single semiconductor quantum dots. *J. Chem. Phys.* **115**, 1028–1040 (2001).

43. Zhao, J., Nair, G., Fisher, B. R. & Bawendi, M. G. Challenge to the Charging Model of Semiconductor-Nanocrystal Fluorescence Intermittency from Off-State Quantum Yields and Multiexciton Blinking. *Phys. Rev. Lett.* **104**, 157403 (2010).

44. Gómez, D. E., Van Embden, J., Mulvaney, P., Fernée, M. J. & Rubinsztein-Dunlop, H. Exciton−Trion Transitions in Single CdSe–CdS Core–Shell Nanocrystals. *ACS Nano* **3**, 2281–2287 (2009).

45. Galland, C. *et al.* Two types of luminescence blinking revealed by spectroelectrochemistry of single quantum dots. *Nature* **479**, 203–207 (2011).

46. Qin, W. & Guyot-Sionnest, P. Evidence for the Role of Holes in Blinking: Negative and Oxidized CdSe/CdS Dots. *ACS Nano* **6**, 9125–9132 (2012).

47. Berkinsky, D. B. *et al.* Narrow Intrinsic Line Widths and Electron–Phonon Coupling of InP Colloidal Quantum Dots. *ACS Nano* (2023) doi:10.1021/acsnano.2c10237.

48. Gibson, N. A., Koscher, B. A., Alivisatos, A. P. & Leone, S. R. Excitation Intensity Dependence of Photoluminescence Blinking in $CsPbBr_3$ Perovskite Nanocrystals. *J. Phys. Chem. C* **122**, 12106–12113 (2018).

49. Peterson, J. J. & Krauss, T. D. Fluorescence Spectroscopy of Single Lead Sulfide Quantum Dots. *Nano Lett.* **6**, 510–514 (2006).

50. Huber, D., Reindl, M., Aberl, J., Rastelli, A. & Trotta, R. Semiconductor quantum dots as an ideal source of polarization-entangled photon pairs on-demand: a review. *J. Opt.* **20**, 073002 (2018).

51. Nasilowski, M., Spinicelli, P., Patriarche, G. & Dubertret, B. Gradient CdSe/CdS Quantum Dots with Room Temperature Biexciton Unity Quantum Yield. *Nano Lett.* **15**, 3953–3958 (2015).

52. Bae, W. K. *et al.* Controlled Alloying of the Core–Shell Interface in CdSe/CdS Quantum Dots for Suppression of Auger Recombination. *ACS Nano* **7**, 3411–3419 (2013).

53. Vaxenburg, R., Rodina, A., Shabaev, A., Lifshitz, E. & Efros, A. L. Nonradiative Auger Recombination in Semiconductor Nanocrystals. *Nano Lett.* **15**, 2092–2098 (2015).

54. Norris, D. J., Efros, Al. L., Rosen, M. & Bawendi, M. G. Size dependence of exciton fine structure in CdSe quantum dots. *Phys. Rev. B* **53**, 16347–16354 (1996).

55. Sercel, P. C. & Efros, A. L. Band-Edge Exciton in CdSe and Other II–VI and III–V Compound Semiconductor Nanocrystals − Revisited. *Nano Lett.* **18**, 4061–4068 (2018).

56. Labeau, O., Tamarat, P. & Lounis, B. Temperature Dependence of the Luminescence Lifetime of Single C d S e / Z n S Quantum Dots. *Phys. Rev. Lett.* **90**, 257404 (2003).

57. Prin, E. *et al.* Revealing the Band-Edge Exciton Fine Structure of Single InP Nanocrystals. *Nano Lett.* **23**, 6067–6072 (2023).

58. Proppe, A. H. *et al.* Highly stable and pure single-photon emission with 250 ps optical coherence times in InP colloidal quantum dots. *Nat. Nanotechnol.* (2023) doi:10.1038/s41565-023-01432-0.

59. Wu, F. *et al.* Fine-tuning the crystal structure of CdSe quantum dots by varying the dynamic characteristics of primary alkylamine ligands. *CrystEngComm* **20**, 4492–4498 (2018).

60. Vogel, M. M. *et al.* Influence of lateral electric fields on multiexcitonic transitions and fine structure of single quantum dots. *Appl. Phys. Lett.* **91**, 051904 (2007).

61. Brodu, A. *et al.* Exciton Fine Structure and Lattice Dynamics in InP/ZnSe Core/Shell Quantum Dots. *ACS Photonics* **5**, 3353–3362 (2018).

62. Sercel, P. C. & Efros, A. L. Band-Edge Exciton in CdSe and Other II–VI and III–V Compound Semiconductor Nanocrystals − Revisited. *Nano Lett.* **18**, 4061–4068 (2018).

63. Ginterseder, M. *et al.* Lead Halide Perovskite Nanocrystals with Low Inhomogeneous Broadening and High Coherent Fraction through Dicationic Ligand Engineering. *Nano Lett.* **23**, 1128–1134 (2023).

64. Sun, W. *et al.* Elastic Phonon Scattering Dominates Dephasing in Weakly Confined Cesium Lead Bromide Nanocrystals at Cryogenic Temperatures. *Nano Lett.* **23**, 2615–2622 (2023).

65. Muller, A., Fang, W., Lawall, J. & Solomon, G. S. Creating Polarization-Entangled Photon Pairs from a Semiconductor Quantum Dot Using the Optical Stark Effect. *Phys. Rev. Lett.* **103**, 217402 (2009).

66. Gywat, O., Burkard, G. & Loss, D. Biexcitons in coupled quantum dots as a source of entangled photons. *Phys. Rev. B* **65**, 205329 (2002).

67. Nguyen, H. A. *et al.* Deterministic Quantum Light Arrays from Giant Silica-Shelled Quantum Dots. *ACS Appl. Mater. Interfaces* **15**, 4294–4302 (2023).

68. Cui, J. *et al.* Direct probe of spectral inhomogeneity reveals synthetic tunability of single-nanocrystal spectral linewidths. *Nat. Chem.* **5**, 602–606 (2013).

69. Cavanaugh, P., Wang, X., Bautista, M. J., Jen-La Plante, I. & Kelley, D. F. Spectral widths and Stokes shifts in InP-based quantum dots. *J. Chem. Phys.* **159**, 134704 (2023).

70. Utzat, H. *et al.* Coherent single-photon emission from colloidal lead halide perovskite quantum dots. *Science* **363**, 1068–1072 (2019).

71. Empedocles, S. A. & Bawendi, M. G. Influence of Spectral Diffusion on the Line Shapes of Single CdSe Nanocrystallite Quantum Dots. *J. Phys. Chem. B* **103**, 1826–1830 (1999).

72. Proppe, A. H. *et al.* Time-Resolved Line Shapes of Single Quantum Emitters via Machine Learned Photon Correlations. *Phys. Rev. Lett.* **131**, 053603 (2023).

73. Besombes, L., Kheng, K., Marsal, L. & Mariette, H. Acoustic phonon broadening mechanism in single quantum dot emission. *Phys. Rev. B* **63**, 155307 (2001).

74. Brodu, A. *et al.* Exciton-phonon coupling in InP quantum dots with ZnS and ( Zn , Cd ) Se shells. *Phys. Rev. B* **101**, 125413 (2020).

75. Hou, L., Tamarat, P. & Lounis, B. Revealing the Exciton Fine Structure in Lead Halide Perovskite Nanocrystals. *Nanomaterials* **11**, 1058 (2021).

76. Sarkar, D. *et al.* Piezoelectric exciton acoustic-phonon coupling in single quantum dots. *Phys. Rev. B* **78**, 241305 (2008).

77. Sarpkaya, I. *et al.* Strong Acoustic Phonon Localization in Copolymer-Wrapped Carbon Nanotubes. *ACS Nano* **9**, 6383–6393 (2015).

78. Liu, J., Neukirch, A. J. & Prezhdo, O. V. Phonon-induced pure-dephasing of luminescence, multiple exciton generation, and fission in silicon clusters. *J. Chem. Phys.* **139**, 164303 (2013).

79. Spinicelli, P. *et al.* Bright and Grey States in CdSe-CdS Nanocrystals Exhibiting Strongly Reduced Blinking. *Phys. Rev. Lett.* **102**, 136801 (2009).

80. Nair, G., Zhao, J. & Bawendi, M. G. Biexciton Quantum Yield of Single Semiconductor Nanocrystals from Photon Statistics. *Nano Lett.* **11**, 1136–1140 (2011).

81. Beyler, A. P. Single-Nanocrystal Photon Correlation: A Versatile Tool for Elucidating Basic Physics and Characterizing Applications-Relevant Properties. (2015).

82. Shulenberger, K. E. *et al.* Multiexciton Lifetimes Reveal Triexciton Emission Pathway in CdSe Nanocrystals. *Nano Lett.* **18**, 5153–5158 (2018).

83. Beyler, A. P., Marshall, L. F., Cui, J., Brokmann, X. & Bawendi, M. G. Direct Observation of Rapid Discrete Spectral Dynamics in Single Colloidal CdSe-CdS Core-Shell Quantum Dots. *Phys. Rev. Lett.* **111**, 177401 (2013).

84. Bischof, T. S., Caram, J. R., Beyler, A. P. & Bawendi, M. G. Extracting the average single-molecule biexciton photoluminescence lifetime from a solution of chromophores. *Opt. Lett.* **41**, 4823 (2016).

85. Beyler, A. P. *et al.* Sample-Averaged Biexciton Quantum Yield Measured by Solution-Phase Photon Correlation. *Nano Lett.* **14**, 6792–6798 (2014).

86. Marshall, L. F., Cui, J., Brokmann, X. & Bawendi, M. G. Extracting Spectral Dynamics from Single Chromophores in Solution. *Phys. Rev. Lett.* **105**, 053005 (2010).

87. Dabbousi, B. *et al.* (CdSe)ZnS Core−Shell Quantum Dots: Synthesis and Characterization of a Size Series of Highly Luminescent Nanocrystallites. *J. Phys. Chem. B* **101**, 9463–9475 (1997).

88. Tessier, M. D., Dupont, D., De Nolf, K., De Roo, J. & Hens, Z. Economic and Size-Tunable Synthesis of InP/ZnE (E = S, Se) Colloidal Quantum Dots. *Chem. Mater.* **27**, 4893–4898 (2015).

89. Resch-Genger, U., Grabolle, M., Cavaliere-Jaricot, S., Nitschke, R. & Nann, T. Quantum dots versus organic dyes as fluorescent labels. *Nat. Methods* **5**, 763–775 (2008).

90. Medintz, I. L., Uyeda, H. T., Goldman, E. R. & Mattoussi, H. Quantum dot bioconjugates for imaging, labelling and sensing. *Nat. Mater.* **4**, 435–446 (2005).

91. Wei, H. *et al.* Single-nanometer iron oxide nanoparticles as tissue-permeable MRI contrast agents. *Proc. Natl. Acad. Sci.* **118**, e2102340118 (2021).

92. Shirasaki, Y., Supran, G. J., Bawendi, M. G. & Bulović, V. Emergence of colloidal quantum-dot light-emitting technologies. *Nat. Photonics* **7**, 13–23 (2013).

93. Jung, H., Ahn, N. & Klimov, V. I. Prospects and challenges of colloidal quantum dot laser diodes. *Nat. Photonics* **15**, 643–655 (2021).

94. Derfus, A. M., Chan, W. C. W. & Bhatia, S. N. Probing the Cytotoxicity of Semiconductor Quantum Dots. *Nano Lett.* **4**, 11–18 (2004).

95. Brunetti, V. *et al.* InP/ZnS as a safer alternative to CdSe/ZnS core/shell quantum dots: in vitro and in vivo toxicity assessment. *Nanoscale* **5**, 307–317 (2013).

96. Xie, S., Zhu, H., Li, M. & Bulović, V. Voltage-Controlled Reversible Modulation of Colloidal Quantum Dot Thin Film Photoluminescence. *ArXiv200805375 Phys.* (2020).

97. Biadala, L., Louyer, Y., Tamarat, Ph. & Lounis, B. Band-Edge Exciton Fine Structure of Single CdSe / ZnS Nanocrystals in External Magnetic Fields. *Phys. Rev. Lett.* **105**, 157402 (2010).

98. Brodu, A. *et al.* Exciton Fine Structure and Lattice Dynamics in InP/ZnSe Core/Shell Quantum Dots. *ACS Photonics* **5**, 3353–3362 (2018).

99. Caram, J. R. *et al.* Exploring size and state dynamics in CdSe quantum dots using two-dimensional electronic spectroscopy. *J. Chem. Phys.* **140**, 084701 (2014).

100. Harel, E., Rupich, S. M., Schaller, R. D., Talapin, D. V. & Engel, G. S. Measurement of electronic splitting in PbS quantum dots by two-dimensional nonlinear spectroscopy. *Phys. Rev. B* **86**, 075412 (2012).

101. Kim, T., Won, Y.-H., Jang, E. & Kim, D. Negative Trion Auger Recombination in Highly Luminescent InP/ZnSe/ZnS Quantum Dots. *Nano Lett.* **21**, 2111–2116 (2021).

102. Brokmann, X., Bawendi, M., Coolen, L. & Hermier, J.-P. Photon-correlation Fourier spectroscopy. *Opt. Express* **14**, 6333 (2006).

103. Krauss, T. D. & Wise, F. W. Coherent Acoustic Phonons in a Semiconductor Quantum Dot. *Phys. Rev. Lett.* **79**, 5102–5105 (1997).

104. Chilla, G. *et al.* Direct Observation of Confined Acoustic Phonons in the Photoluminescence Spectra of a Single CdSe-CdS-ZnS Core-Shell-Shell Nanocrystal. *Phys. Rev. Lett.* **100**, 057403 (2008).

105. Ostapenko, I. A. *et al.* Exciton acoustic-phonon coupling in single GaN/AlN quantum dots. *Phys. Rev. B* **85**, 081303 (2012).

106. Triki, M. & Jaziri, S. Exciton acoustic-phonon coupling in single $In_{0.4}Ga_{0.6}As$/GaAs quantum rings: Exciton acoustic-phonon coupling in single InGaAs/GaAs QRs. *Phys. Status Solidi B* **254**, 1600833 (2017).

107. Salvador, M. R., Graham, M. W. & Scholes, G. D. Exciton-phonon coupling and disorder in the excited states of CdSe colloidal quantum dots. *J. Chem. Phys.* **125**, 184709 (2006).

108. Liu, A., Almeida, D. B., Bae, W.-K., Padilha, L. A. & Cundiff, S. T. Simultaneous Existence of Confined and Delocalized Vibrational Modes in Colloidal Quantum Dots. *J. Phys. Chem. Lett.* **10**, 6144–6150 (2019).

109. Rolo, A. G. & Vasilevskiy, M. I. Raman spectroscopy of optical phonons confined in semiconductor quantum dots and nanocrystals. *J. Raman Spectrosc.* **38**, 618–633 (2007).

110. Kelley, A. M. Electron−Phonon Coupling in CdSe Nanocrystals. *J. Phys. Chem. Lett.* **1**, 1296–1300 (2010).

111. Rolo, A. G., Vasilevskiy, M. I., Hamma, M. & Trallero-Giner, C. Anomalous first-order Raman scattering in III-V quantum dots: Optical deformation potential interaction. *Phys. Rev. B* **78**, 081304 (2008).

112. Mukamel, S. *Principles of Nonlinear Optical Spectroscopy*. (Oxford University Press, 1995).

113. Borcherds, P. H., Alfrey, G. F., Woods, A. D. B. & Saunderson, D. H. Phonon dispersion curves in indium phosphide. *J. Phys. C Solid State Phys.* **8**, 2022–2030 (1975).

114. Reiter, D. E., Kuhn, T. & Axt, V. M. Distinctive characteristics of carrier-phonon interactions in optically driven semiconductor quantum dots. *Adv. Phys. X* **4**, 1655478 (2019).

115. Stock, E. *et al.* Acoustic and optical phonon scattering in a single In(Ga)As quantum dot. *Phys. Rev. B* **83**, 041304 (2011).

116. Jain, V., Biesinger, M. C. & Linford, M. R. The Gaussian-Lorentzian Sum, Product, and Convolution (Voigt) functions in the context of peak fitting X-ray photoelectron spectroscopy (XPS) narrow scans. *Appl. Surf. Sci.* **447**, 548–553 (2018).

117. Califano, M., Franceschetti, A. & Zunger, A. Lifetime and polarization of the radiative decay of excitons, biexcitons, and trions in CdSe nanocrystal quantum dots. *Phys. Rev. B* **75**, (2007).

118. Fernée, M. J., Littleton, B. N. & Rubinsztein-Dunlop, H. Detection of Bright Trion States Using the Fine Structure Emission of Single CdSe/ZnS Colloidal Quantum Dots. *ACS Nano* **3**, 3762–3768 (2009).

119. Takagahara, T. Theory of exciton dephasing in semiconductor quantum dots. *Phys. Rev. B* **60**, 2638–2652 (1999).

120. Uskov, A. V., Jauho, A.-P., Tromborg, B., Mørk, J. & Lang, R. Dephasing Times in Quantum Dots due to Elastic LO Phonon-Carrier Collisions. *Phys. Rev. Lett.* **85**, 1516–1519 (2000).

121. Wijnen, F. J. P., Blokland, J. H., Chin, P. T. K., Christianen, P. C. M. & Maan, J. C. Competition between zero-phonon and phonon-assisted luminescence in colloidal CdSe quantum dots. *Phys. Rev. B* **78**, 235318 (2008).

122. Liu, S., Shu, Y., Zhu, M., Qin, H. & Peng, X. Anomalous Emission Shift of CdSe/CdS/ZnS Quantum Dots at Cryogenic Temperatures. *Nano Lett.* **22**, 3011–3017 (2022).

123. Fan, F. *et al.* Continuous-wave lasing in colloidal quantum dot solids enabled by facet-selective epitaxy. *Nature* **544**, 75–79 (2017).

124. Park, Y.-S., Lim, J. & Klimov, V. I. Asymmetrically strained quantum dots with non-fluctuating single-dot emission spectra and subthermal room-temperature linewidths. *Nat. Mater.* **18**, 249–255 (2019).

125. Lu, X. *et al.* Chip-integrated visible–telecom entangled photon pair source for quantum communication. *Nat. Phys.* **15**, 373–381 (2019).

126. Guo, X. *et al.* Distributed quantum sensing in a continuous-variable entangled network. *Nat. Phys.* **16**, 281–284 (2020).

127. Knill, E., Laflamme, R. & Milburn, G. J. A scheme for efficient quantum computation with linear optics. *Nature* **409**, 46–52 (2001).

128. Madsen, L. S. *et al.* Quantum computational advantage with a programmable photonic processor. *Nature* **606**, 75–81 (2022).

129. Aharonovich, I., Englund, D. & Toth, M. Solid-state single-photon emitters. *Nat. Photonics* **10**, 631–641 (2016).

130. Dietrich, A. *et al.* Observation of Fourier transform limited lines in hexagonal boron nitride. *Phys. Rev. B* **98**, 081414 (2018).

131. Spokoyny, B. *et al.* Effect of Spectral Diffusion on the Coherence Properties of a Single Quantum Emitter in Hexagonal Boron Nitride. *J. Phys. Chem. Lett.* **11**, 1330–1335 (2020).

132. Aharonovich, I. & Neu, E. Diamond Nanophotonics. *Adv. Opt. Mater.* **2**, 911–928 (2014).

133. He, Y.-M. *et al.* Single quantum emitters in monolayer semiconductors. *Nat. Nanotechnol.* **10**, 497–502 (2015).

134. Claudon, J. *et al.* A highly efficient single-photon source based on a quantum dot in a photonic nanowire. *Nat. Photonics* **4**, 174–177 (2010).

135. Nilsson, J. *et al.* Quantum teleportation using a light-emitting diode. *Nat. Photonics* **7**, 311–315 (2013).

136. Salter, C. L. *et al.* An entangled-light-emitting diode. *Nature* **465**, 594–597 (2010).

137. Kuhlmann, A. V. *et al.* Charge noise and spin noise in a semiconductor quantum device. *Nat. Phys.* **9**, 570–575 (2013).

138. Somaschi, N. *et al.* Near-optimal single-photon sources in the solid state. *Nat. Photonics* **10**, 340–345 (2016).

139. Müller, M., Bounouar, S., Jöns, K. D., Glässl, M. & Michler, P. On-demand generation of indistinguishable polarization-entangled photon pairs. *Nat. Photonics* **8**, 224–228 (2014).

140. Dousse, A. *et al.* Controlled Light-Matter Coupling for a Single Quantum Dot Embedded in a Pillar Microcavity Using Far-Field Optical Lithography. *Phys. Rev. Lett.* **101**, 267404 (2008).

141. Efros, Al. L. *et al.* Band-edge exciton in quantum dots of semiconductors with a degenerate valence band: Dark and bright exciton states. *Phys. Rev. B* **54**, 4843–4856 (1996).

142. Nirmal, M. *et al.* Observation of the 'Dark Exciton' in CdSe Quantum Dots. *Phys. Rev. Lett.* **75**, 3728–3731 (1995).

143. Empedocles, S. A. & Bawendi, M. G. Influence of Spectral Diffusion on the Line Shapes of Single CdSe Nanocrystallite Quantum Dots. *J. Phys. Chem. B* **103**, 1826–1830 (1999).

144. Empedocles, S. A. & Bawendi, M. G. Quantum-Confined Stark Effect in Single CdSe Nanocrystallite Quantum Dots. *Science* **278**, 2114–2117 (1997).

145. Fernée, M. J. *et al.* Spontaneous Spectral Diffusion in CdSe Quantum Dots. *J. Phys. Chem. Lett.* **3**, 1716–1720 (2012).

146. Thoma, A. *et al.* Exploring Dephasing of a Solid-State Quantum Emitter via Time- and Temperature-Dependent Hong-Ou-Mandel Experiments. *Phys. Rev. Lett.* **116**, 033601 (2016).

147. Becker, M. A. *et al.* Bright triplet excitons in caesium lead halide perovskites. *Nature* **553**, 189–193 (2018).

148. Won, Y.-H. *et al.* Highly efficient and stable InP/ZnSe/ZnS quantum dot light-emitting diodes. *Nature* **575**, 634–638 (2019).

149. Kelley, A. M. *et al.* Identity of the reversible hole traps in InP/ZnSe core/shell quantum dots. *J. Chem. Phys.* **157**, 174701 (2022).

150. Lange, H. & Kelley, D. F. Spectroscopic Effects of Lattice Strain in InP/ZnSe and InP/ZnS Nanocrystals. *J. Phys. Chem. C* **124**, 22839–22844 (2020).

151. Jang, E., Kim, Y., Won, Y.-H., Jang, H. & Choi, S.-M. Environmentally Friendly InP-Based Quantum Dots for Efficient Wide Color Gamut Displays. *ACS Energy Lett.* **5**, 1316–1327 (2020).

152. Hinuma, Y., Grüneis, A., Kresse, G. & Oba, F. Band alignment of semiconductors from density-functional theory and many-body perturbation theory. *Phys. Rev. B* **90**, 155405 (2014).

153. Yuan, Y. *et al.* Cu-Catalyzed Synthesis of CdZnSe–CdZnS Alloy Quantum Dots with Highly Tunable Emission. *Chem. Mater.* **31**, 2635–2643 (2019).

154. Valencia, D. *et al.* Unravelling the chemical reactions of fatty acids and triacylglycerides under hydrodeoxygenation conditions based on a comprehensive thermodynamic analysis. *Biomass Bioenergy* **112**, 37–44 (2018).

155. Brodu, A. *et al.* Exciton Fine Structure and Lattice Dynamics in InP/ZnSe Core/Shell Quantum Dots. *ACS Photonics* **5**, 3353–3362 (2018).

156. Labeau, O., Tamarat, P. & Lounis, B. Temperature Dependence of the Luminescence Lifetime of Single CdSe/ZnS Quantum Dots. *Phys. Rev. Lett.* **90**, 257404 (2003).

157. Wang, X., Yu, J. & Chen, R. Optical Characteristics of ZnS Passivated CdSe/CdS Quantum Dots for High Photostability and Lasing. *Sci. Rep.* **8**, 17323 (2018).

158. Vikram, A. *et al.* Unraveling the Origin of Interfacial Oxidation of InP-Based Quantum Dots: Implications for Bioimaging and Optoelectronics. *ACS Appl. Nano Mater.* **3**, 12325–12333 (2020).

159. Stein, J. L. *et al.* Probing Surface Defects of InP Quantum Dots Using Phosphorus Kα and Kβ X-ray Emission Spectroscopy. *Chem. Mater.* **30**, 6377–6388 (2018).

160. Marshall, L. F. Spectral dynamics of single quantum dots : a study using photon-correlation Fourier spectroscopy for submillisecond time resolution at low temperature and in solution. (Massachusetts Institute of Technology, 2011).

161. Brokmann, X., Bawendi, M., Coolen, L. & Hermier, J.-P. Photon-correlation Fourier spectroscopy. *Opt. Express* **14**, 6333–6341 (2006).

162. Beyler, A. P., Marshall, L. F., Cui, J., Brokmann, X. & Bawendi, M. G. Direct Observation of Rapid Discrete Spectral Dynamics in Single Colloidal CdSe-CdS Core-Shell Quantum Dots. *Phys. Rev. Lett.* **111**, 177401 (2013).

163. Besombes, L., Kheng, K., Marsal, L. & Mariette, H. Acoustic phonon broadening mechanism in single quantum dot emission. *Phys. Rev. B* **63**, 155307 (2001).

164. Virtanen, P. *et al.* SciPy 1.0: Fundamental Algorithms for Scientific Computing in Python. *Nat. Methods* **17**, 261–272 (2020).

165. Powell, M. J. D. An efficient method for finding the minimum of a function of several variables without calculating derivatives. *Comput. J.* **7**, 155–162 (1964).

166. Muller, A., Fang, W., Lawall, J. & Solomon, G. S. Emission Spectrum of a Dressed Exciton-Biexciton Complex in a Semiconductor Quantum Dot. *Phys. Rev. Lett.* **101**, 027401 (2008).

167. Laferrière, P. *et al.* Unity yield of deterministically positioned quantum dot single photon sources. *Sci. Rep.* **12**, 6376 (2022).

168. Haffouz, S. *et al.* Bright Single InAsP Quantum Dots at Telecom Wavelengths in Position-Controlled InP Nanowires: The Role of the Photonic Waveguide. *Nano Lett.* **18**, 3047–3052 (2018).

169. Coolen, L., Brokmann, X., Spinicelli, P. & Hermier, J.-P. Emission Characterization of a Single CdSe-ZnS Nanocrystal with High Temporal and Spectral Resolution by Photon-Correlation Fourier Spectroscopy. *Phys. Rev. Lett.* **100**, 027403 (2008).

170. Luo, Y. & Wang, L.-W. Electronic Structures of the CdSe/CdS Core−Shell Nanorods. *ACS Nano* **4**, 91–98 (2010).

171. Nasilowski, M., Spinicelli, P., Patriarche, G. & Dubertret, B. Gradient CdSe/CdS Quantum Dots with Room Temperature Biexciton Unity Quantum Yield. *Nano Lett.* **15**, 3953–3958 (2015).

172. Protesescu, L. *et al.* Nanocrystals of Cesium Lead Halide Perovskites (CsPbX3, X = Cl, Br, and I): Novel Optoelectronic Materials Showing Bright Emission with Wide Color Gamut. *Nano Lett.* **15**, 3692–3696 (2015).

173. Proppe, A. H. *et al.* Adversarial autoencoder ensemble for fast and probabilistic reconstructions of few-shot photon correlation functions for solid-state quantum emitters. *Phys. Rev. B* **106**, 045425 (2022).

174. Cortes, C. L., Adhikari, S., Ma, X. & Gray, S. K. Accelerating quantum optics experiments with statistical learning. *Appl. Phys. Lett.* **116**, 184003 (2020).

175. Mangum, B. D., Ghosh, Y., Hollingsworth, J. A. & Htoon, H. Disentangling the effects of clustering and multi-exciton emission in second-order photon correlation experiments. *Opt. Express* **21**, 7419–7426 (2013).

176. Chen, B., Li, D. & Wang, F. InP Quantum Dots: Synthesis and Lighting Applications. *Small* **16**, 2002454 (2020).

177. Quintero-Bermudez, R., Sabatini, R. P., Lejay, M., Voznyy, O. & Sargent, E. H. Small-Band-Offset Perovskite Shells Increase Auger Lifetime in Quantum Dot Solids. *ACS Nano* **11**, 12378–12384 (2017).

178. Chandrasekaran, V. *et al.* Nearly Blinking-Free, High-Purity Single-Photon Emission by Colloidal InP/ZnSe Quantum Dots. *Nano Lett.* **17**, 6104–6109 (2017).

179. Verberk, R. & Orrit, M. Photon statistics in the fluorescence of single molecules and nanocrystals: Correlation functions versus distributions of on- and off-times. *J. Chem. Phys.* **119**, 2214–2222 (2003).

180. Hoang, T. B., Akselrod, G. M. & Mikkelsen, M. H. Ultrafast Room-Temperature Single Photon Emission from Quantum Dots Coupled to Plasmonic Nanocavities. *Nano Lett.* **16**, 270–275 (2016).

181. Fedin, I. *et al.* Enhanced Emission from Bright Excitons in Asymmetrically Strained Colloidal CdSe/CdxZn1–xSe Quantum Dots. *ACS Nano* **15**, 14444–14452 (2021).

182. Canneson, D. *et al.* Blinking suppression and biexcitonic emission in thick-shell CdSe/CdS nanocrystals at cryogenic temperature. *Phys. Rev. B* **89**, 035303 (2014).

183. Louyer, Y. *et al.* Efficient Biexciton Emission in Elongated CdSe/ZnS Nanocrystals. *Nano Lett.* **11**, 4370–4375 (2011).

184. Klein, J. *et al.* Scalable single-photon sources in atomically thin MoS2. Preprint at https://doi.org/10.48550/arXiv.2002.08819 (2020).

185. Tomm, N. *et al.* A bright and fast source of coherent single photons. *Nat. Nanotechnol.* **16**, 399–403 (2021).

186. Jung, H., Ahn, N. & Klimov, V. I. Prospects and challenges of colloidal quantum dot laser diodes. *Nat. Photonics* **15**, 643–655 (2021).

187. Taguchi, S., Saruyama, M., Teranishi, T. & Kanemitsu, Y. Quantized Auger recombination of biexcitons in CdSe nanorods studied by time-resolved photoluminescence and transient-absorption spectroscopy. *Phys. Rev. B* **83**, 155324 (2011).

188. Tyagi, P. & Kambhampati, P. False multiple exciton recombination and multiple exciton generation signals in semiconductor quantum dots arise from surface charge trapping. *J. Chem. Phys.* **134**, 094706 (2011).

189. Canneson, D. *et al.* Enhancing the fluorescence of individual thick shell CdSe/CdS nanocrystals by coupling to gold structures. *New J. Phys.* **14**, 063035 (2012).

190. Zhu, C. *et al.* Room-Temperature, Highly Pure Single-Photon Sources from All-Inorganic Lead Halide Perovskite Quantum Dots. *Nano Lett.* **22**, 3751–3760 (2022).

191. Bischof, T. S., Correa, R. E., Rosenberg, D., Dauler, E. A. & Bawendi, M. G. Measurement of Emission Lifetime Dynamics and Biexciton Emission Quantum Yield of Individual InAs Colloidal Nanocrystals. *Nano Lett.* **14**, 6787–6791 (2014).

192. Brown, R. H. & Twiss, R. Q. Correlation between Photons in two Coherent Beams of Light. *Nature* **177**, 27–29 (1956).

193. Shulenberger, K. E. *et al.* Resolving the Triexciton Recombination Pathway in CdSe/CdS Nanocrystals through State-Specific Correlation Measurements. *Nano Lett.* **21**, 7457–7464 (2021).

194. Utzat, H. *et al.* Probing Linewidths and Biexciton Quantum Yields of Single Cesium Lead Halide Nanocrystals in Solution. *Nano Lett.* **17**, 6838–6846 (2017).

195. Shi, J. *et al.* All-optical fluorescence blinking control in quantum dots with ultrafast mid-infrared pulses. *Nat. Nanotechnol.* **16**, 1355–1361 (2021).

196. Long, Z. *et al.* The Strain Effects and Interfacial Defects of Large ZnSe/ZnS Core/Shell Nanocrystals. *Small* **20**, 2306602 (2024).

197. Goswami, B., Pal, S. & Sarkar, P. A Theoretical Study on the Electronic Structure of ZnSe/ZnS and ZnS/ZnSe Core/Shell Nanoparticles. *J. Phys. Chem. C* **112**, 11630–11636 (2008).

198. Wang, Z.-P. *et al.* Type-I Core–Shell ZnSe/ZnS Quantum Dot-Based Resistive Switching for Implementing Algorithm. *Nano Lett.* **20**, 5562–5569 (2020).

199. Ji, B., Koley, S., Slobodkin, I., Remennik, S. & Banin, U. ZnSe/ZnS Core/Shell Quantum Dots with Superior Optical Properties through Thermodynamic Shell Growth. *Nano Lett.* **20**, 2387–2395 (2020).

200. Sukkabot, W. Influence of ZnSe core on the structural and optical properties of ZnSe/ZnS core/shell nanocrystals: Tight-binding theory. *Superlattices Microstruct.* **75**, 739–748 (2014).

201. Cragg, G. E. & Efros, A. L. Suppression of Auger Processes in Confined Structures. *Nano Lett.* **10**, 313–317 (2010).

202. Laurence, T. A., Fore, S. & Huser, T. Fast, flexible algorithm for calculating photon correlations. *Opt. Lett.* **31**, 829 (2006).

203. Brokmann, X., Bawendi, M., Coolen, L. & Hermier, J.-P. Photon-correlation Fourier spectroscopy. *Opt. Express* **14**, 6333 (2006).

204. Spokoyny, B. *et al.* Effect of Spectral Diffusion on the Coherence Properties of a Single Quantum Emitter in Hexagonal Boron Nitride. *J. Phys. Chem. Lett.* **11**, 1330–1335 (2020).

205. Beyler, A. P. *et al.* Sample-Averaged Biexciton Quantum Yield Measured by Solution-Phase Photon Correlation. *Nano Lett.* **14**, 6792–6798 (2014).